ENSC-2015 n°580

THÈSE DE DOCTORAT
DE L'ÉCOLE NORMALE SUPÉRIEURE DE CACHAN

Présentée par

Mateusz Bogdan

pour obtenir le grade de

DOCTEUR DE L'ÉCOLE NORMALE SUPÉRIEURE DE CACHAN

Domaine

MÉCANIQUE - GÉNIE MÉCANIQUE - GÉNIE CIVIL

Sujet de la thèse

Modélisation morphologique multi-échelles de matériaux cimentaires

—

Application à la prédiction de propriétés effectives de diffusion

Soutenue le 12 juin 2015, devant un jury composé de :

Pr. Thierry J. Massart	Univ. Libre de Bruxelles	*Président du jury*
MCF-HDR. Siham Kamali-Bernard	INSA Rennes	*Rapporteure*
Pr. Ouali Amiri	Univ. de Nantes	*Rapporteur*
Pr. Jean-Michel Torrenti	IFSTTAR	*Examinateur*
Dr. Lavinia Stefan	AREVA NC	*Encadrante*
MCF-HDR. Farid Benboudjema	LMT Cachan	*Co-directeur*
Pr. Jean-Baptiste Colliat	LML, Univ. Lille 1	*Co-directeur*

LMT-Cachan
ENS Cachan / CNRS / PRES UniverSud Paris
61, avenue du Président Wilson, F-94235 Cachan cedex, France

Avants-propos

Ce document, rédigé en anglais, représente la synthèse de mes travaux de doctorat effectués au LMT-Cachan, dans le secteur Génie Civil et Environnement, entre 2011 et 2015, financés dans le cadre d'un accord Cifre avec Areva NC.

Résumé:
L'objectif de la présente thèse et de développer un cadre d'étude et de simulation apte à prédire les propriétés effectives de diffusion dans les matériaux cimentaires saturés. Le principe suivi, fondé sur les *approches multi-échelles séquencées*, permettra de modéliser chaque échelle d'intért, depuis le gel des C-S-H, jusqu'au matériau béton, et ainsi via des simulations de prédire les coefficients de diffusion effectifs.

Le cadre d'étude est donc fondé sur les points clés suivant :

- Des morphologies de type *matrice - inclusion* sont générées via des excursions de champs aléatoires corrélés tri-dimensionnels. Cette approche, combinée avec quelques opérations morphologiques, permet la génération de morphologies inclusionnaires 3D suivant des distributions de tailles imposées. Il est ensuite possible de faire évoluer ces morphologies, depuis un état initial, en fonction d'un modèle prescrit (par exemple en termes de fraction volumiques), via le seuil de l'excursion.

- Les cibles morphologiques de chaque échelle considérées tentent de refléter les résultats expérimentaux et modèles les plus communément admis. En supplément, à l'échelle de la pte de ciment, un modèle *simple* d'hydratation est développé afin de prédire l'évolution de celle-ci dans le temps en termes de fractions volumiques. Le choix a été fait d'utiliser pour fondement un modèle simple (Jennings & Tennis), incorporant des paramètres essentiels, tels que la composition minéralogique du ciment ou le rapport e/c. Des modifications mineures ont été apporté au modèle, afin de prendre en compte de récents résultats expérimentaux, concernant principalement la fin de l'hydratation ainsi que sa cinétique.

- Le cadre d'homogénéisation a été construit pour tre utilisable à toutes les échelles considérées, et il permet ainsi de prédire les propriétés effectives de diffusion avec des considération énergétiques d'équivalence entre échelles. De faon analogue à la théorie de Hill pour l'élasticité, le cadre d'étude assure une séparation d'échelle cohérente vis-à-vis des propriétés effectives de diffusion.

- Enfin, d'un point de vue numérique, les simulations utilisent les méthodes E-FEM, couplées à l'utilisation de maillages non-adaptés sur lesquels les morphologies sont *projetées*. De cette faon, les discontinuités géométriques (discontinuité de propriétés matériaux) sont sont assurés par les élément finis enrichis, et ne requièrent pas d'éléments joint, ou de *moyennage* de propriétés.

Les résultats de chaque échelle sont utilisés comme paramètres d'entrés pour les échelles suivantes. Depuis l'échelle des hydrates (C-S-H), jusqu'à l'échelle du béton, les coefficients de diffusion effectifs sont ainsi estimés.

Abstract:
The aim of the present Ph.D. is to develop a methodology and a simulation framework able to predict as accurately as possible effective properties regarding diffusion in saturated cement based materials. A sequenced multiscale framework is developed to perform numerical homogenization on diffusive properties, and thus predict effective properties. The general outline is to model every scale in concrete-like materials, from the C-S-H gel, to the concrete scale, and with the help of a proper framework, be able to predict effective properties.

The methodology relies on the following key points for every considered scale :

- Inclusion-matrix like morphologies are generated through level set methods applied to multi-dimensional correlated random fields. This approach, together with few morphological operations allows to generate 3D morphologies with given particle size distributions (PaSD), or pore size distributions. Then, it is also possible, from the initial state, to make those morphologies evolve according to any descriptive model (e.g. in terms of volume fraction), via the level set.

- The morphological description of each scale is chosen according to the most acknowledged experimentations and models. In addition, at the cement paste scale, a hydration model was developed to predict the evolution of the cement paste through time, in terms of volume fractions. The choice was made to keep a simple model (Jennings & Tennis), with few but essential input parameters (mineral cement composition, w/c ratio, PaSD). It has only been modified to include recent experimental results, such as the maximal hydration degree, or the hydration rates.

- The upscaling framework was built to suit every considered scale, and allows to assess effective properties based on energy conservation principles. Similar to Hill's theory for elasticity, the framework is build to ensure to proper scale separation regarding effective diffusion coefficients.

- Lastely, the numerical context is based on E-FEM techniques, which allows to use unstructured meshes, on which the morphologies are projected. This way, any material discontinuity in dealt within the FE, and thus does not require averaging properties, or joint elements.

Results from every scale will be used as inputs at the higher scales, and effective diffusion coefficients are thus estimated.

Remerciements

Suite à la rédaction de ce mémoire et à sa soutenance, je souhaite ici remercier un certain nombre de personnes qui m'ont accompagné tout au long de cette thèse.

Dans un premier temps je tiens à remercier les rapporteurs de ce manuscrit, la MCF S. Kamali-Bernard et le Pr. O. Amiri qui ont accepté la lourde tâche de relecture, et ce dans un délai restreint. Leurs commentaires ainsi que les discussions lors de la soutenance ont permis d'améliorer sensiblement ce document. Je tiens également à remercier les examinateur de cette thèse, MM. les Professeurs J.-M. Torrenti et T.J. Massart, qui ont aussi beaucoup contribué aux débats suivant la soutenance.

Mes remerciements vont ensuite à l'équipe qui m'a dirigé et encadré, la Dr. Lavinia Stefan et les Professeurs J.-B. Colliat et F. Benboudjema. Ils ont su m'initier me conseiller tout au long de cette thèse. Avec chacun leurs spécialités ils m'ont montré et illustré la pluridisciplinarité nécessaire dans le monde de la recherche, et ils ont su me garder ouvert à ses différentes facettes.

Un grand merci aussi à Manu et Xavier pour m'avoir dès le M2 introduit au monde de la recherche, m'avoir donné l'envie de poursuivre avec cette thèse, et m'avoir accompagné pendant une bonne partie de celle-ci. Je remercie également Alexis et Mahban pour m'avoir de nombreuses fois « dépanné » informatiquement, et m'avoir permis d'utiliser certains de leurs développements.

Merci aussi au département de Génie Civil de l'ENS Cachan, au *LMT-Cachan* avec son ambiance sans égale, aux personnes qui les composent, le personnel, les étudiants, les (post-) doctorants, les enseignants, les professeurs, ... Une pensée particulière à Frisou, Boubou, Pierre, Pascale, Zouzou, Morgane, Kalach', Alexis, Martin, Maxime, Claire, Agnieszka, Zvon, Ante, Remy, Mehdi, Pascale, Aveline, Caro et à tous ceux que j'oublie...

À tous les potes, au *Boogie Style*, à ces années étudiantes à l'ENS, à ceux de J.-B.S. ; aux coloc' Camille, Jerem' et p'tit Jerem ; aux frères Mialon et à Fontaine, au jardin scéen et à ses apéros ; à la Villa, au Clos, et à tous ces endroits qui ont jonché ma vie parisienne.

Last but not least, je tiens tout particulièrement à remercier ceux qui m'accompagnent depuis toujours, ma famille. Bartek pour tes commentaires réfléchis, posés et ta clairvoyance, Tomek pour avoir été (entre autres...) ma soupape de secours ces dix dernières années, et enfin mes parents, qui ont toujours su être là pour moi, que ce soit le moment ou pas!

École Normale Supérieure de Cachan

ENSC-2015-n°580

Ph.D. Thesis

Morphological multiscale modeling of cementitious materials

—

Numerical homogenization of effective diffusive properties

Defended June 12th, 2015

Author:
Mateusz BOGDAN

Supervisors:
Dr. Lavinia Stefan
Pr. Farid Benboudjema
Pr. Jean-Baptiste Colliat

It's just a temporary thing...

Lou Reed, *1976*

Contents

Contents i

General Introduction 1

1 Cementitious materials, microstructural characterization 5
1 Introduction . . . 6
2 Portland Cement . . . 7
2.1 Portland cement composition . . . 7
2.2 Particle size distribution . . . 8
3 The hydration reaction . . . 8
3.1 Main stages . . . 8
3.2 Meaningful parameters . . . 10
3.2.1 The hydration degree ξ . . . 11
3.2.2 The maximum hydration degree . . . 11
4 Phenomenological hydration modeling . . . 11
4.1 Powers . . . 12
4.2 Jennings & Tennis . . . 14
4.3 Modeling amendments . . . 15
4.3.1 Anhydrous cement composition and individual hydration rates . . . 15
4.3.2 Overall and maximal hydration degree: ξ_{tot} and $\xi_{\max}$ 16
4.4 Hydration modeling simplifications . . . 19
4.4.1 Water content and distribution . . . 19
4.4.2 Implementation's simplifications . . . 20
5 Microstructure and morphology of cementitious materials . . . 20
5.1 Hydrate structure . . . 21
5.1.1 The Calcium Silicate Hydrates: C-S-H . . . 23
5.1.2 The Portlandite: $Ca(OH)_2$ . . . 25
5.1.3 Calcium sulfoaluminate hydrate . . . 25
5.1.4 Anhydrous cement residue . . . 27
5.2 Interstitial solution . . . 27
5.3 Pore network structure . . . 28

5.3.1 Porous materials: definitions . . . 28
5.3.2 Traditional investigation techniques . . . 29
5.3.3 Recent advances in structural characterizations . . . 34
5.3.4 Hydrate pore network . . . 35
5.3.5 Cement paste pore network . . . 38
5.3.6 Mortar and concrete pore network . . . 40
6 Concluding remark . . . 44

2 Morphological modeling of cement based materials 47
1 Introduction . . . 48
2 Morphological modeling framework . . . 48
2.1 Correlated Random Fields . . . 48
2.1.1 Random Variables and Random Fields . . . 48
2.1.2 Gaussian distributions & covariance functions . . . 50
2.2 Excursion set theory . . . 52
2.3 Excursion set measurements . . . 55
2.3.1 Geometrical and topological measures: Lipschitz Killing Curvatures . . . 55
2.3.2 Minkowski functionals . . . 56
2.4 The expectation formula . . . 56
2.4.1 Explicit formula for Gaussian (γ) field . . . 59
2.5 Morphological operations . . . 60
3 Percolation and statistical representativity . . . 61
3.1 Numerical approach to the Statistical RVE . . . 61
4 Application to hydration modeling . . . 66
4.1 Existing models . . . 66
4.1.1 CEMHYD3D . . . 66
4.1.2 HymoStruc3D . . . 67
4.2 Reaching high volume fractions . . . 68
4.3 Polydisperse inclusions and Particle Size Disrtributions . . . 70
4.3.1 General principle: multiple correlation lengths . . . 70
4.3.2 Application with PaSD . . . 76
4.3.3 Application with PoSD . . . 77
4.4 Morphologies evolutions . . . 78
4.4.1 n-phase morphologies . . . 78
4.4.2 The Hydration Process . . . 78
5 Hydration model validation . . . 80
5.1 Total porosity . . . 81
5.2 Pore size distributions . . . 83
5.3 Tortuosity . . . 88
6 Concluding remarks . . . 91

3 Diffusive Properties Prediction in Cementitious Materials 93
1 Introduction . . . 94
2 Diffusion in Cementitious Materials . . . 94
2.1 Diffusion: General Principles . . . 94
2.2 Diffusion through porous materials . . . 95
2.2.1 Diffusion within the porosity . . . 96
2.2.2 Diffusion with interactions, binding . . . 96
2.2.3 Binding and Radioactive decay . . . 97
2.2.4 Infinite volume of water . . . 97
2.3 Diffusion coefficient measurements . . . 98
2.3.1 Natural diffusion . . . 98
2.3.2 Forced diffusion . . . 100
2.4 Cementitious materials: Results . . . 102
2.4.1 Cement pastes . . . 102
2.4.2 Mortar and concrete scale . . . 104
2.4.3 Other influential parameters . . . 108
2.4.4 Nanometric scale . . . 109
3 Analytical homogenization . . . 110
3.1 Analytical Bounds . . . 110
3.2 Analytical Homogenization . . . 111
4 Experimentation based models . . . 113
4.1 NIST approache . . . 113
4.2 Tognazzi's model . . . 114
5 Remarks on (semi-)analytical models . . . 114
6 Numerical homogenization . . . 115
6.1 Literature review . . . 116
6.1.1 Hymostruc Framework . . . 117
6.1.2 Volume FEM approach . . . 117
6.2 Multi-scale approach: Energy Based Framework . . . 119
7 Concluding remarks . . . 122

4 Numerical approach and results 125
1 Introduction . . . 126
2 Finite Element framework . . . 126
2.1 Meshing process . . . 126
2.2 Weak discontinuities . . . 127
2.3 Implementation . . . 128
2.3.1 Truss Elements . . . 129
2.3.2 Volume Elements . . . 129
3 Results . . . 130
3.1 Study case . . . 130
3.2 Mesh dependency . . . 132
3.3 Initial step: the bulk C-S-H . . . 133

3.3.1 C-S-H porosity . . . 134
3.3.2 Pore size distribution . . . 135
3.3.3 Morphologies . . . 135
3.3.4 Effective properties . . . 136
3.4 Cement paste scale . . . 143
3.4.1 Initial morphologies parameters and hydration . . . 143
3.4.2 Effective diffusion coefficient through hydration . . . 145
3.4.3 Remarks and perspectives . . . 147
3.4.4 Mechanical implementation: Young modulus evolution 151
3.4.5 LBM implementation . . . 153
3.5 Mortars . . . 155
3.5.1 Standard B-11 mortar . . . 155
3.5.2 Comparison with glass beads experiments . . . 157
3.5.3 ITZ . . . 158
3.6 Concrete scale . . . 161

Conclusions and Outlooks **163**

Appendices **169**

A Percolation RVE **171**
1 Accounting for side effects . . . 172
2 Representative Volume Element for percolation . . . 174

Bibliography **177**

General Introduction

Cement based materials are nowadays the most used materials for civil engineering applications. From simple constructions, to nuclear power plants or waste storage facilities, they are the second most used "manufactured" products after drinking water. They are used both as a structural material and a containment one, with increasing requirements in terms of durability and resistance to multiple types of loads: thermal, hydric, mechanical and chemical.

In this present work, focus is made on mass transport phenomena, and more specifically on diffusion. The aim, closely linked with durability assessments, is to forecast actual effective diffusion coefficients for cementitious materials, at various scales of interest.

The effective response of such heterogeneous materials to various solicitations can be modeled through various approaches:

- Macroscopic models, that consider the material properties as homogeneous. The complexity of multi-physics responses, however, leads to an increasing complexity for this family of approaches, with an increasing number of parameters more and more difficult to identify.

- Meso- (micro-) models, where the actual heterogeneities are explicitly modeled, at each scale. Their aim is to compute the macroscopic behavior of disorderd meso- (micro-) structures such as the effective diffusion coefficient, or concentration maps.

Due to the intrinsic multi-scale nature of cementitious materials (Fig. 1), the second family of modeling approaches is considered in this work.

Following, the use of sequenced multi-scale frameworks [Feyel and Chaboche, 2000] allow to "upscale" the effective properties of interest from small to large scales.

Such choice is not new, and discrete modeling approaches are very attractive to study transport in heterogeneous materials. To provide some examples, [Jerauld and Salter, 1990] started to study the effect of the pore structure for permeability issues and hysteretic behavior, using networks of spheres and cylinders. Slightly different approaches as in [Sadouki and Van Mier, 1997] used lattices considered as conductive "pipes", in order to study moisture flow in cementitious materials. More recently [Grassl, 2009] used a regular lattice approach to model flows in cracked

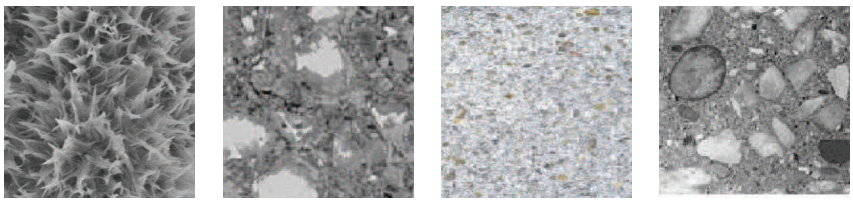

Figure 1: Major scales found in cemetitious materials.

concretes, or [Bolander and Berton, 2004] with random lattices and moisture transport. The same type of studies can be found in [Massart and Selvadurai, 2014], with tetrahedral FE, to study crack induced permeability in rocks.

The overall aim of this work — previously introduced as a forecast method for effective diffusion coefficients in cementitious materials — can be decomposed in three main stages, following the key scientific development undertaken during this Ph.D.:

1. Based on a literature review, a hydration model for cement paste must be retained. It must take into account severals parameters, such as the mineral composition of the cement and the mix-design parameters. It will be able to describe the various volume fractions found in hydrating (and hardened) cement pastes, with an emphasis on a "good" porosity prediction. Additionally, the model should be able to take into account mineral substitution for *Portland* cement, such as fly ashes or blast furnace.

2. An original morphological tool able to represent cementitious materials, suited for all the scales, will be chosen and adapted to the various types of microstructures found in cement based materials.

3. A theoretical and numerical simulation framework suited for diffusion phenomena as well as for a numerical upscalling of effective diffusion coefficients.

To be able to describe as accurately as possible each scale, first an understanding of of the hydration phenomena leading to hardened cement paste is necessary, and presented in **Chapter 1**. It is shown how the cement, as an hydraulic binder, evolves from the initial suspension in water to a solid material. Several models are presented to describe the various phases found in hardened cement paste, along with a description of their evolution through time. Emphasis is then made on the proper description of the pore network, with the corresponding experimental characterization methods. Finally, based on a literature review, a scale separation is proposed,

to be implemented in a sequenced multi-scale framework.

The actual morphological representation tool considered is presented in **Chapter 2**. A consistent framework based upon Correlated Random Fields (hereafter CRFs) and *excursion sets theory* [Adler, 2008] is retained for every scale considered. It is shown how to yield matrix / inclusions like morphologies, and how to control them through a statistical link between the CRF parameters and a threshold on one side, and the geometrical and topological properties of the yielded morphologies on the other side. Several issues related to cementitious materials are then addressed, such as the high volume fractions of inclusions needed either for the initial suspension of cement, or to model the granular skeleton at the mortar and concrete scales ; or the representation of particle / grain size distributions ; or finally the representation of multi-phase morphologies (*e.g.* at the cement paste scale, with in a first approximation the anhydrous cement, the hydrates, and the porosity).

Side results concerning the percolation in a three dimensional space, as well as side effect accounting for percolation phenomena are also derived from the statistical link in previously introduced.

The key parameter for durability issues being the pore network (overall porosity as well as Pore Size Distributions, hereafter PoSD), a morphological tool to "measure" the PoSD and the tortuosity is also briefly introduced, and used to characterize the generated morphologies.

Finally, the previous chapter phenomenological hydration models — describing the evolution through time of cement pastes — are linked with the present morphological framework. A set of qualitative validations is then presented to ensure a good description of the pore space, according to several variables.

In **Chapter 3** a description of diffusion phenomena governing equations is given, with an emphasis on *effective* properties (in opposition to *apparent* ones). Following, various experimental and numerical results are presented, with the same emphasis on *effective properties*.

It is shown that at the thinner scale (hydrate scale – nanometer), the diffusion phenomena are not driven by the same equations [Korb et al., 1998], and the effective diffusion coefficents for hydrates are assessed. At the CP scale, a review of pertinent influential parameters is presented, with obviously the influence of the porosity. Next, at the mortar and concretes scales, the toruosity increase is shown to be compensated by the Interfacial Transition Zone (hereafter ITZ) found around the aggregates. For all the considered scales, results in terms of effective diffusion coefficients are listed, with respect to the most influential parameters such as the porosity, the water to cement (w/c) ratio, and the aggregates volume fractions.

Then, the retained upscalling framework is presented, based on Hill's concept of homogenized properties [Hill, 1963] and dissipated energy equivalence between consecutive scales. It is applied to diffusion phenomena, starting at the hydrate scale (C-S-H), up to the concrete one.

In **Chapter 4**, we finally present a numerical framework suited to heterogeneous materials, based on non-adapted mesh methods, and concentration gradient fields enhancements (E-FEM).

The coupled hydration – morphological – numerical frameworks are then applied as a model at the various scales, starting with cement hydrates. An effective diffusion coefficient is derived for the C-S-H phase found in hardened cement paste. The simplest and most recent experimental results are used as inputs in terms of material and morphological properties (diffusion coefficient for water in confined spaces, and porosity description). Similar results are found with two different numerical approaches, self-supporting each other.

Then, at the CP scale, the same methodology is applied to assess diffusive properties throughout hydration, as for hardened materials. It is shown that the model is able to qualitatively render the porosity influence, with an evolution of the effective diffusion coefficient that has two main modes. For high porosity, the diffusion is driven by the capillary network — which is percolated —, whereas for low porosities, the evolution of the effective porosities shifts to a second mode where the diffusion is driven by the percolated hydrates. However, quantitatively, in a first approach the results are found far off the experimental results. A variety of reason can explain the discrepancies, and the most obvious one is the lack of tortuosity in the pore network. Few attempts are then presented to overcome the biased predictions.

Lastly, at the mortar and concrete scales, where the cement paste is considered as homogeneous, the heterogeneities are the aggregates and the ITZ. The later present some issues in the modeling approach, especially the actual representation through a constant thickness.

1 Cementitious materials, microstructural characterization

Contents

1 Introduction 6

2 Portland Cement 7

2.1 Portland cement composition 7

2.2 Particle size distribution 8

3 The hydration reaction 8

3.1 Main stages 8

3.2 Meaningful parameters 10

4 Phenomenological hydration modeling 11

4.1 Powers 12

4.2 Jennings & Tennis 14

4.3 Modeling amendments 15

4.4 Hydration modeling simplifications 19

5 Microstructure and morphology of cementitious materials 20

5.1 Hydrate structure 21

5.2 Interstitial solution 27

5.3 Pore network structure 28

6 Concluding remark 44

1 Introduction

Cement belongs to the wide family of hydraulic binders: it is a finely ground mineral powder, which reacts when mixed with water to create a paste, which sets and hardens by means of a hydration reaction.

Even if today it remains the most used construction materials on the planet (approximately $1\,m^3$ per year per inhabitant), it is still not fully understood, and it remains the subject of numerous researches. The matrix that "glue" together the granular skeleton, known as the cement paste, is a porous material. Its porosity is taken to be the key feature in most effective material properties, from mechanical responses [Coussy, 2004, Dormieux et al., 2006] to transport properties [Baroghel Bouny, 1994].

The pore sizes in concrete range from around a *nanometer* to few *millimeters*, as illustrated Fig. 1.1, with at each scale a "particular material", from the C-S-H particles to the concrete macroscopic scale.

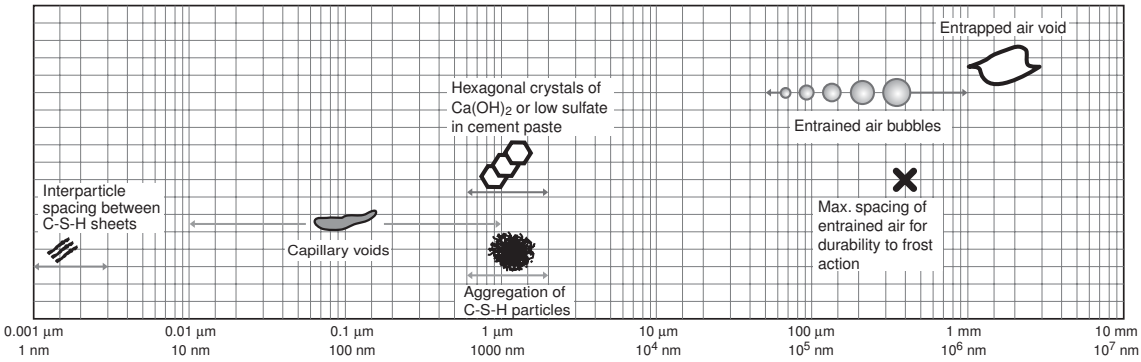

Figure 1.1: Dimensional range of solid and pores in hydrated cement paste – *from* [Mehta and Monteiro, 2005].

This first chapter gives a presentation of cementitious materials, from both a chemical point of view, with the evolution of the hydration mechanisms and the introduction of a simplified hydration model ; and geometrical point of view with the descriptions and characterization of the various hydrates found in hardened cement pastes.

A review of pertinent experimental methods to characterize cement based material microstructures is then made, focusing on the description and and quantification of the poral space. The aim is to highlight the well investigated scales ($\phi \leq 10\,nm$ for example), and the relevant characteristics, but most importantly point out the missing information, and propose a description of the gap between capillary pores and hydrates pores. It will lead to a first scale separation in the overall modeling framework, considering a first modeling stage at the hydrate scale, and a second stage for the cement paste itself.

2 Portland Cement

Portland cement is produced first by heating a mixture of clay and limestone to a temperature around 1450 °C. The partial fusion that occurs allows for clinker formation. The latter is then mixed with approximately five percent of gypsum, and finally finely ground. An overall description of the fabrication process can be found in [Taylor, 1997] or [Mehta and Monteiro, 2005].

2.1 Portland cement composition

Function of the type of structure to be built, various types of cements are available. They differ mostly by their chemical composition, as well as their fineness. Those two parameters will be among the most important in regards to durability, mechanical strength at early ages, and hydration kinetics.

Portland cement consists essentially of various calcium compounds, and they are all made from the same six main oxides. A chemical analysis allows to determine the various oxides content (Tab. 1.1, with the cement industry abbreviations).

The estimation of the compound content is much more difficult. Direct methods require a direct observation of the cement phases. Among the most used methods one can find the X-ray Diffraction (XRD) [Signes-Frehel et al., 1996], X-ray fluorescence (XRF), or Scanning electron microscopy (SEM) [Bentz and Stutzman, 1994].

The most commonly used method remains an indirect one. The Bogue method [Bogue, 1952] is a solution of a set of linear equations, that predicts the compounds' repartition, given that the quantities of the main oxides are known. Even after additional modifications ([Taylor, 1989]), several hypothesis remain for the calculations, and an accurate and detailed knowledge of the oxide composition is required. If data from SEM is the most trustworthy [Bentz et al., 2000a], it can be shown that the Bogue method underestimates the C_3S quantity and overestimates the other compounds, whereas the modified Bogue calculation tends to the opposite. However, it remains a widely used method to get an approximate phase content distribution. A typical content is listed in Tab. 1.2. In addition, *gypsum* is also present in small proportions (up to 5%) in order to regulate the hydration reaction and avoid false setting of the cement paste.

Oxide	Abbreviation	Mass content
CaO	C	60 - 69%
SiO_2	S	18 - 24%
Al_2O_3	A	4 - 8%
Fe_2O_3	F	1 - 8%
MgO	M	0 - 5%
SO_3	$\overline{S}$	0 - 3%

Table 1.1: Main cement oxides – *from* [Taylor, 1997].

Compound	Abbreviation	Mass content	Setting period
$3\,Ca\,0\cdot SiO_2$	C_3S - Alite	50 - 70%	fast (hours)
$2\,Ca\,0\cdot SiO_2$	C_2S - Belite	15 - 30%	slow (days)
$3\,Ca\,0\cdot Al_{203}$	C_3A - Celite	5 - 15%	immediate
$4\,C\,a_0\cdot Al_{203}\cdot Fe_2O_3$	C_4AF - Ferrite	5 - 15%	very fast (minutes)

Table 1.2: Main cement compounds – *from* [Mindess et al., 2003].

2.2 Particle size distribution

Portland cement consists of particles that vary in size from about 1 to 100 µm, with a mean size around 10 - 15 µm. The Particle Size Distribution (PaSD) depends on the type and intensity of the clinker grinding. The PaSD allows also to define the cement *fineness*, which will influence the cement reactivity, and the overall hydration rate. Finer cement particles will have a higher surface area, which will increase the reaction rate. It is usually expressed as the cumulative mass fraction of particles, for a range of equivalent diameters.

Several methods to measure the PaSD and fineness exist, from sedimentation-based methods, laser diffraction, air separator, optical microscopy to air-permeability. All those methods, directly or indirectly, assume that the particles are equivalent to spheres [van Breugel, 1997]. In the following chapters we will rely on the so-called "Blaine fineness" (European standard EN 196-6): the principle is to measure the air permeability of a cement sample, first deduce the specific area, and then under the mentioned assumption of spherical grains, it is possible to retrieve the PaSD. An typical curve is showed Fig. 1.2, obtained with laser granulometry, where the solid line and dashed line correspond respectively to the cumulative volume fraction and the size distribution. Ordinary Portland cement paste have a surface area in the range of 300 - 350 $m^2\,kg^{-1}$.

3 The hydration reaction

The reaction of Portland cement with water is known as *hydration*, and the newly formed compounds are called the *hydration products*. It includes the totality of the reaction taking place resulting in the setting and hardening of the cement paste. We present here only an overall description, and the reader is refered to [Bogue, 1952], [Taylor, 1997] or [Mehta and Monteiro, 2005] for the chemical detailed process.

3.1 Main stages

This complex process can be divided in four main steps, as presented in Fig. 1.3.

I – Pre-induction period

This initial reaction starts within minutes (from 1 to few dozens of minutes,

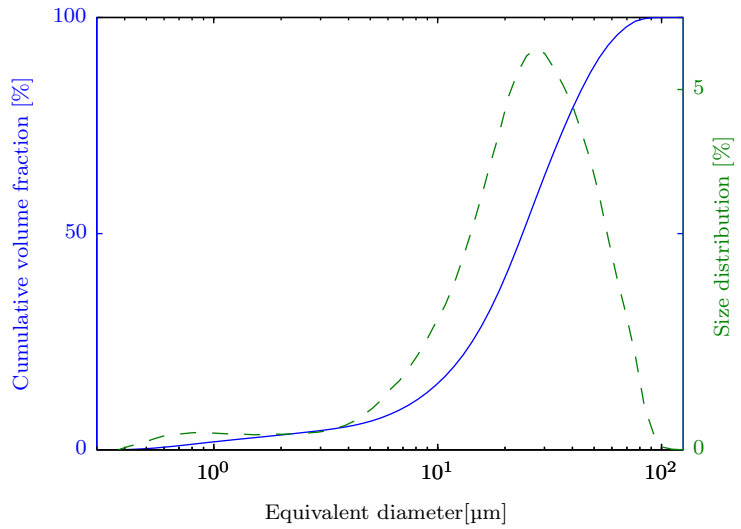

Figure 1.2: Pore size distribution in cement pastes obtained with the *Laser diffraction* procedure - CEM I – *courtesy of* K.Oliver.

depending on the initial mineral composition [Garrault-Gauffinet and Nonat, 1999]) after anhydrous cement is mixed with water (phase **I**, Fig. 1.3). A significant amount of heat is released, and it corresponds to the fast reaction of C_3S and C_3A. The alkali sulfates dissolve completely, followed by a dissolution of the calcium sulfates until saturation. Ettringite rods are yielded on the aluminate surfaces, as well as in the matrix.

II – Induction or dormant period

After the initial dissolution period, the hydration rate slows down for a period of few hours (phase **II**, Fig. 1.3). There is no definitive explanation for this phenomenon, but several theories exist:

- [Jennings and Pratt, 1979] proposed a mechanism where the initial period yields a protective layer around the cement particles. During the induction phase, the hydration kinetics is driven by the slow diffusion through the protective layer, and the Ca^{2+} ions dissolve slowly in the interstitial solution. The end of that period is marked when this layer becomes more permeable, allowing new hydrates creation.

- [Taylor, 1997] proposed a similar mechanism, but they considered a threshold concentration in the interstitial solution. As soon as the solution is saturated in Ca^{2+} and OH^- ions, the new hydrate precipitation is made possible.

III – Acceleration period

When the induction period ends, a large amount of heat is dissipated. The reaction

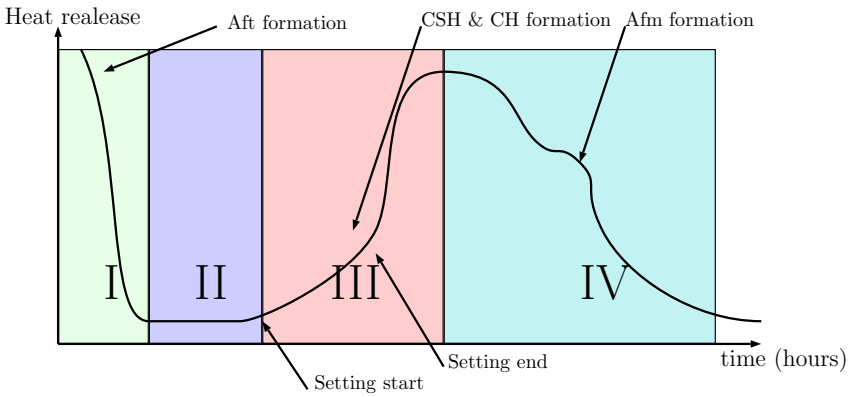

Figure 1.3: Schematic heat release evolution during Portland cement hydration – *adapted from* [Stefan, 2009, Chen, 2006].

is controlled by the nucleation and growth of the new hydration products: C-S-H and CH. They come mainly from the C_3S and C_2S reactions. The new C-S-H are yielded around the cement grains and the ettringite already present, with various morphologies according to the available space. When the new hydrates around adjacent grains come into contact, the solid phase starts to percolate, resulting in the binding of the solids together and the overall strength development. As for the CH, they form massive crystals in the available free space.

IV – Deceleration period

As the hydration slows gradually, the amount of unreacted cement reduces, and the new hydrate layer is thicker. This leads to a last phase where the hydration rate is diffusion-controlled: the remaining water must first diffuse through the newly formed hydrate layer. The C-S-H phase continue to grow, but the C_2S contribution increases, which cause the CH rate formation to decline. As the calcium and sulfate concentration declines, the ettringite formed during earlier stages starts to dissolve and react with the remaining C_3A and C_4AF, yielding the monosulphate.

For this last phase, however, there is no general agreement as for the explanations, as discussed in [Bullard et al., 2011], and several factors are most likely involved at the same time.

3.2 Meaningful parameters

In the following sections, we will introduce various type of modeling approaches concerning the hydration process. They all rely on a number of parameters that we will introduce in the following paragraphs.

3.2.1 The hydration degree ξ

The hydration reaction progress may be described by means of the hydration degree. It has been defined as the ratio of the quantity of reacted cement over the initial cement quantity [van Breugel, 1997]:

$$\xi(t) = \frac{\text{amount of reacted cement}(t)}{\text{initial amount of cement}(t=0)}. \tag{1.1}$$

The evolution of this parameter and hence of the hydration reaction kinetics, is driven by many parameters, such as the temperature, the exact cement composition, its fineness, the water / cement (w/c) ratio, *etc.*. From a local point of view the hydration can be chemically described in terms of reactants and newly formed hydrates. It also can be described macroscopically in terms of mechanical properties evolution, shrinkage, *etc.*. The evolution of such material properties is usually depicted as a function of the hydration degree rather than time. This allows for a possible comparison between various experimental methods, as well as a "common time" for the various physical phenomenon involved.

Experimentally, the hydration degree can be determined by several types of measures: the heat release rate (Fig. 1.3), the free water quantity, chemical analysis to determine the quantity of portlandite, *etc.*.

3.2.2 The maximum hydration degree

According to [van Breugel, 1997], the hydration goes on as long as free water is available, or as long as there is free space for the new hydrates to form. Both limits tend to be reached relatively quickly for high strength concretes, or more generally for low w/c ratios (Fig. 1.4(b)).

According to [Powers and Brownyard, 1947], for w/c ratios below 0.42, the hydration is never complete due to the lack of free space.

Several other models will be introduced in Sect. 4.3.2 of this chapter.

4 Phenomenological hydration modeling

The term phenomenological is here used as a way to describe hydration models that consider the cement paste in its totality, and are able to give an "overall" (macroscopic) description of their evolution through time. Many other modeling approaches exist, with more or less complex sets of equations and the consideration of numerous physical / chemical phenomena. The choice has been made here to focus on simple models, that are able to provide the volume fractions evolution descriptions – more particularly a good estimation of the pore phase – through a reduced set of variables.

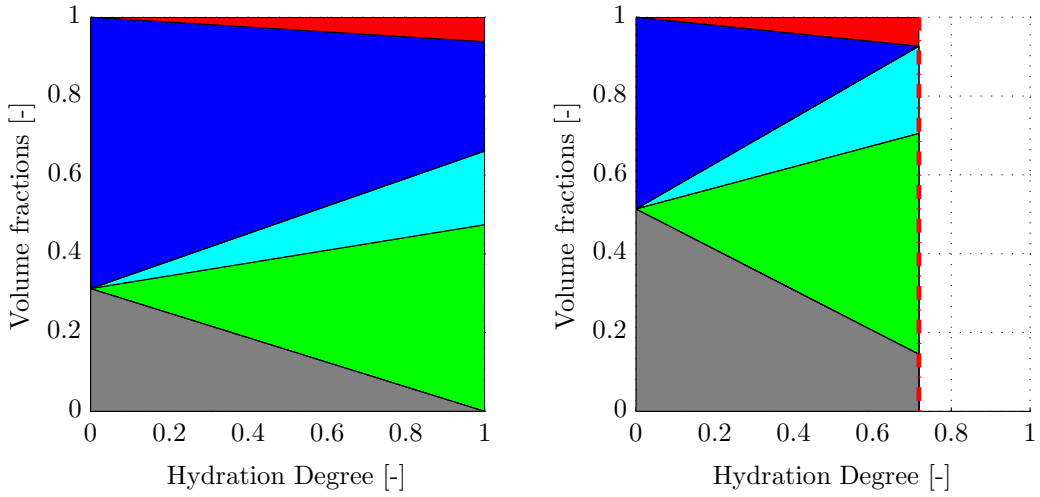

(a) $w/c = 0.7$ (b) $w/c = 0.3$, incomplete hydration

Figure 1.4: Evolution of volume fractions according to [Powers and Brownyard, 1947] - From bottom to top: *anhydrous cement, hydrates, gel water, capillary water, chemical shrinkage.*

4.1 Powers

[Powers and Brownyard, 1947] were the first to attempt a description of the evolution of cement pastes. Even if over half a century old, this model is still used and acknowledged as a reference for simplified applications. Based on chemistry as well as experimental observations of vapor sorption isotherms, the authors developed a five phase global model, which predicts each volume fraction according to the hydration degree. At the initial state, the cement paste is considered to be composed of only two phases: unreacted anhydrous cement and water. Then, as the chemical reaction starts, the cement paste is seen as a five phase model: anhydrous cement (which is slowly reacting) ; hydration products that replace the anhydrous cement and grow around ; water, which is one of three types: free water (contained in capillary pores), gel water (physically bounded inside the C-S-H gel), and lastly chemically bond water (non-evaporable). The sum of the volumes of the first two types of water (free and gel) can be considered as the total porosity.

They introduced an hydration degree ξ ($0 \leq \xi \leq 1$) to describe the state of reaction. Hence, for any given hydration degree, they estimated the volume fraction of each phase according to Sys.1.2:

$$p = \frac{w/c}{w/c + \rho_w/\rho_c}, \tag{1.2a}$$
$$V_{\mathrm{C}} = (1-p)(1-\xi), \tag{1.2b}$$
$$V_{\mathrm{H}} = 1.52(1-p)\xi, \tag{1.2c}$$
$$V_{\mathrm{Wg}} = 0.60(1-p)\xi, \tag{1.2d}$$
$$V_{\mathrm{Wc}} = p - 1.32(1-p)\xi, \tag{1.2e}$$
$$V_{\mathrm{CS}} = 0.20(1-p)\xi, \tag{1.2f}$$
$$V_{\mathrm{C}} + V_{\mathrm{H}} + V_{\mathrm{Wg}} + V_{\mathrm{Wc}} + V_{\mathrm{CS}} = 1, \tag{1.2g}$$

where p the initial porosity, ρ_w and ρ_c the water and cement density, w/c the water to cement ratio (in weight), and finally V_{C}, V_{H}, V_{Wg}, V_{Wc}, V_{CS} are respectively the volume fractions of anhydrous cement, hydration products, gel water, capillary water and chemical shrinkage.

It shall be added that more recent work have adapted this model to silica fumes blended cements. In [Lura et al., 2003] (after [Jensen, 1993]), the authors present an equivalent set of formula to describe the phase composition of a hardening cement paste with silica fume additions. They are not recalled here, but they are very similar, and there is a unique supplementary parameter, the silica fumes over cement weight (s/c) ratio.

However, in a first approximation, Sys.1.2 can be simplified to Sys.1.3 for a first implementation. The simplified model accounts only for three phases: anhydrous cement, hydration products (which now include gel water), and free water. The chemical shrinkage was also neglected, and its volume fraction included into the free water phase. Considering these assumptions, the hydration degree can reach the value of 1, thus a complete hydration, for $w/c \geq 0.42$ (as depicted on Fig. 1.7). It is today acknowledged that this hypothesis is not very reasonable, as it is shown on the same figure with the experimental data, but this first approximation is based only on the available resources in free water.

$$p = \frac{w/c}{w/c + \rho_w/\rho_c}, \tag{1.3a}$$
$$V_{\mathrm{C}} = (1-p)(1-\xi), \tag{1.3b}$$
$$V_{\mathrm{H}} = 2.12(1-p)\xi, \tag{1.3c}$$
$$V_{\mathrm{W}} = 1 - V_{\mathrm{C}} - V_{\mathrm{H}}. \tag{1.3d}$$

Even though those simplifications may seem numerous, they allow for a very simple implementation. For each phase, a volume description is given according to one parameter: ξ. This will be an argument of choice for the modeling framework introduced in the next chapter. However, one has to keep in mind the limitations of such models:

1. The water volume fraction (*i.e.* the porosity) is largely over-estimated, as it includes:
   - shrinkage,
   - chemically bond water.
2. Few phases are represented for a proper and realistic material property up-scaling.
3. The overall description is not made according to time, but to the hydration degree, which makes comparison with other time dependent phenomena more difficult.

4.2 Jennings & Tennis

The second considered model originated from [Jennings and Tennis, 1994]. Developed in the same spirit as Powers' one (few phases, macroscopic description of the evolution of the volume fractions), it is based upon Bogue's [Bogue, 1952] equations, modified by [Taylor, 1989], and on more up to date and accurate experimental techniques for structural characterizations.

The main upgrade this model includes is the accounting for the various mineral phases that compose the anhydrous cement. As in the previous model, authors give a volume fraction description (SYS.1.4) for each phase. The second important novelty is that each phase has now its own hydration kinetics:

$$c = \frac{1}{w/c + 1}, \tag{1.4a}$$

$$V_{\mathrm{C}} = c(1 - \xi_{\mathrm{total}})\frac{1}{\rho_c}, \tag{1.4b}$$

$$V_{\mathrm{CH}} = c(0.189\xi_{\mathrm{C_3S}}p_{\mathrm{C_3S}} + 0.058\xi_{\mathrm{C_2}s}p_{\mathrm{C_2S}}), \tag{1.4c}$$

$$V_{\mathrm{AF_m}} = c(0.849\xi_{\mathrm{C_3A}}p_{\mathrm{C_3A}} + 0.472\xi_{\mathrm{C_4AF}}p_{\mathrm{C_4AF}}), \tag{1.4d}$$

$$V_{\mathrm{C\text{-}S\text{-}H_S}} = c(0.278\xi_{\mathrm{C_3S}}p_{\mathrm{C_3S}} + 0.369\xi_{\mathrm{C_2S}}p_{\mathrm{C_2S}}, \tag{1.4e}$$

$$V_{\mathrm{cap}} = (1 - c) - \sum_{i=1}^{4}(\xi_i p_i \Delta_i), \tag{1.4f}$$

$$V_{\mathrm{C\text{-}S\text{-}H_P}} = 0.219V_{\mathrm{C\text{-}S\text{-}H_S}}, \tag{1.4g}$$

$$V_{\mathrm{tot_pores}} = V_{\mathrm{cap}} + V_{\mathrm{C\text{-}S\text{-}H_P}}, \tag{1.4h}$$

where p_i, ξ_i and V_i are respectively the initial volume fraction, hydration degree, and the volume fraction of phase i during the hydration process, c is the mass fraction of anhydrous cement at the initial state, and finally, C, CH, $\mathrm{AF_m}$, $\mathrm{C\text{-}S\text{-}H_S}$, cap, $\mathrm{C\text{-}S\text{-}H_P}$ and tot_pores represent respectively the anhydrous cement, the Portlandite, the mono-sulfo-aluminates, the solid C-S-H, capillary pores, C-S-H's pores and lastly the

Phase	a_i	b_i	c_i
C_3S	0.25	0.90	0.70
C_2S	0.46	0	0.12
C_3A	0.28	0.90	0.77
C_4AF	0.26	0.90	0.55

Table 1.3: Eq.1.5 coefficients – *from* [Jennings and Tennis, 1994].

total pores volume. In addition, the term Δ_i accounts for the chemical shrinkage. The ξ_i are estimated thanks to a set of *Avrami* like law (Eq.1.5). They are known to to be suited to represent nucleation and precipitation phenomena. Lastly, the overall hydration degree ξ_{total} is a weighted average of the ξ_i.

$$\xi_i(t) = 1 - \exp\left(-a_i(t - b_i)^{c_i}\right) \tag{1.5}$$

The key enhancement this model brings (in addition to the already mentioned accounting for mineral phases composition) is the detailed description of the hydration products, especially with description of the C-S-H porosity which is believed to be an essential parameter for the cement paste response in regards to transport phenomena.

The author would like to remind the reader that there is a variety of models to describe the hydration mechanisms (some more precise in the phases description [Knudsen, 1984], others with more physical phenomena considered [Saglik, 1992], *etc.*.) but the choice has been made to only consider ones that give a "simple" *macroscopic* description. For such models, the developed framework is easily adaptable.

4.3 Modeling amendments

In order to overcome some limitations of the presented hydration models, some points are discussed in the following to improve the hydration framework by taking into account more recent experimental results.

4.3.1 Anhydrous cement composition and individual hydration rates

As explained earlier, the hydration reactions kinetics are driven by a set of *Avrami* type laws. However, for very early ages (less than a day), they present an non-finite derivative at the origin. Physically, it would mean that the hydration reaction starts immediately, which is true, but the growth of new hydrate is delayed by at least few minutes (dissolution time, pre-induction period).

In order to give a more realistic description of these phenomena, and particularly in the spirit of future development aiming at taking into account mineral substitutes of clinker, the individual hydration rates have been first modified by adding a supplementary term, as shown Eq.1.6. It has been chosen after [Stefan, 2009] to fit

Phase	a_i	b_i	c_i	α_i	β_i
C_3S	0.622	0.0	0.280	0.871	10.67
C_2S	0.119	0.0	0.462	0.928	11.64
C_3A	0.712	0.0	0.230	0.788	3.40
C_4AF	0.502	0.0	0.281	0.861	19.22

Table 1.4: Eq.1.6 fitted coefficients.

best experimental results at very early ages as shown on Fig. 1.5. The pre-induction period is not represented by the original model (Fig. 1.5(a)), whereas the modified one fit best (Fig. 1.5(b)).

All the constants (for each mineral phase: 3 from the original model, and 2 new) were fitted over [Tennis and Jennings, 2000] data, using the Matlab *fitting toolbox*. Tab. 1.4 summarize the different coefficients, and Fig. 1.6 shows the corresponding evolution (experimental results and the actual cement composition is taken from [Stefan, 2009] work). The predicted volume fraction does not change for long term predictions, the modification impacts only on very early ages (less than 3 days) only.

$$\xi_i(t) = \left(1 - \exp\left(-a_i(t-b_i)^{c_i}\right)\right) \exp\left(-\left(\frac{\alpha_i}{t}\right)^{\beta_i}\right) \tag{1.6}$$

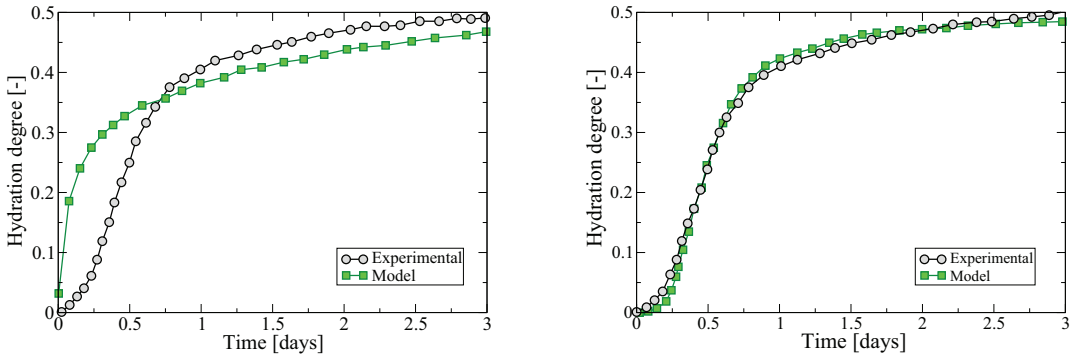

(a) Original model: Eq.1.5 (b) Modified model: Eq.1.6

Figure 1.5: Overall hydration degree according to time, experimental results from [Stefan, 2009].

4.3.2 Overall and maximal hydration degree: ξ_{tot} and ξ_{max}

Overall hydration:

A second point to address is the overall description of the reaction and more specifically the overall hydration degree definition. In their original work, [Jennings

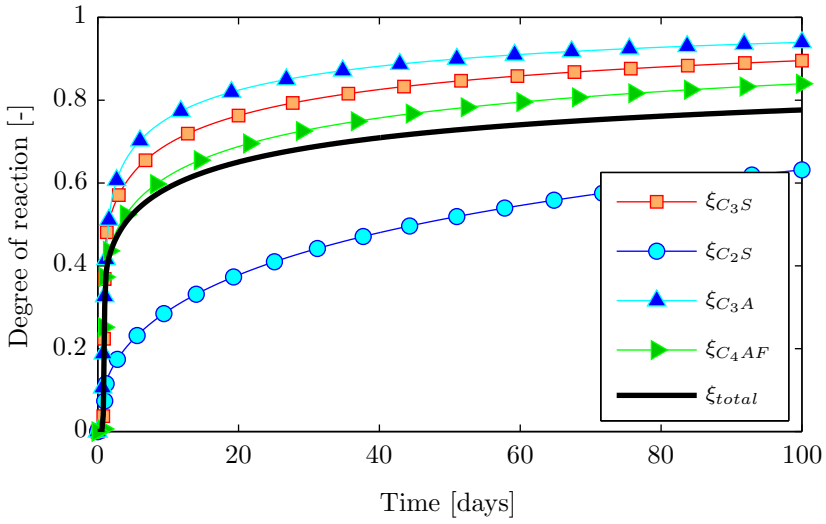

Figure 1.6: Time evolution of the hydration degrees for each anhydrous phase. CEM I standard composition, $w/c = 0.5$.

and Tennis, 1994] defined the latter by a weighted average of the individual hydration degrees of each phase: $\xi_{tot} = \sum_i p_i\xi_i / \sum_i p_i$. However, the sum of the volume fraction of the four main phases does not reach one. Indeed, usually, there is around five percent, in mass, of mineral additions like gypsum and a small percentage of impurities. The latter does react in the sense that it does not produce a specific hydrate, but rather participate in the overall reaction by playing a role in delaying the C_3A reaction.

The overall hydration degree ξ_{tot} has been kept as the weighted sum ($\xi_{tot} = \sum_i p_i\xi_i$) instead of the averaged one, which helps to account for all the anhydrous contributions. Subsequently, the overall hydration degre will not be able to reach 1 anymore, but it will have no influence since it actually never reach complete hydration, as we will see in the next paragraph. We will now review and define properly the concept of maximal hydration degree within the presented framework.

Final hydration degree:

Hydration is supposed to continue as long as the necessary resources are present: anhydrous cement, water, and free space. However, its kinetics is not linear (*cf.* Eq.1.6), and the asymptotic behavior of the hydration degree leads to a definition of a maximal hydration degree. It reflects that after a "long enough" period, the hydration does not evolve anymore (*i.e.* the hydration degree never reach 1).

Several models exist to describe it cement pastes. Among the most used and acknowledged, a first approximation was given by [Powers and Brownyard, 1947] which follows Eq.1.7. It is a function of the initial free space in the microstructure, and accounts for the water disponibility for low w/c ratios.

$$\xi_\infty = \min\left(1; \frac{w/c}{1.31/3.13}\right) \tag{1.7}$$

Further on, Mills [Mills, 1966] suggested a new phenomenological expression, found in Eq.1.8. However, it didn't account for the cement finesse (cement particle bigger than 40 µm in diameter are never fully hydrated, *cf.* subsection 5.1.4 of this chapter) nor its type.

$$\xi_\infty = \frac{1.031 \cdot w/c}{0.194 + w/c} \tag{1.8}$$

Lastly, based on new experimental data and a literature review, [Waller, 1999] suggested another phenomenological model described in Eq.1.9. It helps to correct the constant overestimation of Powers' model for "high" w/c ratios, and underestimation of Mills model for "low" ones (see Fig. 1.7).

$$\xi_\infty = 1 - \exp\left(-A \cdot w/c\right) \tag{1.9}$$

Usually, the constant term A is taken to be $A = 3.3$ for a standard CEM-I composition. It is fitted accordingly to experimental data.

In addition, some experimental data is presented in the following, regarding the final hydration degree measured on cement pastes for various w/c ratios, after long periods ([Parrott et al., 1990], [Justnes et al., 1992a], [Justnes et al., 1992b]). Fig. 1.7 sums up the described models, and gather data for the final hydration degree scaled according to the w/c ratio.

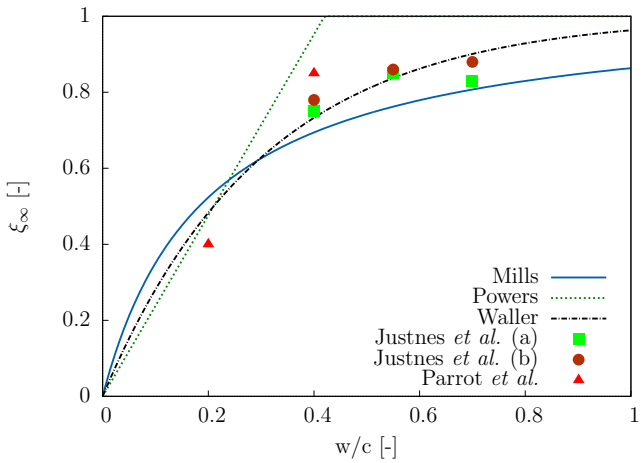

Figure 1.7: Final hydration degree for various w/c.

The Waller's equation has been considered, and used as an input to the hydration model since the hydration degree at the end of the reaction best fits the experimental data.

4.4 Hydration modeling simplifications

Two hydration phenomenological models have been presented. The most accurate one, based on [Jennings and Tennis, 1994] takes into account the mineral composition of the anhydrous cement and the w/c ratio. It allows for each considered phase to have its own kinetics, and the overall hydration degree has now a more physical sense. Furthermore, the upper limit of hydration has been reassessed to fit more accurately experimental observations on the maximal hydration.

In the following some practical points are presented, facilitating the implementation for numerical computations.

4.4.1 Water content and distribution

The capillary water is usually known to be the one in a pore size span ranging from 10 µm to 10 nm, with a differentiation of evaporable water for pore larger than 50 nm (known as bulk water), and smaller (50 to 10 nm) which can evaporate but with a moderate menisci. For the gel pores (C-S-H porosity), the sizes range from 10 nm down to 0.5 nm [Mindess et al., 2003], with again a size distinction at the threshold size of 2.5 nm, above which the water is still considered evaporable but with strong menisci (which can possibly generate stress high enough and damage the surrounding microstructure), and below which the water is set to be non-evaporable (due to inter-molecular interactions).

At even smaller scales, we can lastly depict the intra-C-S-H layer spaces, which are supposed to be smaller than 0.5 nm.

The IUPAC (*International Union of Pure and Applied Chemistry*) classification distinguish three types of pores, sorted according to their diameter ϕ:

- micropores: $\phi < 2\,\text{nm}$,
- mesopores: $2\,\text{nm} < \phi < 50\,\text{nm}$,
- macropores: $\phi > 50\,\text{nm}$.

According to that classification, the modeling procedure will only consider two types of pore, at two distinct scales:

- At the cement paste scale (approximate length-scale of 100 µm), capillary pores will be considered mainly as *macropores* ($\phi \geq 50\,\text{nm}$). The range of pores from 50 nm to 10 nm, still considered as capillary pores, will not be modeled for numerical reasons. Indeed, the latter would require a minimal discretization of at least 10 nm for a modeled *Representative Volume Element* (RVE) of size 100 µm. As it will be shown later, at the cement paste scale we use a morphological discretization of 0.334 µm, which already require to generate random fields with 27×10^6 dofs (degrees of freedom). To be able to represent the full macropore range, the random field should be yielded with a discretization 30

times smaller, *i.e.* 10×10^{11} dofs. The choice of scale separation and porosity separation arises as obvious here, for the computational cost.

- At a thinner scale, as it will be depicted in chapters 3 & 4, when modeling the C-S-H structure, thinner discretizations will become reachable. At this stage, the complete *mesopores* range will emerge, and will represent the C-S-H porosity.

4.4.2 Implementation's simplifications

Several simplification are possible, according to the targeted description. The full model description is not always necessary, and it can be simplified to describe fewer phases. It has been chosen to differentiate the hydration products into two categories. On one side we will consider the CH and AF_m, which are crystalline phases, and thus non diffusive. On the other hand, we will consider the C-S-H phase as the only diffusive one. Its volume fraction will take Jennings' C-S-H_s and C-S-H_p into account (respectively the bulk C-S-H volume fraction, and its porosity). By considering both as one phase, their material properties will be assessed by means of numerical homogenization at a lower nanometric scale.

Number of various simplifications can be done, according to the simulation's aim. They can be presented as follow:

- Two phase morphologies: if the model is used to simulate a mass transfer, *e.g.* permeability, the description of the cement paste can be simplified to a two phase morphology: solid & porosity. Since the transfer will only occur in the pore space, the information about the volume fraction of hydrates is not relevant, and the pore space description is sufficient.

- Three phase morphologies: unreacted cement / hydration product / porosity. It can be used for a first approximation of *e.g.* mechanical properties at hydrated states. Other decompositions are possible, always considering the porosity, but dividing the two remaining solid phases differently: non-diffusive versus diffusive (see Fig. 1.8(a) for example).

- Four phase morphologies: unreacted cement / inner hydration products / outer hydration products / porosity: For diffusivity studies, it will be possible to model the diffusive phase on the rim of the non diffusive one (*e.g.* Fig. 1.8(b)).

5 Microstructure and morphology of cementitious materials

As it has been mentioned in the introduction, when a cement powder is mixed with water, hydration products start to grow, and the amount of anhydrous cement reduces. The main phases of the resulting cement paste are:

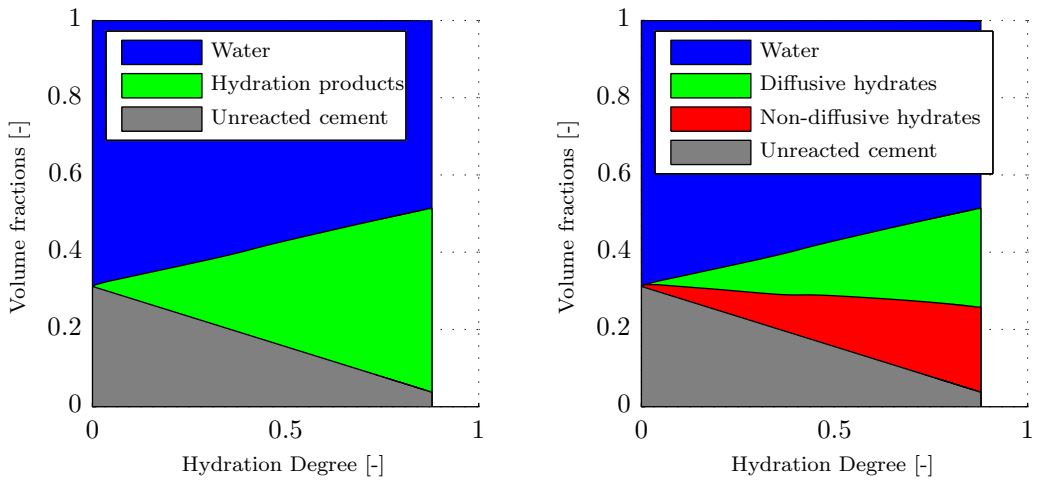

(a) 3 phases: porosity, hydration product, unreacted cement)

(b) 4 phases: porosity, diffusive hydrates, non-diffusive hydrates, unreacted cement

Figure 1.8: Examples of targeted simplifications.

- the Calium-Silicate-Hydrates (C-S-H), which accounts for about 50 to 70% of the hydrates,
- the Portlandite ($CaOH_2$ or CH), which account for about 20 % of the hydrates volumes,
- the Calcium sulfoaluminate (ettringite and calcium monosulfoaluminates hydrates).

On one hand, with the ongoing hydration, the newly formed hydrates fill the free space initially occupied by water. In most cases, those hydrates do not fill completely the free space. The residual volume left is the one of the **capillary pores**. On the other hand, one of the newly formed hydrates has its own porosity: the C-S-H ; and this porosity will be referred to as **hydrates pores**.

A typical Mercury Intrusion Porosimetry (MIP) measure allows to see the distinction. Fig. 1.9 displays such results (from [Verdback and Helmuth, 1968]), in terms of pore size distribution. Two main peaks are noticeable, with a first one around 0.1 μm, which corresponds to the capillary porosity, and the second one in the vicinity of 10 nm, which corresponds to the C-S-H porosity. *These types of measurements will be discussed later, as well as their quality and precision, they are only mentioned here to ease the distinction between the two types of pores.*

5.1 Hydrate structure

The cement paste's microstructure may vary a lot with the few parameters presented previously, namely the anhydrous cement's mineral composition, the initial cement

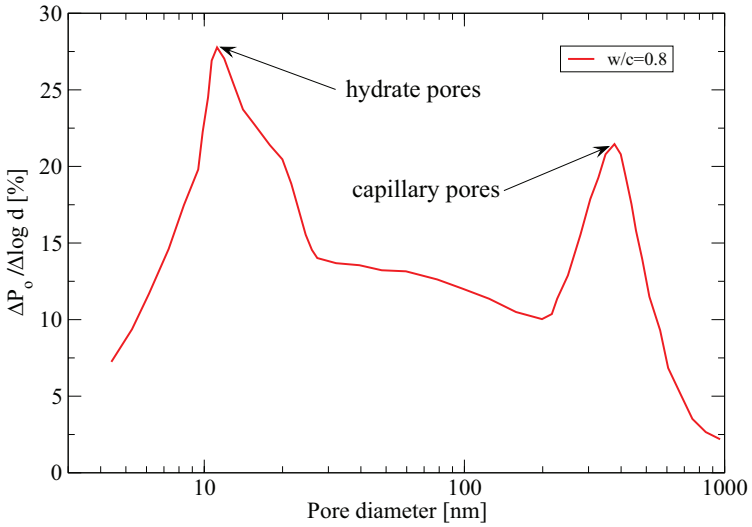

Figure 1.9: Typical pore size distribution in a cement paste, obtained by MIP – *from* [Vercback and Helmuth, 1968].

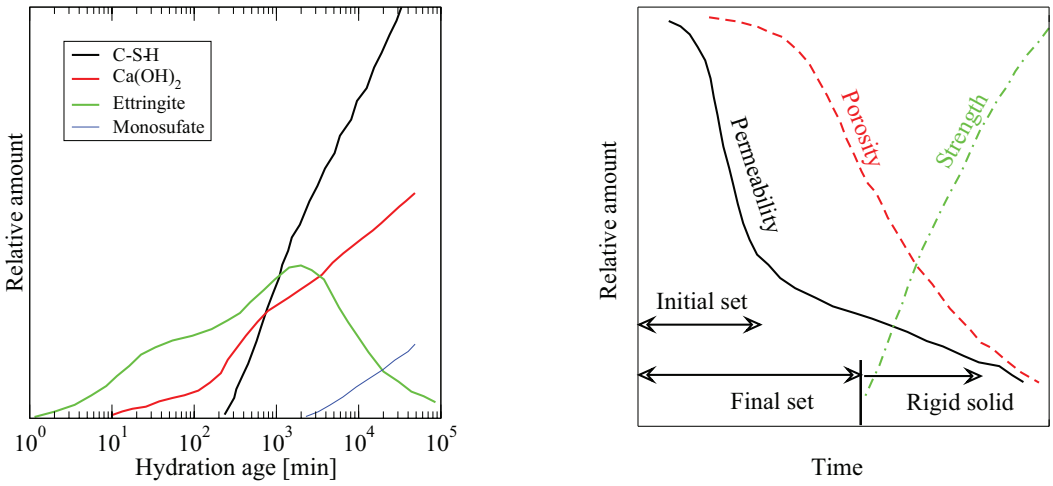

(a) Phase evolution

(b) Properties evolution

Figure 1.10: Typical phase evolutions through hydration – *from* [Mehta and Monteiro, 2005].

paste's w/c ratio, and the hydration degree. However, most of the cement pastes share a number of common features, and so they can be described in terms of:

- C-S-H gel,
- Portlandite,
- few other hydrates in minor proportions,
- some unreacted anhydrous cement,
- pore space,
- interstitial solution.

The particular structure of each hydrate will influence the cement paste response to various phenomenon, *e.g.* the mechanical response, the transport properties, *etc.*. A quick review of those structures is now presented.

5.1.1 The Calcium Silicate Hydrates: C-S-H

Also known as the C-S-H gel, the C-S-H phase is a set of quasi-amorphous particles which contains calcium, silicium and water. It results from the hydration of the C_3S and C_2S in cement. The "gel" word indicates the low degree of crystallization. The C-S-H phase is the main hydrate phase, accounting for 50 to 70 % of the volume of solids in a standard fully hydrated Portland cement paste.

The usual characterization methods (introduced later in this chapter) are not well suited to investigate the C-S-H morphology, due to its low crystallinity. Traditional models describe it as a C-S-H "gel", and the actual structure of the latter is only emerging nowadays with atomistic simulations and Nuclear Magnetic Resonance (NMR) studies. Thus, we present here only the main and most acknowledged models, based on indirect experimentation.

Recent developments will be introduced later on, with experimental data to support those models.

Powers & Brownyard:

[Powers and Brownyard, 1947] considered that the cement paste was mainly made of a colloïdal gel of C-S-H. The gel is modeled as a couple of elementary layers wrapped around themselves (Fig. 1.11(a)), with a high specific surface area. This morphological set up allows for capillary porosity (region **c** on the same figure), within which a layer of adsorbed water molecule is considered, as well as an "interlayer" porosity, which entraps some water molecules.

Feldman & Sereda:

[Feldman and Sereda, 1968]'s model is very similar to the previous one, but the elementary layers are more disordered, which creates more porosity (Fig. 1.11(b)). This allows for a water content in the inter layer space, which is taken into account by the model, as well as water migrations during the hydration and drying.

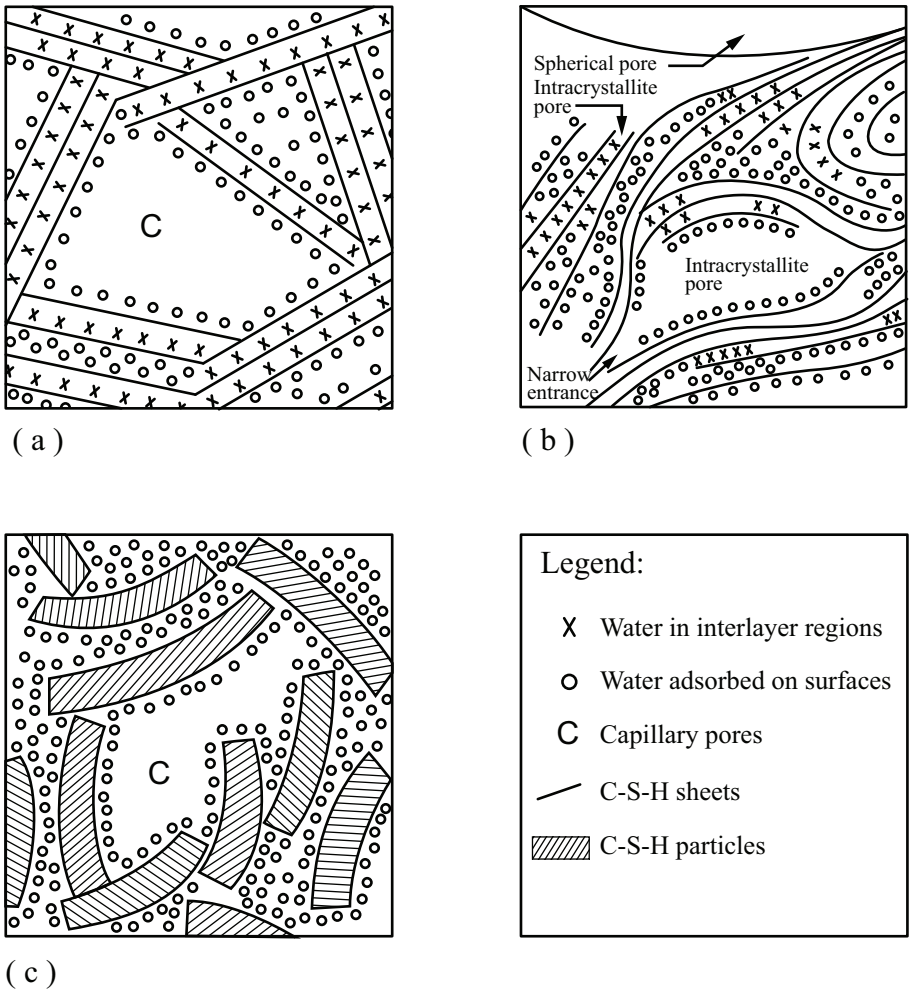

Figure 1.11: The C-S-H models: (a) Powers & Brunauer (1968) – (b) Feldman & Sereda (1968) – (c) Wittman (1976) — *adapted from* [Oberholster, 1986].

Tennis & Jennings:

In this model, [Tennis and Jennings, 2000] also propose a colloidal gel structure, but with elementary spherical particles set to be around 2 nm in diameter. Based on nitrogen desorption experiment, a distinction is also made between low density (LD) C-S-H, and high density (HD) ones (Fig. 1.12).

This key point differentiate this model from all the others, and is the first to investigate microstructural changes and viscous deformation to explain partially creep and shrinkage [Jennings, 2004].

Recent cement pastes observations under a scanning electron microscope (SEM) supports this distinction between the C-S-H phases [Scrivener, 2004]. They display unreacted cement surrounded by a layer of C-S-H called “inner C-S-H”, with a uniform bulk structure, which then is entrapped in a heterogeneous matrix containing the “outer C-S-H”, the Portlandite, the aluminates, as well as the various types of

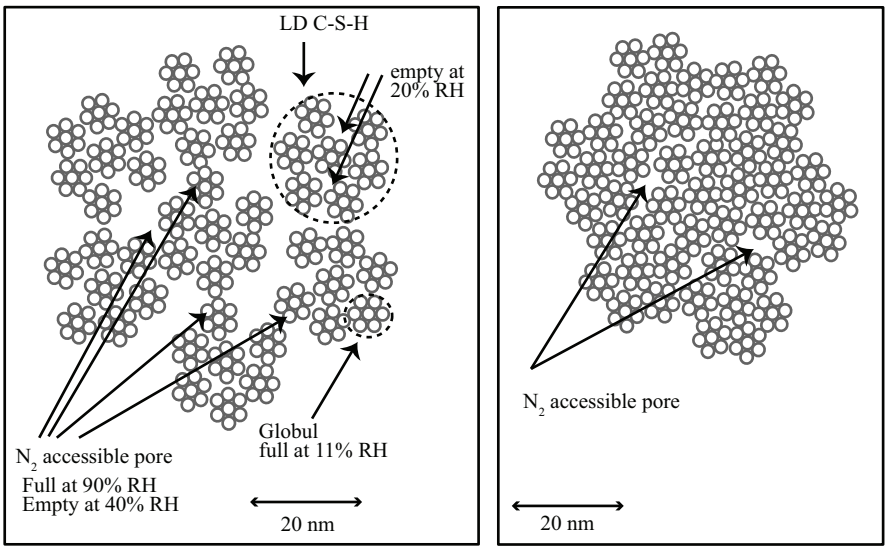

Figure 1.12: Two dimensional schematic of the colloid structure of the C-S-H gel. (a) C-S-H LD – (b) C-S-H HD – *adapted from* [Tennis and Jennings, 2000].

pores (Fig. 1.13). The "inner" and "outer" terms corresponds respectively to the HD and LD C-S-H.

5.1.2 The Portlandite: $Ca(OH)_2$

The calcium hydroxide, known as portlandite, constitute 20 to 25 % percent of the volume of solids in the hydrated paste. It is considered to be one of the few phases that have a complete crystalline structure: a hexagonal crystal pileup.

This phase contributes highly to the cement paste strength and theoretically to durability as large crystals reduce the free space for capillary pores. Fig. 1.14 shows the CH crystals, which here appear irregular on the boundary and densely filled inside. However, those crystals are not very stable due to weak inter-layer bounding [Taylor, 1997]. It is considered to be the weakest element of a cement paste in regards to durability and chemical attacks.

5.1.3 Calcium sulfoaluminate hydrate

The calcium sulfoaluminate hydrates are the minor solid phase, they account for 15 to 20% of the solid volume in a hydrated cement paste.

During the first stages of hydration, the sulfate/alumina ionic ratio in the interstitial solution usually favors first the formation of trisulfate hydrates, known as *ettringite* [Mehta and Monteiro, 2005], which takes the form of needle shaped crystals. Usually, those ettringite crystals eventually transform into monosulfate

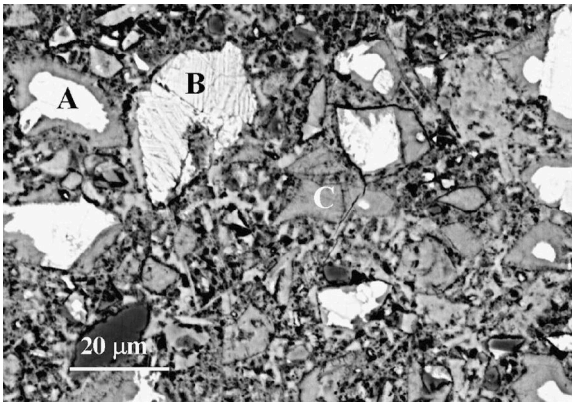

Figure 1.13: SEM image of a hydrated cement paste (CEM I, with $w/c = 0.3$, 100 days). **A**: anhydrous cement grain surrounded by inner C-S-H, **B**: β-C2S partially hydrated, **C**: fully hydrated cement grain – *from* [Diamond, 2004].

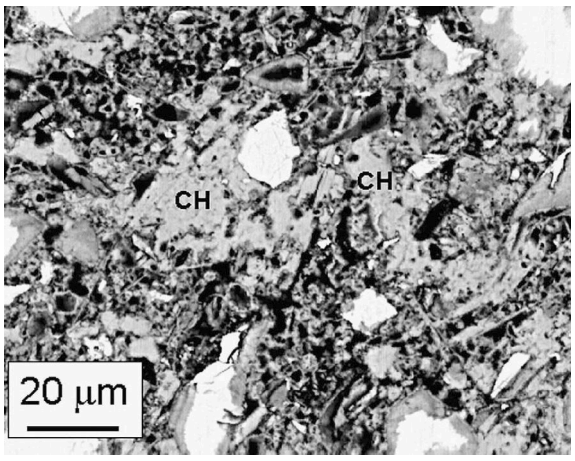

Figure 1.14: SEM image of a hydrated cement paste (CEM I, with $w/c = 0.45$, 7 days) – *from* [Diamond, 2004].

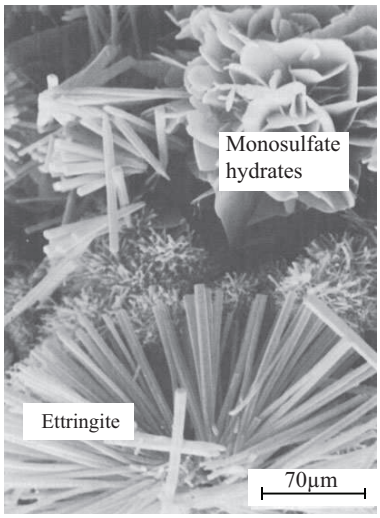

Figure 1.15: SEM micrograph of typical hexagonal crystals of *monosulfate hydrate* and needle-like crystals of *ettringite* – *from* [Mehta and Monteiro, 2005].

hydrates, which form hexagonal plates crystals. They are both visible on Fig. 1.15.

However, depending on the cement mineral compositions, they can be both found in hardened cement paste [Diamond, 2004].

5.1.4 Anhydrous cement residue

Lastly, one can see on Fig. 1.13 (**A**) unreacted anhydrous cement is still present in the cement paste. Function of the particle size distribution of the cement particles, the w/c ratio, and of the hydration degree, unreacted cement can be found. Because of the available space that reduces with time, the hydration products tend to crystallize around the cement grains, creating a coating around the latter. The hydration kinetics is then slowing down as the water has first to diffuse through the hydrated layer to enter in contact with anhydrous cement. In practice, it is considered that a cement particle with a diameter greater than 40 µm will never be fully hydrated, as the 20 µm thickness of the hydrated seems to be the threshold above which the hydration rates reduces significantly.

5.2 Interstitial solution

At the beginning of the hydration reaction, the interstitial solution contain several ions, namely Ca^{2+}, Na^{+}, K^{+}, aluminates, silicates and $SO_4{}^{2-}$. Those ions concentration evolve through time (Fig. 1.16) in the free water, as they are subjected to dissolutions (from solid anhydrous cement or from some "temporary" hydrates to water), and precipitations (new hydrate precipitation).

When the hydration reaction starts, the pH is around 12.5 (the solution is saturated with Ca^{2+}), and then shifts to a pH around 13-14 for the hardened ce-

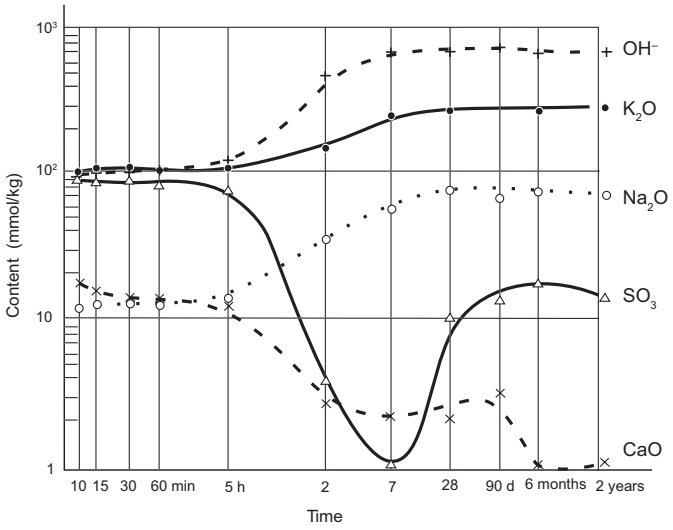

Figure 1.16: Cement paste interstitial solution composition – *from* [Ollivier and Vichot, 2008] *after* [Longuet et al., 1973].

ment paste. This highly alkaline environment with Na^+ and K^+ reduces the lime's ($Ca(OH)_2$) solubility, and thus the Ca^{2+} content stays low.

5.3 Pore network structure

Once the description of the solid phases found in the cement matrix is done, one has to equally take into account the pore network, as well as its description. Two types of porosity were introduced at the beginning of Sect. 5: the capillary pores and the hydrates pores. We here try to characterize both of them, in terms of volume fraction and size distribution. The main experimental techniques will be described in order to assess as closely as possible the "real" microstructures.

5.3.1 Porous materials: definitions

Any type of cementitious material is a multiphase one, with a solid phase, a liquid phase and lastly a gas phase. The solid phase includes the previously described hydrates, unreacted cement, and aggregates (at the mortar and concrete scales). The liquid phase is the interstitial solution, and lastly the gas phase is a mix of air and water vapor.

In order to describe properly the materials porosity, we need to introduce:

- V_a, the apparent volume, as the envelope of the sample,
- V_s, the solid phase volume,

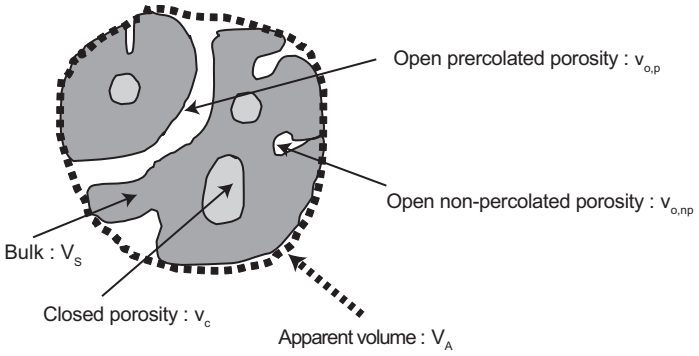

Figure 1.17: Porous material porosities – *from* [Ollivier and Torrenti, 2008].

- v_o, the open porosity volume (existence of a continuous path to the specimen boundary),
- $v_{o,p}$, the percolated open porosity,
- $v_{o,np}$, the non-percolated open porosity,
- v_c, the closed porosity volume.

All those volumes are defined on Fig. 1.17. For practical purposes, it is also common to define the corresponding porosities:

- Open percolated porosity: $p_{o,p} = \dfrac{v_{o,p}}{V_a}$,
- Open non-percolated porosity: $p_{o,np} = \dfrac{v_{o,np}}{V_a}$,
- Open porosity: $p_o = \dfrac{v_o}{V_a} = p_{o,p} + p_{o,np}$,
- Closed porosity: $p_c = \dfrac{v_f}{V_a}$,
- Total porosity: $p = p_o + p_c$.

Remark:
Those definition are given here and will not be reminded later. However the notation may change in the next chapters, only to ease the understanding.

5.3.2 Traditional investigation techniques

A proper knowledge of the pore phase (micro-)structure is essential to assess durability in cement based materials. The different pore modes were previously introduced at the cement paste scales (capillary and hydrate pores), and some other emerge while at higher scales.

Water accessible porosity:
It is the most used method to investigate porous materials. It does not give the size distribution of the pore network, but only the overall porosity, which is a first order parameter for durability assessments.

- The sample is first saturated, which fills completely its pore network, and weighted,
- then, after drying, the sample is weighted again, and the accessible porosity volume is determined from the difference of the two weightings.

The standardized procedure recommends a drying at 105 °C. However, the drying conditions may influence this measure significantly [Gallé, 2001]. Too elevated temperatures may produce micro-cracks in the cement paste matrix. In addition, the conditions may dehydrate some of the newly formed compounds (bounded water becomes free), and they lead to an overestimation of the free water content. As an example of this uncertainty, one can see on Fig. 1.18 the porosity ranges measured for various cement paste, with various techniques. As an example, for a cement paste with $w/c = 0.4$, the MIP technique gives 20% of porosity, whereas water accessible porosity gives results between 30 and 37%, function of the to the drying conditions. Nowadays, a new consensus is emerging to use mild drying conditions (60 °C to 80 °C), or new techniques as the freeze drying or vacuum drying.

Water Vapour Sorption Isotherms (WVSI):
The WVSIs are a translation of the thermodynamical equilibrium between the bulk water content of the hardened material against the ambient humidity, at a constant temperature. A sample is first fully saturated, placed in an environment with a controlled humidity, starting at 100%. Then, as the controlled humidity is set at a different humidity range (HR), the sample is weighted until stabilization and thermodynamic equilibrium between the sample and its environment is reached. The results are showed in terms of a *integral moisture capacity* [Baroghel-Bouny, 2007a], describing the mass water content against the relative humidity.

The main method used to interpret these curves has been proposed by Barret, Joyner and Halenda (BJH) [Barret et al., 1951]. The main assumption is the **coexistence of *capillary* and *adsorbed water* in *cylindrical* pores**. Then, by applying with *Kelvin-Laplace*'s equation (Eq.1.10), it is possible to determine the amount of water in pores of a given radius r:

$$\ln(\mathrm{HR}) = \frac{-2\sigma M \cos\theta}{r R T \rho}, \tag{1.10}$$

where σ is the water surface tension, M its molar mass, , θ its wetting angle, R the universal gas constant, ρ the water density and T its temperature.

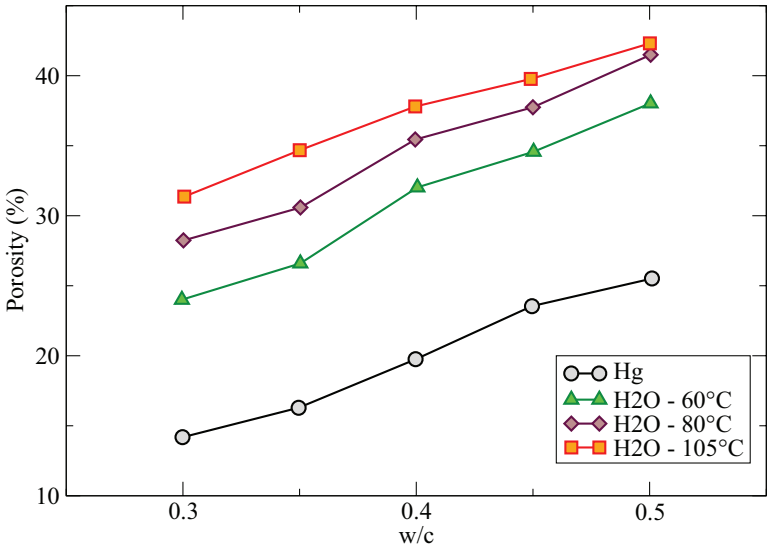

Figure 1.18: Cement paste porosities – *from* [Vu, 2009].

Image Analysis:

The direct visualization of actual materials would be a method of choice for characterization. However, to get pertinent information it would require 3D image acquisition with a resolution covering several orders of magnitude. Electronic microscopy (by transmission, scanning, or both (TEM, SEM, STEM)) can yield 2D images of sample slices, which then can be treated by means of stereological and morphological tools to obtain 3D data. For example, porosity assessments are very straightforward since it is equal to the 2D surface area fraction observed on a slice [Underwood, 1970]. Some developments of this technique allow nowadays to estimate the various phases volume fractions [Scrivener et al., 1988]. However both those techniques are limited in resolution, around 200 nm for optical microscopes, and around 20 nm for electronic microscopy.

To access the complete pore size distribution, X-Ray Computed Tomography (X-ray CT) is used (*e.g.* [Pierret et al., 2002]).

Nevertheless, since the hydrate pores reach the nanometric scale, those techniques do not provide the full range of the porosity distribution.

Mercury Intrusion Porosimetry (MIP):

Concerning the pore size distribution of cement based materials, the most widely used method is still the MIP. A dried sample is isostatically injected with mercury, with an increasing pressure. Mercury is used for its "non-wetting" properties. It

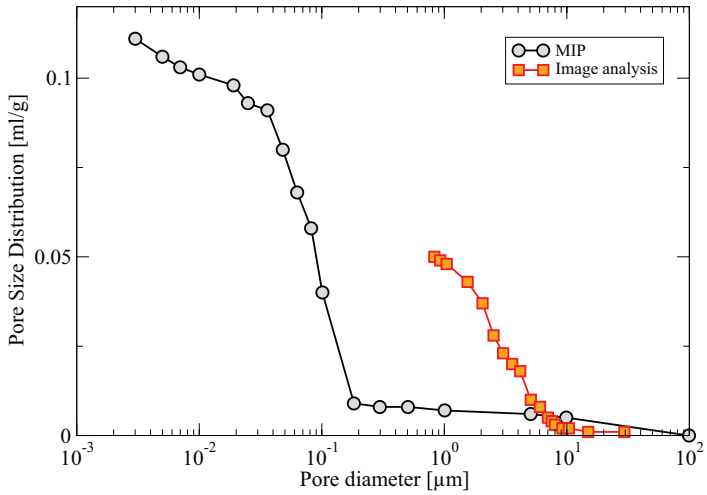

Figure 1.19: Comparison of MIP and image analysis pore size distribution plots for a vacuum-mixed 28-days-old $w/c = 0.4$ cement paste – *from* [Diamond, 2000].

will not penetrate the sample without an applied pressure. Under assumption of cylindrical pores (as for WVSIs curves and BJH method), the Washburn equation (Eq.1.11) may be applied to assess the pore size range reachable at each pressure step:

$$P = \frac{2\sigma_{Hg}\cos\theta}{r}, \tag{1.11}$$

with P the applied pressure, r the pore radius, σ_{Hg} the mercury surface tension ($0.48\,\mathrm{N\,m^{-1}}$) and θ its wetting angle (around 140°).

The MIP procedure requires a preliminary drying which may interfere with the material's microstructural properties. Studies have shown that the drying condition change significantly the results of such tests [Gallé, 2001]. The comparison between various protocols is thus not possible.

The mercury injected from the sample's borders does not penetrate the material until a pressure threshold is reached, corresponding to a pore threshold diameter. Known as the "ink-bottle" effect, this phenomenon leads to an overestimation of small pores volume fraction, and no proper characterization of large pores. As stated in [Diamond, 2000], "[...] *the pore size distribution calculated from the Washburn equation from MIP data departs enormously from reality, most pores being reported one or two orders of magnitude smaller than they actually are* [...]". Fig. 1.19 displays this discrepancy, in terms of threshold diameters (the image analysis is not complete since it is stopped at the lower bound of the microscope resolution).

When using data from this method, it is essential to keep in mind those limi-

tations, and use the results **only** for **comparative studies**, **never for intrinsic information**. This type of data will be used in the next chapter to see whether the overall tendencies are respected, but never to actually characterize a material.

In addition, traditional experimental tests a carried out up to a maximum pressure around 480 MPa. Assuming a contact angle of 130° and an average surface tension of $480 \times 10^3\,\mathrm{N\,m^{-1}}$, the lower limit in terms of pore access diameter is around 3 nm. This size limitation explains a part of the discrepancy in terms of total porosity displayed Fig. 1.18, between mercury and water accessible porosity ; since water can access pores as small as 0.5 nm [Xu, 1995].

Last but not least, to access this range of diameters, due to the applied pressure (around 480 MPa), the microstructure is damaged [Olson et al., 1997] with microcracks appearance, and thus less pertinent information can be retrieved.

The discrepancy just described concern mainly the threshold diameters. As it will be shown in the following, for the hydrate characterization (nanometric scale) the MIP results converge towards other experimental techniques. This fact lead to a proposition on how to look a MIP results: it is believed that the actual size distribution can be approximated by taking regular MIP results, and by applying an homothecy centered around the nanometer, and scaled so that the threshold diameters shifts by two orders of magnitude (from 0.1 µm to 10 µm). Data in between those two extreme bounds should be scaled accordingly.

Recent advances in experimental techniques converge toward the previous descriptions. Originated in [Liu and Winslow, 1995], authors managed to bypass the "accessible effect" with two pressurization cycle, which allowed them to divide the pore network into reversible and irreversible intruded pores. Following, [Yoshida and Kishi, 2008] managed to assess the volumes of connected and disconnected pores with several increasing pressurization / depressurization cycles. They also introduced a new type of pores, located between the gel pores (hydrate pores) and the capillary one, allowing to bridge the gap in the PoSD.

In spite of those clever advances to avoid traditional MIP biases, those techniques can not provide valid estimation of actual PoSD. Finally, in [Zhou et al., 2010], the authors introduced the Pressurization-Depressurization Cycle MIP (PDC-MIP) testing sequenced with the corresponding data analysis method. It allowed them to overcome the previous issue of bottle-ink effect as they determine its volume, as well as the throat pore volumes. The data analysis framework enhanced also the pore size measurements. Comparative results are drawn Fig. 1.20. The dashed green line is a traditional MIP result, with a pore access diameter around the micrometer, and the vast majority of the pore volume attributed at the nanometric scale. The black solid line comes from BSE image analysis, where the access diameter is now over a dozen of micrometers and most of the pore volume resides in pores between 1 and 20 µm. Lastly, of interest here, the PDC-MIP procedure yields results somewhat intermediary, with a pore access diameter similar to BSE images, but with a pore volume repartition much more uniform over three orders of magnitude in terms of

pore sizes.

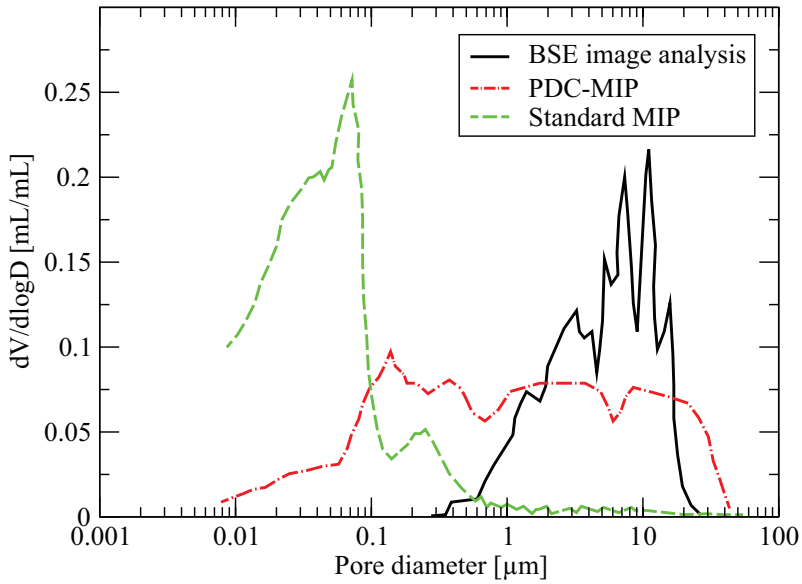

Figure 1.20: Pore size distribution for a 28 days OPC with $w/c = 0.4$, obtained by various techniques – *from* [Zhou et al., 2010].

Thermoporometry:

Introduced by [Brun et al., 1977], thermoporometry (TPM) is a calorimetric method based on the fusion / crystallization point for confined liquids. Using differential scanning calorimeters (DSC) allows to measure precisely small temperature variations during solidification (exothermic) and fusion (endothermic) processes. Unlike the previous methods, it is a non-intrusive measure and it does not require prior drying (no damage made to the microstructure due to capillary tensions). However, several bias may influence the results interpretation, like the volume changes at the freezing point and the cryo-pump effect, which can locally yield stress and damage the microstructure. Lastly, the results interpretation in the range of 0.7 nm to 3 nm are very precise [Vu, 2009]. The method can be extended to a higher upper bound, but other physical phenomenon are to consider, with new uncertainties.

5.3.3 Recent advances in structural characterizations

Small angles diffusion:

Small angles X-Ray / Neutron scattering (respectively SAXS and SANS) are non intrusive methods introduced approximately 35 years ago, and had become a very powerful tool to analyze microstructural and dynamic properties in porous materials (*e.g.* [Allen et al., 1982]). They are non-intrusive methods, thus the material can be analyzed "as is". The overall porosity is easily measured, with a better distinction between the various types of water, and some information about the pores shapes

are accessible. However the interpretation of such experimental results is still a challenge with such highly heterogeneous bulk phases.

Nuclear Magnetic Resonance:

The Nuclear Magnetic Resonance (NMR) relaxation is a recent technique developed to characterize porous materials. First used for mediacal purposes, it is based on the observation of the relaxation time after a magnetic perturbation for the fluids present in the pore space. The general idea is that a the fluid, most of the time water, will relax faster in non-confined space. [Korb et al., 1994] established laws suited for cement based materials, and are able to established relaxation time distribution that reflects the pore size distribution. In addition, they also access topological information at the lowest scale scales, and are able to assess water self-diffusion coefficients at the hydrate scale, specifically in the C-S-H phase [Korb, 2010]. This technique is applicable for wide scales, according to [Halperin et al., 1994], from 1 nm to 100 µm. Other authors, [MacTavish et al., 1996] for example, studied the overall hydration process with the new hydrates apparition, and the porosity evolution. Lastly, [Korb et al., 1998], also managed to take into account para-magnetic impurities such as Fe^{3+}, Mn^{2+}.

A brief summary is presented Fig. 1.21, where each technique is placed with the corresponding application ranges. Both the IUPAC classification and concrete science terminologies are reminded.

However, the direct comparison of each technique remains difficult because of the different hypothesis and various experimental possible biases. Each of these methods seem to qualify for comparative studies, but up to today, acquisition of intrinsic 3D geometrical and morphological information is still an ongoing challenge.

In addition, even though there is a lot of overlap between the experimental methods of structural characterization, they usually have better focuses at particular scales due to various effects: microstructure resistance of the investigated materials (drying conditions, pressure applied), morphological effects (bottle ink effect, pore access diameter, *etc.*). This is the reason why, until today, there is no definite knowledge of the pore structure for cementitious materials. At the hydrates scale, the pore modes are well defined, and the convergence of various techniques weigh in their favor. For the capillary pores and macropores (from 20 nm to approximately 20 µm), there is always a discontinuity in the description. X-Ray CT seems to be the most promising method, given a sufficiently powerful source of radiation (synchrotron sources) – *e.g.* [Juenger et al., 2003, Juenger et al., 2005] for early age mechanisms and hydration understanding, or [Promentilla et al., 2009, Sugiyama et al., 2010] for pore characterization in sound or deteriorated cementitous materials.

5.3.4 Hydrate pore network

At the hydrate scale, two main modes arise (see Tab. 1.5). They are both part of the C-S-H porosity since the other hydrates take a crystalline form.

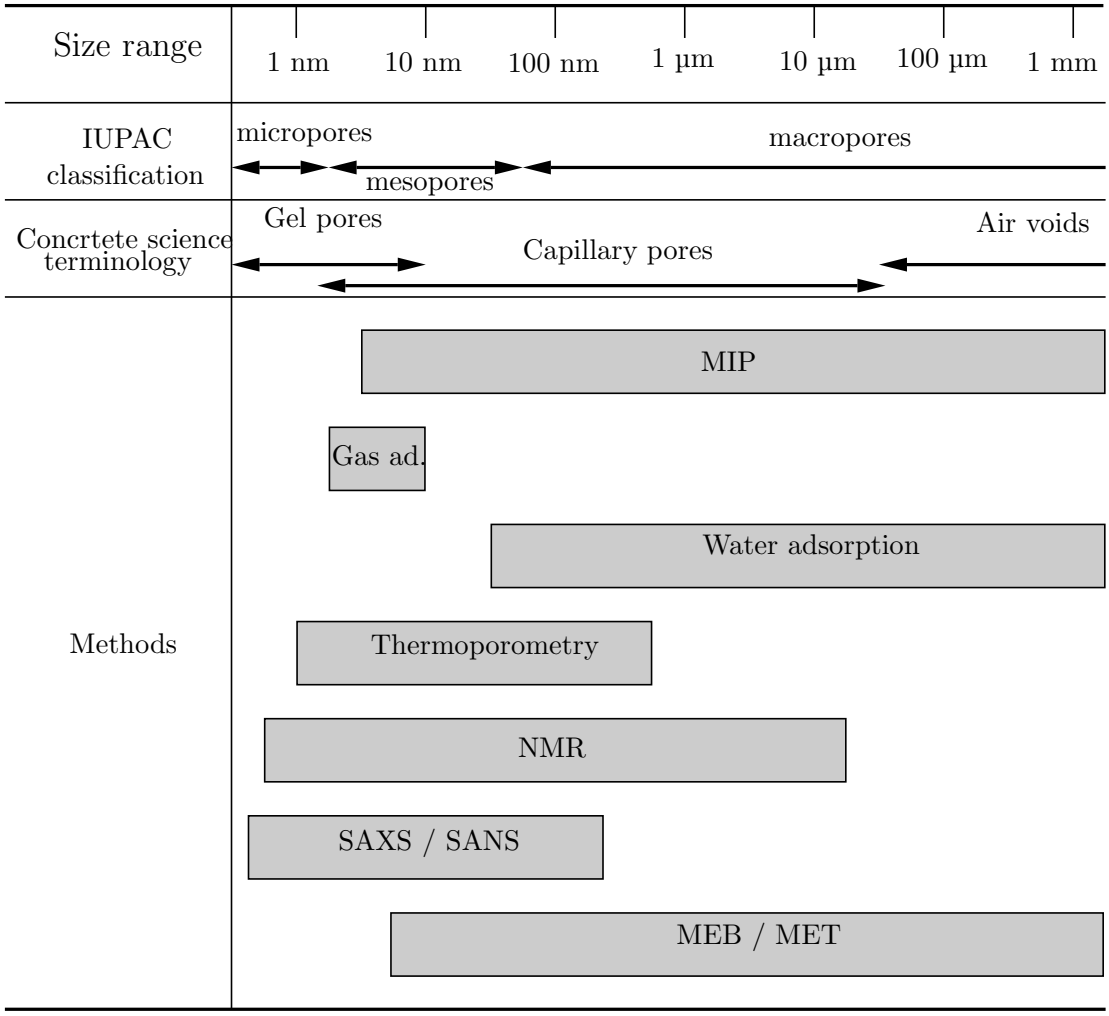

Figure 1.21: Experimental porosity characterization methods & Application ranges.

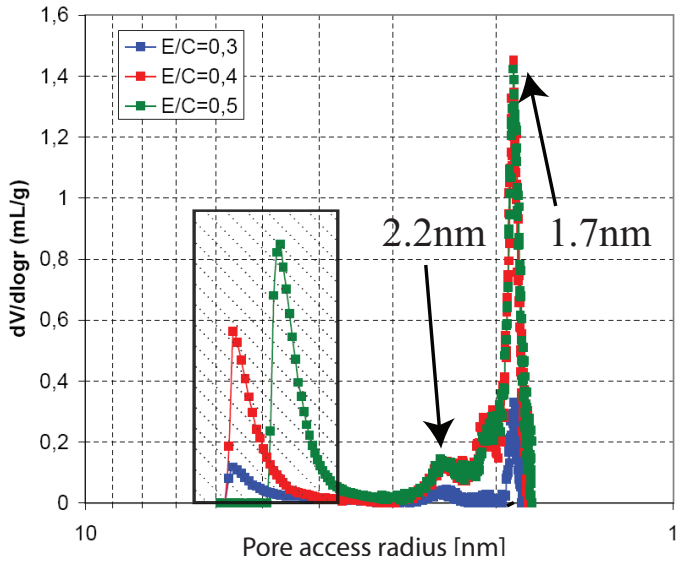

Figure 1.22: PoSD under $\phi \leq 10\,\text{nm}$ obtained by thermoporometry – *from* [Vu, 2009].

The first mode pore radius is around 2 nm. Adsorption techniques [Baroghel-Bouny, 2007a] show a main pore mode, with a maximum located at $r_p \approx 1.7\,\text{nm}$. This value is also supported by water sorption experiments [Vu, 2009]. TPM experiments allow to zoom in on a particular size range from 1.7 nm and 3 nm [Vu, 2009, Valckenborg et al., 2002], and show more precisely peaks with a radius between 1.76 nm to 2.2 nm (Fig. 1.22 displays those two modes, on the right side – the dotted area on left side of the graph is not to consider, it is not attributed to a pore mode but rather to an ice surfusion phenomenon). Those values are in accordance with the aforementioned models for the C-S-H structure: [Feldman and Sereda, 1968] predict a pore mode at 1.85 nm, attributed to inter-sheet space , or the [Tennis and Jennings, 2000] model that predicts a pore mode for the HD C-S-H at 2.83 nm.

The second pore mode is around 4 nm to 5 nm in radius, [Baroghel-Bouny, 2007a] [Baroghel-Bouny, 2007b], and can be attributed to the LD C-S-H [Tennis and Jennings, 2000].

In addition, those values have been confirmed by recent NRM studies [Korb et al., 1994] [Korb, 2010], which point out two main pore families at this scale, at 1.7 nm and 7 nm. They are also interpreted respectively as inter-crystallites and inter-layer pores.

Lastly, there is also a consensus about the low variability for those measures in regards to the cement composition, and the cement paste mix-design, which leads to a conclusion that the C-S-H structure is mostly independent of the cement / cement paste type, and should be consider as an intrinsic information at this scale.

Investigation technique	1st mode HD C-S-H	2nd mode LD C-S-H	References
TPM	1.83 nm		[Vu, 2009]
	2.2 nm		[Baroghel Bouny, 1994]
NMR	1.8 nm	7 nm	[Korb, 2010], [Valckenborg et al., 2002]
WVDI + BJH	1.7 nm		[Baroghel-Bouny, 2007a]
	2 nm	4 nm to 5 nm	[Vu, 2009]
Nitrogen SI + BJH	1.8 nm to 2.2 nm		[Vu, 2009]
MIP	≈ 3 nm	10 nm	[Gallé, 2001]
		10 nm to 30 nm	[Cook and Hover, 1999]

Table 1.5: Pores modes (**radii**) & Investigation techniques - Hydrate scale.

5.3.5 Cement paste pore network

At the cement paste scale, in addition to the hydrate pores, the capillary pores are present. Assessment of the complete pore size distribution at this scale is still an undergoing challenge.

MIP measurements — with their known biases — vastly underestimates the size of pores that are actually present in hardened CP [Diamond, 2004]. However, they can give good comparative descriptions.

During the hydration of a CP, the pore network evolves and the total porosity decreases. The PoSD also evolves, as it is shown Fig. 1.23. The total porosity decrease (left side of the graph) is qualitatively predicted by hydration models (Sect. 4 of this chapter), and the pore access diameter also decreases by an order of magnitude, from 0.8 µm to 0.08 µm. The main pore mode also decreases in a comparable fashion, as it is visible on Fig. 1.24.

Again, the reader is reminded that MIP is only suitable for comparative studies. The qualitative evolution of the pore space is described, but no quantification is made as to the actual CP capillary pore diameter distributions. Data from the advanced techniques presented earlier towards this issues are not yet easily available, as they are still under development / implementation.

As previously mentioned, the offset in terms a pore access diameter between methods is not precisely known. In [Diamond, 2000] (see Fig. 1.19), it seems to be two orders of magnitude in diameter. The MIP measurement interpretation leads to a pore access diameter about 0.1 µm, whereas image analysis leads to 10 µm for the same CP. In [Lange et al., 1994], the same type of offset if found, between 2 and 3 orders of magnitude.

Considering the presented literature review, we believe that at the CP scale,

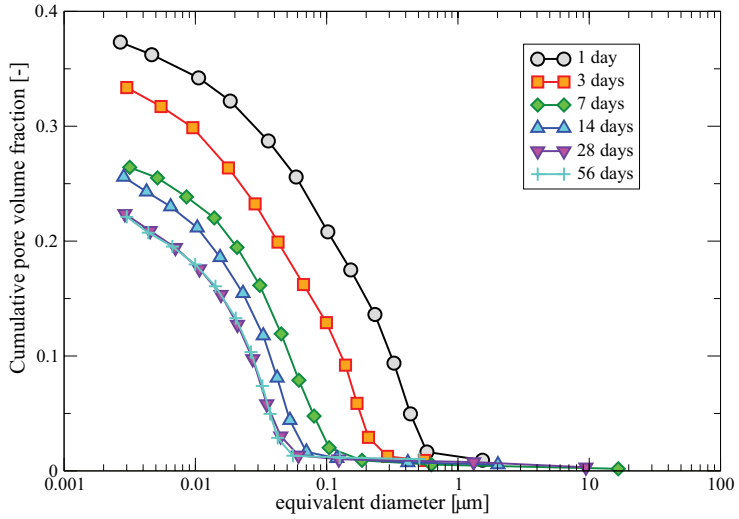

Figure 1.23: OPC with $w/c = 0.5$, with a standard CEM I composition - MIP measurements at 1, 7, 14, 28 and 56 days – *from* [Cook and Hover, 1999].

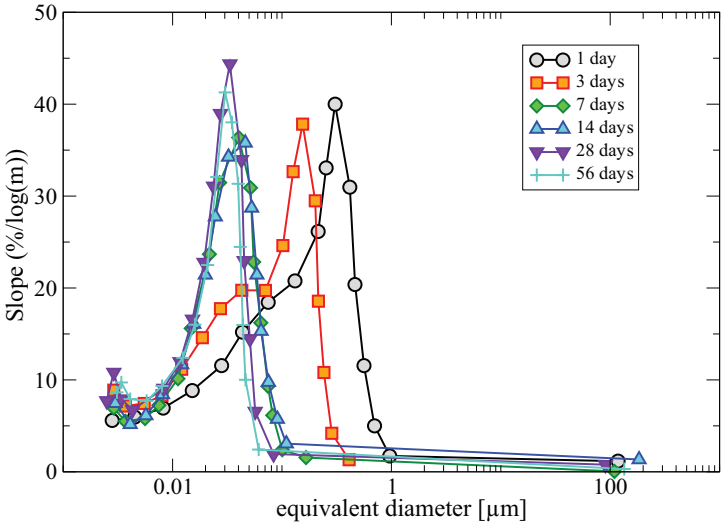

Figure 1.24: OPC with $w/c = 0.5$, with a standard CEM I composition - MIP measurements at 1, 7, 14, 28 and 56 days – *from* [Cook and Hover, 1999].

the pore sizes ranges between 10 µm and 20 nm. Those values are supported by [Mindess et al., 2003]. The upper limit is set to reflect image analysis as well as the PDC-MIP procedure, which is probably the most reliable technique as long as the images resolution is sufficient. This value has also been supported by *Wood's* metal intrusion [Diamond, 2000]. The lower limit, on the other side, is set to distinguish the hydrates pores from the capillary pores. However, at this point no particular assumption is made as to the continuity of the pore network between those two bounds. The size distribution between those bounds is discussed in the following, but it is the author belief that the actual size distribution is rather uniform, as suggested by PDC-MIP data.

Finally, it is necessary to look at the influence of the mix-design, and especially the w/c ratio. The total porosity increases with the w/c (Fig. 1.25), which reflects the fact that there is more water, and thus more pore space available for high w/c ratios. The pore access diameter seems to stay unchanged, when the same experimental procedure is repeated for each sample.

The size distributions for the same samples (Fig. 1.26) display interesting features. The pore access diameter (0.1 µm) stays unchanged with the w/c, and is usually associated with capillary porosity (macroporosity), whereas the second and third pore classes (0.02 µm and few nanometers) are associated with the hydrate pores. This second class ($\approx$ 20 nm) that appears when $w/c \leq 0.4$ is in accordance with 0.38 predicted by [Powers and Brownyard, 1947]. Following the authors, under this threshold ratio, all the water is consumed by the hydration reaction, and only macropores remain. On the other side, above the threshold, the remaining water is consumed to create "outer" hydrates, known as LD C-S-H, with a dominant pore mode at 20 nm (as measured by MIP).

5.3.6 Mortar and concrete pore network

When upscalling to mortars or concretes, one can consider the material as being composed by a matrix (the CP) binding rigid inclusions (sand and/or aggregates). Those aggregates may be classified in two main categories according to their size. For diameters $\phi \leq 5$ mm, it will be consider as sand, and above as gravels.

The CP matrix has its own porosity, as already presented in the previous section. It is visible on Fig. 1.27, where a typical PoSD is presented for a CP and a mortar: the CP exhibits the same pore sizes as the mortar for diameters under 0.1 µm, and the mortar has additional pore modes. Around 1 µm, the mortar curve exhibits a second mode, which is attributed to the presence of aggregates, and an additional smaller mode for sizes greater than 10 µm attributed to entrapped / entrained air. The aggregates inclusions are usually considered impermeable, so the general assumption is that if the porous CP is replaced with impermeable inclusions, the overall porosity will decrease. This assumption is verified as long as there is a limited amount of inclusions, as displayed on the left side of Fig. 1.28: the porosity decreases when the volume ratio of sand over CP increases. However, there is a

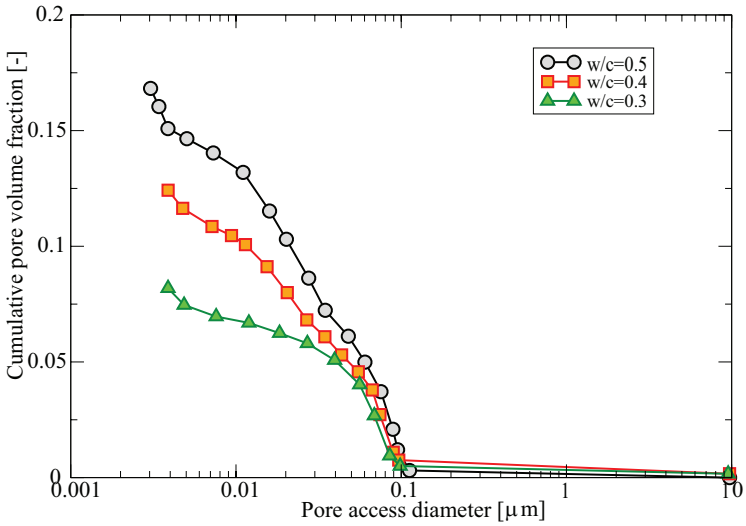

Figure 1.25: OPC, with a standard CEM I composition. MIP measurements – *from* [Gallé, 2001].

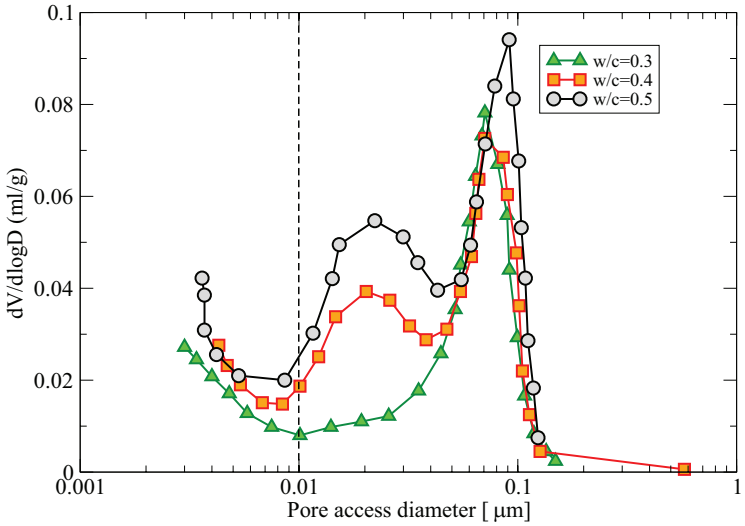

Figure 1.26: OPC, with a standard CEM I composition. MIP measurements – *from* [Gallé, 2001].

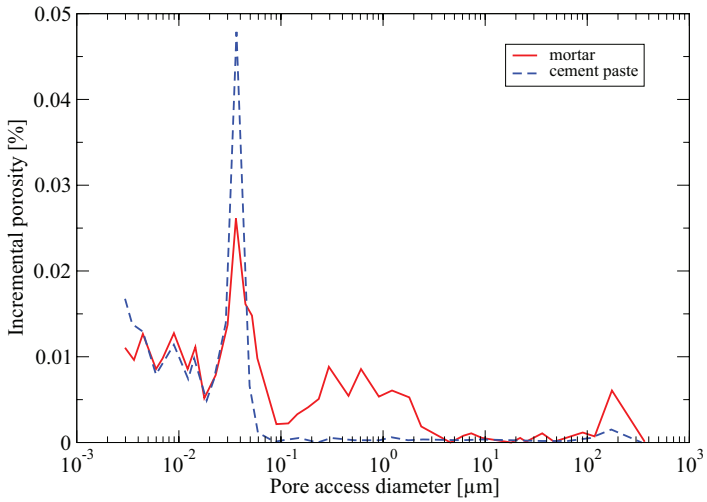

Figure 1.27: MIP pore characterization: CP and mortar, CEM I type, $w/c = 0.4$, 3 month old – *from* [Bourdette et al., 1995].

threshold beyond which the global porosity in mortars starts increasing again. This peculiar feature is explained by the interface effects around the aggregates.

The numerical values presented in this paragraph are derived from MIP data. The same offsets as for the CP scale are to consider.

In the vicinity of aggregates, a porosity increase is noticed. This is known as the *Interfacial Transition Zone* (ITZ). It influences the microstructure up to distance of few dozens of micrometers from the aggregate, as presented on Fig. 1.29.
Several models exists to explain this ITZ:

- [Monteiro et al., 1985] explained the origin of the ITZ by the *wall effect*. The anhydrous grains spacing is higher at the interface vicinity, which lead to more "space" for large crystals to develop during hydration, and thus a bigger porosity in hardened mortars. MEB studies carried out by [Scrivener and Nemati, 1996], [Scrivener et al., 2004], [Diamond and Huang, 2001] among others, confirmed this hypothesis, but a quantitative analysis from their data is extremely difficult, due to the amount of meaningful parameters: aggregates origin, mix-design, cement compositions, curing conditions, age, *etc.*

- [Hoshino, 1988] described the ITZ a micro-bleeding phenomenon. Underneath some aggregates, water is kept trapped as a result of the overall bleeding phenomenon. It leads to a differential porosity between top and bottom of

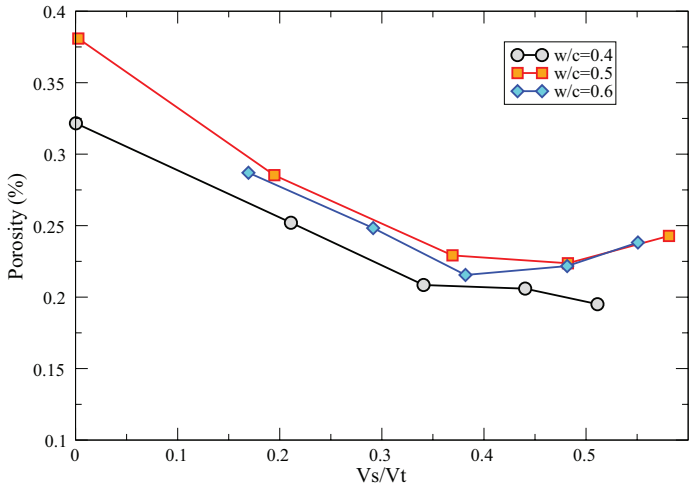

Figure 1.28: Mortar porosities with respect to the sand content for various w/c, CEM I type – *from* [Vu, 2009].

aggregates, as well as a local porosity anisotropy. This bleeding has been observed by [Leemann et al., 2006]. The porosity difference between the top and bottom of aggregate is actually noticeable, and it is sensible to fresh mix vibrations, which help to get a more isotropic ITZ.

- Lastly [Garboczi and Bentz, 1992] attributed the ITZ to new hydrates crystallization orientations. Near the interface they can only grow in one direction and thus those large crystals, again, lead to a higher porosity. However, this explains only short distance relationship between porosity and aggregate distance, and, as it is visible on Fig. 1.29, this effect is noticeable on few tens of micrometers.

Lastly, one can add the differential thermal expansion properties between the aggregate and the hardening CP to explain the ITZ. It would lead to a hardened state with differential deformations at the interface.

The most plausible explanation is that the three phenomena are likely to be involved at the same time.

Finally, mostly for durability purposes, concretes can be deliberately air entrained. Those voids occupy around 15% of the CP matrix. They range in size from 20 µm to 1 mm [Diamond, 2004]. Their shape is mostly spherical, and they do not connect with each other.

In conclusion, at the mortar and concrete scale, the PoSD consists of the following:

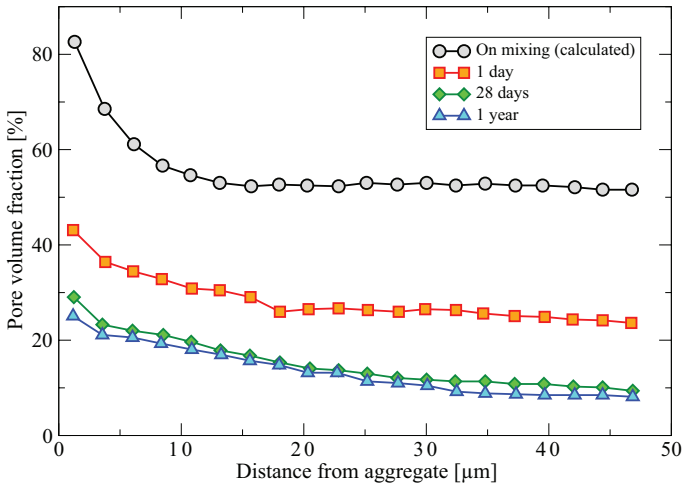

Figure 1.29: Pore size distribution in the aggregate vicinity – *from* [Scrivener and Nemati, 2004].

- CP scale PoSD, previously presented,
- Large capillary pores, up to approximately 10 µm,
- ITZ with a porosity two to three times higher than the CP according to the literature, and a pore access threshold diameter approximately ten times bigger than the CP one,
- Entrained / entraped air, as spherical voids ranging from 20 µm to 1 mm.

6 Concluding remark

In this chapter, an overview of cement materials has been addressed. Starting with the chemical / mineralogical composition of the anhydrous cement description, then the hydration mechanisms and few simple macroscopic models. A hydration modeling framework has been presented based on the literature review, with efforts made to make it as pertinent as possible in regards to experimental results (especially for the overall porosity prediction, and for the hydration "end").

After reviewing the most used experimental characterization procedures, the most plausible description of the pore network, according to the author, has been made in terms of pore size distributions. The remaining morphological aspects of cement paste microstructures will be reviewed in the next chapter.

To fully describe cement based materials, a decomposition into 3 (4) scales is thus considered for the next chapters. Such scale separation is not new, and has been implemented in cementitious materials studies for a long time, however, the *innovation* resides in the hydrate modeling (C-S-H phase). In addition, a clear separation of the various type of porosities should facilitate its modeling, since only one main mode is retained for each scale.

- Starting at the C-S-H scale and its two pores modes (approximately 2 nm and 10 nm). Only the second one will be considered in the following chapters since it is most likely the one where the transport phenomena occur (with presumably no interaction between those two modes [Korb, 2010]).

- Then, scaling up to the cement paste scale, a pore network with a pore size span from 1 µm to 10 µm will be considered, trying to reflect the PDC-MIP data [Zhou et al., 2010]. The lower limit is set to be able to describe properly particles / voids as small as the micrometer, and to keep a reasonable computational time when numerically homogenizing properties, considering RVEs in the 100 µm length-scales (actual sizes are assessed in the next chapters).

- Lastly at the mortar scale an additional feature is introduced — not a new pore mode strictly speaking — where the cement paste porosity increase in the aggregates vicinity. The same feature is observed with concrete and coarse gravels, but with significant changes in its properties (its thickness is rather driven by the median size of the anhydrous cement grains , not the aggregate size [Bentz et al., 1993]). In actual typical concretes, the amount of aggregates reaches up to 75% of the volume fraction. It leaves very little spacing between adjacent aggregates, at most few time the ITZ thickness, leading to a likely fully percolated ITZ [Garboczi and Bentz, 1996].
  It should be noted that at this scale, the ITZ can hardly be considered as a supplementary **phase** since it reflects a transition with a gradient of porosities (as well as phases volume fractions).

2 Morphological modeling of cement based materials

Contents

1 Introduction 48

2 Morphological modeling framework 48

2.1 Correlated Random Fields 48

2.2 Excursion set theory 52

2.3 Excursion set measurements 55

2.4 The expectation formula 56

2.5 Morphological operations 60

3 Percolation and statistical representativity 61

3.1 Numerical approach to the Statistical RVE 61

4 Application to hydration modeling 66

4.1 Existing models 66

4.2 Reaching high volume fractions 68

4.3 Polydisperse inclusions and Particle Size Disrtributions . . . 70

4.4 Morphologies evolutions 78

5 Hydration model validation 80

5.1 Total porosity 81

5.2 Pore size distributions 83

5.3 Tortuosity 88

6 Concluding remarks 91

1 Introduction

The present work is based upon the assumption that the representation part is independent from simulation part. Hence, a tool for spatial representation is introduced in this chapter, and the link with any type of simulation will be made only on the last chapter, with a so-called "projection" stage.

The use of a mathematical tool like *correlated Random Fields* (CRF) brings a major contribution to heterogeneous materials modeling. Indeed, in addition to the usual characteristics of random variables (expectation, variance, *etc.*), CRFs have a spatial structure that can be statistically controlled by setting its covariance function. Thanks to recent major breakthrough results [Adler and Taylor, 2007], several aspects of such structures such as the average distance between maxima, or the shape, can be controlled, bringing a wild range of possible modelings. On one hand, it can be used to directly define material properties as a random field, leading to a continuum definition of the heterogeneities through the parameter space. On the other hand, a discrete approach, using excursion sets of CRF, allows a morphological modeling of the material. Recent results [Adler, 2008] even give the geometrical and topological measures of such so-called excursion sets, providing a powerful and accurate morphological tool for spatial simulations.

2 Morphological modeling framework

This section introduces the morphological framework established in [Roubin, 2013], and all the key notions and concepts are reminded here. The application of the framework to cementitious materials was done in collaboration with E. Roubin (Sect. 4 of this chapter), as well as the *percolation* Representative Volume Elements definition (Sect. 3 of this chapter).

2.1 Correlated Random Fields

In order to understand the definition of the microstructure process, the main concepts are presented in this section, regarding the general scope of random variables and random fields, their characteristics and distributions, and lastly the *excursion set theory*.

2.1.1 Random Variables and Random Fields

A Random Variable (RV), often denoted X, is a variable used to represent the numerical outcome of a random phenomenon. These RV can be either *discrete* or *continuous*.

A RV with a finite number of distinct values is a discrete one, and can be illustrated by the outcome of a coin toss: either heads or tails, or respectively either

0 or 1. In this case the variable can be characterized by the *probability distribution*, which gives the probability of every possible outcome: $P(X = \text{heads}) = 0.5$, $P(X = \text{tails}) = 0.5$, and $\sum_i P(X_i) = 1$.

A continuous RV is one which takes an infinite number of possible outcomes. It is characterized by a *probability density function*. In the following this type of variable will be used. As an illustration example, the time taken for something to be done is continuous, since they are an infinite number of possible times. In this case, the *probability density function* f must satisfy the following condition:

$$\int_{\text{all } X} f(x)dx = 1. \tag{2.1}$$

To best describe and characterize this kind of processes, some definitions from the *theory of probability* are needed to describe the so-called *probability space*, which is a triplet made of:

- A *universe*, denoted Ω. It is the set of all possible outcomes for a RV,
- An *event*, which is a subset of the universe. It represent one possible outcome, and the set of all possible events is denoted $\mathcal{F}$,
- A *probability function*. If ω is the result of a random experiment, the probability theory — developed by Kolmogorov [Kolmogorov, 1950] — allows a quantification of ω to be in an event $F \in \mathcal{F}$ without manipulating ω itself. To achieve the latter, a probability function P is defined, which measures the probability of the event F to occur. It can be seen as a measure of $\mathcal{F}$.

The triplet $(\Omega, \mathcal{F}, P)$ defines the *probability space*. Within this space, let $X : \Omega \to E$ be a measurable function defined over the $(\Omega, \mathcal{F}, P)$ which takes values in a measurable space $(E, \mathcal{A})$ (in which $\mathcal{A}$ is a σ-algebra of E). Hence, for $A \in \mathcal{A}$, the event:

$$X^{-1}(A) = \{\omega \in \Omega, X(\omega) \in A\} \in \mathcal{F},$$

will be denoted $\{X \in A\}$. So in the case where $E = \mathbb{R}$, the RV X can be seen as a function. The associated density function $f_X : \mathbb{R} \to \mathbb{R}_+$ can be defined so that:

$$P\{X \in A\} = \int_A f_X(x)dx, \forall A \subset \mathbb{R}. \tag{2.2}$$

In other words, this probability density function defines the chance for this variable to take a given value. This type of distribution is characterized by its moments. The first two are known as:

- The *expected value* $\mathbb{E}\{X\}$, that can be seen as the mean of a sample which size grows to infinity,

- the *variance* $\mathbb{V}\{X\}$, that can be seen as a characterization of how spread the values are around the expected value.

Based on the previous definition of a RV, a *Random Field* (RF) can be defined by adding a space parameter to the distribution function. Let g be such a field, it is then defined both over the probability space $(\Omega, \mathcal{F}, P)$, and an Euclidean space $M \in \mathbb{R}^N$:

$$g : \Omega \times \mathbb{R}^N \to \mathbb{R}. \tag{2.3}$$

A RF $g(\omega, \boldsymbol{x})$ will be noted $g(\boldsymbol{x})$ to ease notation. At a given point $\boldsymbol{x}$, the field can be seen as a RV, defined by a given distribution called *marginal distribution*. In the given framework, it is assumed the the marginal distribution is the same for all $\boldsymbol{x}$ in the space M. This leads to a global distribution that can statistically define the RF.

2.1.2 Gaussian distributions & covariance functions

Probability distribution functions:

One of the most common probability distribution function, related to real-valued quantities that grow linearly, is the Gaussian distribution (also called *normal* distribution). It is defined by:

$$f_X(x) = \frac{1}{\sigma\sqrt{2\pi}} e^{-(x-\mu)^2/2\sigma^2} \forall x \in \mathbb{R}, \tag{2.4}$$

where μ and σ are respectively the mean and standard deviation of the distribution. If the RV X follows the latter, then the first two moments of the distribution — $\mathbb{E}\{X\} = \mu$ and $\mathbb{V}\{X\} = \sigma$ — are sufficient to fully describe it. These types of distribution functions have numerous advantages, and among them an interesting and useful feature is that decorrelated Gaussian RVs are independent, and a linear combination of such RVs is still Gaussian. Lastly, this type of distributions emerge naturally according according to the *central limit theorem*.

Many other types of probability distribution functions can be defined, to suit other phenomena, however in the present work only *Gaussian related* ones will be used. The excursion set theory that will be presented next section applies to Gaussian and Gaussian related RV. The latter are RVs automatically derived from Gaussian ones. They are the result of a function composition. If X_r is a Gaussian related distribution, there is a possible decomposition of the process into:

$$X_r : \Omega \xrightarrow{\boldsymbol{X}} \mathbb{R}^k \xrightarrow{S} \mathbb{R}, \tag{2.5}$$

where $\boldsymbol{X}$ is a vector of independent Gaussian RV of size k, and S a non-linear application. As an example, the *log-normal* distribution is retrieved when $k = 1$ and $S = \exp$. Another type of distribution, that will be often used further on, is the χ^2 one (with k degrees of freedom). It is the sum of k squared Gaussian RVs.

Herein, the same principle can and will be applied to RFs since they are defined by a unique marginal distribution. If g_r is such a field, then:

$$g_r : \Omega \times \mathbb{R}^N \xrightarrow{\boldsymbol{g}} \mathbb{R}^k \xrightarrow{S} \mathbb{R}, \tag{2.6}$$

where $\boldsymbol{g} = \{g_i\}, i = [1..k]$ is a vector valued Gaussian RF, all the g_i being independent.

Covariance functions:

Given all the previous definitions it is possible to apprehend the notion of RF defined over a parameter space $M \in \mathbb{R}^N$. The last key point is to enforce a spatial structure to the latter, in order to yield a *correlated RF*. The covariance function ensures for any couple of points $(\boldsymbol{x}, \boldsymbol{y}) \in M^2$, that $g(\boldsymbol{x})$ and $g(\boldsymbol{y})$ are not independent anymore. The correlation measure is made through the covariance function $\mathcal{C}$, and can be defined for a zero mean distribution by:

$$\mathcal{C}(\boldsymbol{x}, \boldsymbol{y}) = \mathbb{E}\{g(\boldsymbol{x})g(\boldsymbol{y})\}. \tag{2.7}$$

If the the random field is not correlated at all, meaning that $g(\boldsymbol{x})$ and $g(\boldsymbol{y})$ are independent, the covariance is:

$$\mathcal{C}(\boldsymbol{x}, \boldsymbol{y}) = \mathbb{E}\{g(\boldsymbol{x})\}\mathbb{E}\{g(\boldsymbol{y})\} = 0, \forall \boldsymbol{x} \neq \boldsymbol{y}. \tag{2.8}$$

On the other side, if the RF is perfectly correlated, for a zero mean distribution, the covariance will be:

$$\mathcal{C}(\boldsymbol{x}, \boldsymbol{y}) = \mathbb{E}\{g(\boldsymbol{x})^2\} = \sigma^2, \forall \boldsymbol{x} \neq \boldsymbol{y}. \tag{2.9}$$

In between the two extreme cases, the covariance function $\mathcal{C}$ defines how g is structured, introducing a correlation length (L_c) as a spatial parameter.

In the following, only *stationary* and *isotropic* covariance functions will be considered, which allows to define $\mathcal{C}$ through a unique variable $h = \|\boldsymbol{x} - \boldsymbol{y}\|$. Under the previous assumptions, the Gaussian model (also known as the *squared exponential*) of covariance functions remains one the most used mainly for its simplicity. It is defined by only two parameters: the distribution variance σ^2, and by a correlation length L_c.

$$\mathcal{C}(h) = \sigma \exp\left(-h^2/L_c^2\right) \tag{2.10}$$

The effect of the correlation length is illustrated Fig. 2.1, where Fig. 2.1(a) is a realization of a 2D RF with a L_c half the size of the domain, and Fig. 2.1(b) with L_c about one twentieth of the domain. Following, the effect of the variance is illustrated on Fig. 2.2. All other parameters being equal, on one side a small variance (Fig. 2.2(b), $\sigma = 1$) leads to low RF extreme values (smaller than 10), whereas high values of variance (Fig. 2.2(a), $\sigma = 5$) lead to extreme values one order of magnitude higher, around 250.

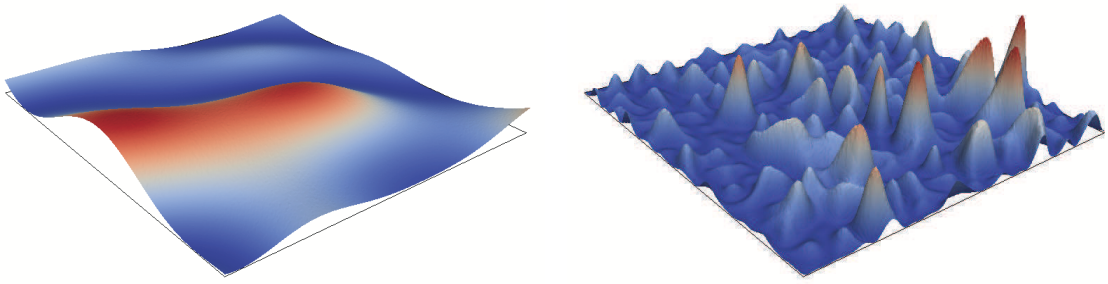

(a) Large correlation length, (b) Small correlation length.

Figure 2.1: Effect of the RF correlation length.

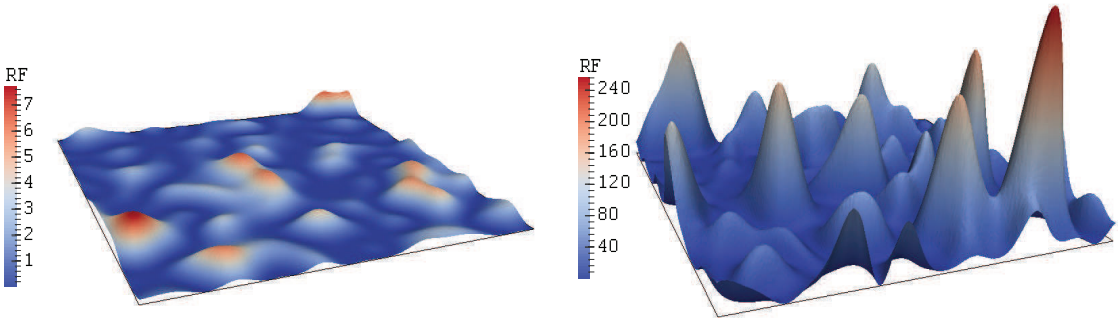

(a) Small variance: $\sigma = 1$, (b) Large variance: $\sigma = 5$.

Figure 2.2: Effect of the RF variance.

It is also worth noting that the choice of the covariance function is not unique, and the complete framework is tractable as long as the $2k^{th}$ derivative of the underlying covariance function at zero exists [Roubin, 2013].

Numerical implementation:

The whole framework being based upon the realization of such Gaussian correlated RFs, efforts had to be made for their numerical implementation. Details about the latter can be found in [Roubin, 2013]. It first relies on the Karhunen-Loève expansion [Loève, 1978], which allows separation between the space variables on one side and the random variables on the other. Secondly, the turning-band method [Matheron, 1973] is used to yield 3D correlated RFs from several one-dimensional correlated RFs (bands).

2.2 Excursion set theory

The *excursion set* is the morphology of a subset of a bounded region defined by thresholding a realization of a correlated RF, creating a set of random shapes. Let

$g(\boldsymbol{x}, \omega_i) = f_i$ be a realization i of $g(\boldsymbol{x}, \omega) : M \subset \mathbb{R}^d \to \mathbb{R}$ defined as above and $D \subset \mathbb{R}$ a given hitting set. The underlying excursion set A_{D_i} is defined by the subset of M where g_i takes its values in D. In other words, an excursion set A_D is defined by:

$$A_D \triangleq \{\boldsymbol{x} \in M \mid g(\boldsymbol{x}, \omega) \in D\}\,. \tag{2.11}$$

And if $D = [u; \infty[$:

$$A_D(u) \triangleq \{\boldsymbol{x} \in M \mid g(\boldsymbol{x}, \omega) \geq u\}\,. \tag{2.12}$$

An example of this principle in dimension $d = 1$ with $D = [u; \infty[$, is shown on FIG. 2.3. A_u shall denote the excursion set for such hitting set of threshold u.

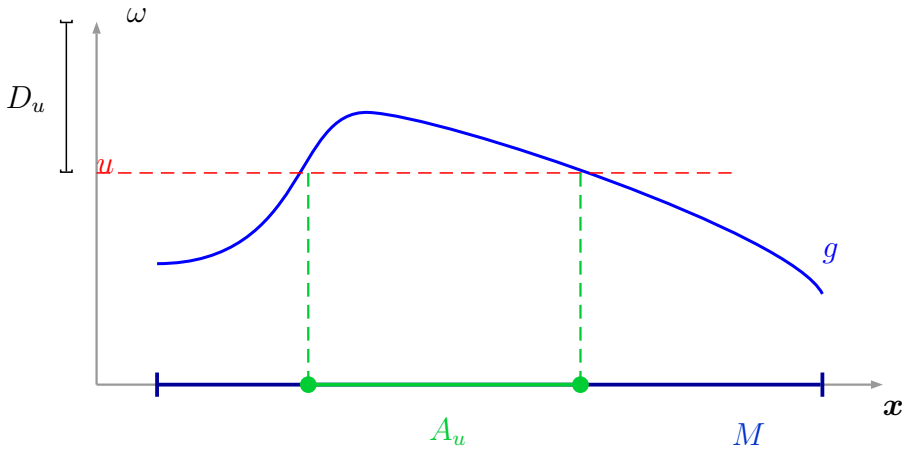

Figure 2.3: Schematic representation of a one-dimensional excursion set A_u.

Herein, applications will be made with $d = 3$. Realizations in such space naturally define three-dimensional excursion sets. The two excursions represented in FIG. 2.4 are made from the same realization with two different threshold values. It arises that, by changing the threshold, a large range of varied morphologies can be generated. This example shows that "low" values of u ($D = [u; \infty[$) produce excursions mainly made of handles with high volume fraction, giving a "sponge" like topology (FIG. 2.4(a)). This type of morphology is very useful for modeling porous media. On the other hand, "high" values of u produce excursions made of several disconnected components with a lower volume fraction (FIG. 2.4(b)). This second type of morphology will be well suited to model inclusion-matrix media, such as mortars or concretes.

The correlation length role is illustrated on FIG. 2.5, where two excursion sets are presented. They correspond to two realizations of RFs with the same properties ($T = 100$, $\sigma = 1$ and $\mu = 0$), but two different correlation lengths $L_c = 5$ and 20. The threshold value is the same in both cases ($u = 2$). On one side FIG. 2.5(a)

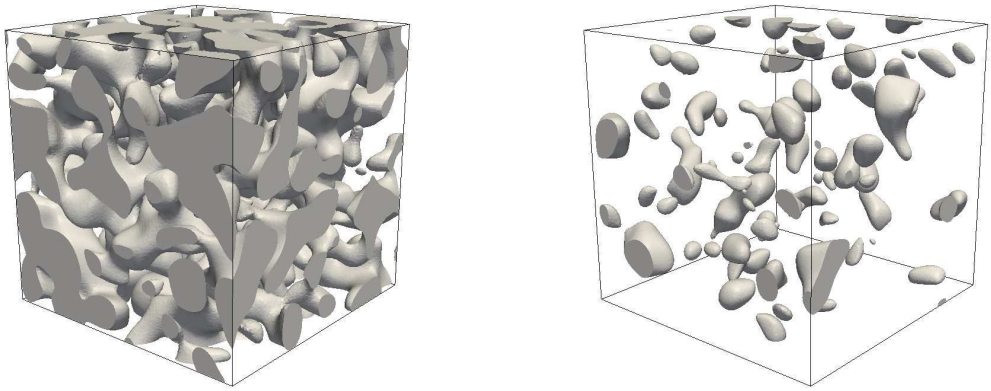

(a) "Low" threshold (b) "High" threshold

Figure 2.4: $T = 100$, $L_c = 10$ – Effect of threshold value on tri-dimensional excursion topology.

displays only "few" components, mostly disconneceted, and their spacing is in the L_c vicinity, whereas FIG. 2.5(b) contains plenty of small components.

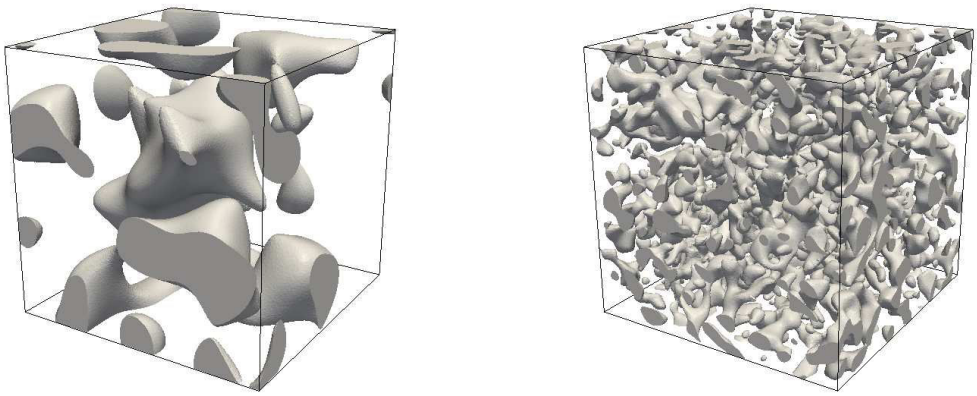

(a) $L_c = 20$ (b) $L_c = 5$

Figure 2.5: $T = 100$, $u = 2$ – Effect of correlation length on tri-dimensional excursion topology.

2.3 Excursion set measurements

For the presented tool to be suitable to a modeling framework, it is necessary to be able to *control* the created morphologies according to a given measure. We introduce here the necessary mathematical notions, as well as the probabilistic link established between the created morphologies characteristics and the RF parameters.

2.3.1 Geometrical and topological measures: Lipschitz Killing Curvatures

The entire framework is based upon a particular measure of the space, called the *Lipschitz Killing Curvatures* [Federer, 1959] (LKCs in the following). Like every measure, for a subset M of a N-dimensional space, it gives $N+1$ descriptors. It is the minimum number of descriptors to captures the entire geometry *and* topology. Each LKC, $\mathscr{L}_i(M)$ can be seen as a volume measure in the ith dimension, with $0 \leq i \leq N$.

In the three dimensional case, that will be used in the following, the LKCs of a subset $M \in \mathbb{R}^3$ are:

- $\mathscr{L}_3(M)$ is the three dimensional volume of M,
- $\mathscr{L}_2(M)$ is half the surface area of M,
- $\mathscr{L}_1(M)$ is twice the calliper diameter of M,
- $\mathscr{L}_0(M)$ is the Euler Characteristic (hereafter EC) of M, which contrary to the other LKCs is a topological measure.

This last measure, the EC, will be of interest in future paragraphs so a summary of its properties is presented. It has been first introduced in the 18th by L. Euler for polyhedra, as a topological invariant, *i.e.* a number to describe a shape regardless of its deformation: the alternate sum of the number of vertices (V), edges (E) and faces (F) for a convex polyhedra is constant and $V - E + F = 2$. For example, a tetrahedron or a cube are topologically identical. This concept was then applied to more than one polyhedron. If P polyhedron are considered, with at least one common face, this time the invariant is different, and $V - E + F - P = 1$. Lastly, if unions of such polyhedra are to consider, each intersection (considered as a hole) reduces the EC by one. From those consideration, the EC has been defined for topological studies of solids (divisible into polyhedra) as:

$$\mathscr{L}_0(M) = V - E + F - P. \tag{2.13}$$

Not so long after, during the 19th, C.F. Gauss contributions to differential geometry led to the introduction of a Gaussian curvature. At a point on a surface, it may be defined as the product of the maximal and minimal curvatures $K = k_{\min} k_{\max}$. Then, following the *Gauss-Bonnet* theorem and the integration of the Gaussian

curvature over an entire surface, a link (not developed) is made with the previous definition when compact surfaces are considered. It allows to retrieve a global topological information – the invariant – from locally integrated information.

Lastly, in the same spirit of higher dimension considerations, the EC can be defined for an entire manifold (instead of its surface) as the alternate sum of the j-dimensional features. In three dimensions it leads to:

$$\mathscr{L}_0(M) = \#\{\text{connected components}\} - \#\{\text{handles}\} + \#\{\text{holes}\} \tag{2.14}$$

The LKCs and their meaning have been rapidly introduced in the context of 3D morphological representation. They are an intrinsic measure (independent of the measure chosen in a Euclidean space). A second type of measure is now introduced to characterize the probability space, called the *Minkowski* functionals.

2.3.2 Minkowski functionals

The *Minkowski* functionals are another popular measure. However, they are closely related to the LKCs, and can be defined for a subset $A \subset \mathbb{R}^N$ by:

$$\mathscr{M}_{N-j}(A) = (N-j)!\omega_{N-j}\mathscr{L}_j(A). \tag{2.15}$$

They have been often used in many disciplines to measure morphological strucures, as in the astrophysics community (*e.g.* [Mecke et al., 1993]). Contrary to LKCs, this measure is not intrinsic, and thus depend on the used measure.

In the presented context, following [Taylor et al., 2006] it is used to measure the probability for a Gaussian RV to be in the aforementioned *hitting-set*. In this sense, these functionals can be seen as a measure of the probability space. The development and equation are not presented here, for more details and development please refer to the work [Taylor et al., 2006, Adler and Taylor, 2007, Adler, 2008, Roubin et al., 2015]. Only the final expressions of concern are made explicit in the following paragraphs, in Sys.2.21 for Gaussian distributions and Sys.2.22 for the χ^2 ones, and the link with the probability space appears more comprehensible.

2.4 The expectation formula

Following [Adler and Taylor, 2007, Adler, 2008], a probabilistic link has been made between excursion set properties and random field thresholding parameters giving an explicit formula for the expectation of the LKCs - $\mathbb{E}\left\{\mathscr{L}_i\left(A_u\left(f,M\right)\right)\right\}$.

$$\mathbb{E}\left\{\mathscr{L}_i\left(A_D(f,M)\right)\right\} = \sum_{j=0}^{N-i} \left[\begin{array}{c} i+j \\ j \end{array}\right] \left(\frac{\lambda_2}{2\pi}\right)^{j/2} \mathscr{L}_{i+j}(M)\mathscr{M}_j(D) \;\; ; \;\; 0 \leq i \leq 3 \tag{2.16}$$

where λ_2 is the second spectral moment of f, $\mathscr{M}_j$ the Gaussian *Minkowski functionals* and $[\bullet]$ represent the combinatorial *flags coefficients*. One can notice that the $\mathscr{L}_i$

relate to the spatial measure (M), whereas the $\mathscr{M}_j(D)$ relate to the probability measure of the hitting set D. It is not the purpose to give details on these formulae, however, full proof can be found in [Adler and Taylor, 2007], and details about the explicit form in [Roubin, 2013].

FIG. 2.6 represents the excursion set's volume and Euler's characteristic for different thresholds values in the three dimensional case.

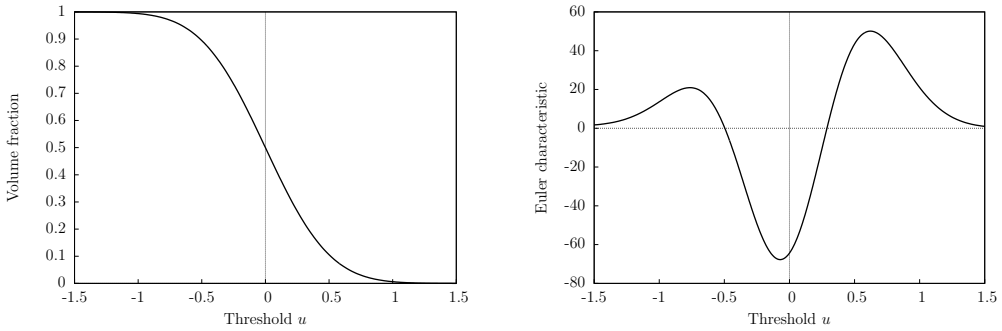

(a) Volume fraction (b) Euler Characteristic

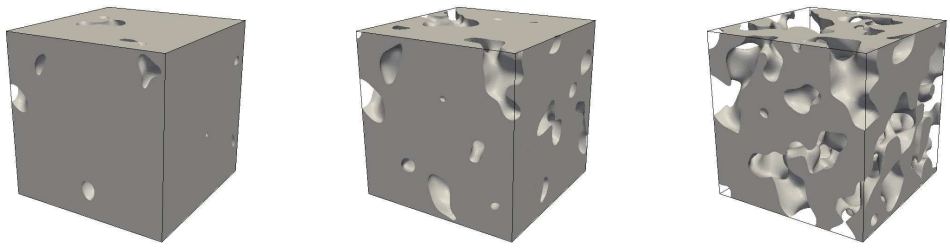

(c) $u = -1$ (d) $u = -0.5$ (e) $u = 0$

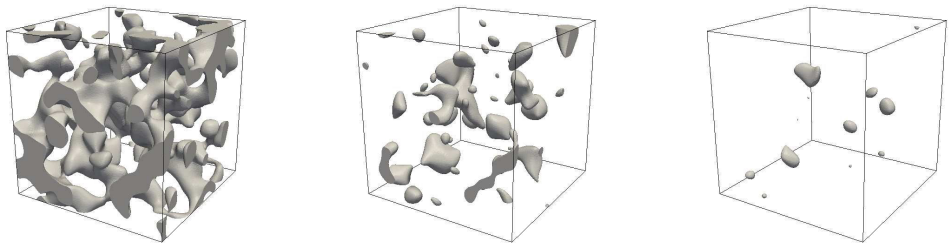

(f) $u = 0.5$ (g) $u = 1$ (h) $u = 2$

Figure 2.6: LKCs of excursion sets of a Gaussian correlated RF in terms of threshold values.

The constant decreasing shape of the volume fraction curve in terms of u clearly reflects the effect of the threshold level on the "size" of A_u. In this case, it is defined by the tail distribution function of the underlying Gaussian random field. Even if more peculiar, the EC curve shape reflects also easily the effect of the threshold

on excursion sets topology. For values of u lower than the lowest value of f, the EC is the one of the full cube ($\mathscr{L}_0 = 1$). By increasing u, several holes appear, counting in positive for the Euler characteristic ($\mathscr{L}_0 > 1$). Then, the expansion of the holes starts to form handles which lead to a sponge like topology ($\mathscr{L}_0 < 0$). By increasing u even more, handles disappear forming a "meatball" like topology of connected components ($\mathscr{L}_0 > 0$). Finally, the EC decreases to $\mathscr{L}_0 = 0$ when no more connected components remain. It should be noted that even if $\mathscr{L}_0$ is a RV, its expectancy $\mathbb{E}\{\mathscr{L}_0\}$ is a continuous function.

From the comparison between theoretical values and measures on one realization, we can point out that the variability of the numerical generation is very low. Therefore, although Eq.2.16 gives only expectations of the LKCs, for this range of excursion sets we can assume that $\mathbb{V}\{\mathscr{L}_i(A_u)\} \ll 1$. This correlation between actual and expected characteristics has been made in the founding work of E. Roubin. As a validation of the numerical implementation, over a 100 realizations of Gaussian correlated RFs — zero mean, standard deviation $\sigma = 5$ and a correlation length $L_c = 10$, over a cube of size $T = 100$ — were yielded and characterized for various thresholds, in terms of volume fraction (f_v) and Euler characteristic (EC). Results are presented Fig. 2.7, with the solid lines representing the expectations, and the crosses the average value over the 100 realizations.

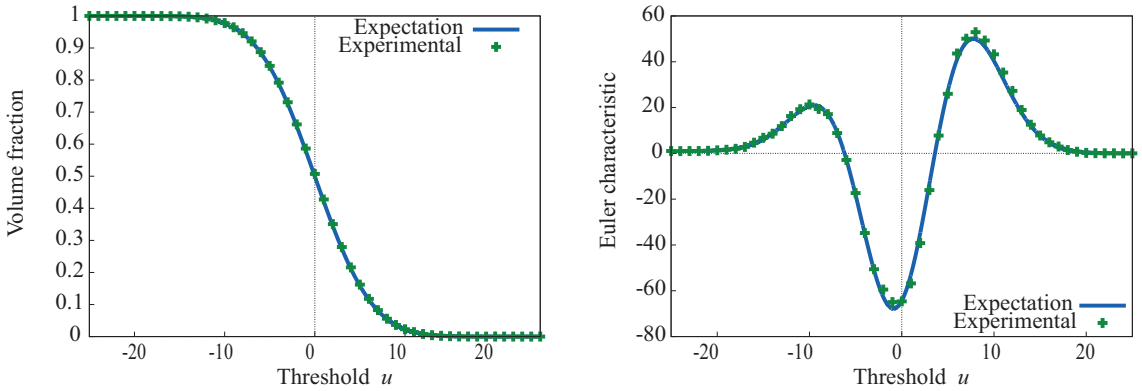

Figure 2.7: Validation of the numerical implementation – *from* [Roubin, 2013].

The quality of the apparent rather good fit is analyzed through the mean square error for both the volume fraction and EC (results are given in Tab. 2.1).

Characteristic	Mean	Variance	Coefficient of variation
Error on f_v	0.006	10^{-5}	0.6
Error on EC	3.3	0.5	0.2

Table 2.1: Statistical quality of the expected characteristics.

The very low variance of the errors ensure that even *one* realization of a targeted morphology will be representative. Their will be no need to iterate over numerous

realizations to ensure a proper morphological representation (given a sufficient size, as discussed in the following SECT. 3.1).

Additional examples are shown later (FIG. 2.15 and 2.16 for one correlation length) with comparison between expected characteristics and experimental ones.

2.4.1 Explicit formula for Gaussian (γ) field

From EQ.2.16, a first development leads to SYS.2.17, in the case of $M = \prod_1^3[0,T]$ — a cube in $\mathbb{R}^3$ — and $D = D_u$:

$$\mathbb{E}\{\mathscr{L}_0(A_u)\} = T^3\left(\frac{\lambda_2}{2\pi}\right)^{3/2}\mathscr{M}_3(D_u) + 3T^2\left(\frac{\lambda_2}{2\pi}\right)\mathscr{M}_2(D_u) + 3T\left(\frac{\lambda_2}{2\pi}\right)^{1/2}\mathscr{M}_1(D_u) + \mathscr{M}_0(D_u), \tag{2.17a}$$

$$\mathbb{E}\{\mathscr{L}_1(A_u)\} = T^3\left(\frac{\lambda_2}{2\pi}\right)\mathscr{M}_2(D_u) + 3T^2\left(\frac{\lambda_2}{2\pi}\right)^{1/2}\mathscr{M}_1(D_u) + 3T\mathscr{M}_0(D_u), \tag{2.17b}$$

$$\mathbb{E}\{\mathscr{L}_2(A_u)\} = 2T^3\left(\frac{\lambda_2}{2\pi}\right)^{1/2}\mathscr{M}_1(D_u) + 3T^2\mathscr{M}_0(D_u), \tag{2.17c}$$

$$\mathbb{E}\{\mathscr{L}_3(A_u)\} = T^3\mathscr{M}_0(D_u). \tag{2.17d}$$

At this point only the *Minkowski functionals* remain unknown, and they are the ones that must be differentiated for each family of RF. Those have been made explicit for a hitting set D_u in the work of [Adler and Taylor, 2007] for Gaussian RF, using *Steiner's* tube formula. They are presented in SYS.2.21, given the following functions:

- The complementary cumulative density function (or tail distribution):

$$\Psi(u) = \frac{1}{\sigma\sqrt{2\pi}}\int_u^\infty e^{-x^2/\sigma^2}\,dx, \tag{2.18}$$

- the Gamma function:

$$\Gamma(k) = \int_0^\infty t^{k-1}e^{-t}\,dt, \tag{2.19}$$

- The incomplete upper Gamma Function:

$$\overline{\Gamma}(k,u) = \int_u^\infty t^{k-1}e^{-t}\,dt\,/\,\Gamma(k). \tag{2.20}$$

For a Gaussian correlated RF with values in $\mathbb{R}$:

$$\mathscr{M}_0(D_u) = \Psi(u), \tag{2.21a}$$
$$\mathscr{M}_1(D_u) = \frac{1}{\sigma\sqrt{2\pi}} e^{-u/2\sigma^2}, \tag{2.21b}$$
$$\mathscr{M}_2(D_u) = \frac{1}{\sigma^2\sqrt{2\pi}} \frac{u}{\sigma} e^{-u/2\sigma^2}, \tag{2.21c}$$
$$\mathscr{M}_3(D_u) = \frac{1}{\sigma^3\sqrt{2\pi}} (\frac{u^2}{\sigma^2} - 1) e^{-u/2\sigma^2}. \tag{2.21d}$$

As previously stated in Sect. 2.1.2, the present morphological framework is also suitable to Gaussian related RF. A useful transformation is the squared Gaussian RF, also known as χ^2 RF ($\chi^2_k = \sum_{i=1}^{k} \gamma^2$). In this case given the following *Minkowski functionals* $\mathscr{M}_i$ (Sys.2.22), it is also possible to develop the probabilistic link from Sys.2.17 into an explicit set of equations using the following (still for $D_u = [u; +\infty)$):

$$\mathscr{M}_0(D_u) = \overline{\Gamma}(\frac{k}{2}, \frac{u}{2\sigma^2}), \tag{2.22a}$$
$$\mathscr{M}_1(D_u) = \frac{2^{1-\frac{k}{2}}}{\Gamma(\frac{k}{2})\sigma^k} u^{\frac{k-1}{2}} e^{-u/2\sigma^2}, \tag{2.22b}$$
$$\mathscr{M}_2(D_u) = \frac{2^{1-\frac{k}{2}}}{\Gamma(\frac{k}{2})\sigma^k} u^{\frac{k}{2}-1} \big(\frac{u}{\sigma^2} - (k-1)\big) e^{-u/2\sigma^2}, \tag{2.22c}$$
$$\mathscr{M}_3(D_u) = \frac{2^{1-\frac{k}{2}}}{\Gamma(\frac{k}{2})\sigma^k} u^{\frac{k-3}{2}} \big(\frac{u^2}{\sigma^4} - (2k-1)\frac{u}{\sigma^2} + (k^2-3k+2)\big) e^{-u/2\sigma^2}. \tag{2.22d}$$

Details, development and all the formulae for the other hitting sets can be found in [Adler and Taylor, 2007, Adler, 2008, Roubin, 2013]. Lastly, by substituting Sys.2.21 or 2.22 into Sys.2.17 it is possible to obtain a fully explicit expression for the expectancies of the morphological measures.

One has to keep in mind that the results presented in this section can also be applied with non-zero mean Gaussian distribution and to the larger family of ***Gaussian related random fields*** *with different covariance functions (only the second spectral moment has to be finite).*

2.5 Morphological operations

A collaboration with another on-going Ph.D. by *Mahban Hosseini*, at the *LML-Lille* allowed for supplementary morphological characterizations. In the following sections, this collaboration allowed to measure pore / particle size distributions, *i.e.* granulometry, as well as morphological tortuosities. However, they only constitute a characterization method, and are completely independent of the morphological creation process.

Both measure rely on mathematical morphology [Matheron, 1967, Serra, 1982] operations. They are four basic operations: *dilation*, *erosion*, *opening* and *closing*. We simply define the two measures, but the implementation is not addressed here.

Granulometry:
The granulometry is defined through a set of morphological operations [Matheron, 1967, Serra, 1982] : an *erosion* followed by a *dilation* by a structuring element. Combined together, those two operations constitute a so-called *opening*. Various form of structuring elements can be implemented, but in this work's scope sphere approximations are used, so that results can be compared to experimental data using the same type of hypothesis.

The principle is to iterate openings with a structural element increasing in size, over a set M – in 3D in the following – in order to "sieve" the morphology by a grid with an increasing elementary size.

Tortuosity:
The *morphological tortuosity* of a path between two points $\boldsymbol{x}$ and $\boldsymbol{y}$ with the same subset is defined as the ratio between the *geodesic distance* over the *Euclidean distance* separating the two points. The geodesic distance between two points $\boldsymbol{x}$ and $\boldsymbol{y}$ — within a subset A — is equal to the minimal geodesic arc length between them. It can be calculated with *geodesic dilation* from a point to another within the same subset.

3 Percolation and statistical representativity

In this section we depict few side results derived from the morphological creation process. Two types of results were found. A first concerning the critical volume fraction in regards to percolation (mainly a link between the Euler characteristic and percolation properties of random medias, for infinite and finite size problems, established during a collaboration with *E. Roubin* developed in Appendix **A**). A second type of results, presented in the following, allow to link the size of the inclusions one models within a given domain and its representativeness in terms of volume fraction.

3.1 Numerical approach to the Statistical RVE

In order to be statistically representative of a random media, two main exclusive assumptions can be made:

- The simulated morphology is large enough to contain all the meaningful features, and a unique simulation is necessary. The problem is then to assess this unique size.

- The simulated volume is too small to contain all relevant information, and numerous realization are needed to capture the relevant features. In this case the problem is to find a the link between the (smaller) size, and the number of needed realizations to be representative.

Due to computational costs and programs complexities, it is usually chosen to make the second assumption.

As shown in [Kanit et al., 2003], the size of a RVE should **never** be unique, but rather defined for a given *physical property* Z, a given *contrast*, a given *precision* and the number of realizations. Theoretically, if the size of the domain generated is an actual RVE for the property Z, the dispersion must vanish, and in practice, it is defined for a *given error* ϵ. Samples theory stipulates that the Confidence Intervals (CI) are as follow:

$$I_{95\%} = \left[\overline{Z} - \frac{1.96\sigma_Z}{\sqrt{n}}; \overline{Z} + \frac{1.96\sigma_Z}{\sqrt{n}}\right], \tag{2.23}$$

$$I_{99\%} = \left[\overline{Z} - \frac{3\sigma_Z}{\sqrt{n}}; \overline{Z} + \frac{3\sigma_Z}{\sqrt{n}}\right], \tag{2.24}$$

where $\overline{Z}$ is the mean of property Z over n realizations, and σ_Z its standard deviation. Thus, from the 99% confidence interval, the absolute relative error follow respectively Eq.2.25 and 2.26:

$$\epsilon_{\text{abs}} = \frac{3\sigma_Z}{\sqrt{n}}, \tag{2.25}$$

$$\epsilon_{\text{rel}} = \frac{3\sigma_Z}{\overline{Z}\sqrt{n}}. \tag{2.26}$$

From this relative error, the statistical RVE can be defined by Eq.2.27 for the RVE at 1%:

$$V_Z^{\text{RVE}} = \{V | \epsilon_{\text{rel}}(V) = 0.01\}. \tag{2.27}$$

Volume fraction:

The results in this part are all presented with an abritrary length unit (mm), but they all are applicable to any sizes, as long as all the parameters are used with the same length units.

In this section, for several correlation lengths, six different volumes sizes were studied, ranging from $1000\,\text{mm}^3$ to $216\,000\,\text{mm}^3$, with $n = 101$ realizations each time. Two different target volume fractions were also assessed, at 20% and 40% of inclusions. These where chosen arbitrary and does not reflect any particular material.

Fig. 2.8 shows the results in terms of volume fraction and CI (for the $n = 101$ realizations), for the two targeted volume fractions, and $L_c = 1mm$. The tendencies in terms of CIs seems are very similar. It is worth noting that the variability is very

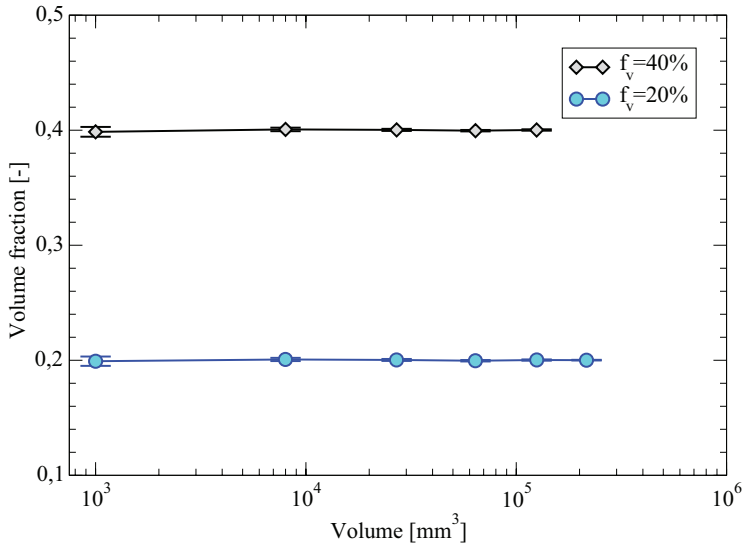

Figure 2.8: Average volume fraction and 99% CI for $n = 101$ realizations with $L_c = 1$.

small even for small volumes. To be able to see it the confidence interval at 99% was plotted (instead of the traditional 95%). This can be easily explained by the fact that with a small L_c, not only the inclusions will be "small", but the next neighbor distance is also "small". So starting with inclusions in the vicinity of a unit size, the smaller cube, 1000 mm^3, already includes almost all relevant information.

The results in terms of relative error are presented Fig. 2.9. The discrete results are then fitted by a decreasing exponential:

$$f_e(V) = \alpha \exp\left(-\left(\frac{V}{\beta}\right)^{1/3}\right) + \gamma, \tag{2.28}$$

where α and γ can be respectively seen as the initial and offset error, and β the error decreasing rate. The fitted parameters are given Tab. 2.2. It is interesting noting that for smaller targets of volume fraction, the relative error decreases slower. This reflects the fact, already mentioned, that with a given correlation length, smaller volume fraction intended translates to smaller inclusions, with a higher average neighbor distance.

The RVEs are found to be $V_{40\%}^{RVE}$ =2100 mm^3 (a cube of size $T \approx$13 mm) for a target at 40% of volume fraction, and $V_{20\%}^{RVE}$ =4300 mm^3 (a cube of size $T \approx$16 mm) for a target at 20%.

The exact same procedure is then applied with a different RF correlation length: L_c =5 mm. Fig. 2.10 and Fig. 2.11 show respectively the average volume fraction

		α	β	γ
$L_c = 1$	$f_v = 20\%$	6.381	492.8	0.2328
	$f_v = 40\%$	3.464	428.3	0.1506
$L_c = 5$	$f_v = 20\%$	29.84	2976	1.075
	$f_v = 40\%$	18.15	2663	0.598

Table 2.2: RVE $f_e(V)$ fitting coefficients for the volume fraction

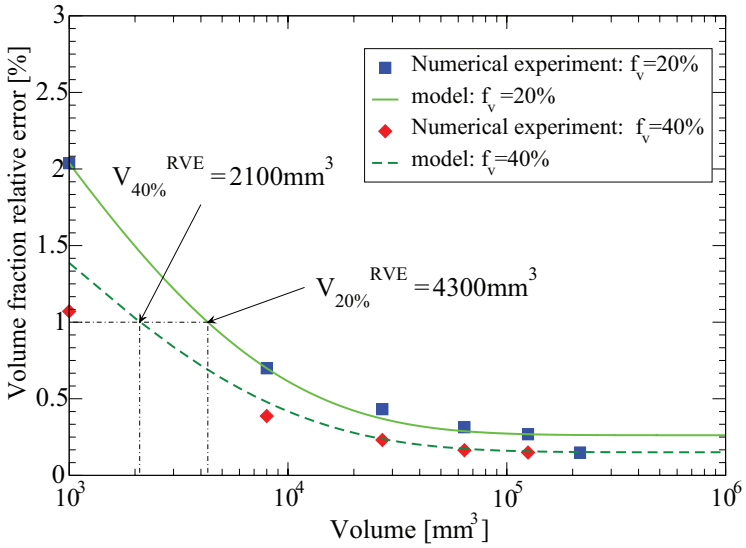

Figure 2.9: Relative error for $n = 101$ realizations with $L_c = 1$.

with the 99% confidence interval for $n = 101$ realizations as well as the relative error. Here the 99% is more visible than in the first case, and it narrows fast to almost vanish for greater sized morphologies. This time the RVE is larger than earlier, with $V_{40\%}^{RVE}$ =140 000 mm^3 (a cube of size $T \approx$51 mm) for a target at 40% of volume fraction, and $V_{20\%}^{RVE}$ =10 $\times$ 10^6 mm^3 (a cube of size $T \approx$100 mm) for a target at 20%.

The higher the correlation length, the larger the statistical RVE for volume fraction is. This is quite understandable in the sense that higher correlation lengths bring larger inclusions, but they also are further apart from each other. Hence, to capture all relevant information, larger sizes have to be modeled.

Conclusions:

For numerical reasons, the percolation RVE will be difficult to reach. If the correlation length is imposed ($L_c = 1$ or 5), the 5% RVE correspond to a cube of size $T \approx 400$. With a minimum discretization corresponding to a fraction of the correlation length (to capture all relevant geometrical information, $\delta \leq 0.5$ for

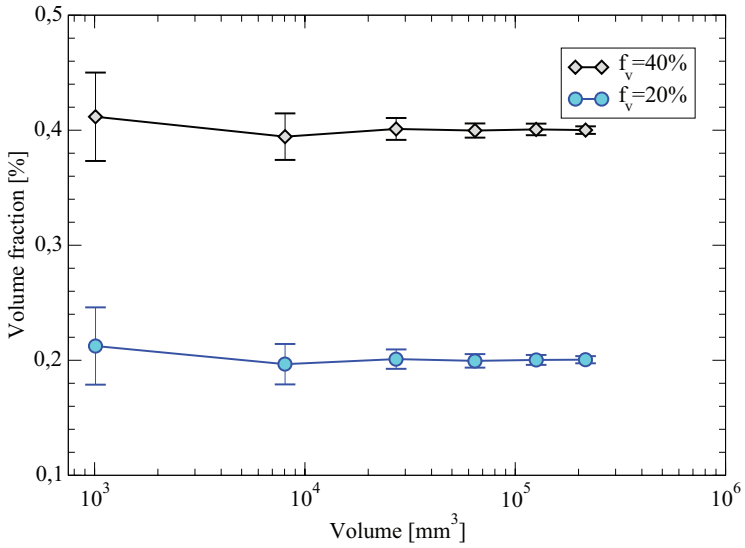

Figure 2.10: Average volume fraction and 99% confidence interval for $n = 101$ realizations with $L_c = 5$.

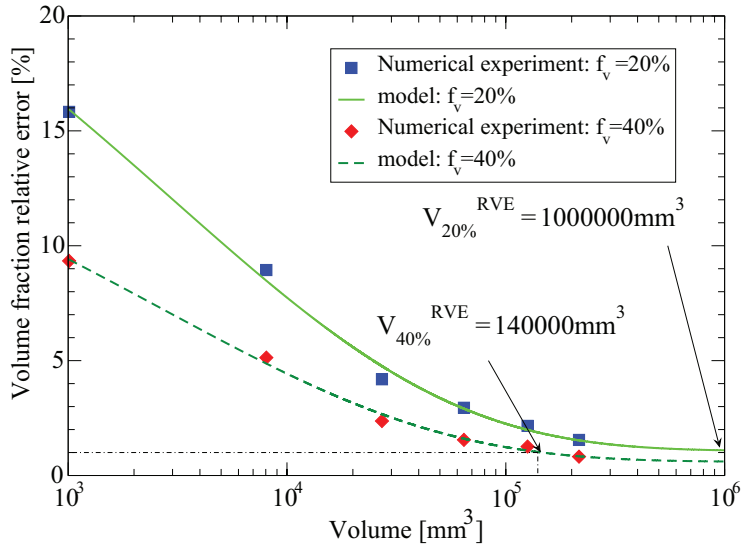

Figure 2.11: Relative error for $n = 101$ realizations with $L_c = 5$.

$L_c = 1$) it would require a minimum of 5×10^8 dofs, which is not reasonable for numerical reason.

However the volume fraction is reached more easily, and present no specific numerical challenge.

Both presented approach to define a RVE are not in competition, they are rather complementary. In regards to the modeling framework, compliance to the first kind of RVE will be ensured (percolation), as the connected component are the driving parameter regarding the morphological heterogeneous modeling aspects. The volume fraction RVE will be considered in a second order, and approached as close as possible when possible. In practice, results will always be averaged over at least 5 realizations of a morphology, to diminish the volume fraction bias.

4 Application to hydration modeling

After introducing a morphological framework for heterogeneous materials modeling, we will now apply it to cementitious materials.

4.1 Existing models

The very first published simulation model was made by [Jennings and Johnson, 1986], using a so-called "off-lattice" approach [Meakin, 1985]. Cement particles were represented by spheres placed inside a cubic volume of paste, and the hydration was simulated as a decrease in the radii of the anhydrous phase, and a concentric layer of C-S-H on the surface of those spheres. It could also account for many factors such as the particle size distribution (PaSD), the volume changes associated with dissolution of the anhydrous phase, *etc.*The framework the authors developed was rather detailed. However, due to limited computational power available at the time of development, it was never widely used. Nevertheless, this pioneering work prepared the way for more recent microstructural simulations as the ones described in the following. Two main types of models can be found:

1. Discrete models, that "pixelize" the material, for which the evolution of the microstructure is handled at the voxel level (locally) through time.

2. Continuous models, that generate inclusions (most of the time spherical ones) within a RVE , for which the evolution of the microstructure is handled by each inclusion evolution and properties.

4.1.1 CEMHYD3D

Within the first kind of models, the most acknowledged one would be CEMHYD3D, initiated by [Bentz and Garboczi, 1991], and updated since by [Bentz, 1997, Bentz et al., 1999, Bentz, 2005] at the *National Institute of Standards and Technology* (NIST). This model use a voxelized REV, and each voxel is given a material property.

The initial morphology can be completely random, and each voxel is attributed a phase given the chemical composition of the modeled cement ; or initial grains are

generated following experimental observations, using Rosin-Rammler distribution functions fitted over experimental observations. They are then randomly split in different minerals according to the composition (see FIG. 2.12). The evolution of the microstructure is then made following a set of stoichiometric equations, using simple laws of dissolution / collision / nucleation. At each iteration (linked with time), each voxel, if eligible, evolves.

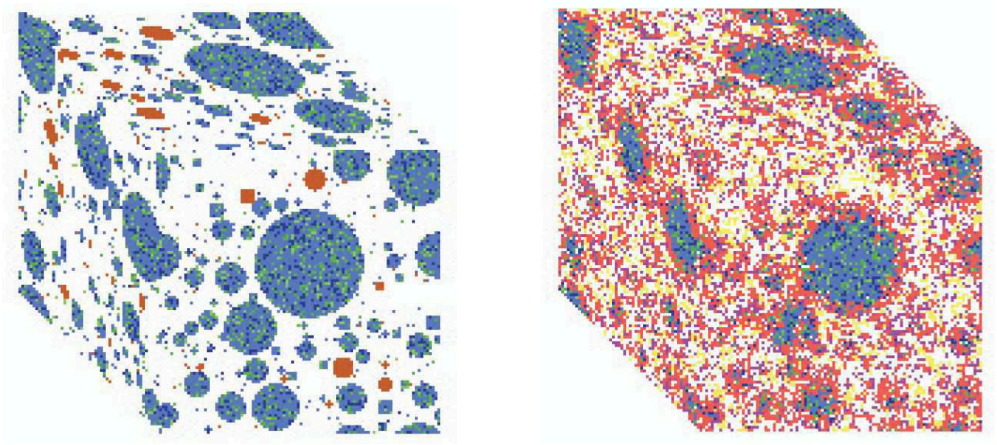

(a) Initial microstructure (b) Hydrated microstructure

Figure 2.12: Initial (a) and Hydrated (b) microstructures obtained with CEMHYD3D – $100 \times 100 \times 100$ voxels. *blue*: cement; *brown*: gypsum; *red*: C-S-H; *yellow*: CH; *white*: water – $w/c = 0.5$; CEM 32.5 R.

The first key feature of this model is that the initial morphology generation is based on experimental data, and thus takes into account the actual mineralogical composition of the cement, and of any mineral addition, *etc.*The second is the way the particles (voxels) interact with each other, allowing precipitation in the pore space as well as on the surfaces. However, first it needs parameter fitting over experimental data, and numerically speaking, it is limited to a certain size of microstructures ($100 \times 100 \times 100\,\mu m$), with a voxel size limited to $1\,\mu m$. This does not give the possibility to properly represent the pore network, since it has long been established that the pore size distribution in cement paste ranges $50\,\mu m$ to over $10\,\mu m$.

4.1.2 HymoStruc3D

Within the continuous models, the best known is HYMOSTRUC 3D. Developed by [van Breugel, 1997] at Delft university, this model uses 3D virtual microstructures filled with sphere following again the Rosin-Rammler model. With hydration, new layers of hydrates appear concentrically around cement grains, and the contact between neighboring growing spheres colluding is handled with particle embedding. One or two hydrates are considered, with inner and outer hydrates, and various

mass and volume balance rules dictate the microstructural changes. However the model consider the evolutions in a global way, and there is no following of each individual particle. This makes the model very light numerically speaking, but very little localized information is retrievable in the original model. Further development allowed to access these kind of information by post-treating the 3D morphologies [Ye et al., 2003a, Ye et al., 2003b].

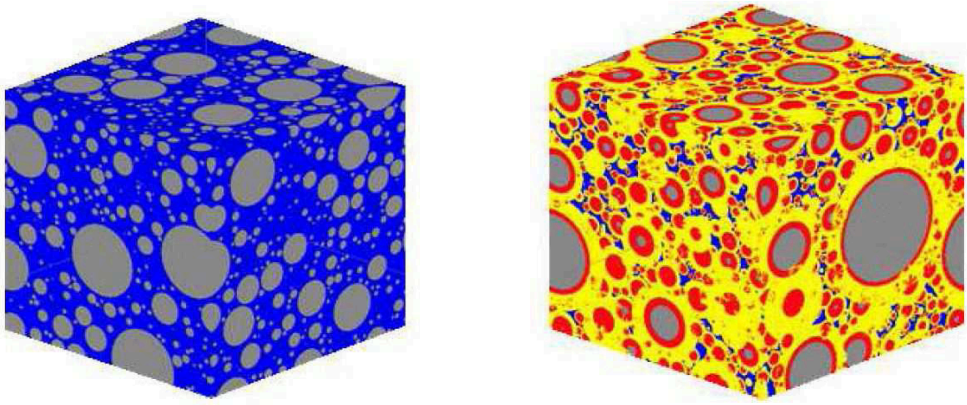

(a) Initial microstructure (b) Hydrated microstructure

Figure 2.13: Initial (a) and Hydrated (b) microstructures. $100 \times 100 \times 100$ pixels. grey:cement; red: inner C-S-H; yellow: outer C-S-H; blue: water; $w/c = 0.45$; CEM I 32.5 R.

The main advantage of this model is that it is developed and updated since 1997, and is still under improvement. Numerically speaking, this software was designed to be able to run on personal computers, so the size and the resolution of the yielded microstructures are limited. The main drawback, from a morphological point of view, is the spherical shape of the initial particles and concentric hydration products. Contrary to the previous hydration model, here phases can only appear concentrically, and there is no possible apparition of precipitated hydrates in the pore space or at the hydrates surfaces.

4.2 Reaching high volume fractions

The presented morphological approach is based upon Gaussian correlated random fields. However if one is to use exclusively Gaussian random fields, some limitations appear.

In terms of "matrix-inclusions" like morphology, with disconnected components, one will be limited to volume fractions around 15% (*cf.* Appendix **A** of this chapter). This means that if we impose a positive EC, we will be restrained on the achievable volume fraction. In order to represent the initial state of a cement paste, we will need more important fractions to even come close to what can be observed

experimentally: for a classic concrete with a w/c around 0.4, one will need above 70% of solid volume fraction to be accurate.

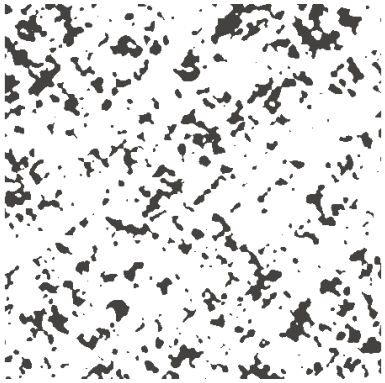

(a) Gaussian random field realisation: γ

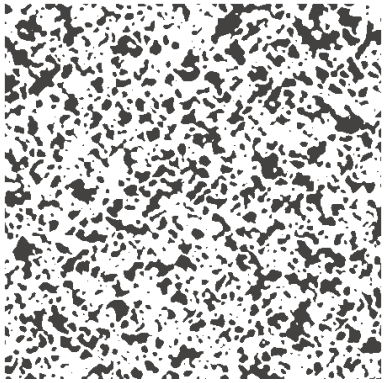

(b) χ^2_1 random field realisation: $\chi^2_1 = \gamma^2$

Figure 2.14: Comparison between Gaussian (a) and χ^2_1 (b) realisations, with the same threshold.

However, any kind of random field can be used, and they will yield various type morphologies. As far as those RFs are Gaussian related, it is possible to preserve the probabilistic link (Eq.2.16 developed into Sys.2.17) that exists between the excursion set and the field parameters. As shown previously, χ^2 are useful to increase the volume fraction, but some other CRFs might be considered in the future. They allow to double the achievable volume fraction up to 31%.

As we can see on Fig. 2.15, even though it is not a Gaussian RF any more, but a χ^2_1 one, the expected volume fraction for any threshold is a very good fit with the experimental one, and the EC is a good fit too. One has to keep in mind that this test was made just over one realization of the RF. Taking a look at Fig. 2.16, where the same experiment is averaged over just 5 realizations of the same RF, the EC experimental points have been smoothed, and fit better with the expectations, which tends to show the low variability between successive realizations, as previously mentioned in the Gaussian case.

The new CRFs introduced, χ^2_1, are a great enhancement in terms of volume fraction, but might not be enough to model cementitous materials. An additional amendment to the original framework will allow to increase the latter, and in the process yield various size of inclusions, of great interest for cementitous materials.

Note:
When considering χ^2_i CRFs, part of the percolation theory introduced is not valid anymore, as those CRFs are only defined in $\mathbb{R}^+$, and thus a unique percolation threshold exists. It represent the percolation of the inclusions. The complementary phase is always "depercolated".

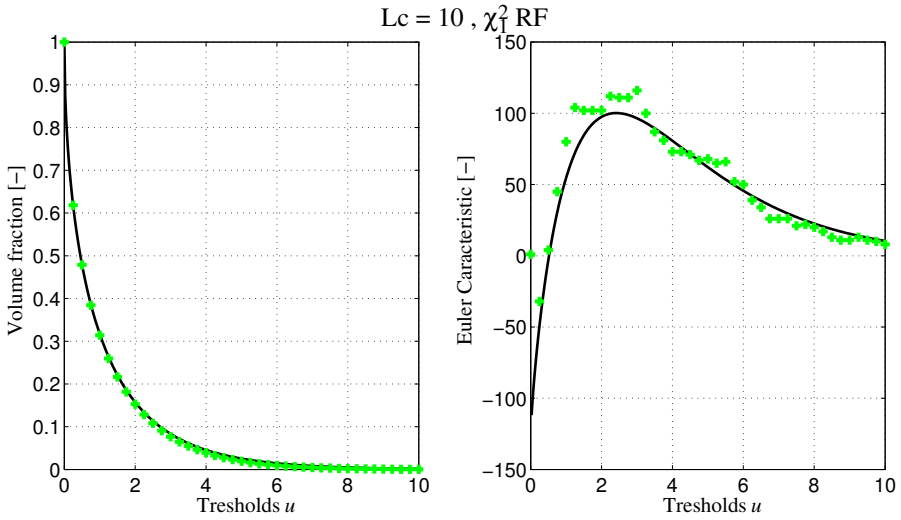

Figure 2.15: Expectations (-) vs. Numerical experiments (+): $L_c = 10$, with χ_1^2 RF.

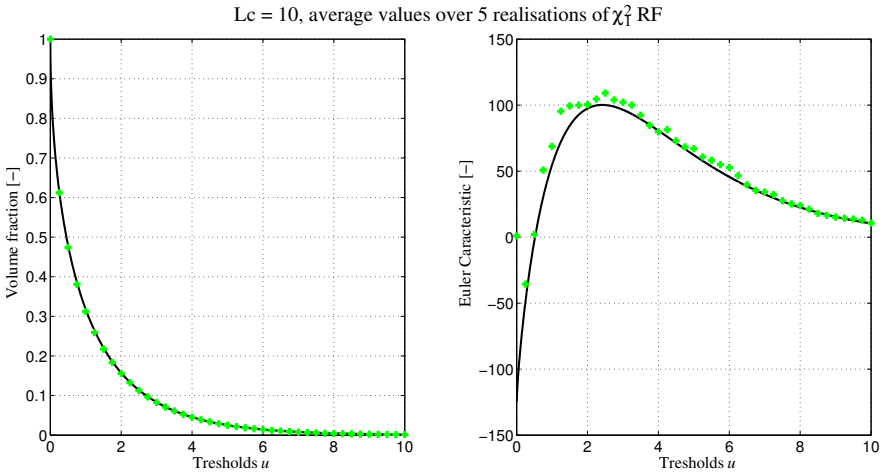

Figure 2.16: Expectations (-) vs. Numerical experiments (+): $L_c = 10$, with χ_1^2 RFs, averaged over 5 realisations.

4.3 Polydisperse inclusions and Particle Size Disrtributions

4.3.1 General principle: multiple correlation lengths

The general idea is to use two (or more) independent random fields: one with a "large" correlation length, which by thresholding will provide only few big disconnected components to the morphology (volume fraction improvements) ; and a second one with a "small" correlation length, which will bring small disconnected components (connectivity improvements) (see FIG. 2.17). When used together, such combinations not only can prevent some of the previous limitations, but it also

makes the yielded morphologies much more realistic, since cement grains are not mono-sized, as they follow a given PaSD curve. In this framework, several RF will be used to model several types of cement, and the choice of the multiple correlation lengths will be closely linked to the actual PaSDs.

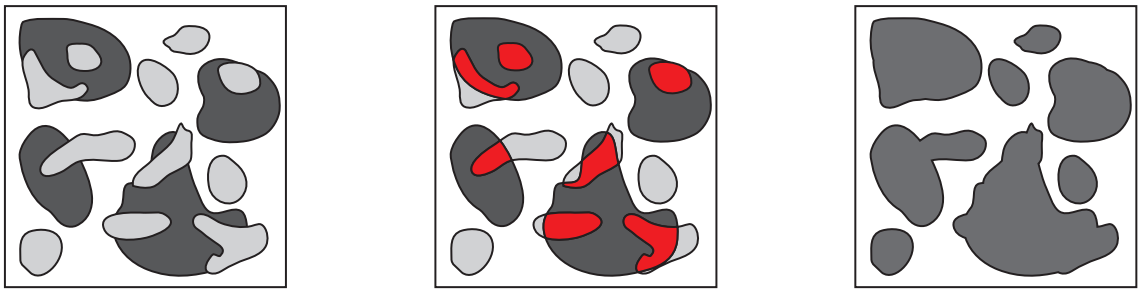

(a) 2 excursions on top of each other

(b) Intersection of 2 random fields

(c) Union of 2 random fields

Figure 2.17: Union of random fields excursions.

In order to achieve the latter, the idea is to use two (or more) realizations of random fields, and consider the union:

$$A_D^{\cup} = \bigcup_{k=1}^{K} A_D^i, \tag{2.29}$$

where each A_D^i has of course its own L_c^i. The other field parameters will be kept constant across all fields not to over-complicate the following equations.

The challenge is to be able to keep the crucial link between the different random field parameters and the yielded excursion set. It has been shown previously that for Gaussian or Gaussian related random field, Eq.2.16 provides us geometrical and topological informations about the excursion. Knowing each independent realization properties, it is needed to introduce the measure of unions principles.

For any given geometrical or topological property, the principle of measures of unions is used. In the general case, one has to satisfy Eq.2.30, where the subscript i stands for the chosen property, and the ①,②,... refers to the random fields, sorted by descending correlation length (*In order to simplify the equations, we will deal with specific values, so* $\mathcal{L}_i$ *will stand for* $\mathbb{E}\{\mathscr{L}_i/T^3\}$).

$$\mathcal{L}_i^{\textcircled{\cup}} = \mathcal{L}_i^{\textcircled{1}} + \mathcal{L}_i^{\textcircled{2}} + \cdots - \mathcal{L}_i^{\textcircled{\cap}} \tag{2.30}$$

Since we have all the information for each independent field, all terms with ⓘ subscript are known. Hence the only approximation one has to do is on the ⋂ term.

If interested in $\mathcal{L}_3$ (the volume fraction), Eq.2.30 suggests that the volume fraction of the union is equal to the volume fraction of the first excursion set ①, plus the volume fraction of the second excursion set ②, from which we must deduce the

volume fraction of the intersection (part of ② inside ①). Under assumptions of sufficient ergodicity for the random field, and keeping a L_c/T ratio that ensure a morphological RVE, the volume fraction of the intersection is approximated by the product of the two volume fractions, ① and ② respectively. In other terms, and for any interest quantity, the intersection terms will be approximated by Eq.2.31.

$$\mathcal{L}_i^{\textcircled{\cap}} \approx \mathcal{L}_3^{\textcircled{1}} \times \mathcal{L}_i^{\textcircled{2}} \tag{2.31}$$

So if combining two random fields, Eq.2.32 can be used to describe the properties such a union.

$$\mathcal{L}_i^{\textcircled{\cup}} \approx \mathcal{L}_i^{\textcircled{1}} + \mathcal{L}_i^{\textcircled{2}} \times \left(1 - \mathcal{L}_3^{\textcircled{1}}\right) \tag{2.32}$$

The generalization to N fields is straight forward. Keeping the same assumptions (the subscript i stands for the chosen property, and the ①,②,... refers to the random fields, sorted by descending correlation length), and considering N independent RFs, a recursive reasoning gives:

$$\mathcal{L}_i^{\textcircled{\cup}} \approx \mathcal{L}_i^{\textcircled{1}} + \sum_{j=1}^{N-1} \left\{ \mathcal{L}_i^{\textcircled{j+1}} \times \left(1 - \bigcup_{k=1}^{j} \mathcal{L}_3^{\textcircled{k}}\right) \right\}, \tag{2.33}$$

where the term $\bigcup_{k=1}^{j} \mathcal{L}_3^{\textcircled{k}}$ can be re-written according to the *Inclusion-Exclusion Principle*, also known as the *Poincaré formula*:

$$\bigcup_{k=1}^{N} \mathcal{L}_3^{\textcircled{k}} = \sum_{j=1}^{N} \left((-1)^{k-1} \sum_{1 \le k_1 \le \cdots \le k_j \le \cdots \le N} \mathcal{L}_3^{\textcircled{k_1}} \cap \mathcal{L}_3^{\textcircled{k_2}} \cap \ldots \mathcal{L}_3^{\textcircled{k_j}} \right). \tag{2.34}$$

In order to use such combination of random field realizations, a verification of the previous approximation has to be done first. To avoid side effects of the inclusions, one should keep the ratio L_c^1/T smaller 0.05 (the subscript 1 still belonging to the bigger correlation length). The side effects on percolation properties are then evaluated to be within a 10% margin error compare to infinite size problems, which can define our first morphological RVE. However, the numerical experiments made here allowed us to test some different parameters, and we observed that even with a L_c^1/T ratio around 0.3, the averaging over just 3 realizations would yield the desired properties.

In the following figures (Fig. 2.18, Fig. 2.19, for a union of two and three RF respectively), one can see the theoretical expectations as the solid line, and the actual properties averaged over 3 realizations of the same random fields (+). The excursions sets are defined by the upper tail, also known as $D_u = [u; +\infty[$. For

high thresholds, the error vanishes extremely fast, and for thresholds between 0 and around 2.5, experiments tend to underestimate the specific EC, and thus the morphologies are always "over-connected". However, one has to keep in mind that the experimental values are only averaged over 3 realizations, and since we are dealing with χ^2 fields, all the connectivity issues are in the vicinity of the threshold equal to the smaller correlation length. Furthermore, when dealing with the union of tree or more random fields, the errors that one can notice in the vicinity of the smallest correlation length are substantial. It becomes difficult to rely on the expectations only, and some "visual" verification is necessary over few realization to ensure the proper connectivity properties.

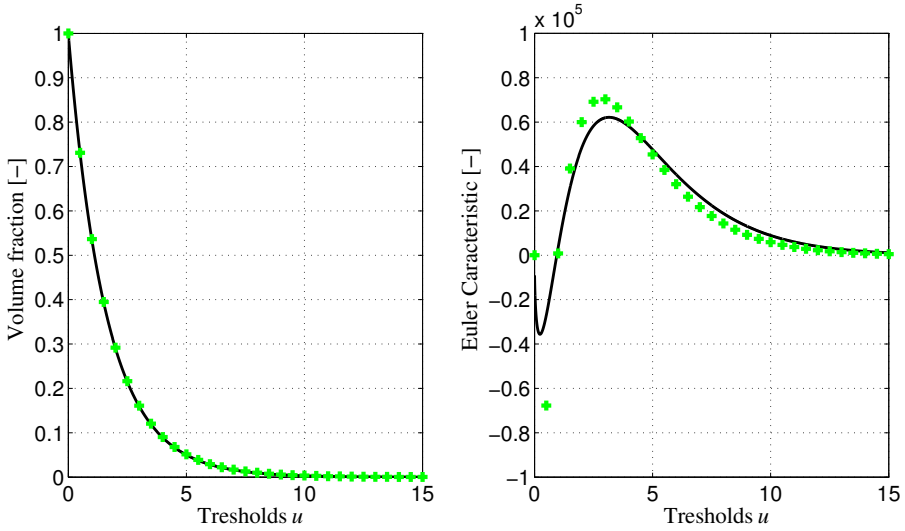

Figure 2.18: Comparison between expectations -) and numerical experiments (+): Union of 2 RF: $L_c^1 = 5$ and $L_c^2 = 1$, left: Volume Fraction; Right: EC. Unions results averaged over 3 RF realisations.

As shown on Fig. 2.20, the main advantage is the volume fraction increases (for a given threshold) according to the number of unions. The counterpart is that there is no big effect on the EC, except that the morphologies yielded are more connected. No matter how connected a small group of inclusions can be, one big inclusion will connect them all.

The same way the statistical RVE has been defined in regards to the volume fraction, for a unique correlation length, it can be done for a union of RFs.

Using the same two correlation length ($L_c = 1$mm and $L_c = 5$mm), results are presented on Fig. 2.21 and Fig. 2.22.

Remark:
The results are given in mm, but they can be transposed to any scale, as long as the unit is the same all along.

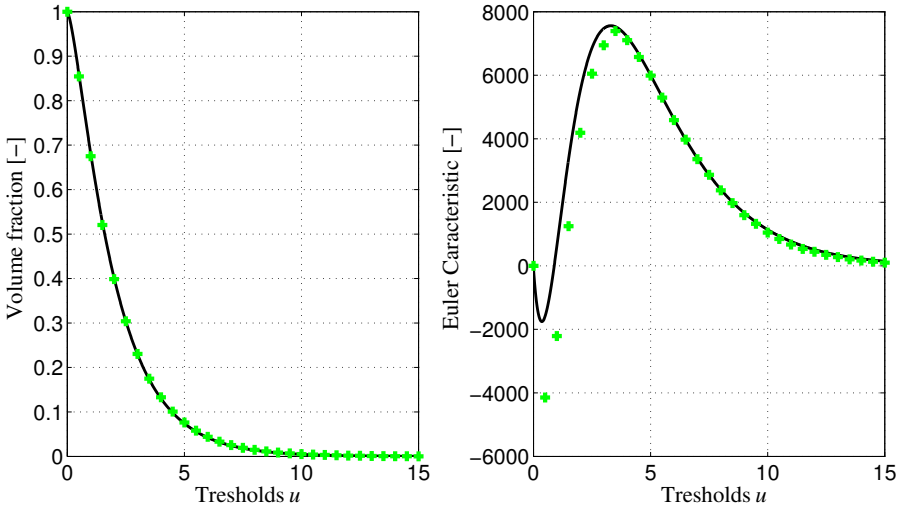

Figure 2.19: Comparison between expectations -) and numerical experiments (+): Union of 3 RF$L_c^1 = 15$, $L_c^2 = 10$ and $L_c^3 = 2$, left: Volume Fraction; Right: EC, results averaged over 3 RF realisations.

		α	β	γ
$L_c = 1$ and 5	$f_v = 20\%$	19.04	3181	0.7205
	$f_v = 40\%$	12.45	2863	0.4354

Table 2.3: RVE $f_e(V)$ fitting coefficients for the volume fraction.

The volume fraction RVE, in this case, is $V_{40\%}^{RVE}$ =85 000 mm^3 (a cube of size $T \approx 43$ mm) for a target at 40% of volume fraction, and $V_{20\%}^{RVE} = 240\,000$ mm^3 (a cube of size $T \approx 62$ mm) for a target at 20%. Those values are less apart from each other than in the unique correlation length case.

One can notice that in the presented equations (Eq.2.32, 2.33, 2.34) the absence of the thresholds. The assumption was that the union was made with the individual RFs in terms of maxima, and no previous shift was operated. It means that the "unified" RF bear in each point the maximal value of the n constituting RFs. This simple way to unify the RFs allows for the presented formula to be completely explicit with a unique threshold. Another approach — developed later in this section — could be to chose n RFs, each with its own threshold, and thus be able to follow the PaSD not only in terms of sizes, but also in terms of each size volume fractions. However, this second modeling development make the union's approximation much more difficult to estimate, especially when the volume fraction are evolving.

Remark:

In light of those explanation, the first approach will be used for modeling evolving morphologies (*e.g.* cement paste), and the second (developed in the following) will be applied to "fixed" morphologies (*e.g.* mortar or concrete scale).

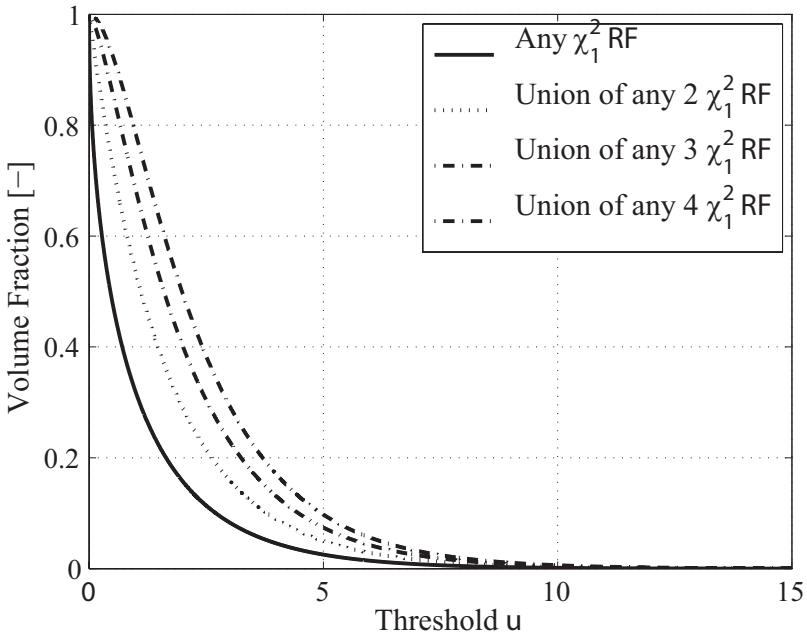

Figure 2.20: Unions volume fraction, for zero mean, unit variance, χ_1^2 RFs.

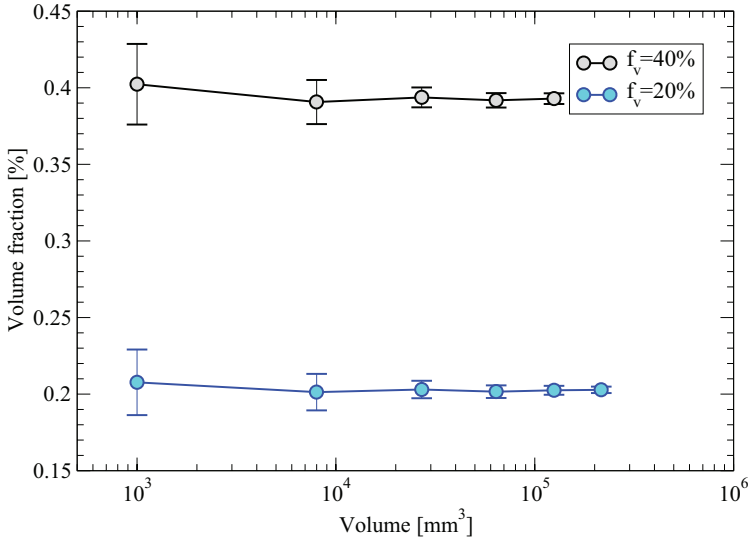

Figure 2.21: Average volume fraction and 99% confidence interval for $n = 101$ realizations with a union of 2 RFs: $L_c = 5$ and $L_c = 1$.

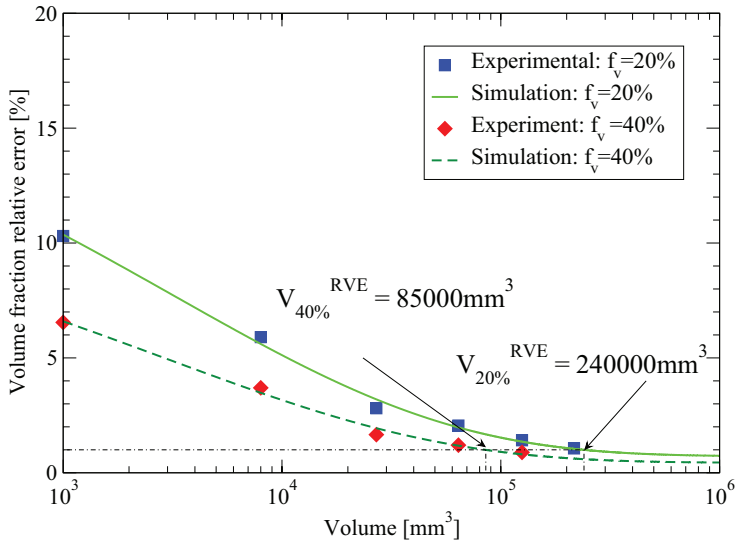

Figure 2.22: Relative error for $n = 101$ realizations with a union of 2 RFs: $L_c = 5$ and $L_c = 1$.

4.3.2 Application with PaSD

An application of the presented tool is made here. The aim is to follow a given PaSD to generate the CP morphologies. The latter is applicable at the CP scale, when modeling the initial cement particles as a suspension in a water matrix, of for higher scale when modeling the aggregate PaSD to be entrapped in a CP matrix.

As a first applied example, focus is made on a given cement, and on how we determine the random fields needed, and how to yield the corresponding morphologies. The example uses a standard cement from LAFARGE ™, designated: "CEM-I 52.5 CE CP2 N". Its PaSD is shown FIG. 2.23.

Given a PaSD curve, correlations lengths are chosen to fit best the PaSD.

For any field we noticed that the maximal volume fraction achievable with disconnected components was always in the same vicinity in terms of threshold, and the average size was always in the vicinity of the correlation lengths. We first set up the inferior and the superior ones, with different considerations.

The superior one is chose to limit as far as possible the side effects of the inclusions. Further explanation is given in APPENDIX **A**. For a modeled cube of size $T = 100\,\text{um}$, the biggest correlation length will be $L_c^{max} = 20$. Then for the inferior correlation length, we chose to limit ourselves to a size $L_c^{\min} = 2$ so that numerically we are able to represent them. Finally, we set up a third correlation length, that would fit in the middle of the PaSD curve between L_c^{max} ad $L_c^{\min}$, here in the example $L_c^{\text{middle}} = 7$. This constitute the aforementioned first way to generate morphologies

with polydisperse inclusions.

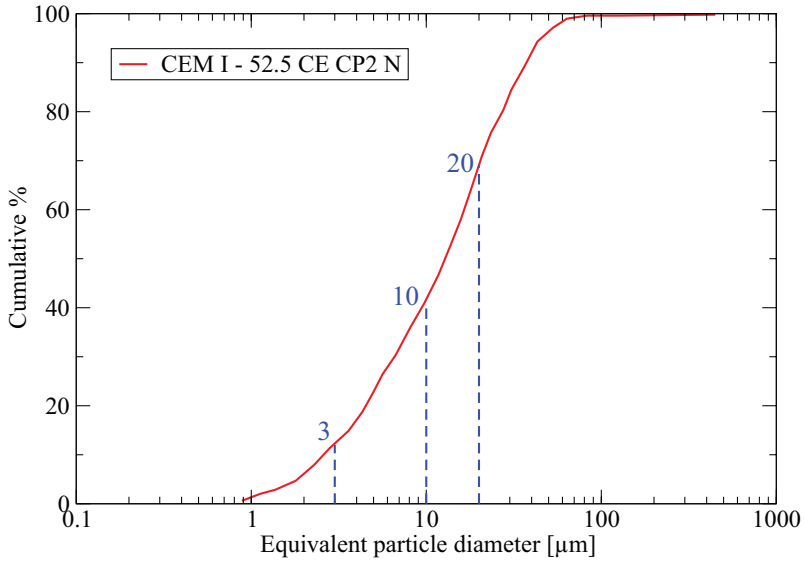

Figure 2.23: PSD curve from LAFARGE ™, and L_c's choice.

This first approach will be used, for CP modeling for example, when the morphologies are suppose to evolve. Indeed, the crucial probabilistic link is preserved with a relatively simple set of equations.

The second approach aforementioned, is to take into account each size volume fraction within the morphology. It will be applied to model mortar and concrete scale, we can chose the actual volume fractions of each size. It requires Each RF realization can be thresholded at a chosen value, and only then the union is made.

As an example, if the total targeted porosity is noted Φ, and each excursion set targeted porosity are denoted Φ_i with $\Phi_1 = 0.25\Phi$, $\Phi_2 = 0.5\Phi$ and $\Phi_3 = 0.25\Phi$:

$$\Phi_1^{\text{Target}} = \Phi_1 = 0.25\Phi, \tag{2.35a}$$

$$\Phi_2^{\text{Target}} = \frac{\Phi_2}{1-\Phi_1} = \frac{0.5\Phi}{1-0.25\Phi}, \tag{2.35b}$$

$$\Phi_3^{\text{Target}} = \frac{\Phi_3}{1-\Phi_1-\Phi_2} = \frac{0.25\Phi}{1-0.75\Phi}. \tag{2.35c}$$

4.3.3 Application with PoSD

Even if not developed here, the exact same modeling procedure can be applied in an "inverse" way. Instead of generating inclusions within a matrix, it is possible to generate voids within a matrix. They can — the same way as inclusions — follow

a PoSD. This approach will be used in Chapter 4 to yield C-S-H morphologies, given a pore size distribution model. The presented formulas are very similar, the only parameter that changes is actually the hitting set A_u, which will be taken as $A_u = [0; u]$ instead of $[u; \infty[$.

4.4 Morphologies evolutions

Once one has an initial morphology, the next step is to make it evolve. Therefore one will need a "physical" description of the studied process, described in Sect. 4.1 and 4.2 of the previous chapter. Since we will need at least three phases, we will first show how to create three phase morphologies (and extension to $n-$phases), and then how it can be applied to the previously described cement.

4.4.1 n-phase morphologies

We have seen in the previous section that thresholding a realization of a random field yields a two phase morphology. We will now consider three phase morphologies. An example is shown on Fig. 2.24. The same way applying a threshold will separates the random field values in two distinct subsets (Fig. 2.24(a)) and create a two phase morphology (Fig. 2.24(b)), two thresholds will separate it in three (Fig. 2.24(c)) and create a three phase material (Fig. 2.24(d)). We will now be able to represent the matrix, inclusions, and a concentric phase around the latter.

For each one of those three phases, Eq.2.16 and 2.33 is adapted to keep the statistical link between the random field, the thresholds, and the geometrical and topological properties of the actual morphologies. Instead of using the excursion set $D = D_{u^+} = [u; +\infty[$, we had to adapt Eq.2.16 to $D = D_{uv} = [u; v]$ and $D = D_{u^-} = [0; u]$ (since we use χ^2 random fields, the lower limit will be 0, for Gaussian random field we would have had the last hitting set $D = D_u =]-\infty; u]$). Eq.2.33 stays unchanged for any hitting set.

4.4.2 The Hydration Process

After introducing the procedure to generate multiphase morphologies, we now take into account the chemistry involved in the cement hydration's reaction. As a first example, the Powers model is used, to give a simple example. Described by Sys.1.3, it gives the initial volume fraction of anhydrous cement for the initial state of hydration, and then give a volume fraction description of the three main phases (anhydrous cement, hydration products and water) according to the hydration degree ξ.

	C_3S	C_2S	C_3A	C_4AF	Gypsum
Standard CEM-I cement (%)	56.5	19.5	10	9.5	4.5

Table 2.4: Standard CEM-I oxyde composition.

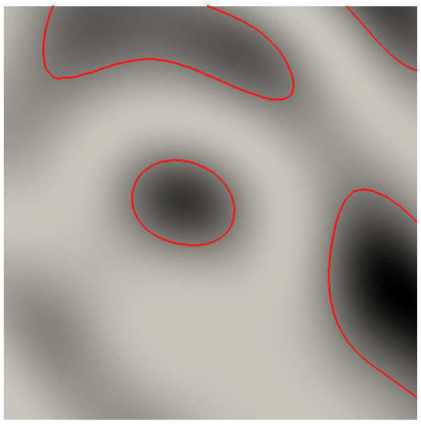

(a) One random field realisation, thresholded at u

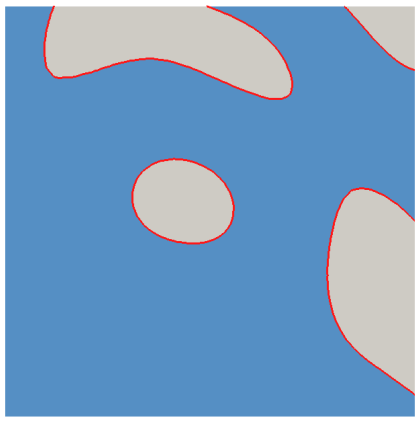

(b) Initial morphology: cement grains and water

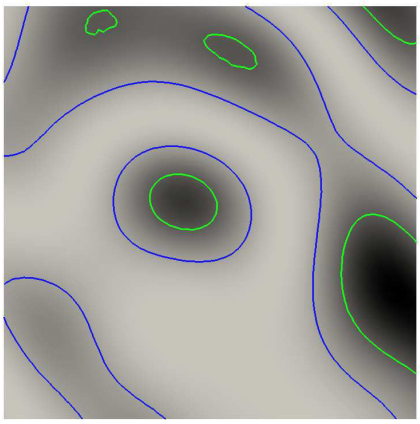

(c) Same realisation, with $v \geq u$, and $w \leq u$

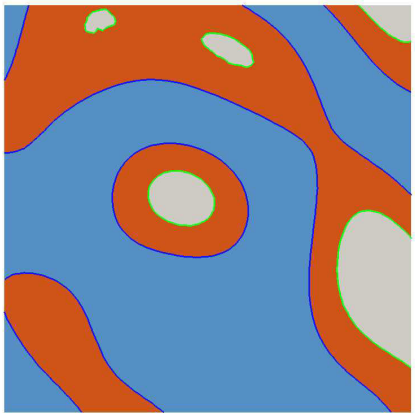

(d) Cement hydration: cement grains, water, and hydrates

Figure 2.24: From the random field creation to cement paste morphology yielding - *grey: unreacted cement; blue: water; orange: hydration products.*

Given the standard CEM-I composition provided in Tab. 2.4, it is possible to determine the initial porosity of the cement paste, and thus be able to generate a representative morphology of the cement grains. It is be obtain by generating a union of three RF chosen to fit the standard CEM-I PaSD ($L_c = \{3; 7; 20\}$), and thresholding it at a given scalar u_0 such as the excursion's volume fraction $\mathcal{L}_3(u_0) = p$ (p from Powers model Sys.1.3). This threshold will be directly linked to the hydration degree ξ. As ξ evolves from 0 to 1, the threshold will move from an initial value u_0, to u_1. Then in order to model the appearing new phase, we will need to determine a second threshold, which will yield the "concentric" phase around anhydrous cement. This second threshold u_2 will be chosen so that the overall expected volume fraction of the new phase matches Powers model. It requires to

invert SYS.2.21 to yield the relationship for u_1 and u_2 according to ξ, and the result is drawn in SYS.2.36, and plotted on FIG. 2.25.

$$u_1 = 2\sigma^4(\text{erf}^{-1}(1 - V_w(\xi)))^2 \tag{2.36a}$$
$$u_2 = 2\sigma^4(\text{erf}^{-1}(V_c(\xi)))^2 \tag{2.36b}$$

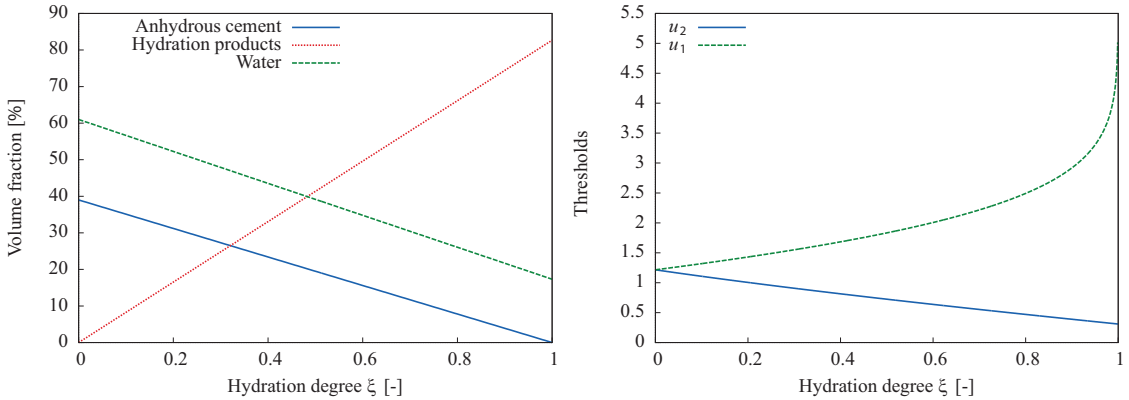

(a) Simplified Powers model (b) Corresponding threshold evolution

Figure 2.25: Simplified modeling of a CP, with $w/c = 0.52$.

The output for the initial morphology can be seen FIG. 2.26. We can notice first the cement grain repartition on FIG. 2.26(a), then by adding the complementary phase (FIG. 2.26(b)), we model water. Then, for a given hydration degree, we modify accordingly to EQ.2.21 and 1.3 the thresholds, and we yield FIG. 2.26(c) and 2.26(d).

5 Hydration model validation

The presented model will now be confronted to experimental data, to assess its quality and precision. This first verification will be done according to two properties that we consider most relevant in terms of morphology characterization :

- the overall porosity prediction,
- the pore size distributions.

Those characterizations concern only the pore network since we believe it is of uttermost importance for a "correct" morphological representation. In addition, since the general framework is aimed at diffusivity studies, a proper description of the pore structure is a requirement.

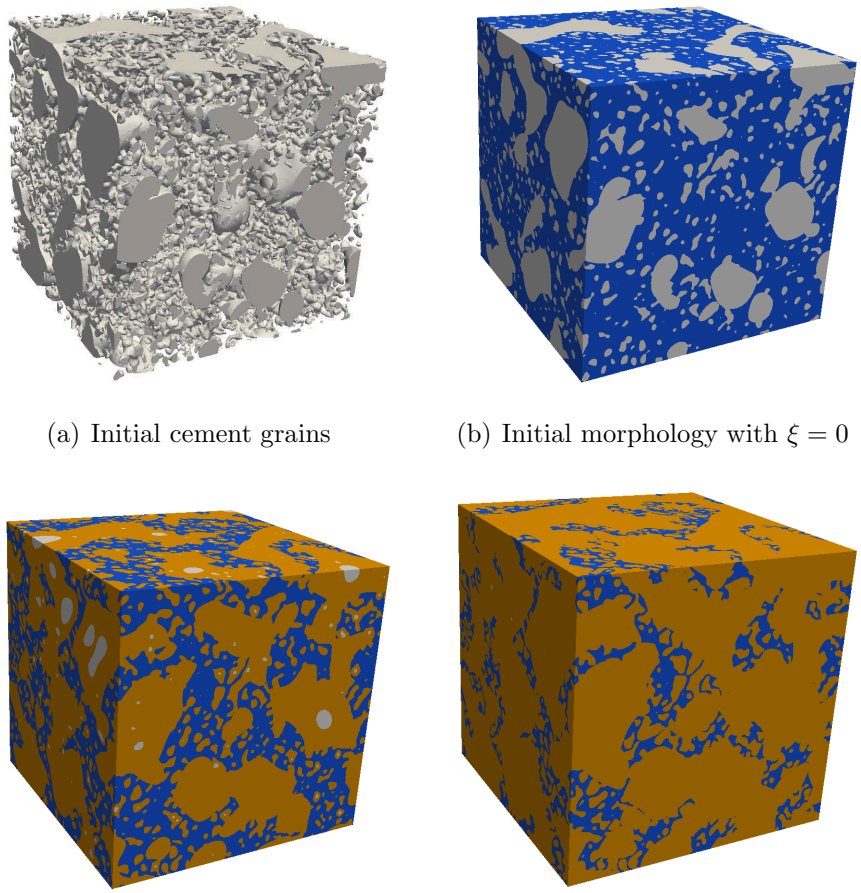

(a) Initial cement grains

(b) Initial morphology with $\xi = 0$

(c) Cement paste morphology for $\xi = 0.2$

(d) Cement paste morphology with $\xi = 0.8$

Figure 2.26: Cement paste morpholgies creation and hydration – Standard CEM-I CP, $w/c = 0.52$.

5.1 Total porosity

Even before generating actual CP microstructure, a first validation is made in terms of porosity prediction. The aim is to assess the quality of the hydration models introduced in the first chapter. Only then, it will be possible to assess the microstructural representativity in terms of pore size distributions.

Fig. 2.27 displays experimental values of measured porosities on cement pastes, according to their w/c ratios, measured with various techniques. The hydration analytic models are thus compared to various authors results. It can be seen that the porosities yielded by Powers model correspond to the lower limit of the experimental points. To the contrary, the Jennings model tends to overestimate the volume of pores.

The second model (Jennings), is also differentiated for two hydration degree:

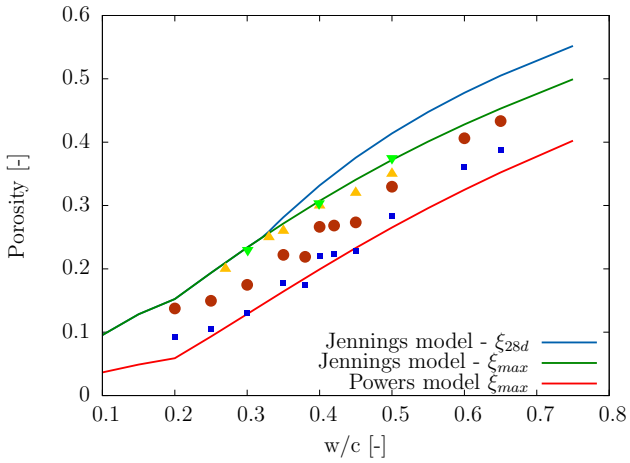

Figure 2.27: Evolution of porosity according to the water-cement ratio. ■: [Richet, 1992]: Hg porosimetry, ●: [Richet, 1992] model , ▲: [Tognazzi, 1998] H_20 poro, ▼ [Béjaoui et al., 2006].

ξ_{28d} and ξ_{max}. The porosity is overestimated in both cases, but the difference is only noticeable for high w/c ratios. Indeed, for $w/c \leq 0.4$, the rapid consumption of all the available water stops the hydration reaction, and thus the porosity does not evolve. On the other side, for $w/c \geq 0.4$ the water availability and free space allow for the hydration to continue, new hydrates to form, and thus a supplementary porosity reduction. This supports the new definition of the maximal hydration degree ξ_{max}.

On one side, in the simulations, no distinction has been made between total and open porosity. Within the presented framework, we only have an analytic expression for the total porosity. The experimental measures, on the other side, access only the open porosity. It is hence believed that the experiments tend to underestimate the total porosity, and so the analytic estimation of the total porosity is believed to be rather good.

Using a tool earlier introduced, the morphological operations, it is possible to distinguish the amount of opened porosity, and compare it to the total one. Here, analytic expression does not exist anymore, and actual microstructure have to be generated. At the cement paste scale, the RF generation is done on a regular cubic grid of $300 \times 300 \times 300$ voxels, with a discretization of 0.334 µm for a RVE of 100 µm. For the standard CEM-I cement paste, with $w/c = 0.5$, the measured total and open porosity are listed in Tab. 2.5. Even though it can be seen that the difference between the two tends to increase — which was expected, the small pores tend to close faster, entrapping parts of bigger pores to the connected porosity — the numerical values are very low ($\approx 10^{-3}\%$). The most plausible explanation is the "coarse" discretization in regards to the actual pore network of a hardened cement paste, and the RFs' "smoothness".

Hydration degree ξ	Total porosity	Open porosity	Difference (%)
0.1	0.58	0.58	2.4×10^{-3}
0.3	0.53	0.53	3.39×10^{-3}
0.5	0.47	0.47	5.10×10^{-3}
0.73	0.38	0.38	7.81×10^{-3}

Table 2.5: Total and open porosity through hydration: OPC, $w/c = 0.5$. Microstructure generated with a 0.34 µm discretization.

Remark:
It should be noted that thinner discretizations are obviously possible when generating the CRFs. It is the author belief, at this stage, that such morphologies would have a more significant difference between total and open porosity.

It is also reminded that the present framework, from the hydration stand point, do not consider phenomena like dissolution and precipitation since the various phases volume fractions are only predicted in a macroscopic fashion, and their distribution is fixed concentrically to the anhydrous grains. In real microstructures, some hydrates are formed and later on dissolved, new hydrates can appear by precipitation on almost any surface given a threshold concentration in the interstitial solution.

Keeping in mind those limitations, we only assess qualitatively the morphologies in the following.

5.2 Pore size distributions

Once the actual microstructures are generated according to a hydration model, the second verification concerns the pore size distributions.

A typical result is displayed Fig. 2.28, where 2.28(a) represent the cumulative pore size distribution within a hardened cement paste, and 2.28(b) the corresponding size distribution. The lower bound on those analysis is set by numerical discretization of the RFs. For a RVE's size of 100 µm, the typical dicretization is 0.334 µm.

The verification is first done on a cement paste ($w/c = 0.5$) of a standard CEM I cement (composition as in Tab. 2.4), for various stages of hydration. Results are drawn Fig. 2.29 and Fig. 2.30. The first figure displays the cumulative volume fraction of the pore network through hydration. We can notice the overall diminution of porosity with hydration, and it is possible to assume that the pores maximum size decreases also. The dominant pore mode is more explicit on the next figure (Fig. 2.30), where the pore size distribution is drawn, for various hydration degree. It becomes more clear here that the maximum porosity size decreases (and the associated volume also decreases), whereas the small spores volume distribution increases. This last point is important since it shows that we do not only "shrink" the initial porosity, we also create a new one at a smaller sizes, which supports the overall morphological yielding process.

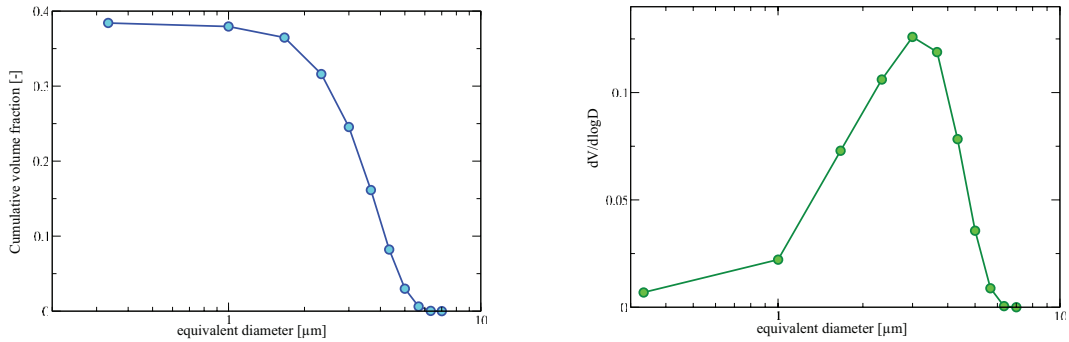

(a) Cumulative porosity volume fraction (b) Pore size distribution

Figure 2.28: OPC with $w/c = 0.4$, with a standard CEM I composition.

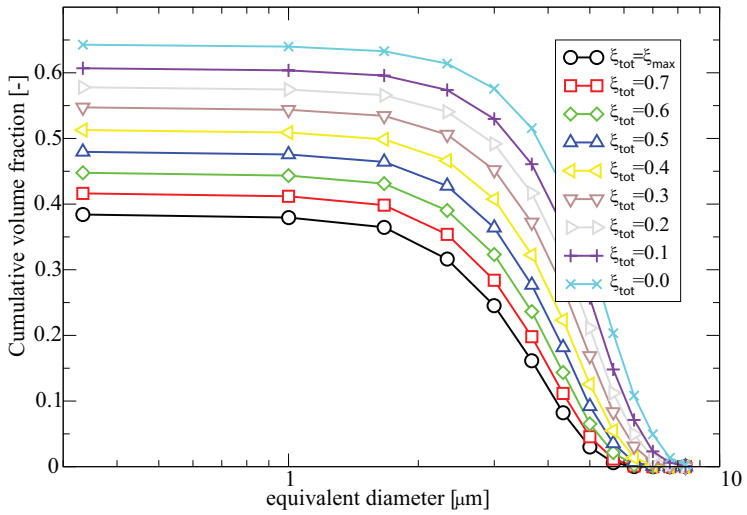

Figure 2.29: Cumulative volume fraction for a OPC with $w/c = 0.5$, with a standard CEM I composition.

Then, the influence of the w/c ratio is considered. The comparison has been done on fully hydrated CP microstructures, for various w/c. Results are drawn Fig. 2.31. Again, the overall porosity decrease is noticeable as the w/c ratio decreases. Fig. 2.32 allows to see better the effect on the main pore mode, where it decreases from 4 µm to 2 µm. An important feature that is not represented by the actual combination of hydration analytic model and the morphological framework,

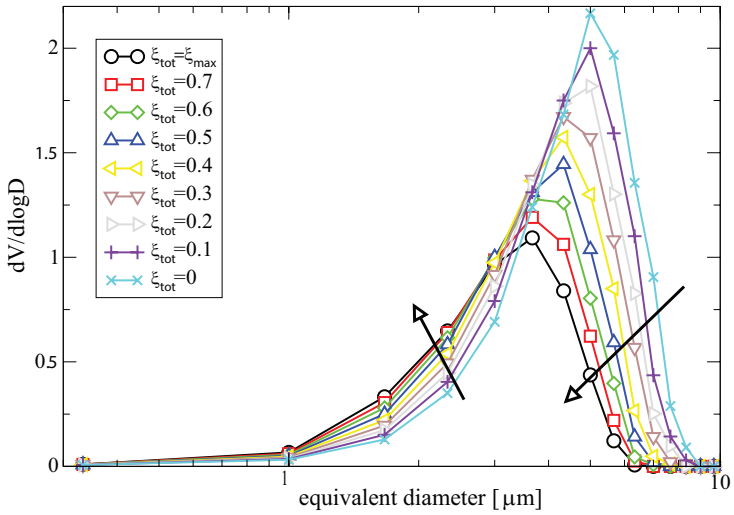

Figure 2.30: Distribution of pore sizes for a OPC with $w/c = 0.5$, with a standard CEM I composition.

is the w/c threshold around 0.4, under which a second familly of pores is supposed to appear (first chapter, section 5.3.5, representing the outer hydration products.

The comparison with experimental results is much more difficult, due to the large number of characterization means, introduced in the first chapter. Since MIP is one of the first and more commonly used technique (with known flaws), only a qualitative comparison of the the tendencies is done. First, we compared single CP for various hydration stages. On Fig. 2.29 the evolution of the cumulative porosity volume fraction is drawn, and compared to Fig. 1.23, which displays equivalent experimental results (taken from [Cook and Hover, 1999]). A first look at the two sets of curves shows similar trends. As the cement paste is hydrating, the amount of porosity decreases, and at the same time all the pores are getting smaller. In the experimental results, the threshold equivalent diameter starts around 1 µm, and diminish to less than 0.1 µm. The small capillary pores, on the other side, tend to close, and shift from capillary to hydrate pores. In the numerical simulation, only the general trend is respected (decrease of the overall porosity). The threshold diameter stays almost unchanged through hydration, and even though small pores are created, they do not correspond to the hydrates pores. The influence of the w/c ratio on hydrated CP can also be looked at. Such experimental results were drawn on Fig. 1.25 (taken from [Gallé, 2001]). Again, qualitatively the tendencies are respected in regard to the overall porosity between experimental and simulation results, but the quantitative comparison is not possible.

However, given all the previous hypothesis concerning the experimental mea-

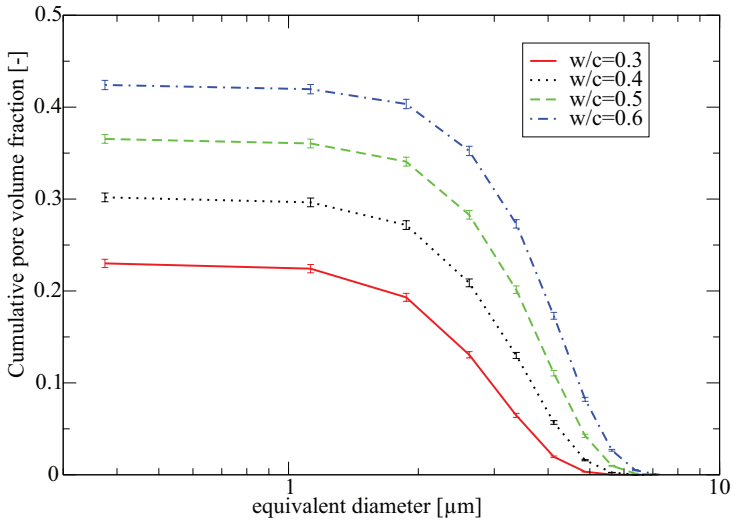

Figure 2.31: Cumulative pore size distribution for an OPC with different w/c ratios – standard CEM I composition – *averaged over 10 realizations, with the 95% CI.*

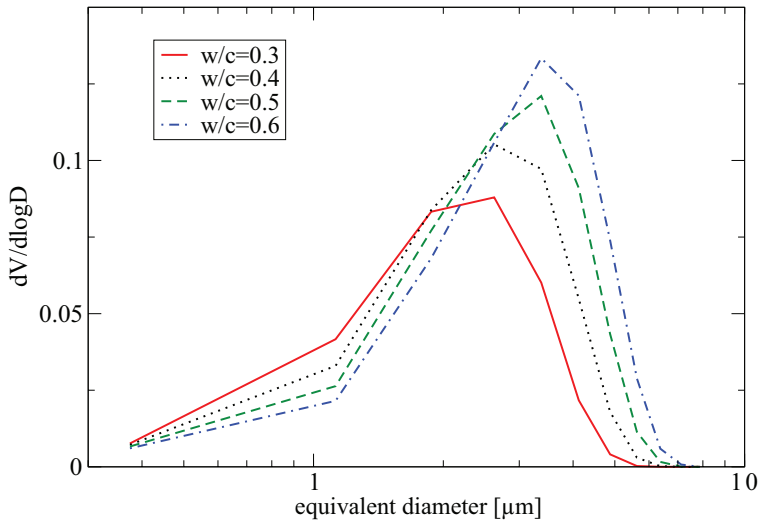

Figure 2.32: Distribution of pore sizes for an OPC with different w/c ratios – standard CEM I composition – *averaged over 10 realizations.*

surements, as well as the simulation ones, we were able to compare some simulation to experimental results. The results are drawn Fig. 2.33 and 2.34. The first figure exhibits cumulative pore size distributions, as measured by [Cook and Hover, 1999], using standard MIP measurement protocols, on a standard CEM-I cement paste, with $w/c = 0.5$, as well as the equivalent simulated results.

As it has been said previously, the tendencies through hydration are respected, and the overall porosity decrease is about 20% in both cases. This fact tends to support the hydration model presented earlier. However, the size distributions suffers the discrepancies of the previous paragraphs. We are unable to reproduce the decrease by two orders of magnitude in terms of access diameter. This diameter should indeed decrease, but it is the authors belief that the reduction is overestimated by MIP measurements, as discussed in the first chapter.

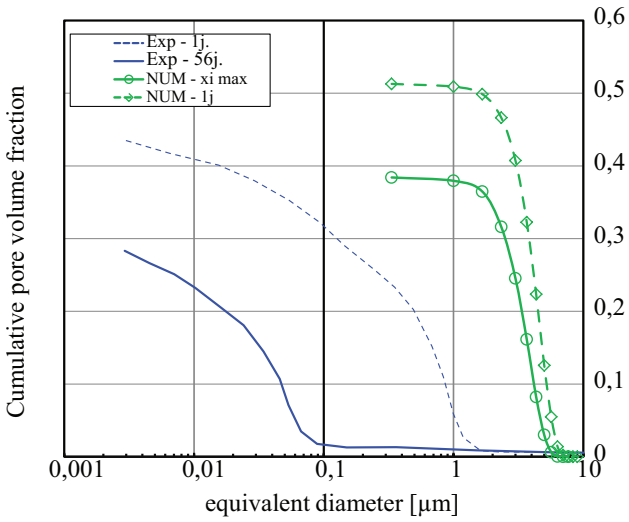

Figure 2.33: Qualitative comparison between experimental [Cook and Hover, 1999] and simulation results through hydration, $w/c = 0.5$.

Lastly, the influence of the w/c ratio was studied for hardened cement paste, using once again [Cook and Hover, 1999] data. The results (Fig. 2.34) present all the previous biases, but one noticeable fact is missing in our simulation.

For hardened cement paste (56 days), the experimental pore access diameter decrease by half an order of magnitude, as the w/c ratio decreases from 0.6 to 0.3. The simulation results, even if shifted, do not exhibit that feature, and the pore access diameter seems to stay unchanged with respect to the w/c.

Again, it is reminded that the quantitative comparison of such results is not yet fully possible, since no experimental mean of microstructural characterization has reached a consensus for cementitious materials.

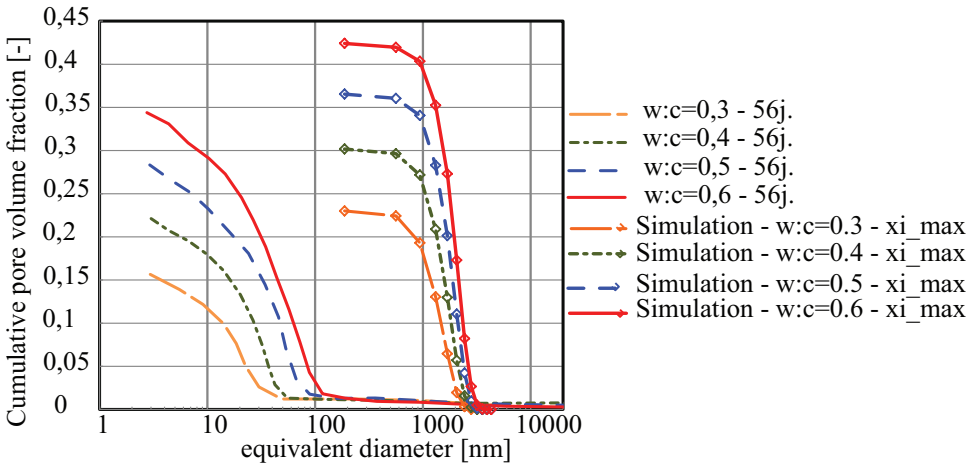

Figure 2.34: Qualitative comparison between experimental [Cook and Hover, 1999] and simulation results through hydration, influence of the w/c ratio.

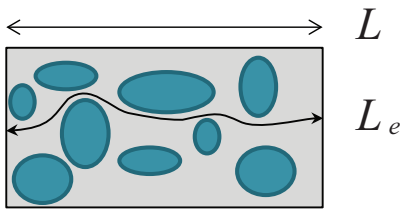

Figure 2.35: Lengths illustration.

5.3 Tortuosity

In Sect. 2.5 of this chapter the concept of toruosity has been introduced. Using the morphological operations briefly introduced — in particular the geodesic reconstruction — it is possible, for a two phase morphology, to detect the shortest of all paths from a border to its center, within a given phase. In particular, for cement pastes, it allows to measure the actual length of the porous network, L_e, and compare it to the macroscopic length of the sample, L, as illustrated on Fig. 2.35. In other words, by taking this ratio, we were able to measure the tortuosity, τ, defined, for porous materials in regards to diffusion phenomena by Eq.2.37.

It should be remembered that we consider only the shortest path, and not the average length of all paths, or the average of all streamlines. Thus the value presented here are to be seen as lower bounds of tortuosity.

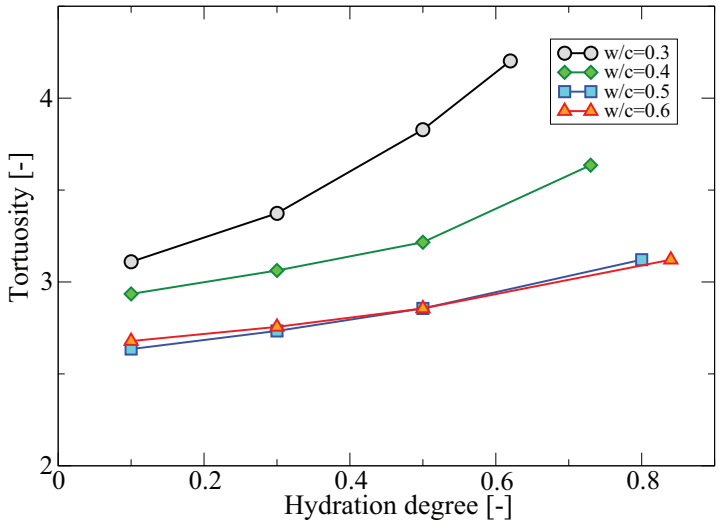

Figure 2.36: w/c ratio and hydration influence on tortuosity - *averaged over 3 realizations* - Jennings & Tennis hydration model, standard CEM-I composition and PaSD.

$$\tau = \left(\frac{L_e}{L}\right)^2 \tag{2.37}$$

The influence of the initial mix design is first noticeable on the left side of Fig. 2.36. As the w/c ratio increases, there is more water in the initial mix, leading to a lower tortuosity. Once the hydration reaction starts, the overall expected tendencies are respected, the tortuosity increases with time. For low w/c, this increase is stronger, going from 3.1 to 4.2 at the end of the hydration process whereas for the higher w/c, the increase is only about 0.4.

Overall, the tortuosities values measured on the generated morphologies may appear low, but again, we only measure here the lower bound, and as far as the author can tell, no direct measurements of this parameter can be found in the literature. Several attempts were done in order to measure this parameter, such as found in [Promentilla et al., 2009], relying on acquisition of 3D microstructures by means of X-ray CT and *random walk* algorithms ; or relying on indirect methods, coupling the measured diffusivity to the diffusion tortuosity (see *e.g.* [Sen, 2004]).

Interestingly enough, by scaling the same data according to the total porosity instead of the hydration degree, all the points regroup along a single curve. Various regression are then possible, in order to establish a theoretical *tortuosity-porosity* relation. Among the numerous possible regression, an simple power law (Eq.2.38, with two fitting parameters) is used. The fitting parameters are presented in Tab. 2.6.

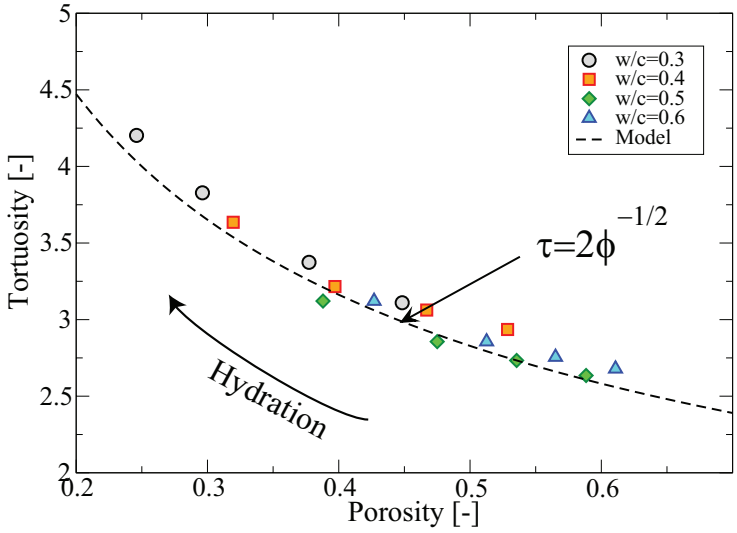

Figure 2.37: Porosity influence on tortuosity - *averaged over 3 realizations per w/c per ξ* - Jennings & Tennis hydration model, standard CEM-I composition and PaSD.

$$\tau = \alpha\phi^{\beta} \tag{2.38}$$

Constant	α	β
Power regression	2.02	-0.51
95% confidence interval	(1.94, 2.12)	(-0.56, -0.46)

Table 2.6: Fitting parameters for Eq.2.38.

To keep a simple expression, and given the fitting parameters identification, Eq.2.39 is proposed as a theoretical link between porosity and tortuosity for hydrating cement pastes.

$$\boxed{\tau = 2\phi^{-1/2}} \tag{2.39}$$

Note:
This expression of the link between the tortuosity and porosity, even if based on simulation data, can not be applied without care. As the porosity tends to zero, the tortuosity tends toward infinity (when the pore space is depercolated, the length of the actual shortest path can be considered as infinite) ; however the other limit case is less meaningful, as the porosity tends towards the unity, the tortuosity tends towards

two (instead of 1). In those regards, expression of Eq.*2.39 should be used with care, and for porosities below 70%.*

To overcome the lack of physical meaning of the previous expression, as the porosity tends to unity (the tortuosity should also tends to 1), additional fitting functions can be defined, like for example $\tau = \alpha \exp(\beta\phi^n)$ with $\alpha e^{\beta} = 1$, or $\tau = \exp(\beta(\phi^n - 1)$, however those fit are unable to match our data (coefficient of determination $r^2 < 0.5$).

A critical review of the tortuosity in regards to diffusion phenomena can be found in [Shen and Chen, 2007], with various mathematical definition and the corresponding scopes of application.

6 Concluding remarks

In this chapter an original morphological framework was introduced, allowing to model complex and randomly shaped morphologies. The statistical link that allow to control both geometrical and topological informations originated in [Adler, 2008] and first implemented by E. Roubin during his *Ph.D*[Roubin, 2013]. The development of the framework and its application to cementitious materials – as well as the percolation results – presented in this chapter are the result of a collaboration at the *LMT-Cachan*.

The first adaptation concerned the way to reach high volume fractions for inclusions / matrix morphologies, as a limitation of 16% appears for a moprhology with disconnected components. The latter is achieved by coupling two distinct enhancement. First, as the entire modeling framework is designed for Gaussian Correlated RF, it also is tractable as long as the correlated RF is Gaussian related (*i.e.* transformation of Gaussian CRFs). It allows to use χ^2_1 RFs and thus double the volume fraction for disconnected inclusions. Secondly, by using unions of CRFs, not only it becomes possible increase further the volume fraction for disconnected morphologies, it also allow to model various size of inclusions. This last feature becomes essential for cementititous material modeling — at every scale, from the C-S-H porosity description, to the cement particle / sand / aggregate size distributions.

Following, the framework was extended to multiple thresholds, in order to yield concentric phases around the initial inclusions. The modeling approach was then linked to the hydration model introduced in the first chapter.

Finally, the cement paste morphologies porosity were characterized, as an overall target of the hydration model, as well as its PoSDs. The tendencies are consistent with data taken from the vast literature on the subject (*cf.* Chap. 1) ; however quantitative analysis concern only the total porosity, since as it has been explained, their is no definite knowledge of actual cement pastes pore size distributions over the complete pore's size span.

3 Diffusive Properties Prediction in Cementitious Materials

Contents

1 Introduction 94

2 Diffusion in Cementitious Materials 94

2.1 Diffusion: General Principles 94

2.2 Diffusion through porous materials 95

2.3 Diffusion coefficient measurements 98

2.4 Cementitious materials: Results 102

3 Analytical homogenization 110

3.1 Analytical Bounds 110

3.2 Analytical Homogenization 111

4 Experimentation based models 113

4.1 NIST approache 113

4.2 Tognazzi's model 114

5 Remarks on (semi-)analytical models 114

6 Numerical homogenization 115

6.1 Literature review 116

6.2 Multi-scale approach: Energy Based Framework 119

7 Concluding remarks 122

1 Introduction

Cement based materials, as it has been described in the first two chapters, can be seen as porous materials with matrix bulk phase (considering as hardened, or evolving infinitesimally), and a pore phase filled with a liquid in equilibrium with the solid phase. Those materials are all the more sustainable and durable as they resist to any type of penetration from external sources as soils or water or radionuclides releases in the nuclear context of confinement. The mass transport phenomena that occurs in this class of materials have two distinct origins: on one hand a pressure gradient which may generate fluid flows in the porous network, and on the other hand concentration gradients within a phase which generate mass transport towards equilibrium. In cementitious materials studies, the general assumption is made that those two phenomena can be decoupled, and that mass transfer occur mainly through diffusion [Richet et al., 2004]. In addition, in the waste storage context where materials are usually saturated, the current state of knowledge indicates that diffusion phenomena are the leading ones compare to convection ones [Larbi, 2013].

First a formal definition and mathematical context — based on Fick's equations — is given for general diffusion processes, then applied to porous materials. Then a rapid description of the existing most used experimental set-ups to measure diffusion coefficient is given, with various experimental results relating to all concrete subscales. Finally forecasting method are introduced, either to determine diffusion coefficients at given scales, or to upscale this information between consecutive scales.

2 Diffusion in Cementitious Materials

2.1 Diffusion: General Principles

Diffusion is the process by which a substance (usually ions, molecules or isotopes) migrates from a high concentration region to a low one. A distinctive feature of this phenomenon is that it results in a mass transport (*e.g.* ions or molecules), without any bulk motion.

In mathematical terms, the diffusion in an isotropic medium is based upon the assumption that the flux quantity $\boldsymbol{J}$ of the diffusive species through a given surface is proportional to the concentration gradient along the surfaces normal. It is described by the first Fick's law. He was the first in late 19th century to describe quantitatively the diffusion process using analogy with the heat equation, developed few decades earlier.

For a unidirectional diffusion process, the first Fick's law is given by Eq.3.1:

$$\boldsymbol{J}_i = -D_i \frac{\partial C_i}{\partial \boldsymbol{x}}, \tag{3.1}$$

where i is the diffusive specie, $\boldsymbol{J}_i$ (mol.m^{-2}.s^{-1}) the flux of species i along $\boldsymbol{x}$, C_i its concentration (mol.m^{-3}) and lastly D_i the diffusion coefficient of the specie (m^2.s^{-1}).

The latter depends on the specie, on the medium where the diffusion occurs, and on the temperature. This last parameter will be neglected in the following. Thus, here the concentration gradient is the driving force, and the negative sign shows that the flux is oriented towards concentration regions.

If, in addition, we consider a conservative equation, the second Fick's law arise, and is given by Eq.3.2, and allows to determine $C_i(\boldsymbol{x}, t)$ for the specie i.

$$\frac{\partial C_i}{\partial t} = \frac{\partial}{\partial \boldsymbol{x}} \left(D_i \frac{\partial C_i}{\partial \boldsymbol{x}} \right) \tag{3.2}$$

In the case of a constant diffusion coefficient D_i, independent from $\boldsymbol{x}$ and C_i, the equation becomes:

$$\frac{\partial C_i}{\partial t} = D_i \frac{\partial^2 C_i}{\partial \boldsymbol{x}^2}. \tag{3.3}$$

In a model semi-infinite case, based on the analogy with the heat equation, analytic solutions exist. For a unidirectional process along direction $\boldsymbol{x}$, it takes the following form:

$$\frac{c(x,t) - c_s}{c_0 - c_s} = \operatorname{erfc}\left(\frac{x}{2\sqrt{Dt}} \right), \tag{3.4}$$

where $c_0 = c(x, 0)\ \forall x > 0$ is the initial condition, and $c_s = c(0, t)\ \forall t > 0$, the boundary condition.

2.2 Diffusion through porous materials

A porous material consists of a bulk matrix and pore space. In a first approximation, we will consider the latter filled with an aqueous phase (*where the diffusion occurs*), in equilibrium with the matrix (*no diffusion*).

In order for diffusion to take place, the pores have to be continuous, *i.e.* open and connected. The porous space could also be simply filled with a gas phase (where diffusion also occurs, but at a very different rate), but in regards to the upcoming studies, the material will always be considered fully saturated.

As soon as the observation scale is larger "enough" in comparison to the pore sizes, the diffusion in the material can be described from a macroscopic standpoint by Eq.3.5, similarly to Ficks first law, but with an *effective* diffusion coefficient D_e:

$$\boldsymbol{J} = -D_e \frac{\partial C}{\partial \boldsymbol{x}}. \tag{3.5}$$

The effective diffusion coefficient depends, as previously, on the diffusive specie, the pore network characteristics, the possible interactions with the matrix, and possible interactions with other species in the pore space.

2.2.1 Diffusion within the porosity

In the case where the specie i diffuse through a porous material, and there is no interaction with the bulk matrix, its concentration C_b (kg.m^{-3} of material) can be expressed according to C_i, the total i specie concentration in the pore phase (given that it is the only carrying phase):

$$C_b = \phi C_i, \tag{3.6}$$

where ϕ is the porosity contributing to diffusion (referred as $p_{o,p}$ in the first chapter, the open percolated porosity). So Eq.3.3 becomes:

$$\frac{\partial C_i}{\partial t} = \frac{D_e}{\phi}\frac{\partial^2 C_i}{\partial \boldsymbol{x}^2} = D\frac{\partial^2 C_i}{\partial \boldsymbol{x}^2}. \tag{3.7}$$

This equation is very similar to Eq.3.3, only this time the effective diffusivity arise, and can be expressed with Eq.3.8. The ionic flux through a surface, thanks to this parameters, can be expressed considering either the homogenized material, or under the assumption that diffusionoccurs only in the porosity. Most importantly, the *effective diffusivity* is the one reachable experimentaly. However, is still do not take into account possible interaction with the bulk matrix.

$$D_e = \phi D \tag{3.8}$$

2.2.2 Diffusion with interactions, binding

When there is an interaction between the diffusive specie i and the bulk matrix, the concentration C_b can be decomposed into C_{bl}, the concentration in the liquid phase, and C_{bb} the concentration bonded to the matrix. In this case, Eq.3.3 becomes:

$$\frac{\partial C_{bl}}{\partial t} + \frac{\partial C_{bb}}{\partial t} = D_e\frac{\partial^2 C_i}{\partial \boldsymbol{x}^2}. \tag{3.9}$$

Again, it is possible to express C_{bb} as a function of C_b, the concentration of the bounded specie relatively to the specimen mass, the porosity ϕ and the solid dry density ρ_s. The simplest form suppose a linear binding isotherm [Tuutti, 1982], and can be written as:

$$C_{bb} = (1-\phi)\rho_s C_b. \tag{3.10}$$

Using now Eq.3.6, Eq.3.9 can be re-written as:

$$\frac{\partial C_i}{\partial t} = \frac{D_e}{\phi + (1-\phi)\rho_s\frac{\partial C_b}{\partial C}}\frac{\partial^2 C_i}{\partial \boldsymbol{x}^2} = \frac{D_e}{R\phi}\frac{\partial^2 C_i}{\partial \boldsymbol{x}^2}, \tag{3.11}$$

with:

$$R = 1 + \frac{1-\phi}{\phi}\rho_s K_d, \tag{3.12}$$

a dimensionless parameter which translates the delay due to porosity and matrix interactions, and K_d (m^3/kg):

$$K_d = \frac{\partial C_b}{\partial C}, \tag{3.13}$$

which characterize the interaction between the diffusive specie and the porous media. This leads to a definition of an *apparent* diffusion coefficient as follow:

$$D_a = \frac{D_{\text{eff}}}{\phi + \rho_s K_d (1 - \phi)}. \tag{3.14}$$

The linear binding isotherm hypothesis upon which this paragraph's equations is is valid for low concentrations, or for field-exposed concretes. It is a well suited to tritiated water for example, as the interactions are almost negligible. However other models exist, like the *Langmuir* isotherm, derived from physical chemistry, or the *Freundlich* binding isotherm, that are more suited to describe the interactions for high concentrations of chlorides.

2.2.3 Binding and Radioactive decay

Radioactive elements decay naturally according to an exponential law. If the diffusive element is radioactive, this decay is taken into account by replacing in Eq.3.11 the term $\frac{\partial C}{\partial t}$ by $\frac{\partial C}{\partial t} + \lambda C$:

$$\frac{\partial C_i}{\partial t} = \frac{D_e}{R\phi} \frac{\partial^2 C_i}{\partial \boldsymbol{x}^2} - \lambda C_i, \tag{3.15}$$

where $\lambda = \frac{\ln 2}{T_{1/2}}$, $T_{1/2}$ being the half-time, *i.e.* the time taken for the elements activity to decay by half.

2.2.4 Infinite volume of water

In the case were the diffusion occurs in an idealized infinite volume of water, with no imposed motion to the diffusive specie, the diffusion coefficient can be calculated with the help of *Stokes-Einstein* relation:

$$D_i = \frac{RT}{6\pi\eta a N}, \tag{3.16}$$

where R is the perfect gas constant, T the temperature, η the water viscosity, N *Avogadro*'s number, and a the size of the diffusive specie. Given the various constant terms and their values, it can be foreseen that any specie will have a diffusion coefficient in the neighborhood of $1 \times 10^9\,m^2\,s^{-1}$. The coefficient has only little variation depending on the specie, and most of the time it is in a relatively small range: $0.5 \times 10^{-9}\,m^2\,s^{-1} \leq D_i \leq 2 \times 10^{-9}\,m^2\,s^{-1}$.

[Richet, 1992] gave a few values for some ions found in cement pastes, at a room temperature of 20 °C:

- Tritiated water: $D_{\mathrm{HTO}} = 2.24 \times 10^{-9}\,\mathrm{m^2\,s^{-1}}$,
- Chlorides: $D_{\mathrm{Cl^-}} = 2.03 \times 10^{-9}\,\mathrm{m^2\,s^{-1}}$,
- Sodium: $D_{\mathrm{Na^+}} = 1.33 \times 10^{-9}\,\mathrm{m^2\,s^{-1}}$,
- Calcium: $D_{\mathrm{Ca^{2+}}} = 1.56 \times 10^{-9}\,\mathrm{m^2\,s^{-1}}$.

2.3 Diffusion coefficient measurements

According to the scale of interest, various experimental techniques exist to assess a material diffusive properties. We present here the experimental results at each scales, with the according experimental procedures. First we introduce the traditional investigation techniques, which allow to measure an *effective* or *apparent* diffusion coefficient for cementitious materials. Later one, more recent results are presented at the C-S-H scale, mainly NMR and MD simulation results, since they appear to be the only ones valid at the nanometer scale.

2.3.1 Natural diffusion

Steady state:

The most simple experimental protocol consists of a sample of cement paste / mortar / concrete, saturated, place in-between two compartment with different concentrations of a given ionic specie (usually null in the "down" compartment). Under the concentration gradient between two opposite sides of the specimen, the ions are able to diffuse through the pore network and / or through various phases. The concentration of the "up" compartment is usually kept constant by regularly renewing the ionic content. A schematic representation is drawn Fig. 3.1(a), considering only the dashed frame area.

A regular chemical dosing of the down compartment allow to determine the ionic flux through the sample. Fig. 3.1(b) shows a schematic evolution of the ionic amount Q (mol) in the down compartment ; W, S and c_{up} being respectively the width (m), area ($\mathrm{m^2}$), and the upstream concentration ($\mathrm{mol.m^{-3}}$). The steady state is characterized by the linear part of the curve. The constant diffusive flux ($\Delta Q/S\Delta t$) alows to determine the *effective* diffusion coefficient (*cf.* Eq.3.5):

$$J_e = D_e \frac{c_{\mathrm{up}}}{W}, \tag{3.17}$$

with J_e the effective flux through the specimen in steady state ($\mathrm{mol.m^{-2}.s^{-1}}$). The effective diffusivity, D_e ($\mathrm{m^2.s^{-1}}$), is the slope of the linear part of Fig. 3.1(b). It is a first order approximation, since the flux expression in the first Fick's law is incomplete. To be more accurate, it would be necessary to take into account the local electric field generated by the ionic diffusive specie.

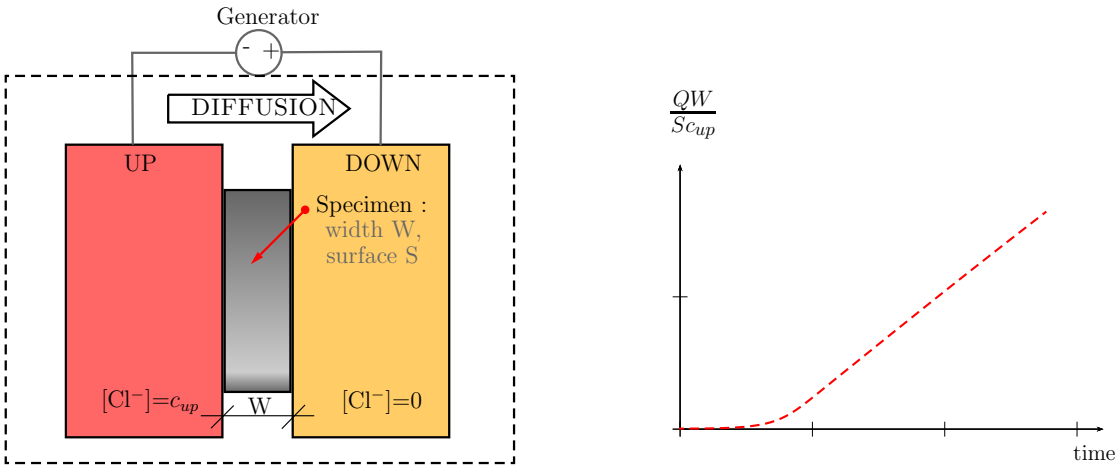

(a) Diffusion cell

(b) Ionic flux in the down compartment

Figure 3.1: Measuring diffusion coefficients in mortars.

The duration of such experiments may vary according to the specimen width, the type of concrete (cement, sand, aggregate, w/c ratio, *etc.*). However, reaching a steady state may take as long as a year for a 3 cm wide specimen.

Transient state:

To reduce the experimental duration, two options are easily conceivable: either measure the diffusion coefficient in transient state, or increase the concentration gradient by increasing the upstream ionic concentration c_{up}. For such experimentation, a sample, usually cylindrical, of cement paste / mortar / concrete is saturated and covered with an impermeable resin on all but one side. A schematic representation is drawn FIG. 3.2(a). It allows a unidirectional ionic flux.

According to the standards, the minimal duration of the experiment may vary from 35 to 100 days, and the ionic concentration from 30 to 165 g/l. At the end of the experiment, a concentration profile is drawn (schematic representation on FIG. 3.2(b)). From this profile, under the approximation of a model semi-infinite domain, with uni-directional diffusion, EQ.3.4 provide the diffusion coefficient. Attention must be drawn here to the fact that this diffusion coefficient is an *apparent* one, D_a.

It will differ from the previous experiment, as it also takes into account the possible ionic fixation / interactions. The main advantage is the experimental duration. However, the procedure to obtain the profile, by dosing nibbled material powder at various depths, is still time consuming and fastidious.

The diffusive process being overall rather slow, the steady or transient state experiments in natural condition are not satisfying enough for young materials (microstructure evolution during the experiment), or for fast results (numerous experiment, formulation comparisons, *etc.*). To reduce further the experiment duration,

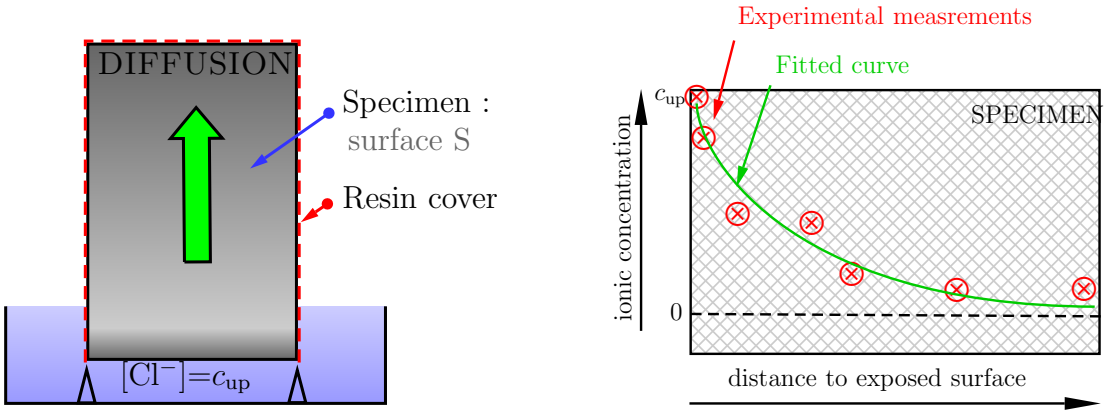

(a) Immersion experiment

(b) "contaminated" profile after immersion

Figure 3.2: Measuring diffusion coefficients in transient states.

the diffusion can be *forced*, by applying an electrical field between the up- and down-stream compartments.

2.3.2 Forced diffusion

Migration experiments were developed to reduce as far as possible the experimental duration of diffusion experiments. A difference in electrical potential is applied between the two sides of the specimen. Under its influence, the ions will migrate faster.

The same distinction exists with steady and transient state measurements:

Steady state:

The exact same procedure as previously is applied, with an additional voltage generator (FIG. 3.1(a)) connected to the two compartments. The electrical field created is usually around $4\,\mathrm{V\,cm^{-1}}$ (*i.e* 12 V for a 3 cm thick specimen). Higher voltage are not recommended since the duration improvement is already significant, but prevent a temperature rise from happening, as well as perturbation close to the electrodes [Prince et al., 1999]. Some authors also developed theoretical frameworks that are suited for a large span of applied electrical fields [Bourbatache et al., 2013].

The result interpretation follow the same procedure as previously, and once the steady state is reached, the effective diffusion coefficient is calculated with the hypothesis that the only driving force is the electrical field. With the help of the *Nernst-Planck* equation, the relation becomes:

$$J_e = D_e \frac{c_{up} F U}{W R T}, \tag{3.18}$$

where F and U are respectively the *Faraday*'s constant and the electrical potential difference, and R and T are the perfect gas constant and the temperature.

Some other interpretations are possible. For example, in [Truc and Ollivier, 2000] the upstream compartment is considered. The steady state is reached faster, and it allows measurements in already contaminated specimens. In [Amiri et al., 2001], instead of dosing the up- or down-compartment, they study the variation in the electrical field — avoiding the chemical dosages. This last method is found to be much simpler.

Overall, those experiment are faster than previously, but the steady state establishment is still a limiting time factor.

Transient state:

The last type of experiment is the fastest. It combines the transient state of diffusion, as well as the imposed electric potential difference. The main advantage is that it is possible to get a diffusion coefficient in 24 hours. The experiment principle are the same as previously: the saturated specimen is placed between two compartments with different ionic concentrations, an electrical field is then applied. At the end of the experiment (duration set by standards), the sample is split by slitting, and the penetration depth is assessed with a developing spray (usually silver nitrate).

The theoretical background here is more complex, and relies on supplementary hypothesis. It will not be developed here, but analytic expressions of the *apparent* diffusion coefficient exist for this experimental setup.

Such experiments were also realized at the *LMT-Cachan* during *Z. Djamaï* internship in 2013. The experimental set up is presented Fig. 3.3. The actual diffusion experiments were carried out using a *Proov'it* device, complying to the following American standards : AASHTO T 260, ASTM C 114, ASTM C1152, ASTM C1218.

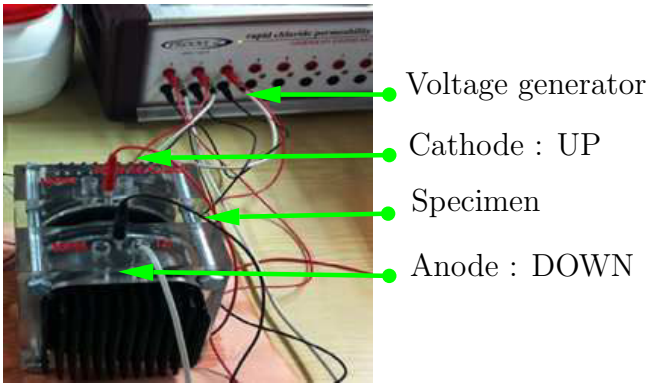

Figure 3.3: Experimental diffusion cell.

The results yielded with this experimental set-up are presented in Sect. 2.4.2.

2.4 Cementitious materials: Results

After describing various experimental protocols to measure the diffusion coefficients in cementitious materials, results are presented for the different scales of interest.

2.4.1 Cement pastes

At the cement paste scale the diffusion coefficients have been investigated for a long time. A short literature review is presented, based on the experiments described in Tab. 3.1.

Reference	Cement type	Diffusing specie
[Richet, 1992]	CEM-I	Tritiated water
[Tits et al., 2003]	CEM-I	Tritiated water
[Béjaoui et al., 2006]	CEM-I and CEM-V	Tritiated water
[Sugiyama et al., 2008]	CEM-I and CEM-I with silica fumes	Uranium
[Tognazzi, 1998]	CEM-I	Chlorides
[Mejlhede, 1999]	CEM-I	Chlorides
[Ngala, 1995]	CEM-I	Chlorides

Table 3.1: Cement pastes diffusion coefficient measurements: main experimental characteristics.

Porosity and w/c ratio influence:

Various experimental results are presented Fig. 3.4, in terms of effective diffusivity in regards to the water accessible porosity, for CEM-I classical cement pastes. Given that the results are plotted for various diffusive species, only the *effective* diffusion coefficient is of interest here, as chloride ions tend to interact with the bulk matrix.

It can be seen that the effective diffusion coefficient is hardly influenced by the diffusive specie and it seems that it is only influenced by the amount of porosity.

The relation between the water accessible porosity and the w/c ratio being not linear, part of the same results and some new ones are drawn Fig. 3.5. Overall the same tendencies as previously are observed. An additional feature more noticeable with this scaling, is the change of general slope for $w/c \approx 0.35$. For $w/c > 0.35$, the diffusion is believed to be driven by the capillary pores, and their relative amount. Below this threshold, as the slope becomes stiffer, the capillary pores tends to close up, and the diffusion is now believed to be driven by hydrates pores, an order of magnitude smaller.

Blended Cement - admixture influence:

Lastly at this scale, the effect of admixtures is considered, to assess the effective diffusivity of blended cement pastes. Results are drawn Fig. 3.6.

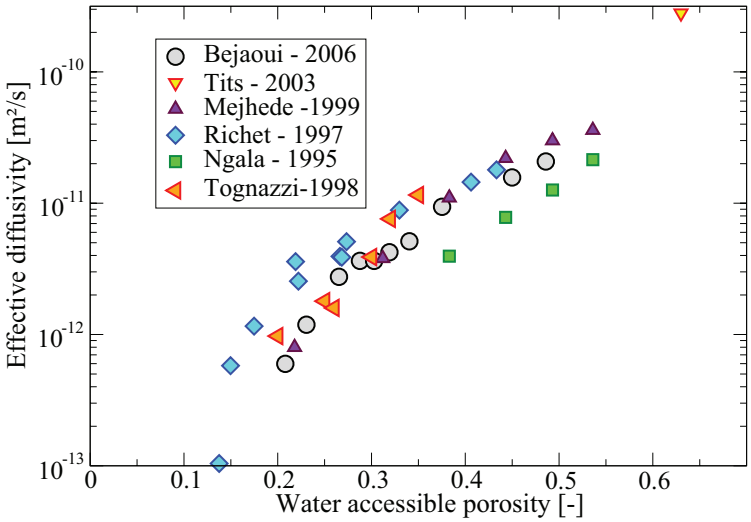

Figure 3.4: Effect of the porosity on the effective diffusivity of CEM I cement pastes.

Results from [Béjaoui et al., 2006] compare two types of cement: a standard CEM-I and a CEM V (usually with fly ashes and blast furnace slag). In the experiment, the CEM V cement paste had higher porosities, some values are as listed in Tab. 3.2.

w/c [-]	CEM I	CEM V
0.3	0.230	0.272
0.4	0.303	0.350
0.5	0.375	0.411

Table 3.2: Calculated porosities.

Even if the porosity increase with the blended cement, the effective diffusivity itself decreases by an order of magnitude, and this difference tends to increase for high w/c. It reflects the fact that the total porosity is not a good enough description for the pore space, as it does not reflect the connectivity and size distributions.

The second type of results, from [Sugiyama et al., 2008], concerns silica-fumes addition (30% in mass). For $w/c = 0.7$, as previously, over an order of magnitude in terms of effective diffusivity is observed ($D_{\text{blend}} \ll D_{\text{cement}}$). However, for $w/c = 0.35$, the values are almost the same ($D_{\text{blend}} \approx D_{\text{cement}}$). The silica fumes are very small particles, between 50 and 200 nm in size, which make them very reactive. They react via a pouzzolanic reaction, and help hydrates precipitate when free space is

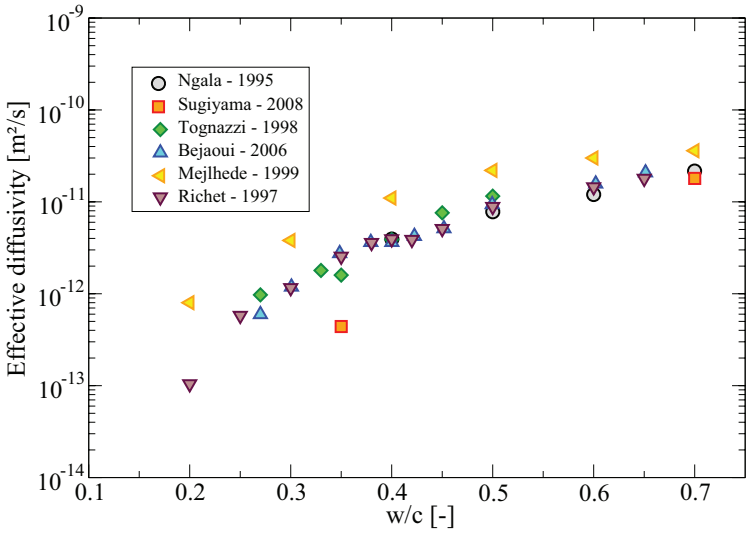

Figure 3.5: Effect of the w/c ratio on the effective diffusivity of CEM I cement pastes.

available (high w/c ratios). The cement paste with the silica fumes has almost a constant effective diffusivity, and the w/c ratio does not play any major influence.

2.4.2 Mortar and concrete scale

New experimental data is used to assess the diffusion coefficient while upscalling to mortars and concretes. The main features of the tests are listed in Tab. 3.4. As previously, only *effective* diffusion coefficient are considered.

A feature already mentioned when considering upscalling from cement pastes to mortar and concretes, is the ITZ. This transitional zone around the aggregates has a higher porosity. In a first approximation, the addition of aggregates belittle the overall amount of cement paste, and one would expect that the diffusion occurs slower, since the ionic migration / diffusion path is stretched out (tortuosity increase, porosity decrease). However, due to the ITZ, even though the tortuosity increases, the overall porosity stays almost unchanged compared to a cement paste.

The more aggregates are added, the higher percentage of cement paste belong to the ITZ. This was already illustrated on Fig. 1.28. As the amount of sand increases in a mortar, the total porosity first decreases, but for a volume fraction exceeding 0.5, the porosity starts to increase again. This change of slope is attributed to the increasing volume of ITZ formed around the aggregate. It translates, for the diffusion coefficient measurement, into an rather unexpected increase [Larbi, 2013]. Such results are drawn Fig. 3.7. Beyond 55% of sand, the effective diffusivity shows a

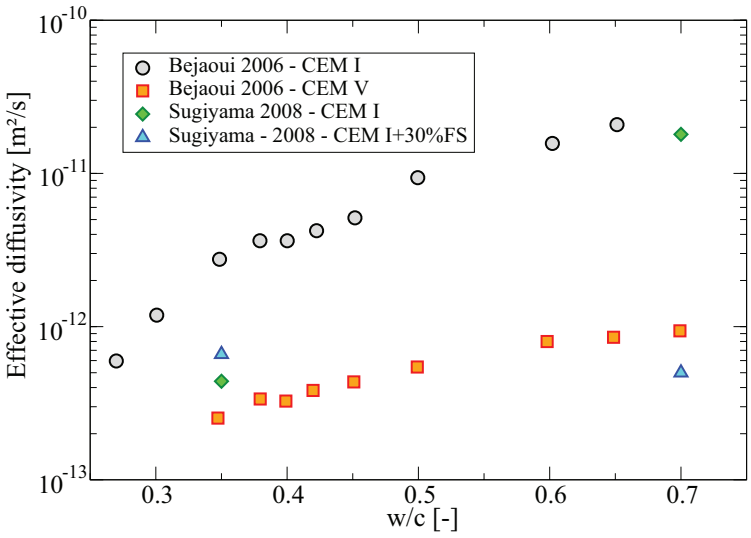

Figure 3.6: Diffusivity evolution for blended cements.

great increase in comparison to the slow decrease in the first part of the graph. At first it follows very well a simple dilution model, and then above the sand volume fraction threshold, the volume of ITZ and its connectivity reach a point where the diffusion occurs faster, even though the path is more tortuous.

Note:
Such volume fraction of sand are very rare in actual mortars, they would lead to the apparition of defects (rheological nature) and thus to a in-homogeneous material. For concrete, such volume fraction are often reached, but with much more coarse aggregates, which limits the ITZ amount, as shown now.

An additional experiment [Caré and Hervé, 2004] is also considered, to illustrate the sand's fineness influence. For a mortar with w/c ratio of 0.45, various fineness of sand were used: a fine one with particles in the (0.315/1 mm) grading class, and a coarse one respectively in the (2/4 mm). Their results are also plotted on Fig. 1.28, with the right / left triangles. The study showed the fine sand produces much more ITZ in terms volume fraction, which leads an increase in effective diffusivity even for values as low as 25% of inclusions, whereas the coarse sand follow a more expected path, with a quasi linear effective diffusivity decrease for 25% and 50 % of inclusions.

As mentioned in Sect. 2.3.2 of this chapter, experiments were done at the *LMT-Cachan*, using a forced diffusion (migration in transient states). A standard CEM-I

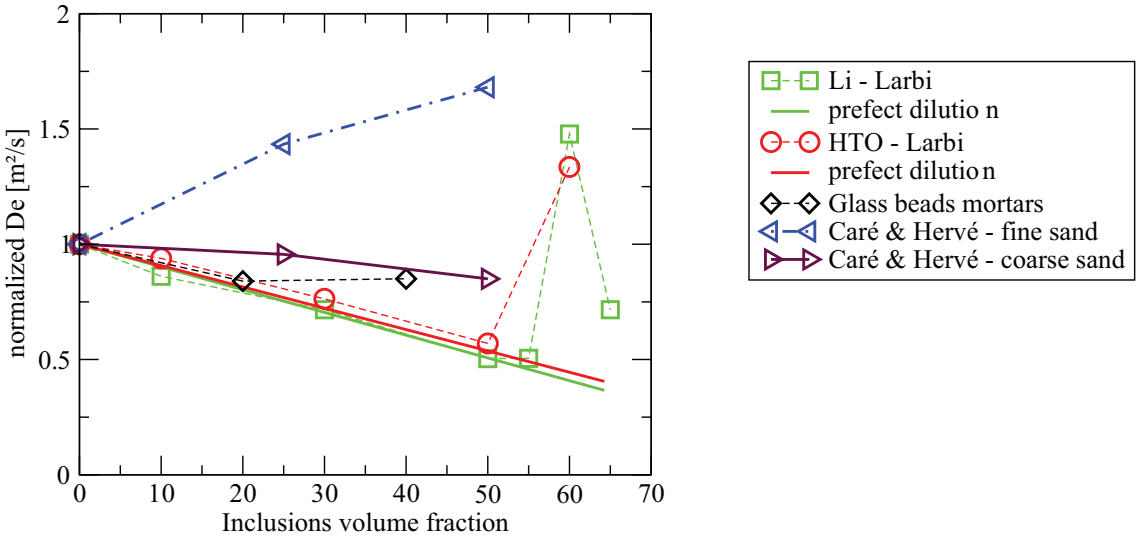

Figure 3.7: Influence of the sand amount on the diffusion coefficient – Normalized values.

Glass beads volume fraction (%)	0	20	40
D_a *(experimental)* (10^{-11}m^2 s^{-1})	2.81	2.69	3.09
porosity	0.21 *(measured)*	0.168 *(calculated)*	0.126 *(calculated)*
solid dry density (10^3kg.m^{-3})	1.524 *(measured)*	1.719 *(calculated)*	1.914 *(calculated)*
D_e *(calculated)* (10^{-12}m^2 s^{-1})	8.04	6.83	6.85

Table 3.3: Results at 28 days for glass bead mortars.

mortar was designed with $w/c = 0.45$, and three different glass beads proportions (2 mm in diameter) were used. Glass beads were chosen to limit sand's PaSD influence, and have only mono-sized, inert, inclusions.

The results of the tests are listed in Tab. 3.3, and reported on Fig. 3.7, in terms of apparent diffusivity (measured) and effective (calculated). Those results were obtained using Eq.3.14, and the following assumptions:

- The porosity of the mortar was determined using H_2O porosimetry at 28 days,
- The density was determined using a hydrostatic weight measure,
- The binding isotherm is considered constant, and a value of K_d =5 $\times$ 10^{-5} m^3 kg^{-1} in considered.

The effect of the first 20% of beads follow the trend observed by Larbi, very similar to a simple dilution model . However, the same way Larbi's results showed

an increase in diffusivity when more than 55% were used, here the 40% beads mortar exhibit a higher diffusion coefficient than the 20% one. The increase is really small, but rather interestingly, the dilution law in not observed any more. Several causes can explain this discrepancy, with first the increase of tortuosity of the pore network (which stretches the particle path). Secondly, as theorized in [Larbi, 2013], the amount of ITZ is increasing, and above a threshold, those ITZ percolates and facilitate even more the mass transport in cementitous materials.

This second hypothesis has been investigated, however SEM images — obtained at the *LMT-Cachan*, after slicing and polishing mortar specimens — of such samples did not seem to exhibit any ITZ around the glass beads (Fig. 3.8). Even with a resolution approaching $0.8\,\mu m\,pix^{-1}$ for the left image, and $0.18\,\mu m\,pix^{-1}$ for the right one, no significant increase in porosity can be noticed (the ITZ porosity, as measured by MIP is believed to be approximately at the micrometer scale; it should be detectable with the higher magnification). Few phenomena could however explain this increase. A plausible explanation is that for high volume fractions the differential deformation can induce cracking [Briffaut and Benboudjema, 2013], as it is visible on the south-west corner of Fig. 3.8 (not exactly at the interface, but not far). In addition undesirable effects like packing defects at 40% of volume fraction, possibly some ionic interactions between the interstitial solution and the glass beads can also explain it.

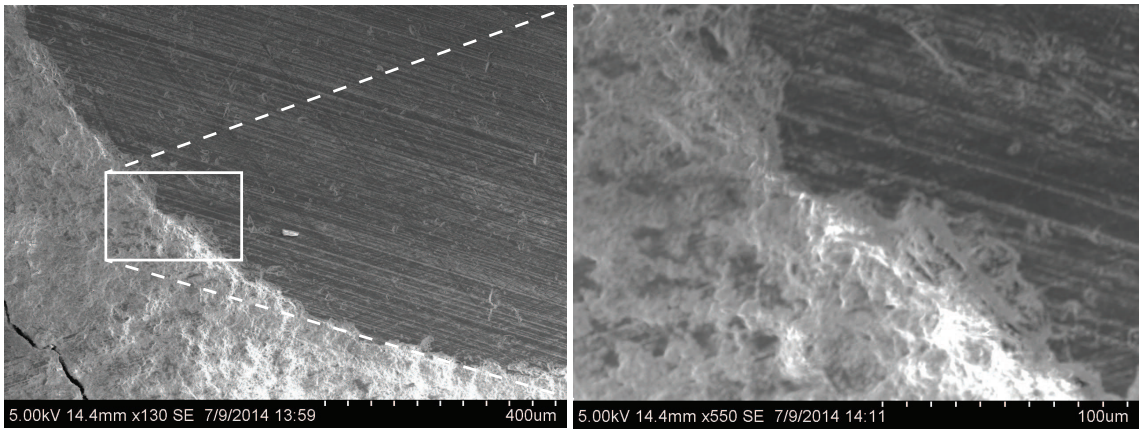

Figure 3.8: SEM image of glass beads mortar – *courtesy of* A. Darquennes.

For concretes and mortars (with traditional mix proportions found in civil engineering applications, references listed in Tab. 3.4), experimental results are drawn Fig. 3.9, with only the mortar and concrete results highlighted. In the background, the experimental points for cement pastes are also drawn in transparency. Remarkably, there is almost no difference between the tested concretes and cement pastes. It is explained by the presence of the ITZ. It can also be noticed, based on [Carcassès et al., 2005] results, that the type of cement do not have a big influence. The results for blended cement are a little lower in terms of effective diffusion coefficient, but

not as far appart as on FIG. 3.6. The ITZ seems to diminish the influence of the mineral additions.

Reference	Cement type	Diffusing specie
[Carcassès et al., 2005]	CEM-I, II, III, IV and V	Chlorides
[Tang, 2003]	CEM-I	Chlorides
[De Larrard, 2010]	CEM-I + Fly ashes (23% in mass)	Chlorides
[Caré and Hervé, 2004]	CEM-I	Chloride

Table 3.4: Mortar and concrete diffusion coefficient measurements: main characteristics.

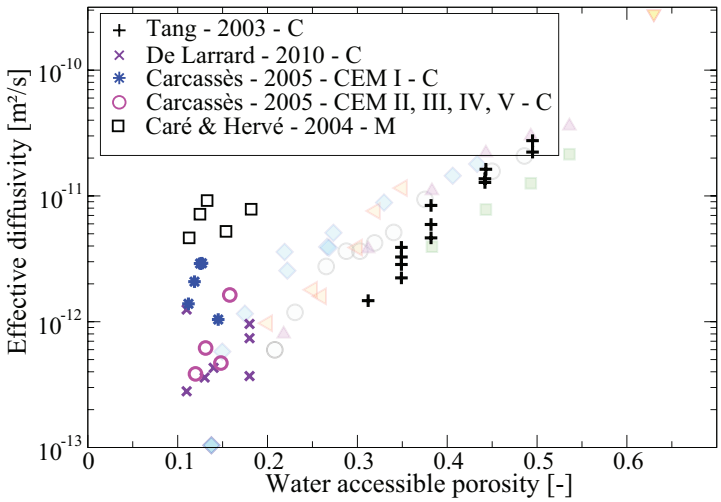

Figure 3.9: Mortar and concrete diffusion coefficient evolution (in transparency, results from CP scale.)

For those reasons, the actual effective diffusivity stays almost unchanged while upscalling, when scaled according to the accessible porosity.

2.4.3 Other influential parameters

In addition to the mix design parameters introduced at the cement paste and mortar scale, some other features may influence the diffusion process:

Temperature: The temperature may have an impact on diffusion. As it rises, the vibrating frequency of the diffusive specie increases, and it can be modeled with an *Arrhenius* like law:

$$D_T = D_0 \exp\left(\frac{U}{R}\left(\frac{1}{T_0} - \frac{1}{T}\right)\right), \tag{3.19}$$

where T and T_0 are the actual and reference temperature (K), D_0 the diffusion coefficient at T_0, R the perfect gas constant and U the activation energy for the diffusion process (function of the cement type and w/c ratio). A rise in temperature from 5 °C to 40 °C would multiply the effective diffusivity by 7. So the temperature is a controlling parameter in diffusion studies, however, we will always consider ideal laboratory conditions, and always assume a constant temperature of 20 °C.

The saturation degree: (or *humidity range*) Since the ionic diffusion occurs only in the interstitial solution, the saturation degree of the material plays an important role in the diffusion process. Under a saturation threshold around 0.5 [Francy and François, 2001], the liquid phase in the pores are not continuous any more, and the diffusion is blocked. Above this threshold, the diffusivity increase with the saturation degree. This parameter, however, will not be considered at all, since experimental results are always obtained in fully saturated conditions, and the numerical simulation will always make the same assumption.

(Micro-) cracking: two main types of cracks are to consider. First, the family of microcracks due to incompatible deformation (cement paste / aggregates), hydric and / or thermal gradient, *etc.*, is usually more diffuse. Its influence is not significant [Ollivier and Torrenti, 2008]. The second type of cracks concerns through cracks, due to a mechanical loading, or restrained deformations. Those types of cracks are not considered in the same way as the precedent one. Here the diffusion through a cracked sample is function of the crack opening. As soon as it is large enough ($\approx$ 100 µm, the effective diffusion coefficient tends very fast to the one in pure water (around $1.4 \times 10^{-9}\,\mathrm{m^2\,s^{-1}}$) [Djerbi et al., 2006]. In the modeling framework applied in the second and last chapters, the (micro-) meso-structures will always be considered sound, with no (micro-) cracks.

Ionic interactions: There are many interactions that have not been described, like the electrostatic field induced by other ions, the adsorbed layer of ions at the pore surfaces, or the diffusion coefficient that depends on the concentration. The modeling of such interactions is much more complicated (with many non-linearities) than the equation presented at the beginning of this chapter, and thus they will be neglected.

2.4.4 Nanometric scale

In very confined spaces, traditional investigation techniques are not well suited due to molecules confinement leading to surface driven phenomena. However, two recent

techniques — Nuclear Magnetic Resonance and Molecular Dynamics Simulations — allow to verify this hypothesis, and yield diffusion coefficients at this particular scale.

RMN has shown two pore modes in the C-S-H [Korb et al., 2007a, Korb, 2010] (*cf.* Chap. 1.) The first one (smaller one) is believed to be a inner porosity, where diffusion can occur only within, and no interactions with the exterior were observed. At those scale, the water diffusion coefficients are found to be :

- $5 \times 10^{-11}\,\mathrm{m^2\,s^{-1}}$ for the smaller pore more, corresponding to inner channels, that do not connect to the exterior (pore mode around 1.7 nm),
- $6 \times 10^{-10}\,\mathrm{m^2\,s^{-1}}$ for the above surface water molecules (pore mode around 7 nm).

MD simulation, based upon the assumption that the C-S-H structure is very close to the *tobermorite* one [Pellenq et al., 2009, Yoon and Monteiro, 2013], yield the same distinctions in terms of pore modes, as well as diffusion coefficients. The excellent level of agreement between those two distinct techniques provides a good support of their validity.

Both those values (RMN studies or MD simulations) are significantly less than diffusion coefficients found in bulk water with the same experimental setup: $2.3 \times 10^{-9}\,\mathrm{m^2\,s^{-1}}$ [Korb et al., 2007b].

Remark:

This last point is of crucial importance, since it will be used as the first material **input** for the predictive upscalling framework.

3 Analytical homogenization

Numerous analytic homogenization schemes exist to predict composite materials response. Every such model is based upon strong morphological hypothesis (spherical / ellipsoidal inclusions, concentric phases, *etc.*). A first category of approaches allow to bound the composite response, and a second one, more accurate, gather several schemes that allow for actual prediction (homogenization) of diffusive properties.

3.1 Analytical Bounds

Voigt & Reuss:

These simplest bounds rely only the volume fractions partition, and the only consideration taken into account is their placement: either serial or parallel (actually based on assumption of respectively uniform strain or stress in elasticity problems). They can be seen as extreme cases of a power law:

$$D_e = \sum_i f_i D_i^{\alpha}, \tag{3.20}$$

where f_i and D_i are respectively the volume fraction and diffusion coefficient of phase i, and α is a constant, usually between -1 and 1. In those extreme cases, the *Voigt* and *Reuss* (upper and lower) bounds are found. For a 2-phase material, with a volume fraction f_i of inclusions (D_i) within a matrix (D_m), the relations are given Sys.3.21:

$$\alpha = 1 \quad \text{(Voigt)}: \quad D_e = f_i D_i + (1 - f_i) D_m \tag{3.21a}$$

$$\alpha = -1 \quad \text{(Reuss)}: \quad D_e^{-1} = f_i D_i^{-1} + (1 - f_i) D_m^{-1} \tag{3.21b}$$

Hashin & Shtrikmann bounds:

Assuming an isotropic material response for each phase, [Hashin and Shtrikman, 1963] proposed narrower bounds, which also rely only on the volume fractions partitions (based on elastic energy derivation from a reference isotropic state) for elastic properties. For a 2-phase material with a volume fraction f_i of inclusions (D_i) within a matrix (D_m), with $D_m > D_i$ (*e.g.* a mortar with sand inclusion within a cement paste matrix), the relations can be re-written for diffusion according to Sys.3.22:

$$D_{HS}^{+} = D_m + f_i \left[\frac{1}{D_i - D_m} + \frac{1 - f_i}{3D_m} \right], \tag{3.22a}$$

$$D_{HS}^{-} = D_p + (1 - f_i) \left[\frac{1}{D_m - D_i} + \frac{f_i}{3D_i} \right]. \tag{3.22b}$$

Those bounds are tighter than Voigt & Reuss ones. An example of those bounds is given Fig. 3.10. It considers a mortar, with a volume fraction f_i of impermeable sand that does not diffuse, and the matrix — in this case the cement paste — has a diffusion coefficient taken to be $1 \times 10^{-11}\,\mathrm{m^2\,s^{-1}}$ (average value for a standard CEM I cement paste with $w/c = 0.5$). The lower bounds is strictly at 0 since the inclusions are supposed to be impermeable. When no inclusions are found, the effective diffusion coefficient is the one of the matrix, and on the other side when only inclusions are found, the diffusion coefficient falls to zero.

Those bounds remain very wide, due to material property contrast found in cementitious materials (over an two orders of magnitude: $D_{\text{hydrates}}/D_{\text{porosity}} = 10^{-2}$ to 10^{-3} at the CP scale, and $D_{\text{CP}}/D_{\text{aggregates}} \to \infty$ at the mortar / concrete scale) which makes systematically on phase completely insignificant.

3.2 Analytical Homogenization

In order to predict actual values of effective diffusion coefficients, and not only bounds, several models exist. Based upon various hypothesis, those analytical models can be decomposed into three main steps:

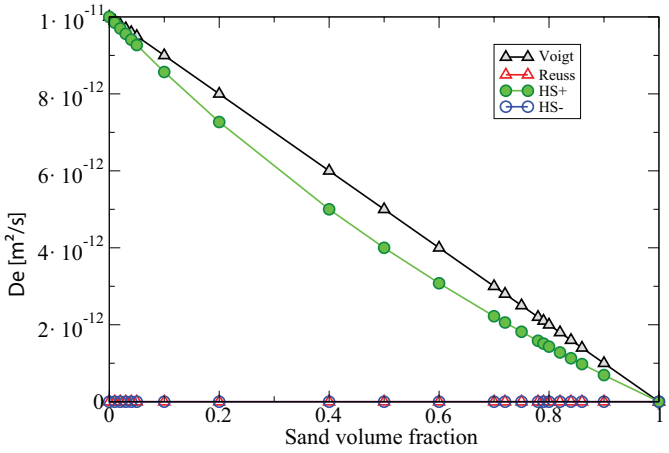

Figure 3.10: Analytical bounds for mortar diffusive coefficients.

- First the **representation**, which describes the materials at the microscopic scale, with the definition of the various phases, as well as their distribution and local behavior.

- Secondly, the **localization** that defines the diffusive behavior, and allows to establish a link between the micro- and macro equivalent quantities.

- Lastly, the **homogenization** itself, which identify the macroscopic material response by averaging the previous step solutions.

These type of schemes predict analytical expressions of the diffusion coefficient, based on Mean Field Eshelby-based Homogenization (MFH) schemes.

The MFH schemes are based on Eshelby's tensor [Eshelby, 1957]. In their original work, it was used to estimate average strains and stresses inside a micro-inclusions embedded in an elastic matrix ans account for their shape and orientation. Equations will not be developed here, but several authors gave analytic expressions according to the geometry and distribution of inclusions (*e.g.* [Mura, 1987, Christensen, 1991]). The various schemes are only briefly introduced here, the equations are not developed (they all can be found in [Do, 2008], applied to homogenization of the thermo-hydro-mechanical behavior of argillite):

- *Eshelby*'s method, or dilute model, which does not account for the interaction between particles. It is hence suited as long as the inclusions have a low volume fraction (*e.g.* mortar studies with less than 30% of inclusions, as drawn on Fig. 3.7, under "perfect dilution").

- *Mori-Tanaka* model, credited to [Mori and Tanaka, 1973], allows to handle the particle interactions, and considers both spherical and ellipsoidal inclusions, and is best suited to "inclusion – matrix " morphologies.

- *Self consistent* schemes, introduced by [Hershey, 1954] and [Hill, 1965] for ellipsoidal inclusions, as previously. It is an implicit scheme, and it requires to solve iteratively non linear equations.

- Some other methods exist, like the *differential* scheme [Roscoe, 1952], or the *Effective field approach* [Kanaun and Levin, 1994].

All those models can yield homogenized expressions of the quantity of interest, with rather good predicaments as long as the inclusions geometries are well defined (spheres, ellipsoids, polyhedron, *etc.*). The analytic expressions stay simple enough as long as two phase materials are considered. The later is usually too poor to describe cementitious materials at any scale. Some authors have implemented such analytic homogenization schemes in a multi-scale fashion [Stora et al., 2008] to predict correct bounds for diffusive properties at the CP scale. Indeed, at the cement paste scale one will consider microstructures with at least three phases (porosity, hydrates and unreacted cement for example), and at the mortar and concrete scale, the apparition of the ITZ will also lead to three phase microstructures. Three phase models exists, and were developped ([Christensen, 1991] for example). Usually, in spite of the third phase and the more accurate *representation*, these family of schemes have the same flaws as the previous ones, namely the fair accounting of two (or more) very different rate of diffusion (*e.g.* within the pore space *and* the hydrates) and do not take into account the percolation phenomena naturally (they can be enforced by defining percolation thresholds, or with the S-C scheme, the apsect ratio influences the percoltaion threshold: the more elliptic the inclusions are, the lower the percolation threshold).

4 Experimentation based models

Numerous authors tried to model the diffusivity evolution based on the porosity evolution, modeled or predicted, by using empirical relations linking porosity and diffusive properties. Those relations are some times based upon numerical experiments [Garboczi and Bentz, 1992], or on actual experiments (*e.g.* [Tognazzi, 1998]).

4.1 NIST approache

Based on numerical experimentation realized upon upon the CEMHYD-3D hydration model and a numerical framework, [Garboczi and Bentz, 1992] proposed explicit relations (Eq.3.23) linking the D/D_0 ratio (D being the cement paste diffusion coefficient, and D_0 the porosity diffusion coefficient) to the capillary porosity ϕ.

Additional authors modified those equations according to various parameters, like the silica fumes content [Bentz et al., 2000b], or the accounting for surface precipitation in the pores (mainly calcite and brucite, unlike the ettringite which precipitate without substrate) [Guillon, 2004].

$$\frac{D}{D_0} = 0.001 + 0.07\Phi^2 + 1.8H(\phi - 0.18)(\Phi - 0.18)^2, \tag{3.23}$$

where H is the Heaviside function.

It can be seen that in such relations, the cement paste diffusivity D do not tend towards D_0 ($D/D_0 \to 1$) when the porosity is increasing, which clearly reflects a lack of proper description. The results of such models are usually off by an order of magnitude or so. Some authors proposed to feedback the results and try iteratively to improve the analytic expressions (by tuning the D_0 parameter), however the expressions had even less physical meaning.

4.2 Tognazzi's model

Based upon traditional experiments, the following model was introduced by [Tognazzi, 1998]. Assuming that the diffusivity only depends on the porosity, the experimental results showed a certain linearity in *log* diagrams, expressed by:

$$D = D_0 \mathrm{e}^{k\Phi}, \tag{3.24}$$

with D_0 =$2.31 \times 10^{-13}\,\mathrm{m^2\,s^{-1}}$, and $k = 9.9$, identified with experimental results. It allow to yield correct results for high w/c, but not for low ones, as drawn Fig. 3.11. In addition, the D_0 value does not have a physical meaning, as this value should be infinite in a perfect material with no porosity, or at least reflect the diffusion properties of the hydrates ; as for the other hand, for $\phi = 1$, the value is D =$4.6 \times 10^{-9}\,\mathrm{m^2\,s^{-1}}$, with the given set of parameters, which is close to the diffusivity in water ($2 \times 10^{-9}\,\mathrm{m^2\,s^{-1}}$).

Other models of this type exist, but they all require parameter fitting over experimental data, and are thus not suited to forecast properties without any experiment.

5 Remarks on (semi-)analytical models

If we consider only the models that do not require experimental fitting, the analytic models and schemes are not well suited for cementitious materials studies, due to their intrinsic heterogeneous morphologies.

A first feature that can not be captured with this family of approaches is the size distributions of the inclusions. Thus, comparing two cement paste with the same composition (same volume fractions) but different PaSD will yield the same results.

A second prerequisite for those models is that they all require, as an input, the diffusion coefficient in each phases. The latter are not always very well known. As

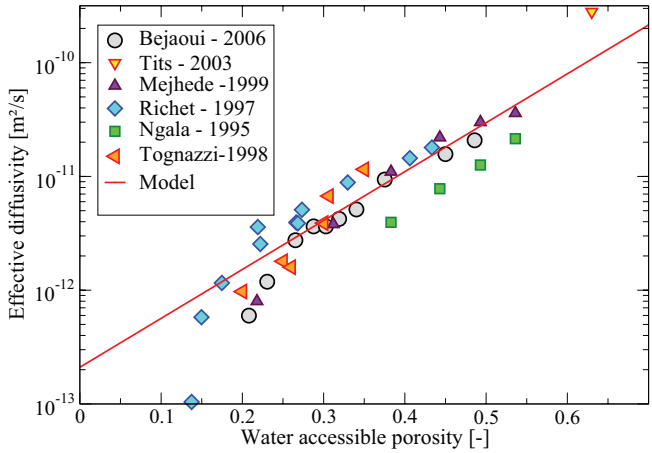

Figure 3.11: [Tognazzi, 1998] simulation against experimental data.

an example, the ratio between the pores and hydrates diffusivities, $D_{\text{C-S-H}}/D_{\text{poro}}$, vary between approximately 3×10^{-2} [Stora et al., 2008] to approximately 2×10^{-3} [Garboczi and Bentz, 1992].

Another feature that those model do not incorporate accurately is the percolation of the pore space (and the other phases). It is believed that for high w/c the diffusion is driven by the connected capillary pore network. However, as the w/c decreases, the capillary pores tend to close-up, and the diffusion occurs then mostly through the hydrates, that are now percolated. In between those extreme cases, diffusion occurs partly in one or the other phase, making the percolation threshold very important to define the frontier between the two diffusive modes. The same remarks are valid at the mortar / concrete scale when considering the ITZ.

In conclusion, the poor description of the geometrical features of such analytical models, and the experimental fitting for the phenomenological models, leads naturally to numerical explicit modeling of such materials, upon which diffusion numerical tests will be made.

6 Numerical homogenization

The need for numerical simulation was already introduced, and here we present some general points found in most of the numerical simulation studies, as well as few results. The main difficulties when modeling cementitious materials can be addressed as follow:

- The porosity sizes span in cementitious materials covers several orders of magnitude, from few nanometers up to a hundred of micrometer (for the CP scale).

3D simulation frameworks do not have yet the ability to reach discretizations thin enough to cover it.

- For very confined spaces, like in the C-S-H porosity, the ionic interaction and diffusion rules are modified, and their is no certainty on how to account for those modifications.
- Lastly, the contrast of material properties in cementitious materials is very high (when not infinite), and results yielded by various numerical approaches may diverge significantly.

The numerical investigation of hydrating cement pastes morphology (introduced in the first chapter) are rather recent, and their application to diffusion studies even more.

6.1 Literature review

Most of the numerical simulation for hardened cementitious materials consist in upscalling information, and thus bridging the gap between consecutive scales using "simple" diffusion tests (Fig. 3.12), used among other in [Stefan, 2009, Kamali-Bernard et al., 2009, Zhang et al., 2011, Abyaneh et al., 2013]. These types of simulations enter in the so-called family of sequenced multi-scale approaches. Such simulations are always undertaken with similar hypothesis: the pore space is saturated, there is no bulk motion of the water (no pressure gradient to generate a fluid flow), and most of the time only *effective* diffusion coefficient are assessed.

The principle is to consider a (cubic) sample, and realize three simulations (one per direction), by applying a constant macroscopic concentration gradient between two opposite side, and impose a null flux on the others. The solution of such problems results in the calculation of the ionic flux through the outer surface, from which is deduced the effective diffusivity.

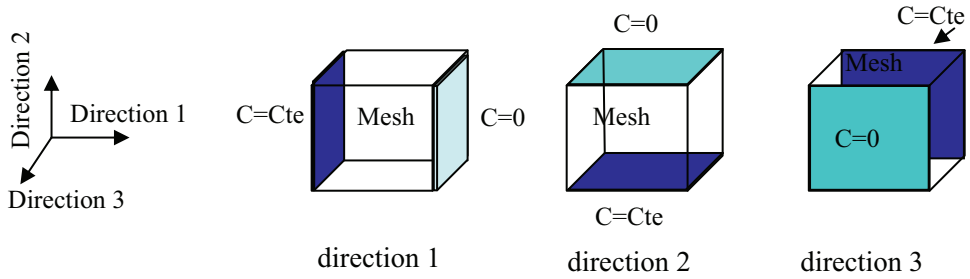

Figure 3.12: Three different boundary conditions used in simple diffusion tests ; boundaries with no concentration specification have a null flux condition – *adapted from* [Kamali-Bernard et al., 2009].

The results are averaged over the three directions. If the macroscopic response of the material is isotropic, the three directions will yield very similar results, and

it is possible to assume that the diffusion coefficient is a scalar. In a orthotropic case, the diffusivity can be described as a vector, with diffusion coefficients for each directions (one per direction / simulation).

Such methods can be applied in a consecutive manner to upscale information across consecutive scales, given a sufficient discretization of each scale domain.

Remark:
All the models relying on such sequenced multiscale framework have one common drawback when the smaller scales are considered. The input parameters have to be well understood and defined. For example, when modeling RVE of cement paste, a first approximation consists of three phase morphology, with unreacted cement (that do not diffuse), the pore space, where it is usually assumed that the diffusion coefficient is the one found in pure water ($\sim 1 \times 10^{-9}\,\mathrm{m^2\,s^{-1}}$), and lastly the hydrates. For this last phase, authors diverge on the value of the diffusion coefficient, ranging from $1 \times 10^{-12}\,\mathrm{m^2\,s^{-1}}$ to $1 \times 10^{-10}\,\mathrm{m^2\,s^{-1}}$, according to the determination method (homogenization, inverse analysis, RMN results, MD simulation *etc.*).

6.1.1 Hymostruc Framework

Based upon the hydration model introduced in Sect. 4.1.2 of the second chapter, Hymostruc-3D, several authors proposed frameworks to assess diffusion coefficients in cement pastes.

First using an underlying lattice model, [Zhang et al., 2011] discretized cement paste microstructures are used to estimate effective diffusivities for various w/c, according to the presented "simple" simulation tests. Results for a standard CEM-I cement paste are drawn Fig. 3.13.

To enhanced their simulations, [Zhang et al., 2012] used Lattice Boltzmann Methods (LBM) to study diffusion in non-saturated cement based materials. A first LBM simulation determine the water distribution in the pore space for a given RH, and then simulation are performed, still with LBM, to assess diffusivity in such microstructures. They found effective diffusivity for standard CEM-I mortar to range from $5.5 \times 10^{-12}\,\mathrm{m^2\,s^{-1}}$ to $20.2 \times 10^{-12}\,\mathrm{m^2\,s^{-1}}$ for corresponding saturation degrees between 53% and 100%. Their results highlight the influence of the saturation degree, as the results in terms of effective diffusivity differ by an order of magnitude.

Following, the same team ([Zhang et al., 2014a, Zhang et al., 2014b]) developed recently a mutliscale lattice Boltzmann-finite element modeling framework, where LBM is used as a micro solver to assess the diffusion coefficients in the cement paste and the ITZ, while the regular finite element method is used to solve the problem at the mortar and concrete scale.

6.1.2 Volume FEM approach

A similar approach to the present Ph.D. has been done based upon the work of [Stefan, 2009]. The cement paste description was achieved through a modified Jennings

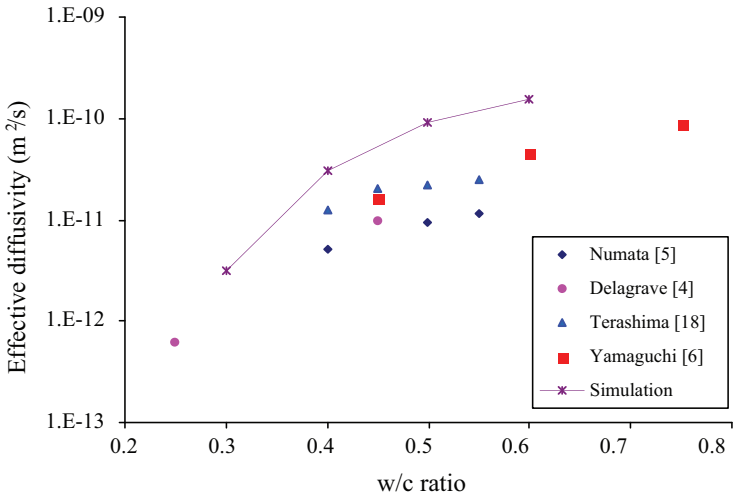

Figure 3.13: Influence of w/c on the effective diffusivity – *from* [Zhang et al., 2011]..

& Tennis hydration model, and the microstructure generation was randomly done on cubic meshes [Stefan et al., 2010].

Then, diffusion studies [Benboudjema, 2012] were done using Cast3m code and its thermal module. Some results are drawn Fig. 3.14, for various scenarios:

1. Diffusion occurs only in the capillary porosity, and $D_{\text{pores}} = 2 \times 10^{-9}\,\text{m}^2\,\text{s}^{-1}$,
2. Diffusion is allowed in the external hydrates (C-S-H), and $D_{\text{pores}} = 2 \times 10^{-9}\,\text{m}^2\,\text{s}^{-1}$, and $D_{\text{C-S-H}} = 10^{-2} \times D_{\text{pores}}$,
3. Same as number 2, with $D_{\text{C-S-H}} = 10^{-4} \times D_{\text{pores}}$,
4. Capillary and hydrates pores are considered as one phase, and $D_{\text{pore+C-S-H}}$ is estimated from a lower scale modeling approach proposed by [Caré and Hervé, 2004].

The prediction tendencies are rather good, with an excellent fit for the model 1-2-3 above 40% of water accessible porosity, which corresponds to a capillary driven diffusion. However, beneath the porosity threshold, the simulations diverge as none of those 3 simulation scenario have intrinsic information on the C-S-H structure. Only the last model incorporate such information, and it is the only one whose prediction are in in good agreement with experimental points for porosity below 0.4. In this area, the diffusion occurs mainly through the hydrate pores, and it is the only model to explicitly account for them.

Remarks:

For this last model, as for the previous one, it is the author belief that they

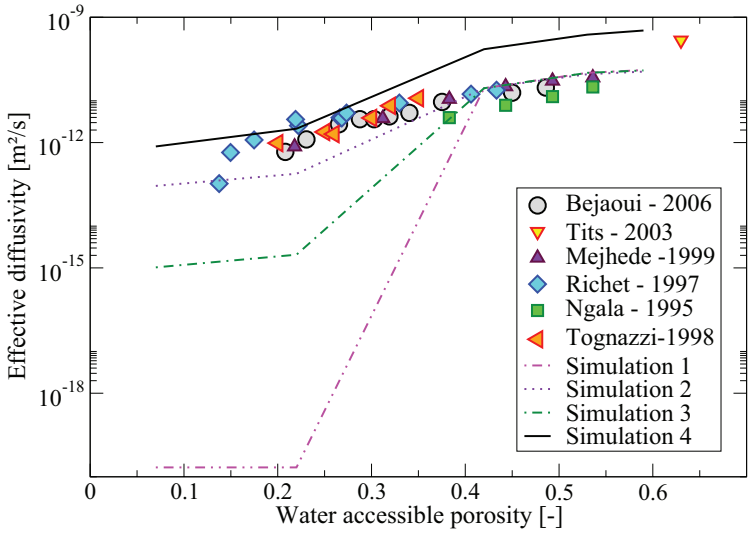

Figure 3.14: Influence of modeling approach – *from* [Benboudjema, 2012].

will never manage to properly express the complete span of pore size distributions found in cementitious materials, and thus will never be able to "simply" predict homogenized diffusion coefficients based on explicit heterogeneity representation.

Unless an innovative numerical framework is found that is able to handle morphologies with thinner discretization than 10^6 dofs, as well as the corresponding solver, additional intermediate scale(s) will have to be considered.

6.2 Multi-scale approach: Energy Based Framework

To avoid some simplification as well as macroscopic behavior hypothesis, a less simplified upscalling framework is introduced, where there is no assumptions whatsoever concerning the material response.

The choice has been made to use a energy based framework to upscale information. It ensures a proper scale separation, and is suitable for every scale. In Chap. 4 this framework will be used exactly the same way to upscale information through four scales. Such approaches have been used in several fields, from mechanics [Hill, 1963, Kanit et al., 2003, Benkemoun et al., 2010], to thermal conductivities assessments [Ostoja-Starzewski and Schulte, 1996, Jiang et al., 2002], or for a Darcy's fluid flows [Du and Ostoja-Starzewski, 2006].

Based on Fick's equations (re-written in Eq.3.25 in a tensorial form), we hereafter define ψ, the energy dissipation due to the diffusion process. Analogously to

thermal dissipation, the local energy dissipation is defined by Eq.3.26.

$$\begin{cases} \boldsymbol{J} = -\mathbb{D}_i \cdot \boldsymbol{\nabla} c \\ \dfrac{\partial c}{\partial t} + \mathrm{div}\boldsymbol{J} = 0 \end{cases} \tag{3.25}$$

where $\mathbb{D}_i$ is the local diffusivity matrix, $\boldsymbol{J}$ the flux vector, $\boldsymbol{\nabla}$ the gradient operator, and c the concentration of the diffusive specie.

$$-\psi = \frac{\boldsymbol{J} \cdot \boldsymbol{\nabla} c}{c} \tag{3.26}$$

The effective material properties are determined by subjecting a REV to boundary conditions satisfying Hill's energy criterion [Hill, 1963] which relates the microscopic energy and the mesoscopic one. For mechanical elasticity, it stipulates that for a REV, the spatial average of the local energy (Eq.3.26) must be equal to the upper scale energy computed with averaged fields. In our case that will mean that Eq.3.27 must be verified to be sure that the scale separation is large enough to be a REV:

$$\langle \boldsymbol{J} \cdot \boldsymbol{\nabla} c \rangle \overset{!}{=} \langle \boldsymbol{J} \rangle \cdot \langle \boldsymbol{\nabla} c \rangle, \tag{3.27}$$

where $\langle \bullet \rangle$ denotes volume average over a representative volume element.

In order to find boundary conditions which satisfies Hill's criterion, one have to introduce fluctuations $\breve{\bullet}$ of each field:

$$\begin{cases} \breve{\boldsymbol{J}} := \boldsymbol{J} - \langle \boldsymbol{J} \rangle \\ \breve{\boldsymbol{\nabla}} c := \boldsymbol{\nabla} c - \langle \boldsymbol{\nabla} c \rangle, \end{cases} \tag{3.28}$$

which by definition must vanish after averaging if the RVE is large enough:

$$\langle \breve{\boldsymbol{J}} \rangle \overset{!}{=} 0 \text{ and } \langle \breve{\boldsymbol{\nabla}} c \rangle \overset{!}{=} 0. \tag{3.29}$$

Combining the last 3 equations yields:

$$\begin{aligned} 0 &\overset{!}{=} \langle \boldsymbol{J} \cdot \boldsymbol{\nabla} c \rangle - \langle \boldsymbol{J} \rangle \cdot \langle \boldsymbol{\nabla} c \rangle \\ \Leftrightarrow 0 &= \langle (\boldsymbol{J} - \langle \boldsymbol{J} \rangle) \cdot (\boldsymbol{\nabla} c - \langle \boldsymbol{\nabla} c \rangle) \rangle \\ \Leftrightarrow 0 &= \langle \breve{\boldsymbol{J}} \cdot \breve{\boldsymbol{\nabla}} c \rangle. \end{aligned} \tag{3.30}$$

Then, since we want to compute this dissipation from surface values:

$$\begin{aligned} \langle \breve{\boldsymbol{J}} \cdot \breve{\boldsymbol{\nabla}} c \rangle &\overset{!}{=} 0 \\ &= \langle \boldsymbol{J} \cdot \boldsymbol{\nabla} c \rangle - \langle \boldsymbol{J} \rangle \cdot \langle \boldsymbol{\nabla} c \rangle \\ &= \frac{1}{V} \int_V (\boldsymbol{\nabla} c - \langle \boldsymbol{\nabla} c \rangle) (\boldsymbol{J} - \langle \boldsymbol{J} \rangle) \, dV. \end{aligned} \tag{3.31}$$

Using the conservation equation – $\mathrm{div}(\boldsymbol{J}) = 0$ – and the *Green*'s theorem:

$$\begin{aligned} 0 &= \frac{1}{V}\int_V \mathrm{div}\left\{\left(c - \langle \boldsymbol{\nabla} c\rangle \cdot \boldsymbol{x}\right)\left(\boldsymbol{J} - \langle \boldsymbol{J}\rangle\right)\right\} dV \\ &= \frac{1}{V}\int_\Gamma \left(c - \langle \boldsymbol{\nabla} c\rangle \cdot \boldsymbol{x}\right)\left(\boldsymbol{J}\cdot\boldsymbol{n} - \langle \boldsymbol{J}\rangle \cdot \boldsymbol{n}\right) d\Gamma. \end{aligned} \tag{3.32}$$

$$\langle \check{\boldsymbol{J}} \cdot \check{\boldsymbol{\nabla}} \boldsymbol{c}\rangle = 0 \Leftrightarrow \frac{1}{V}\int_\Gamma \left(c - \langle \boldsymbol{\nabla} c\rangle \cdot \boldsymbol{x}\right)\left(\boldsymbol{J}\cdot\boldsymbol{n} - \langle \boldsymbol{J}\rangle \cdot \boldsymbol{n}\right) d\Gamma = 0 \tag{3.33}$$

The trivial solutions of the Eq.3.33 are given by:

- $c = \langle \boldsymbol{\nabla} c\rangle \cdot \boldsymbol{x}$ on Γ: *Kinematic Uniform Boundary Condition* (*KUBC*), that may be called here the *Uniform Concentration Gradient* (UCG), which yields the tensor $\mathbb{D}^{\mathrm{K}}$,
- $\boldsymbol{J}\cdot\boldsymbol{n} = \langle \boldsymbol{J}\rangle \cdot \boldsymbol{n}$ on Γ: *Static Uniform Boundary conditions* (*SUBC*), that may be called here the *Uniform Particle Flux* (UPF), which yields the tensor $\mathbb{D}^{\mathrm{S}} = (\mathbb{P}^{\mathrm{S}})^{-1}$.

These UGC and UPF conditions will allow us to estimate respectively an upper and a lower bound of the property of interest. It can be shown ([Huet, 1990a], [Hazanov and Huet, 1994a]) that those bounds are tighter than Voigt and Reuss or Hashin-Shtrikman ones. In addition, as the studied microstructure size increases, those bound will converge to the effective properties of a REV. A full example will be shown in the next chapter. However, it is useful to note that the UGC boundary conditions seem more natural for such simulations, and it is easier to apprehend the notion of an imposed concentration on a heterogeneous surface than the notion of an imposed flux, especially when in presence of non-diffusive heterogeneities.

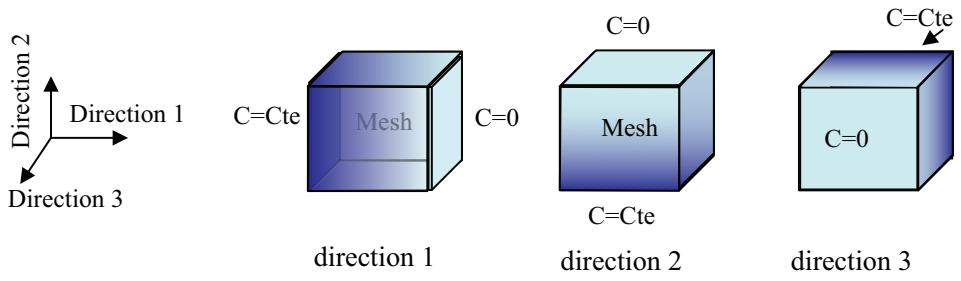

Figure 3.15: Three different boundary conditions used in KUBC diffusion tests (concentrations are prescribed on all sides).

7 Concluding remarks

In this chapter we introduced :

- Diffusion general principles, and application to porous materials,
- a particular emphasis on cementitious materials specificities in regards to diffusion,
- experimental protocols and results for cement pastes and mortar in terms of effective diffusivity,
- predictive approaches, based either on analytical / phenomenological / numerical homogenization,
- a multi-scale sequenced framework suited for cementitious materials in regards to diffusion.

With this last point, we will create a 4 level upscalling framework, from the C-S-H scale to the cement paste scale, and then to mortars and lastly concretes. The input / output parameters of the framework are listed Tab. 3.5. Each scale output (right column, framed), is used as an input the the following one.

Level	Input			Output
	Transport	Chemical	Mix-Design	(Numerical homogenization)
I: C-S-H matrix	$D_{\text{intra-C-S-H}}$	$f_{\text{poro C-S-H}}$		$\boxed{D^{\text{eq}}_{\text{C-S-H}}}$
II: Cement paste				
Clinker			PaSD_c	
C_3S	-	f_{C_3S}		
C_2S	-	f_{C_2S}		
C_3A	-	f_{C_3A}		
C_4AF	-	f_{C_4AF}		
C-S-H matrix	$\boxed{D^{\text{eq}}_{\text{C-S-H}}}$			
Water	D_{w}			
Other hydrates	-			$\boxed{D^{\text{eq}}_{\text{CP}}}$
III: Mortar				
CP-matrix	$\boxed{D^{\text{eq}}_{\text{CP}}}$		$f_{cp} = 1 - f_s$	
Sand ($\leq$5 mm)	-		f_s, PaSD_s	$\boxed{D^{\text{eq}}_{\text{M}}}$
IV: Concrete				
Mortar matrix	$\boxed{D^{\text{eq}}_{\text{M}}}$		$f_M = 1 - f_g$	
Aggregate ($\geq$5 mm)	-		f_s, PaSD_g	$\boxed{D^{\text{eq}}_{\text{C}}}$

Table 3.5: Input-output of the 4 level upscaling framework

4 Numerical approach and results

Contents

1 Introduction 126

2 Finite Element framework 126

2.1 Meshing process 126

2.2 Weak discontinuities 127

2.3 Implementation 128

3 Results 130

3.1 Study case 130

3.2 Mesh dependency 132

3.3 Initial step: the bulk C-S-H 133

3.4 Cement paste scale 143

3.5 Mortars 155

3.6 Concrete scale 161

1 Introduction

As an application of the overall framework, composed of the "scale separation + hydration + upscalling" parts, several studies at each scale found in cementitious materials are presented.

First, the numerical FE context is given, with non-adapted mesh methods, and properties "projection" allowing the conversion from the description to actual FE meshes. The interpolation between the two sides are made possible through an enhancement of the FE basis, allowing the elementary elements (truss elements or tetrahedron) to bear two material properties.

Emphasis is made on proper inputs for each scales, concerning both effective diffusion coefficients of the heterogeneities (*cf.* Chap. 3) as well as volume fractions (*cf.* Chap. 1). The main reason is that the sequenced multi-scale framework should be able, once the morphological inputs properly set, to forecast effective diffusion coefficients with only two inputs: the effective diffusion coefficient found in water at the C-S-H scale, and the effective diffusion coefficient found in capillary porosity.

Then, the several scales results are presented. At every scale, simulations are made to estimate the effective diffusion coefficients, along with sensibility studies to ensure a proper upscalling.

In addition, as certain results do not fall in the experimental expected ranges, some additional studies are done to attempt a forecast improvement in terms of effective diffusivities.

2 Finite Element framework

2.1 Meshing process

When dealing with heterogeneous materials at a (micro-) meso-scopic scale, the (two) three dimensional numerical representation of the latter is confronted to the meshing creation process. To deal with this representation issue, two main ways exist. The first, which may seem more natural, consists in a interface meshing, which demands that the position of the nodes is constrained by the actual geometry of the interfaces. Once all the interfaces are meshed, the rest of the volume is processed. This way, each node will be within a given phase, or at an interface, and thus all the elements between the nodes will be in one and only one phase. However, as we explained previously, most of our morphologies are supposed to evolve (hydration process), or require to be able to change parameters which means that at each step of the hydration we will need to re-mesh. This meshing process is very demanding in numerical resources, so this approach does not suits well the "evolutive" aspects of the morhologies.

The second method is the so-called *non-adapted meshes*, used in this study. The main idea here is that the nodes position is not constrained by anything related to the geometry of the modeled material. It can be seen as a "homogeneous" mesh

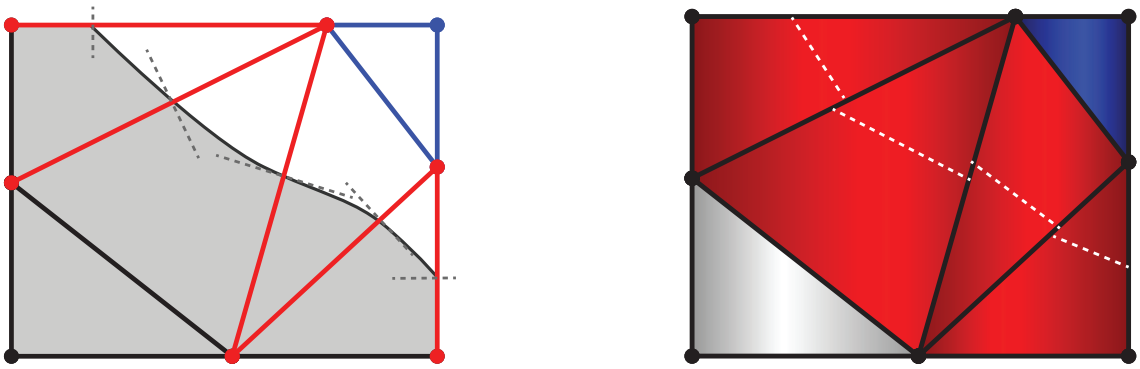

(a) Truss elements (b) Mesh elements

Figure 4.1: Non-adaptative meshes principle – 2-D morphological projection: application to truss and mesh elements.

with independent nodes. The geometrical interfaces will be projected onto and handled within the elements. Their definition will be done through a *morphological projection*. An example is shown in FIG. 4.1, for truss and mesh elements: in light grey the actual geometry of the material is shown, and superimposed, the nodes are placed randomly, and finally the elements that connect the nodes create our mesh. Hence, the cut elements (in red), will have to bear the geometrical information of the interface (the dotted normal), as well as be able to represent two material properties. Since they will have two different material properties, they will have flux field with a discontinuity at the interface, called in literature a weak discontinuity. This way, both geometrical and material properties are handled by the elements, and the nodes stay free of constraints. The meshing software, GMSH, used was developed by [Geuzaine and Remacle, 2009].

After introducing the meshing strategy (non adapted meshes), and the consequence on the "cut" elements (finite jump in the flux field: weak discontinuity),we will introduce the main methods which allow us numerically to take into account that discontinuity, first introduced by [Ortiz, 1987]. They all rely on a so-called kinematic enhancement of the FE basis.

2.2 Weak discontinuities

They are many ways of handling the discontinuities and introducing the weak discontinuity inside a non-adapted mesh. The two main families are described in the following.

- ***eXtended Finite-Element Method*: X-FEM**
  First, we can cite the eXtended Finite Element Methods (X-FEM) [Moës et al., 1999], which when coupled to a level set method allows [Moës et al., 2003, Sukumar et al., 1999] to model two phase materials in two and three dimensions. The X-FEM method rely on a combination of the classical FE

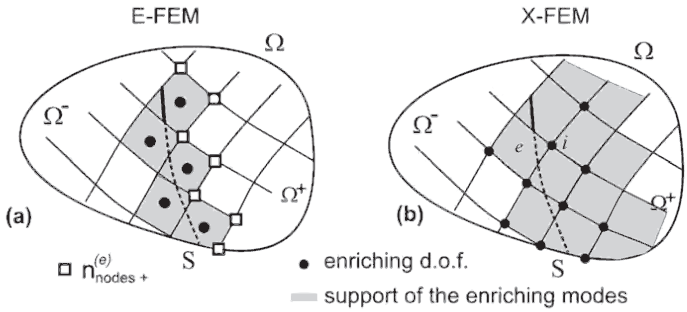

Figure 4.2: Nodal and elemental enrichments – *from* [Oliver et al., 2006].

methods and on the Partition of Unity method. The classical FE space is enriched by supplementary degrees of freedom at the nodes. The support of the enriched nodes is cut by an interface with associated enriched functions (see FIG. 4.2(b)). For more details about the enriched function, please refer to previous references.

- ***Embebbed Finite-Element Method*: E-FEM**
  The second main way to deal with the discontinuities is the Embedded Finite-Element Method (E-FEM) [Ortiz, 1987]. It allows to authors like [Hautefeuille et al., 2009, Benkemoun et al., 2010, Roubin, 2013] to model two phase materials in respectively two and three dimensions. Again, this method rely on the classical FE Methods and the Partition of the Unity. This time the classical FE space is enriched not at the nodes, but in the elements themselves, which are cut by an interface with enriched functions associated (see FIG. 4.2(a)). The main advantage of this approach is the total separation of the flux field in a global part (same as for a "conventional" FE problem) and a local part (enriched), which allows to locally determine the local unknown added.

Comparative studies on those two types of approaches have not investigated extensively, however [Oliver et al., 2006] recently exhaustively reviewed specific study cases, giving a modest advantage to the E-FEM approaches in terms of computation time. This last point lead us to keep the E-FEM approach based on the beforehand assumption that fine discretizations will be needed to properly describe the morphological features of cement based materials. In addition, the present PhD is in line with previous doctoral research undertaken at the *LMT-Cachan* [Benkemoun, 2010, Roubin, 2013, Jourdain, 2014], developing this methods.

2.3 Implementation

From a theoretical point of view, this framework follows the Ph.D. work of D. Markovic where Constant Strain Triangles (CST) were considered [Markovic et al., 2005] ; and from a numerical point of view it follows two other Ph.D. from N.

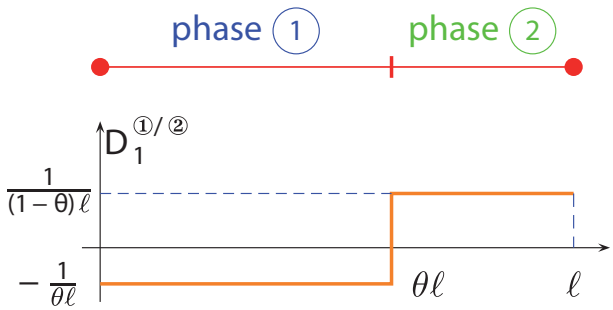

Figure 4.3: Weak discontinuity for a bi-phase 1D element – *from* [Benkemoun et al., 2010].

Benkemoun and E. Roubin at the *LMT-Cachan* for a three dimensional discretization of heterogeneous media by means of spatial lattices [Benkemoun et al., 2010] and spatial meshes [Roubin, 2013].

2.3.1 Truss Elements

To be able to bear two different material properties, the truss elements that are cut (in red Fig. 4.1(a), with the grey normal), the weak discontinuity enhancement for an element of length l, with a normal defined by the θ parameter is drawn Fig. 4.3.

2.3.2 Volume Elements

Following the work of [Roubin, 2013], the following volume finite element were used.

The representation of the enrichment function in 3D being not easy, one can only notice that instead of having a unique parameter θ as previously to separate the element, but the normal vector is needed $\boldsymbol{n}$ (Fig. 4.4(a).

Since the element can represent two different materials, it will have two different material properties (respectively for $(+)$ side, the matrix for instance, and the $(-)$ part as the inclusion). Since in the overall element we need to have a continuous flux, we will enhance the concentration gradient field. This way, along the interface we will have normal flux continuity between the two phases.

In the spirit of maintaining the development of a code build upon numerous Ph.D.'s (2008 – 2014), and developing further the available methods, the CoFeap [Kasiotis and Hautefeuille, 2008] module of the FE code Feap [Taylor, 2003] is used to solve mechanical, thermal and chemical problems, using CTL [Niekamp, 1995] as a middleware. This particular set of programs is justified by the non-intrusive implementation of E-FEM fitting in Feap's architecture.

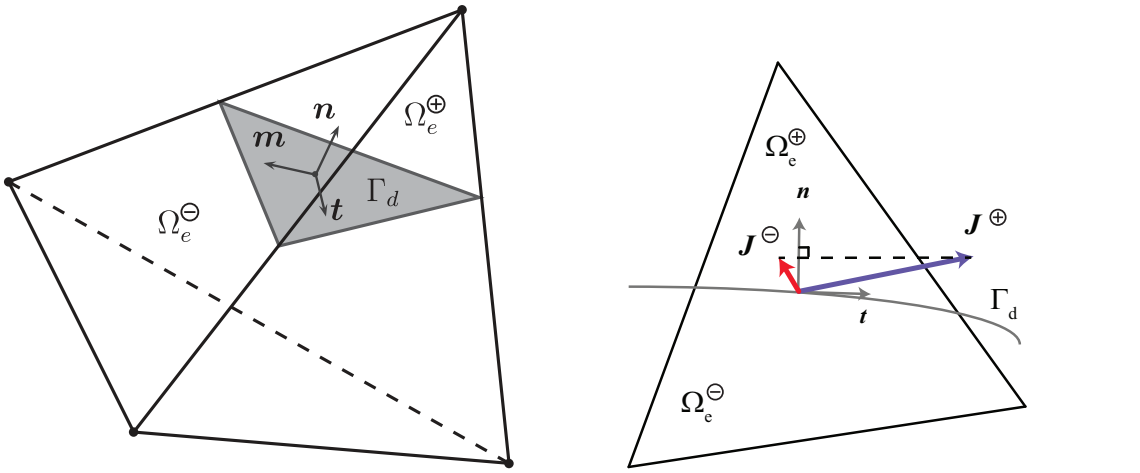

(a) Weak discontinuity for a bi-phase 3D element – *from* [Roubin, 2013].

(b) Two dimensional representation of the enrichment condition.

Figure 4.4: 3D E-FEM enhancement principle.

3 Results

3.1 Study case

A first validation of the simulation framework is done by comparing numerical results to an analytic solution in a trivial model case. A cube is considered with a single spherical inclusion placed at its center, according to Fig. 4.5(a). As an input, traditional values found in cement paste simulation where used: the matrix was assigned a diffusion coefficient of $D_{\mathrm{m}} = 2 \times 10^{-9}\,\mathrm{m^2\,s^{-1}}$ (similar the the diffusion coefficient in pure water of most ionic species), and the inclusion was assigned $D_{\mathrm{i}} = 2 \times 10^{-12}\,\mathrm{m^2\,s^{-1}}$ (as a traditional value found in literature for the C-S-H phase). The size units are arbitrary, and the modeled cube is considered to be of size $T = 100$, and the sphere size grows from 0 to 80.

Results are drawn Fig. 4.5(b). Up to a sphere radius of 50, the numerical simulation and MT scheme yield the exact same results (errors are lower than 1%), which was expected from the MT schemes hypothesis. A small divergence can be observed as the radius keep increasing, up to 15% of error for a radius of 80. This small discrepancies were also expected, as in this radii span, the MT scheme hypothesis are not respected any more (predominance of the inclusion phase instead of the matrix one).

Fig. 4.6 displays the same data scaled according to the volume fraction. The fit between the numerical sphere simulation (black dashed line) and the MT scheme (red dashed line). On the same figure, an additional set of simulations is displayed. By taking a morphology "cement paste like" (*cf.* Chap. 3, Sect. 4.3.2, with three distinct correlation lengths), and thresholding it, morphologies with growing fraction are created. They are then projected onto an unstructured mesh with 4×10^5 dofs

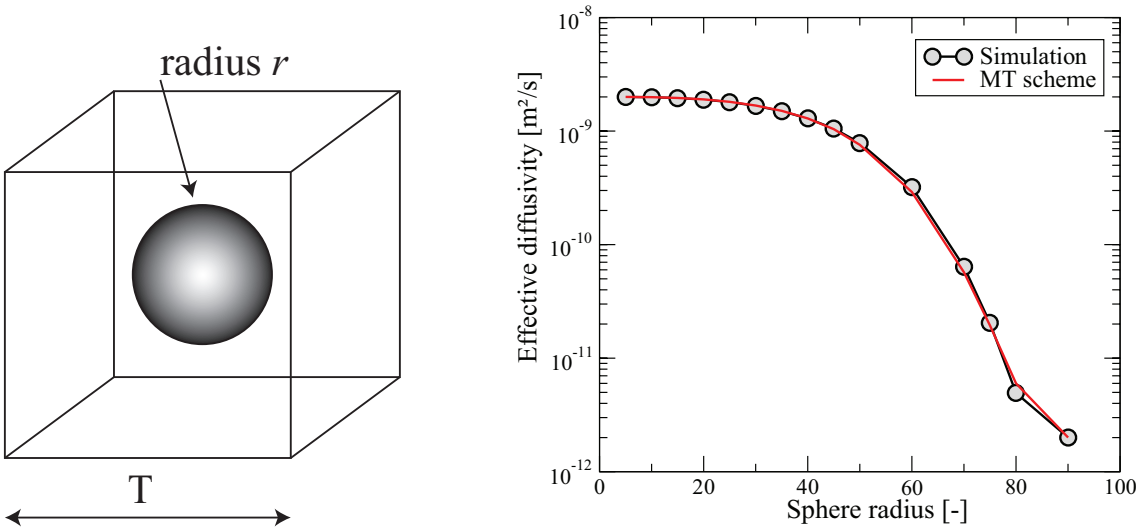

(a) Model case, $T = 100$, $r \in (0; 80)$.

(b) Results in terms of effective diffusivity.

Figure 4.5: Simulation validation.

(the same mesh is kept all along to only characterize one phenomenon, and 11 realizations of the same excursion are generated, and the results displayed are averaged, with the 99% CI). For small volume fractions, the simulation results yields the same results as the sphere simulation, or the MT analytic scheme. Over 20% of volume fraction, the discrepancy increase, and this is due to the growing inclusions which start to coalesce, and percolate. At this point, none of the MT scheme hypothesis are respected any more, as this scheme do not take into account the interaction between inclusions.

The far right end of the excursion sets morphologies results needs additional explanations. The plateau observed from 85% of volume fraction up to 95% is most probably due to the lack of proper material representation on the FE mesh. As the porosity decreases, its size follow the same tendencies. At a critical point, the mesh used for this study was not fine enough, and even though the morphological description can be as fine as possible, the projection stage induce a loss of information if the element sizes are too coarse to capture the fine geometrical evolutions. Lastly, after the plateau, the simulations results drops to $2 \times 10^{-12}\,\mathrm{m^2\,s^{-1}}$. As previously, even if the morphological description bear few percent of porosity, the projection stage tends to homogenized the final material representation on the FE mesh, and thus generate only a bulk matrix with no voids.

This also support the use of a unique mesh across a single study, and even though for low volume fractions the fineness can be excessive, it is required for higher ones. This issue arise typically when studying a hydrating cement paste. In light of those conclusions, the next section addresses precisely this issue, with the choice of meshes according to the volume fraction span.

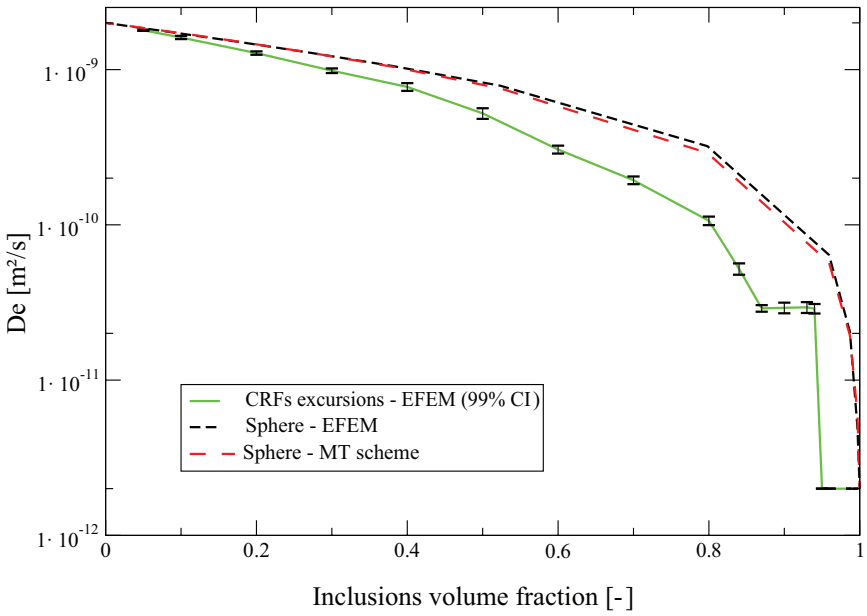

Figure 4.6: Morphological influence: Sphere vs. Excursion sets.

3.2 Mesh dependency

Using the same material properties as previously, various morphologies are now created with various targeted volume fraction. They are completely random, realized with unions of three CRFs. The realizations are generated with a RF discretization of 27×10^6 dofs. The realizations are then projected on various meshes, ranging from 7×10^3 dofs to 2×10^6 dofs. A unique morphology is used for each targeted volume fraction — as the morphological RVE for volume fraction was already defined and it has been established (Sect. 2.4) that the morphological variability is very low — to only focus on the mesh dependence.

An example of a realization with various volume fractions is drawn Fig. 4.7.

After the projection step, those morphologies are submitted to an imposed concentration gradient boundary condition and the effective diffusivity is derived. Results are reported in Fig. 4.8. It can be seen that for low volume fraction, the results yielded with coarse discretizations converge almost instantly to an asymptotic value. It can be understood in the sense that a low volume fraction of inclusions is represented well even with few FE elements, and despite the fact that the geometrical features are not well represented, the targeted volume fraction is rapidly reached. On the other hand, for high volume fraction (85% for example), the effective diffusivity increases first, which reflects the fact that coarse discretization, this time, do not capture most of the diffusive phase, and only at thinner discretization — when the FEM elements are able to follow the geometry — the morphology is well represented. Contrary to the previous case, since the diffusion occurs mainly in the sparse matrix, thinner discretization are needed to capture it.

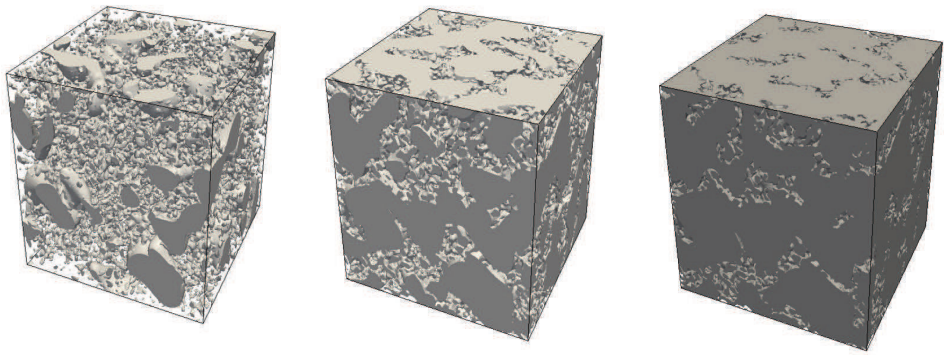

(a) Inclusions

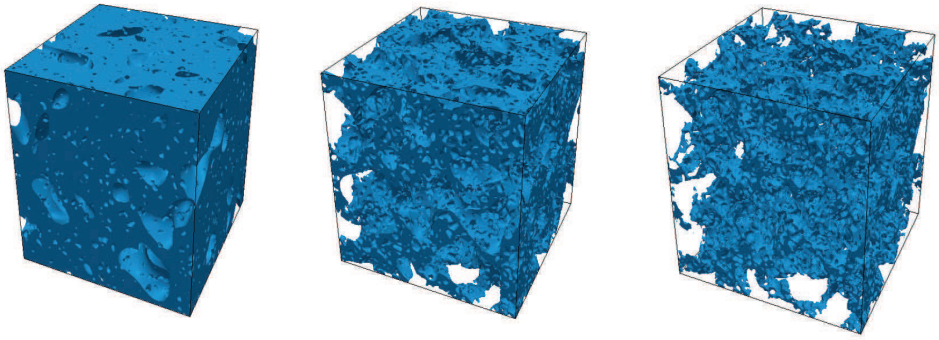

(b) Matrix

Figure 4.7: Morphologies at 23%, 67% and 85% of inclusions volume fraction – size T=100.

This mesh dependency study supports for the E-FEM numerical implementation since steady results are observed FE discretizations below the RF discretizations. At 1×10^6 dofs, the three series of calculation converge significantly below the RF 27×10^6 dofs.

In light of this study, meshes up to 1×10^6 dofs will be used in the following studies. It should be reminded here that this "limit" is set in a general fashion, but as inclusions or porosity sizes become too small, higher discretizations may be needed. It emphasizes again the need of proper scale separations for numerical purposes.

3.3 Initial step: the bulk C-S-H

As it has been described previously, due to a number of uncertainty regarding material properties, the choice has been made to model the elementary block of a hardened cement paste: the C-S-H gel. The aim is to predict the effective diffusivity of a sound nano-structure. The geometrical supposed description at this scale was draw in the first chapter. A short summary is reminded:

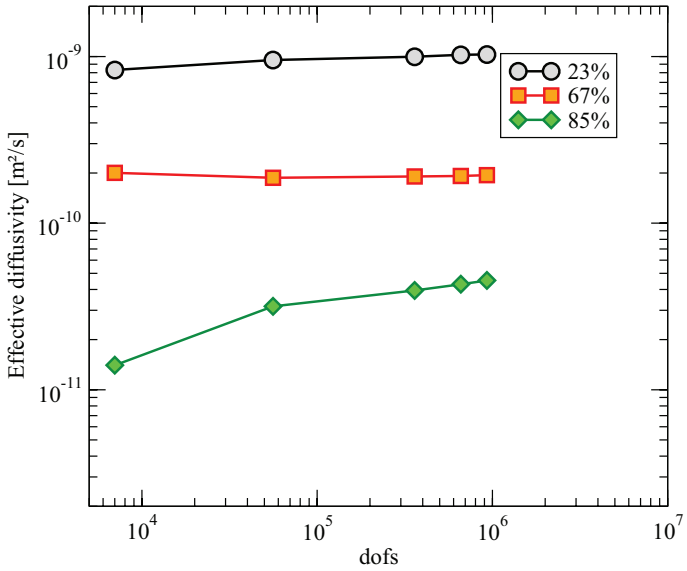

Figure 4.8: Mesh dependencie, according to the modeled volume fraction.

- The relative independence of the C-S-H structure over mix design parameters allows for its separate modeling,
- Two main pore modes are to consider, around 1.8 nm and around 4 nm to 7 nm in **radii**, which — as is has been suggested by RMN studies and MD simulations — do not connect.

3.3.1 C-S-H porosity

The chosen hydration model (Chap. 1, Sect. 4.2) imposes the porosity of the C-S-H phase. It is set to 21.9% (Eq.1.4), and this value has been assessed by measuring differences in specific volumes between saturated C-S-H and D-dried C-S-H [Jennings and Tennis, 1994]. The same authors proposed few years later [Tennis and Jennings, 2000] a refined model with two types of C-S-H, each with its own porosity. Since we only model one type of C-S-H, the original value has been kept. The constant ratio proposed, hydration degree - independent, has been already proposed by [Powers and Brownyard, 1947], and experimentaly verified in [Baroghel Bouny, 1994]. However, despite the constant ratio, the former model predicts a porosity of 28%, and the latter rather around 18%. Other authors considered a porosity of 35% [Masoero et al., 2014], corresponding to Jennings colloid model of C-S-H model. Additional work by [Olson and Jennings, 2001] had the same conclusions but with a 25% porosity. Lastly, experimental work by [Baroghel-Bouny, 2007a] showed a C-S-H porosity in the vicinity of 20%, or just under for some cement pastes with mineral additions.

For the sake of the framework, the original value of the hydration model is kept here, as the total C-S-H porosity, but additional calculations where made to cover the span of the various models porosities.

3.3.2 Pore size distribution

The pore mode found at this thin scale are briefly reminded here, they follow the more extended presentation of the first chapter.

Recent RMN results [Korb, 2010] has shown that the small pores do not connect with the bigger ones, and thus do not participate in a significant way to the diffusion process (or at best as a second order contribution).

Consequently, we suppose that the pore volume fraction is fully distributed at a unique **radius** size of $\phi_{inter} \approx 4\,\text{nm}$ to $5\,\text{nm}$. This hypothesis did not seem to strong, since the pore volume fraction dictated by Jennings & Tennis original model was deduced from specific volumes measurements on saturated and D-dried C-S-H, which does not remove the intra-layer pore content.

In addition, the chosen pore volume fraction is above the percolation threshold, which will ensure the connectivity of the pore phase.

3.3.3 Morphologies

The morphological modeling framework that has been introduced in Chap. 2 allows to yield morphologies with randomly shaped inclusions, and as the thresholds evolves, those inclusions starts to enlarge until they connect, and finally an "opposite" morphology arise with randomly shaped voids that are disconnected (if the thresholds evolves far enough). On either sides, voids or inclusions will be rather isotropic, in the sense that their evolution will follow the isotropic CRF. Here, to follow at least qualitatively the actual C-S-H morphology (with either model, Feldman & Serada or Jennings), a "layered" porosity is preferable.

Based on a qualitative study, unions of CRFs are used, but with similar parameters. Introduced to be able to model various sizes at higher scales, this technique allows also in the present case to yield more "rough" morphologies, as each RF "penetrates" the other when their parameters are in the same vicinity (L_c and σ). When the L_c are close, the size distribution stays narrow. However, by changing the CRF variances, it is possible to shape the pore network according to one dominant mode (the high variance RF, *i.e.* high "peaks" and "valley", Fig. 4.9(a)). The other CRF excursions, with smaller variances will only contribute to the general shape in a second order proportion. Their role is mostly to "disturb" locally the overall shape (smaller variances is to be seen as smaller "peaks / valley", Fig. 4.9(b)4.9(c)), and thus increase the tortuosity of the network. The overall pore network stays monomodal Fig. 4.9(d).

A qualitative study led to the choice of a set of parameters allowing to create morphologies (CRFs correlation length, mean, variance as well as the threshold), and they were validated accordingly through the PoSD (see Fig. 4.10(d)). The final parameter-set unfold as follow:

- A maximal size of micro-structure of 500 nm will be considered (the RVE definition will be partially done in respect to diffusion properties, in addition

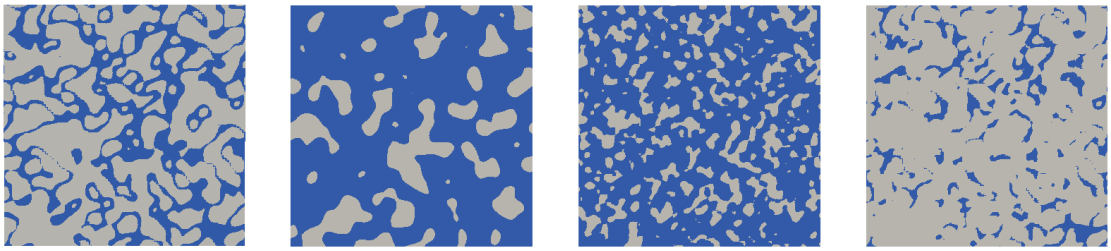

(a) 1st mode: $\sigma = 3$ (b) "perturbation field" 1, $\sigma = 1$ (c) "perturbation field" 2, $\sigma = 1$ (d) Union

Figure 4.9: C-S-H modeling principle – T =500 nm, $u = 2.5$ (arbitrary, for illustration purposes).

to the previous morphological and percolation RVE defined in Chap. 2).

- The excursion are yielded using a union of three CRFs, with correlation lengths (and respective variances) in the range $L_c^1 = 25$ ($\sigma_1 = 1$), $L_c^2 = 20$ ($\sigma_2 = 3$) and $L_c^3 = 10$ ($\sigma_3 = 1$).
- Since we intend to model and simulate morphologies with various pore volume fraction, the thresholds have to be determined for the span of porosities from 10% to 35%. Since the variances are not unitary, and more peculiarly different for every RF, the relation linking the union's volume fraction to the threshold is not as trivial as in Sys.2.36. The explicit relation is not given for simplicity's sake, but it is obtained using Eq.2.32 without the presented simplifications.

An example of resulting morphology is provided Fig. 4.10, and the characterization of such a realization is drawn Fig. 4.10(c) and 4.10(d) in terms of pore volume fraction (both cumulative and distribution).

The actual volume fraction predicted by the hydration model is 0.219. However, in this study, a span of C-S-H porosity is assessed, ranging from 0.1 to 0.35 to cover the all the models described in the first chapter.

3.3.4 Effective properties

It has been proven that at such thin scale, the diffusion phenomena are disrupt from the the ideal semi-infinite case, and that in such confined space, the surface interactions play an increasing role. As mentioned in the first chapter, the diffusion coefficient in the C-S-H's pore space is one order of magnitude lower than expected in pure water (D_{water} =$2 \times 10^{-9}\,\text{m}^2\,\text{s}^{-1}$), and is considered to be $D_{\text{inter C-S-H}}$ =$4 \times 10^{-10}\,\text{m}^2\,\text{s}^{-1}$ [Korb, 2010]. This value is used in the following as the **only** material **input** of the model, as detailed in Tab. 3.5 *(given the total volume fraction of porosity and pore size span of the previous paragraph).*

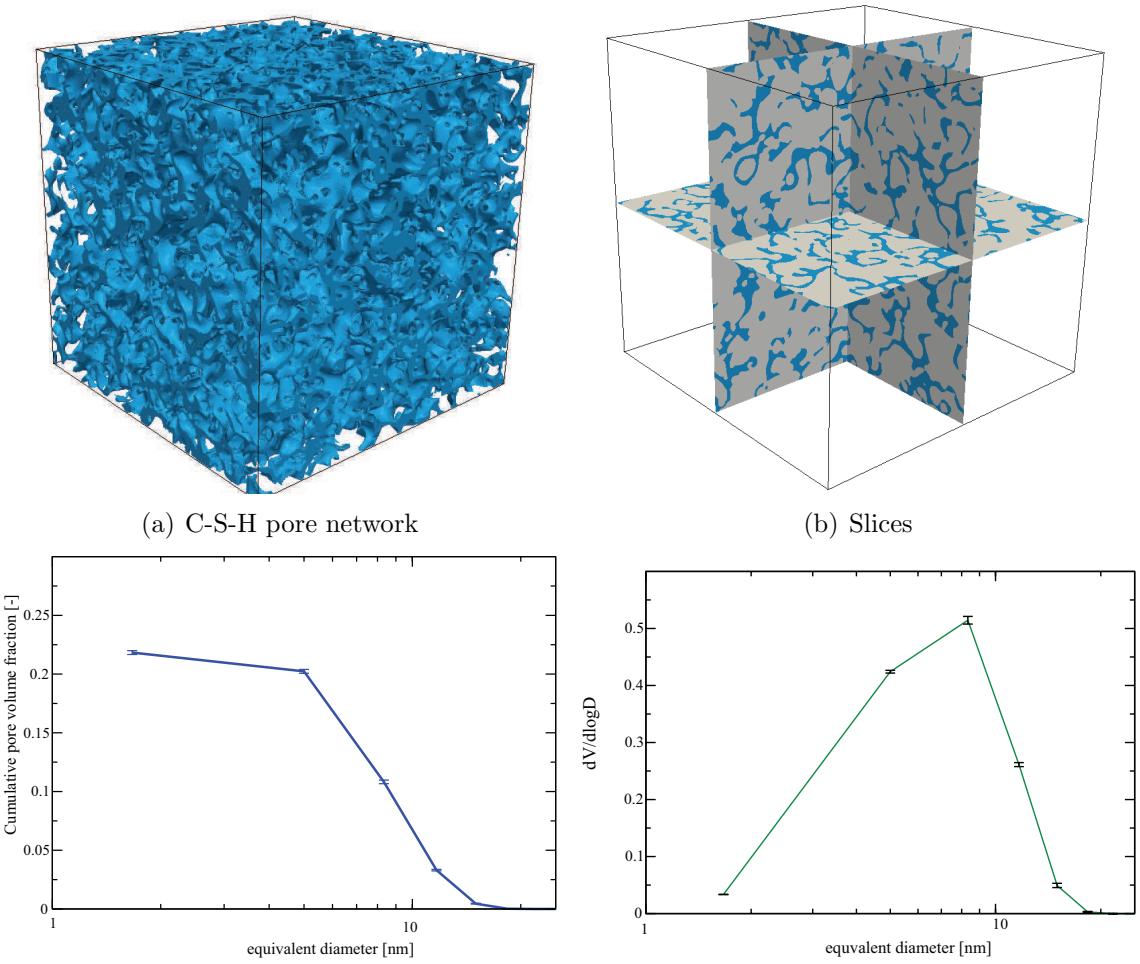

(a) C-S-H pore network

(b) Slices

(c) Cumulative pore volume fraction

(d) Pore sizes distribution

Figure 4.10: C-S-H modeling and characterization — 21.9% porosity – simulation of $500 \times 500 \times 500$ nm, with a discretization of 1.42nm/vox.

For this first scale of the framework, as the predominant phase reaches high volume fractions (up to 90% of bulk), and the diffusion coefficient ratio in-between the two phases is infinite, an additional convergence test has been done to confirm the choice of mesh fineness. A typical C-S-H morphology was generated (a cube of side size T =500 nm, with a discretization of 1.42 nm vox^{-1}), and projected on meshes with an increasing number of dofs (ranging from 10×10^3 dofs to 4×10^6 dofs). The results are drawn Fig. 4.11, with the 99% CI for 1 realization, based on five experiments. At first, for very coarse discretization none of the relevant information is captured by the FE mesh, and only a lower bound of the expected value is computed, but past 2×10^4 dofs the effective response (in terms of effective diffusion coefficients) increases as more and more morphological details are taken into account. However, an expected plateau is not reached for increasing *dofs*. But higher discretizations were hardly possible numerically speaking, and so a maximal fineness of 1×10^6 dofs is kept throughout this study.

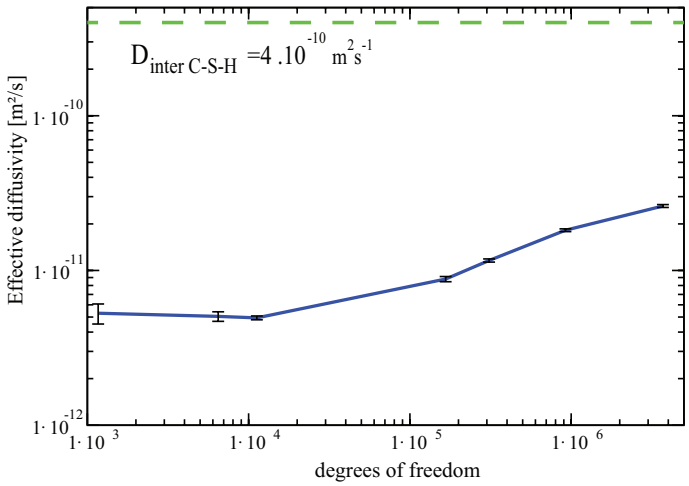

Figure 4.11: Mesh dependency at the C-S-H scale.

As discussed in the previous chapters, the more "natural" boundary condition that can be applied are the KUBC ones, otherwise known as UCG. Examples of C-S-H microstructures submitted to such boundary conditions are shown Fig. 3.3.4.

Final results in terms of effective diffusion coefficient for the C-S-H phase are presented on Fig. 4.13, according to the volume fraction of porosity considered.

The actual volume fraction assessed by the hydration model is 0.219. For the hydration model predicted porosity, the effective diffusion coefficient is assessed at $D^{\text{eff}}_{\text{C-S-H}}$ =1.94×10^{-11} m^2 s^{-1}. It is one order of magnitude than the "traditional" numeric values used in the literature, but as it has been discussed in the third chapter, the input value for the diffusion at those thin scales was also taken one order of magnitude higher.

In addition to the effective diffusivity coefficient, the 95% CI are drown for a set of 10 calculations. They exhibit an interesting feature, as the variability of the

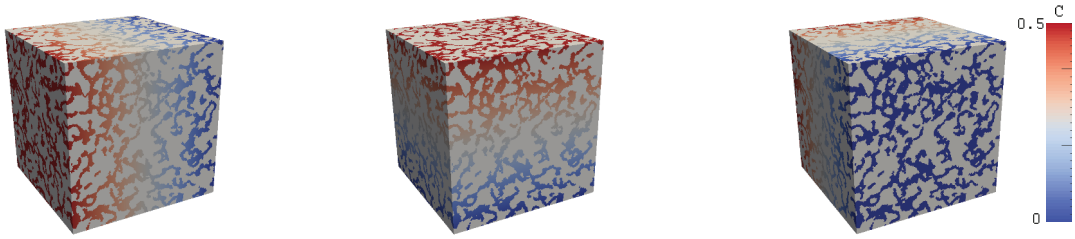

(a) X direction (b) Y direction (c) Z direction

Figure 4.12: Imposed macroscopic gradient of concentration – simulation of V =0.125 µm^3 (T=0.5 µm with 9.2×10^5 dofs).

results increases in the vicinity of the percolation threshold (18%).

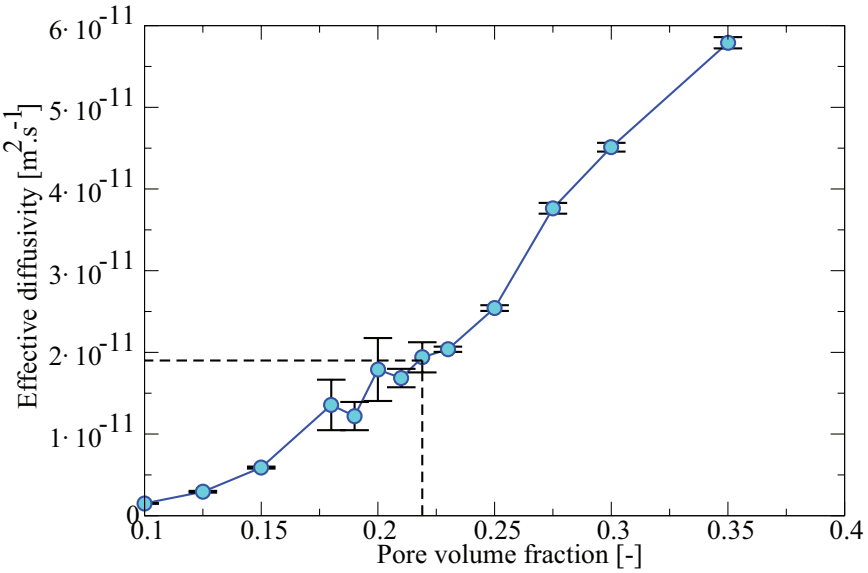

Figure 4.13: C-S-H effective diffusivity – results averaged over 10 realizations, with 99% CI.

In addition at this first scale, the numerically homogenized results are compared to few analytic homogenization schemes previously mentioned, with the *Voight-Reuss* bounds, the *Hashin-Shtrikmann* bounds, and then with *Mori-Tanaka*'s scheme as well as with the *Self-Consistent* one. It should be noted that the diffusion coefficient contrast between the porosity and the bulk matrix of C-S-H is infinite in theory, but for the sake of the analytic comparison, the bulk matrix was assigned a diffusion coefficient $D_{\text{matrix}} = 10^{-9} D_{\text{inter C-S-H}}$. The results are displayed in Fig. 4.14.

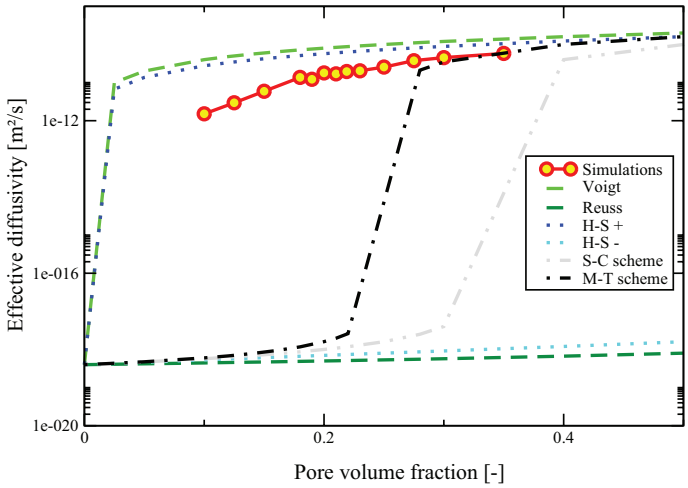

Figure 4.14: Simulations *versus* analytic schemes (estimation with spherical incluions) and bounds.

It can be seen that the numerically homogenized effective properties lie between the bounds, and rather close to the upper ones. However, the homogenization schemes do not yield appropriate results, due to the high contrast in material properties (herein infinite) and the inclusion phase rather far from the scheme's geometrical hypothesis.

Additional implementation:

For the sake of the framework, and to compare the presented numerical framework to other existing ones, an additional convergence test towards a new RVE definition is presented.

In this implementation, the use of the commercial code Cast3m was chosen, with the use of classical volume elements (8 node cubic FE). The morphological discretization was directly transferred onto a regular cubic volume FE mesh. The boundary conditions applied here reflects the two possible ones described in the previous chapter, known as UPF and UCG boundary conditions.

Example of C-S-H microstructures are presented on Fig. 4.15, with a constant discretization of $3\,\mathrm{nm\,pix^{-1}}$.

The results are presented below (Fig. 4.16 for a set of realizations. The number of realizations is low due to a time consuming mesh creation process, to "translate" the morphological phases description into a cubic Cast3m FE mesh. Mean value are presented over 5 simulations, along with the 95% CI. The UCG values stabilize fast, and very little variation in terms of mean value is observed. At the opposite, for the UPG boundary conditions, the values of effective diffusivity starts three orders of magnitude lower, and slowly increases by one. Theoretically it should be increasing until the CI of the two boundary conditions overlap, but it seems in the type of cases the the RVE are of gigantic sizes [Dirrenberger et al., 2014], not reachable due

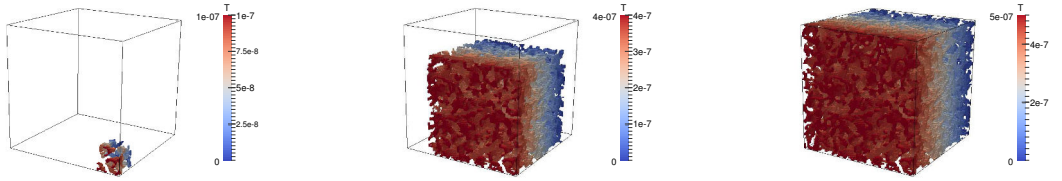

(a) Side size $T = 100$ nm (b) Side size $T = 400$ nm (c) Side size $T = 500$ nm

Figure 4.15: Increasing volume for CAST3M simulations.

to numerical resources.

In [Kanit et al., 2003], similar results are shown, for thermal studies with a two phase materials with a contrast of $c = 100$ in terms thermal conductivities, the UGC boundary conditions (as the Periodic ones, not introduced in this work), converge very fast and do not vary much as the size increases, as compared to the UPF boundary. For those reasons, only the first type of boundary condition will be considered in the following.

Numerical complexity:

The computational cost in terms of execution times is presented on FIG. 4.17. The simulations were made on the same node of a calculator, with 8 processors and 32Go of RAM memory. No particular effort were made towards parallelization, however, the FEAP and CAST3M may parallelize some routines or sub-routines internally, with no control over it. The obvious difference in terms of execution time is most probably due to the FE code architecture, as CAST3M is a multi-physics code, with many "modules" and "toolboxes", not always optimized. On the other hand, the FEAP architecture is rather standard, but the *Object Oriented Programming*, as well as the *Component Template Libraries* allow to call only required "modules", and thus avoid all unnecessary computational allocations. It should be noted that for both approaches, the so-called "projection stage" is not accounted, as in both approaches it is a time consuming step, of approximately equal duration.

The programs complexity is described hereafter according to its asymptotic behavior:

- FEAP + COFEAP + CTL + E-FEM : $\mathcal{O}(n)$,
- CAST3M + FEM : $\mathcal{O}(n^2)$.

However, it is not to mistake as a comparative study of the type of FE, but rather as global indicator of the "FE method + software + solver" performances. So it does not specifically comfort the choice of elemental enrichment, but rather the overall choice of simulation framework.

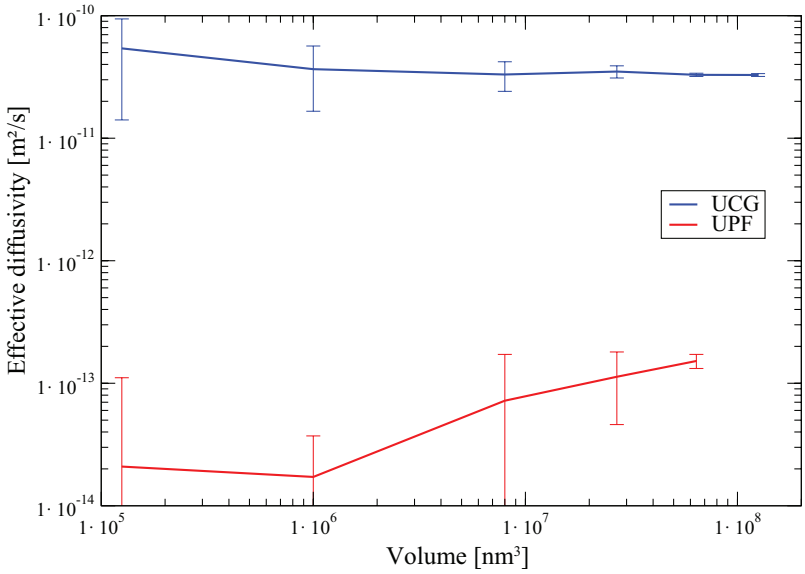

Figure 4.16: Dispersion and mean value of the effective diffusion coefficient, function of the domain size for two different boundary conditions.

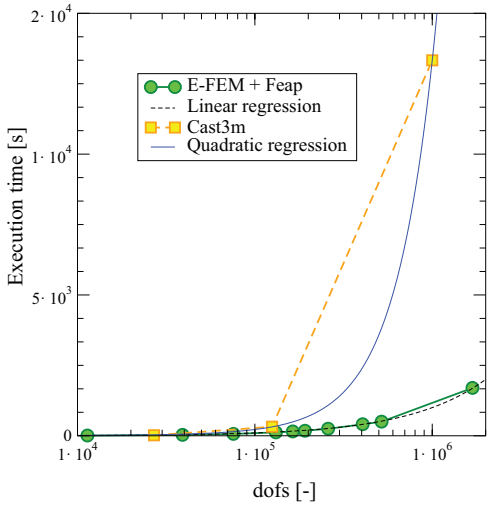

Figure 4.17: Complexity analysis.

Notes:

The numerical value evaluated for the C-S-H is now $D_{\text{C-S-H}} = 1.94 \times 10^{-11}\,\text{m}^2\,\text{s}^{-1}$.

It is one order of magnitude higher than usual values found in the literature (usually around $2 \times 10^{-12}\,m^2\,s^{-1}$, *e.g.* $5.1 \times 10^{-12}\,m^2\,s^{-1}$ in [Zhang et al., 2011] — obtained by analytical homogenization — or $2.24 \times 10^{-12}\,m^2\,s^{-1}$ in [Kamali-Bernard et al., 2009] obtained by back-fitting numerical results). Few of our simulation hypothesis may explained this discrepancy. First the use of the first Fick's law is probably debatable, but since we take as an input an actual value for this type of very thin scale, the assumption did not seem strong. Secondly, and most importantly, the morphological (experimental) description of this scale is still based upon several assumptions, which has never been fully verified. Very recent results by [Taylor et al., 2015] showed – with TEM Nanotomography – a tubular network of pores, which do not agree with the established models.

3.4 Cement paste scale

At this key scale for cementitious materials, more attention is drawn to the evolution of properties through time, as most of the resulting concrete properties take origin at this scale. Indeed, the cement paste is to be seen as the matrix that holds together the inclusions of higher scales (sand and aggregates).

3.4.1 Initial morphologies parameters and hydration

As a main subject of studies, a standard CEM-I cement paste will be considered (cement's composition is listed in Tab. 2.4). The initial morphology is defined through the cement PaSD, and the initial mix-design parameters.

The initial morphologies are generated to represent a standard CEM-I cement paste, with the grading curve presented in the first chapter (Fig. 1.2), as well as the RVE consideration presented in the second chapter to limit the side effects. For mesostructure in the size of T =100 µm, the CRFs parameters are first set to the one introduced in the second chapter, Sect. 4.3.2. This choice of parameters do not allow to model the larger cement particles expected to be found in fresh cement paste, as the bigger cement particles are in the same size's vicinity as the RVE.

As inputs at this scale, in a first attempt the diffusion coefficient follow first the previous results with $D_{\text{C-S-H}} = 1.9 \times 10^{-11}\,m^2\,s^{-1}$, and for the liquid fully filling the pore space, a diffusion coefficient of $D_{\text{poro}} = 2 \times 10^{-9}\,m^2\,s^{-1}$ is considered. The remaining hydration products are considered as non-diffusive. The spatial repartition of the various phases will thus be done accordingly:

- The anhydrous volume fraction, and non-diffusive hydrates as first inclusions,
- then, concentrically, the C-S-H phase is modeled (only in a macroscopic fashion, the phase's volume fraction is used, and no local information – like the thickness – is considered).
- The remaining volume is attributed to porosity (fully saturated).

This type of 3-phase morphologies is thus defined by two thresholds. An example of threshold evolution is presented Fig. 4.18, after achieving a numerical inverse resolution of Sys.2.17 (Jennings & Tennis hydration model, with discussed modifications ; valid for any PaSD, as long as the morphology is based upon a union of 3 CRFs excursion sets)

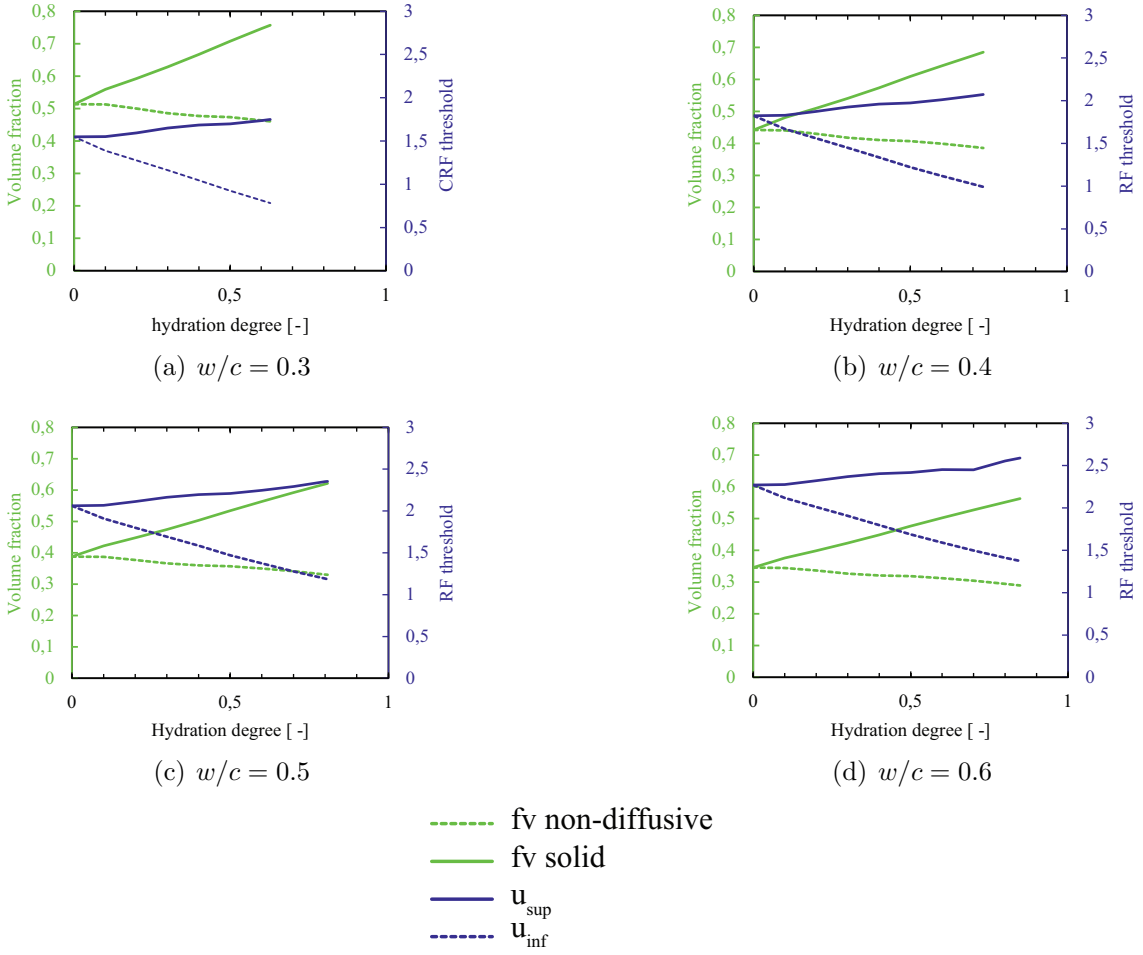

(a) $w/c = 0.3$

(b) $w/c = 0.4$

(c) $w/c = 0.5$

(d) $w/c = 0.6$

(e) legend

Figure 4.18: Relation between the hydration model phases evolution and the corresponding thresholds.

From a numerical stand point, the "projection" stage leads to morphologies with 6 distinct type of FE, as presented Fig. 4.19. They can be sorted into two families: a first one where the elements are fully immersed in a phase (anhydrous, C-S-H, or porosity) ; and a second one with embedded discontinuity following the interfaces (anhydrous to C-S-H – C-S-H to porosity – anhydrous to porosity). The last type of element described, modeling the interface between anhydrous cement grain and the porosity is the less physical one, and actually appear in the projection process due

to interpolation between the CRFs node values and the FE mesh nodes. They can be found at very early stages, when the hydrate layer is very thin, or when there is a too high discrepancy between the CRF and FE discretizations.

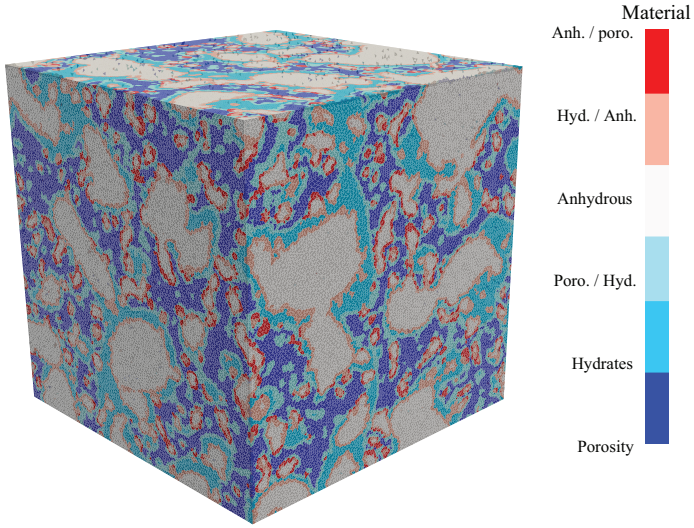

Figure 4.19: Example of a CP morphology – 3 phases – projected on volume FE mesh : T =100 µm.

3.4.2 Effective diffusion coefficient through hydration

A first set of results is presented for hydrating cement paste. Always using the standard CEM-I cement paste, as well as the aforementioned morphological hypothesis, the effective diffusivity is up-scaled by modeling cement paste microstructures and their evolutions.

Such first results are drawn Fig. 4.20. The first simulation are done for a hydration degree of 0.1, up to the maximal hydration degree prescribed by the hydration model (it is the reason why the curves do not stop at the same abscissa).

For high w/c, our framework yields almost linear results, and the difference between $w/c = 0.5$ and 0.6 is almost negligible. For lower ones, some non-linearity appears as the hydration degree increases, and the final effective coefficient decrease a little faster towards hydration's end.

However, the final results (maximal hydration degree) are far off the expected values found experimentally: approximately one order of magnitude for high w/c ratios, and about 1.5 - 2 for low ones. It is more visible on Fig. 4.21, where some experimental values are also represented. The [Zhang et al., 2011] results are also drown, and it is visible the same gap is present for high w/c ratios, but their

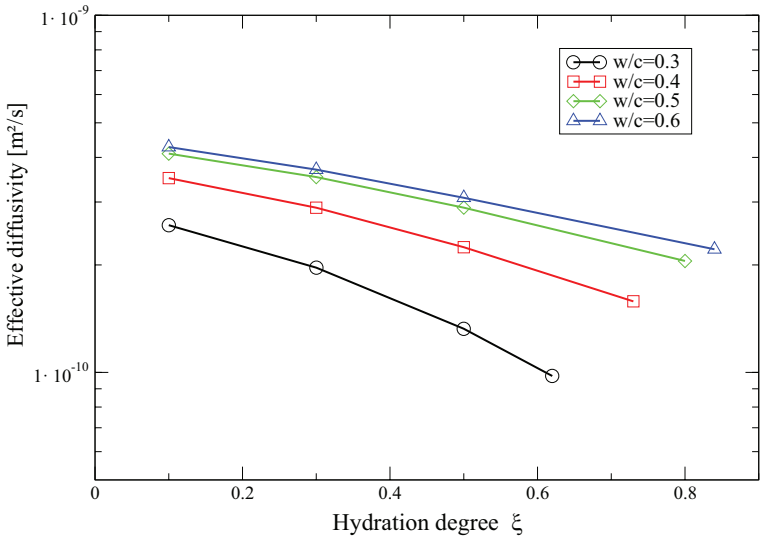

Figure 4.20: Effective diffusion coefficients evolution.

hydrating frmawork handles apparently better the particle inter-connections for low w/c, and the hydrates are more percolated.

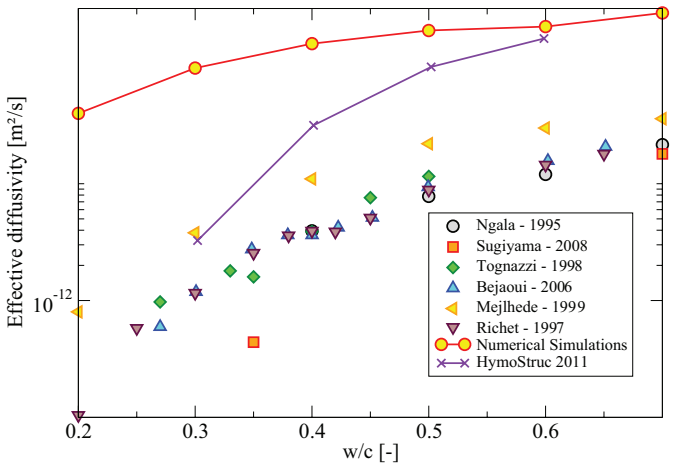

Figure 4.21: Effective diffusion coefficients for hardened cement pastes.

The same results scaled according to the accessible porosity (as it has been discussed, in the present framework it represents the total porosity) tend to align as a single set of data (as it has been the case in the cement paste tortuosity measurements). But the same discrepancy is observed in terms of effective diffusivity.

In some early estimation made during the second year of this Ph.D., Powers

model was first implemented, and the hydration framework was less restrictive, especially concerning the hydration's end. The morphologies were able to evolve as long as anhydrous cement was present in the morphology. Even though the hardened cement paste were under-estimating the total porosity with this hydration model, the results in terms of effective diffusivity were slightly better, at least for low w/c ratios, as presented on FIG. 4.22. The very low w/c morphologies could not be realistically modeled because the initial microstructures were almost fully percolated. However, the results for $0.4 < w/c < 0.5$ were much more closer to the expected range of effective diffusivity. Further above, the same offset as previously is found.

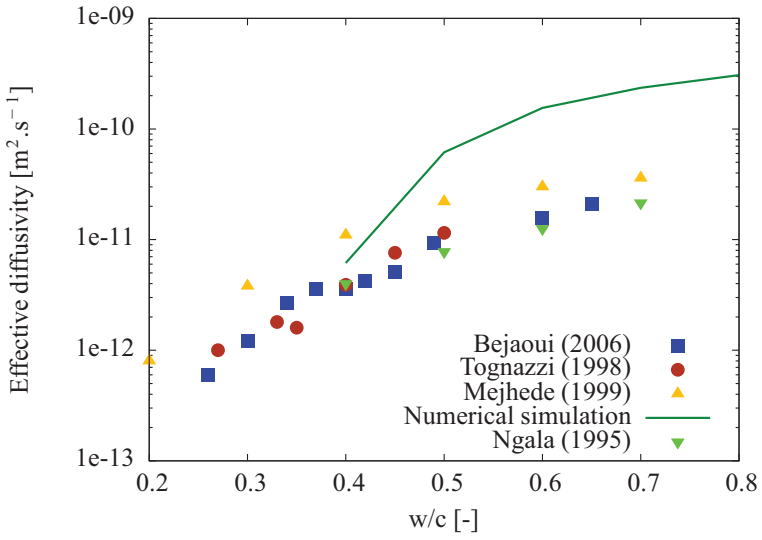

Figure 4.22: Effective diffusion coefficients for hardened cement pastes.

3.4.3 Remarks and perspectives

They are several explanations as to the huge discrepancies found at this particular scale:

$D_{\text{C-S-H}}/D_{\text{poro}}$ sensitivity:

At first, it is possible to think that one order of magnitude could be explained by the material properties. Since as an input of this scale we used a rather unusual value for the C-S-H phase diffusivity ($D_{\text{C-S-H}} = 1.9 \times 10^{-11}\,\text{m}^2\,\text{s}^{-1}$), an additional sensibility study was done to see the influence of the $D_{\text{C-S-H}}/D_{\text{poro}}$ ratio on the final numerically homogenized effective diffusion coefficients. Results are drawn FIG. 4.23, for hydrated morphologies, and $D_{\text{C-S-H}}/D_{\text{poro}}$ ratios spanning from 10^{-2} to 10^{-5}.

The influence seem almost negligible, which was expected for high contrast material properties, but it can be noted that the lower the w/c ratio is, the more change

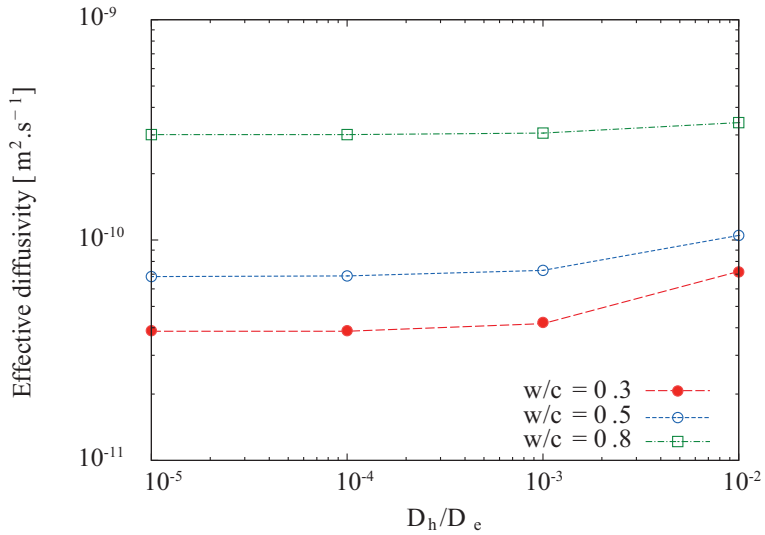

Figure 4.23: Influence of D_{C-S-H}/D_{poro} ratio on the final numerically homogenized effective diffusion coefficients.

can be observed. For increasing w/c ratio, the fraction of C-S-H (overall as well as percolated) is rather small, and the dominant phase remains the porosity. So decreasing the C-S-H diffusion properties from $1 \times 10^{-11}\,\mathrm{m^2\,s^{-1}}$ to $1 \times 10^{-15}\,\mathrm{m^2\,s^{-1}}$ will not change the overall response as the pore space is still very percolated. On the other hand, for low w/c, the C-S-H fraction is more important, and the influence (even is little) of the $D_{\text{C-S-H}}/D_{\text{poro}}$ ratio is visible between 10^{-2} and 10^{-3}. Further down, the contrast is too high for the numerical framework to notice it.

Back-fitting:

A way to overcome the discrepancy found by the present framework could be to "back-fit" the input values of the model. It is here presented only since our results are far off the expected trends, but it is **not** in the spirit of the present work, as it introduces non-physical material properties.

First, based on the gap of effective diffusion coefficients found for high w/c, the diffusion coefficient of the pore space is reduced by an order of magnitude, down to $D_{\text{poro}} = 2 \times 10^{-10}\,\mathrm{m^2\,s^{-1}}$, and at the other hand, for low w/c where 1.5 - 2 orders of magnitude are found, the value of $D_{\text{C-S-H}}$ can be decreased by the same magnitude down to $D_{\text{C-S-H}} = 4 \times 10^{-13}\,\mathrm{m^2\,s^{-1}}$. The yielded results are presented on Fig. 4.24, with the puprle curve of interest.

The results are — necessary — better. The right end of the results is in the expected range, however, on the left side, for low w/c, the framework still misses some information as the results are still over by 0.5 - 1 order of magnitude. The main reason lies probably in the actual morphologies, as they are probably too smooth due to the yielding process, and the porosity (and C-S-H phase) not tortuous enough.

Instead of tuning the input parameters, a more physical approach to improve

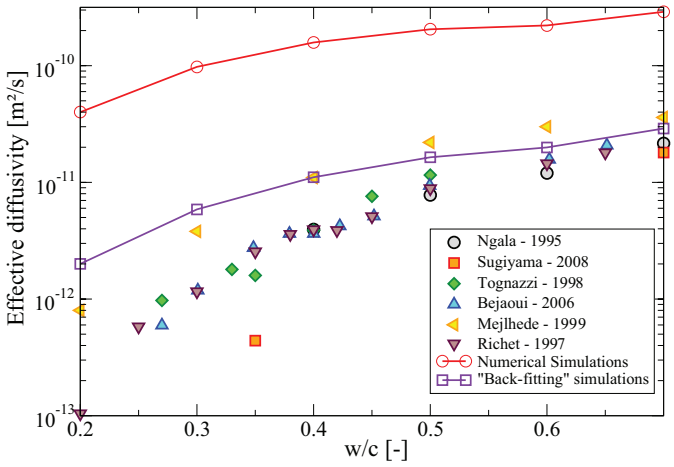

Figure 4.24: Backfitt of the input parameters at the CP scale.

the predictive quality of the model could be to modify the hydration process, either from the macroscopic stand point by changing the volume fraction's evolutions, or more locally by allowing hydrates to form non-concentrically. Those two paths are explored in the following.

Hydration modification:

C-S-H porosity: Some parameters like the C-S-H porosity (fixed by the hydration model) could influence the overall response. By decreasing the C-S-H porosity, and keeping the overall porosity constant (in regards to the hydration model where capillary and hydrate pores are counted together), the capillary one could decrease enough to enhance the effective results. Tests were performed to address this issue, by varying the C-S-H porosity through the experimental span of values found in the literature, from 0.2 to 0.35.

For two w/c ratio often found in practical applications, 0.4 and 0.5, the C-S-H porosity was modified (corresponding effective diffusion coefficients are thus taken from the C-S-H modeling part results). The application was done only on hydrated CP. For $w/c = 0.4$, when the C-S-H porosity is set to 0.219, the capillary porosity given by the hydration model is of 0.31, but when the C-S-H porosity was assigned at 0.35, the capillary porosity decreased by few percent to 0.27. In terms of effective diffusion coefficient for the cement paste, it translates into a decrease from $D_{\mathrm{CP}} = 1.42 \times 10^{-10}\,\mathrm{m^2\,s^{-1}}$ to $D_{\mathrm{CP}}^{\mathrm{shift}} = 1.13 \times 10^{-10}\,\mathrm{m^2\,s^{-1}}$, which is almost negligible given the badness of the presented results. The same shift applied for a cement paste with $w/c = 0.5$ yield similar results, with at first $D_{\mathrm{CP}} = 1.88 \times 10^{-10}\,\mathrm{m^2\,s^{-1}}$ and after the maximal shift $D_{\mathrm{CP}}^{\mathrm{shift}} = 1.63 \times 10^{-10}\,\mathrm{m^2\,s^{-1}}$.

No particular improvements were possible through this approach.

Hydrates distribution: Finally, a last attempt to improve this stage of the framework is tested. This time, the overall hydration model is kept as is, and only morphological changes are considered. In order to try to increase the tortuosity of the pore network, as well as the C-S-H phase one, the volume fractions allowed to all the *non-diffusive* hydrates were generated separately. In other words, the yielding process was similar, with a first threshold following the anhydrous cement volume fraction, and a second one to yield only the C-S-H. However, the volume fraction associated to the remaining hydrates has been generated by a set of regular inclusions (cubes of side size 2 µm), regularly placed inside the previous excursion set. An example of such a hydrated cement paste is drawn Fig. 4.25.

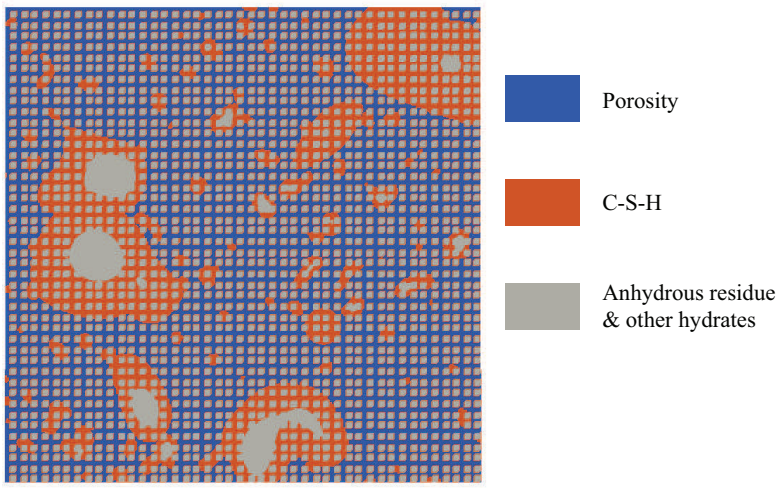

Figure 4.25: Modeling attempt to enhanced the diffusive and pore phases tortuosity.

One drawback of this attempt is that the C-S-H phase, even if perturbed, is now smaller in terms of circumference, and thus is much less percolated.

The results, however, tend to show an interesting enhancement of the predicted effective diffusion coefficients, as for cement paste with a w/c ratio of 0.45 hydrated through the Jennings model, the first implemented results yields a value of $D_{\mathrm{CP}} = 1.83 \times 10^{-10}\,\mathrm{m^2\,s^{-1}}$, the hydrate separation and re-distribution into regular inclusions yields a diffusion coefficient $D_{\mathrm{eff}} = 4.65 \times 10^{-11}\,\mathrm{m^2\,s^{-1}}$. This value, even if improved, is not yet in the expected range for cement pastes, as experimental values span from $2 \times 10^{-12}\,\mathrm{m^2\,s^{-1}}$ to $1 \times 10^{-11}\,\mathrm{m^2\,s^{-1}}$.

This decrease is explained by the overall tortuosity improvements, even though, as it is visible on Fig. 4.26, the regular spacing of the cubic inclusions generate paths where most the the diffusion occurs.

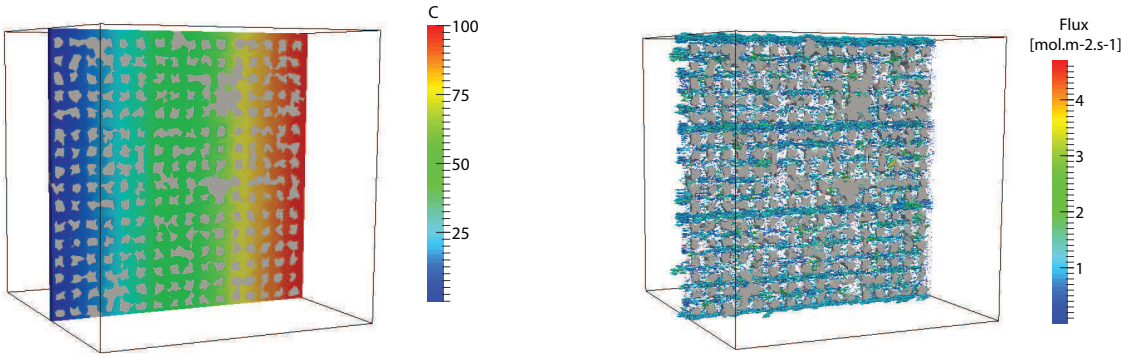

Figure 4.26: Regular inclusions: concetration (left) and fluxes (right) maps in the free space.

Overall modeling remarks

As discussed at the end of the second chapter, the present framework do not represents the closed porosity that is expected in an hardened cement paste. Two main reasons can explain this fact: first the morphological discretization (of the underlying CRFs) may not be fine enough, and, more likely, the lack of physics in the hydrate growth which results in morphologies too "smooth" (even if the total porosity may be good, the pore size distributions targeted are only postulated, with no proper experimental background at this scale). Several ways exist to enhance the roughness of the morphology:

- First, to keep all things as they are in the present framework, different covariance functions may be used, like for example the *Matérn* class of function (which brings an additional parameter to perturb the smoothness), which are still suitable for the probabilistic link between the CRFs probabilistic variables and the excursion sets morphological properties.
- An iterative approach for the hydration could be considered, similarly to the heart of HYMOSTRUC3D model, where some hydrate are embedded within others as the hydration evolves.

Lastly, the duality between the two discretizations (CRFs yielding and mesh generation) kept may not be good enough. It is also possible that if the geometrical description is done with a given fineness (CRFS dofs), similar refinements (mesh dofs) should be used for the transport simulations.

3.4.4 Mechanical implementation: Young modulus evolution

During the first stages of development of the present work, an application has been made with truss elements [Benkemoun et al., 2010]. The boundary condition introduced in CHAP. 3 for diffusion phenomena are here implemented in their initial

form [Hill, 1963] for mechanical studies, reflecting a triaxial tension (KUBC) and pure shear (SUBC) tests, applied only for linear elasticity.

The initial morphology were generated to reflect a standard CEM-I cement paste, with a standard fine cement PaSD. Microstructures of hydrating cement pastes (with the simplified Powers hydration model) were submitted to such calculations (Fig. 4.27).

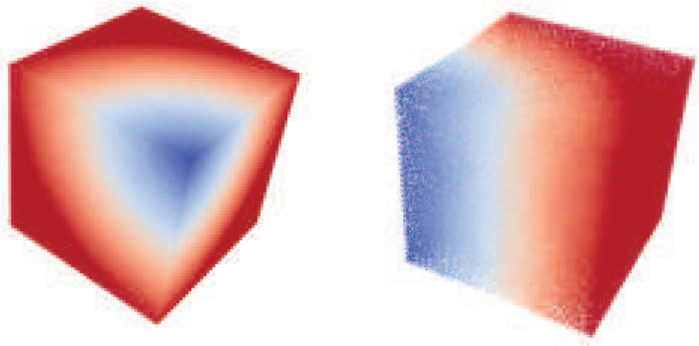

Figure 4.27: Boundary condition for mechanical properties prediction – T =100 µm.

With the truss elements earlier mentioned, a first parameter identification was necessary to relate meso- and macroscopic quantities (not developed, see [Roubin, 2013]). It led to a choice of parameters described in Tab. 4.1.

	E [GPa]	ν [-]
anhydrous	135	0.25
hydrates	25	0.25
porosity	10^{-3}	0.27[1]

Table 4.1: Materials property inputs.

The results in terms of Young modulus evolution are presented on Fig. 4.28. The drawn results can be decomposed in three stages. First, for a hydration degree under 0.2, no response is recorded, as the predominant phase is the porosity, then in-between 0.2 and 0.5, a non linear increase of the Young modulus arise, reflecting the growing volume fraction of connected components, and finally from 0.6 to the hydration's end, the evolution is rather linear.

The final predicted Young modulus is in the expected range, however, the transition zone (reflecting the setting of the cement paste) seems to be too smooth (no evident threshold). From a hydration stand point, such discrepancy is expected, as

[1]Upper bound – numerically speaking – of the input with the truss implementation. Theoreticcaly should be set at 0.5

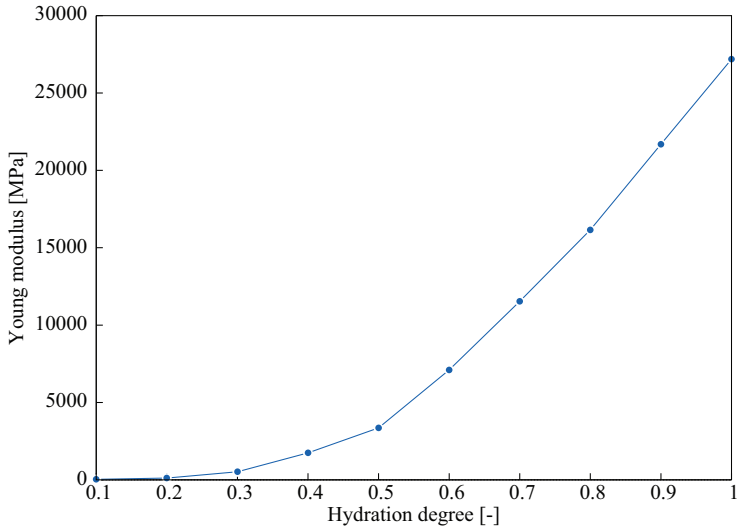

Figure 4.28: Young modulus evolution for a standard CEM-I CP, $w/c = 0.45$, T =100 µm.

it is considered the it is the C-S-H phase that "glue" the others together, and here all the hydrates are considered as one. However, it also might be due to a too small number of simulations, and when averaged over dozens of realization, this setting point may be more effectively (precisely) defined, as it should in the vicinity of a hydration degree of 0.2, and more abrupt [Stefan et al., 2010]. Also, no softening is observed (for this CP, with $w/c = 0.45$), which is rather normal, but additional calculations should be done, as for low w/c, the onset is much more stiff, with a large softening part, whereas for high w/c the onset is directly followed by a linear evolution up to a complete hydration.

3.4.5 LBM implementation

A collaboration with an on-going Ph.D. by Edouard Walther at the *LMT-Cachan* led to a similar application of the hydration framework [Walther et al., 2015]. In addition to a numerical study of LBM instability with high contrasts in material properties, an application led to a estimation of the diffusivity in hydrating cement paste. However, the latter has been achieved only on 2D morphologies, taken as slices from the presented 3D hydrating morphologies. For a classical CEM-I CP ($w/c = 0.4$), hydrating according to the introduced Powers simplified hydration model (Sys.1.3).

An example of 2D realization of such morphologies is drawn Fig. 4.29 for two distinct hydration degree, with the corresponding resulting concentration maps. The simulations were carried out over 200 realizations of 2D morphologies, with traditional diffusion coefficients (results from the previous C-S-H modeling study were not available at the time): D_{poro} =$2 \times 10^{-9}\,\text{m}^2\,\text{s}^{-1}$ and D_{hyd} =$2 \times 10^{-12}\,\text{m}^2\,\text{s}^{-1}$. The

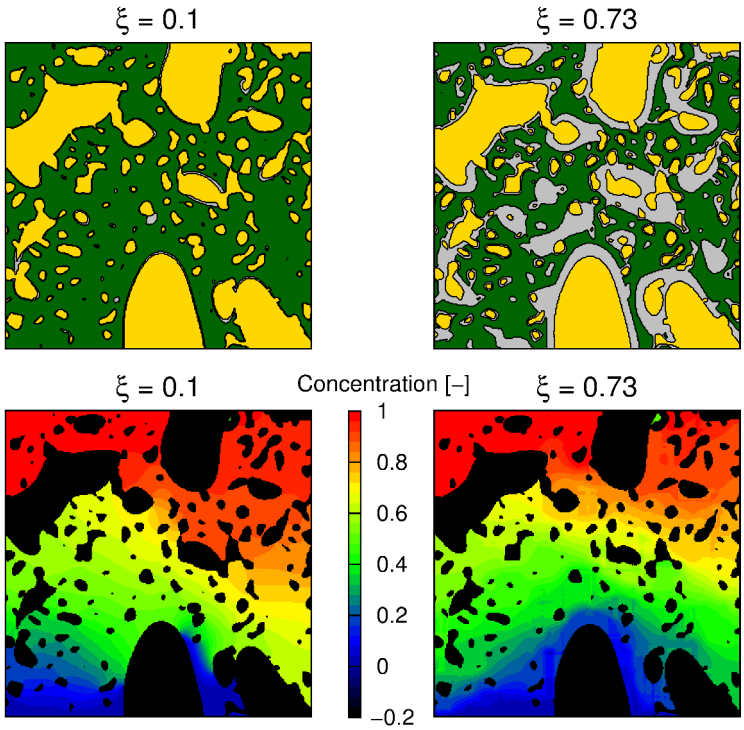

Figure 4.29: Example of a simulated standard CEM-I CP: morphology (green: porosity, yellow: non-diffusive phase, grey, C-S-H) and concentration maps, $w/c = 0.4$, $T = 100\,\mu m$.

remaining anhydrous cement was considered as non-diffusive. Results throughout hydration are presented Fig. 4.30, with average value as well as the 95% CI.

For early stages of hydration, the effective diffusion coefficient is close to the one found in pure water, and as the hydrates volume fraction increases, the effective diffusivity decreases: first relatively smoothly to a hydration degree of 0.4, then a change of slope can be observed, with at the same time the CI that widen, to finally diminish for the fully hydrated morphologies. Those results seem correct in a first approximation, as for low hydration degree, the predominant phase is the porosity, and diffusion occurs mainly within (narrow CI reflects the low variability of such morphologies). Then, at the change of slope, the hydrates start to percolate (more or less according to the CRF realization and excursion, hence the wider CI), and thus steer the results towards their diffusion coefficient.

The final value of effective diffusion coefficient is very low, and actually matches the hydrates one: $D_{\text{eff}} = D_{\text{hyd}} = 2 \times 10^{-12}\,\text{m}^2\,\text{s}^{-1}$. It can be first explained by the simplified hydration model — as shown Fig. 2.27, it underestimates the overall porosity at fully hydrated states — and secondly, all the previous consideration about percolation are no longer valid in 2D (the percolation threshold is much higher in 2D, 50%).

An interesting development of this study would be to compare, with the LBM

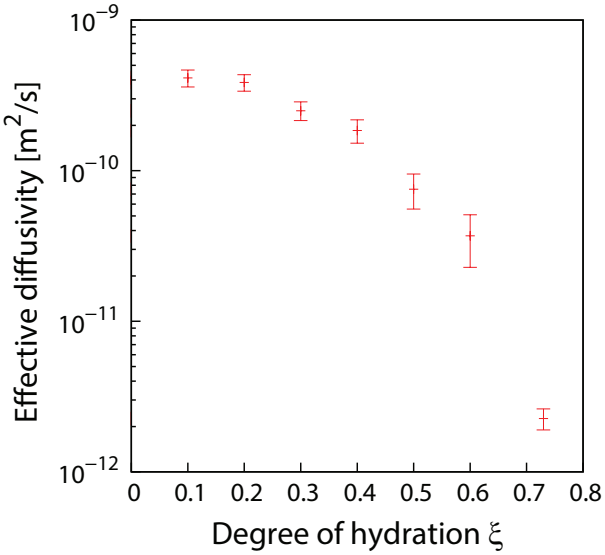

Figure 4.30: Simulated averaged effective diffusivity T =100 µm, 0.5 µm per voxel.

method, results from 2D and 3D simulations, in order to look for correlation between 2D and 3D geometrical and topological informations (percolation threshold, pore size distributions), as well as in terms of effective diffusivity. It may lead to a simplified 2D model representative enough of 3D microstrucure, and thus allow a substantial gain in computational time.

3.5 Mortars

While upscalling to the mortar scale, several simulations and experimental comparisons are carried out, with first a typical mortar used in nuclear industry, so-called "B11" concrete, then with a model material (sand replaced by glass beads), and finally some experimental mortars are simulated to assess the quality of the upscalling scheme.

3.5.1 Standard B-11 mortar

As an application of the framework for this third scale, a first modeling approach consists into reproducing the mortar used in *Civaux* nuclear power plant. The material used is a so-called "B11" concrete with the following composition:

Cement [kg m^{-3}]	Sand (0/4) [kg m^{-3}]	Gravel (5/12) [kg m^{-3}]	Gravel (12/20) [kg m^{-3}]	Water [L m^{-3}]	Plasticizer [kg m^{-3}]
350	772 (dry)	316 (dry)	784 (dry)	201 (effective)	1.3

Table 4.2: "B-11" concrete composition.

As it is only intended to model first the mortar part, attention is drawn to sand particles: their grading range is shown on FIG. 4.31 (black curve).

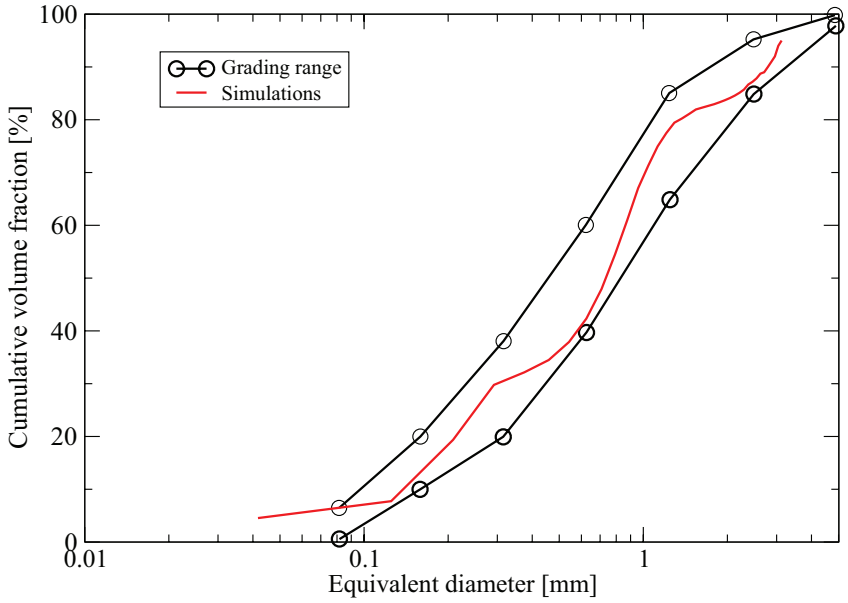

Figure 4.31: B11 mortar grading range (sand 0/5) and morphology control (*results averaged over 3 realizations*).

The usual sizes modeled at this meso-scale range from 5.25 mm [Kamali-Bernard and Bernard, 2009], 7.5 mm [Abyaneh et al., 2013], to 8 mm [Zhang et al., 2014b]. However, considering the previous morphological consideration of RVE, a maximal size of 12.5 mm is considered in the following.

In order to fit within the prescribed bounds, after several iterations, a set of parameter was found to suit the purpose, using the methodology described in CHAP. 2, SECT. 4.3.2. For a cube of side size T =12.5 mm, the expected morphology is composed of a union of 3 excursion sets, with L_c^1 =0.2 mm, L_c^2 =1 mm and L_c^3 =3.75 mm. A typical results in terms of particle size distribution is presented on FIG. 4.31, in red, and an example of a morphology is drawn on FIG. 4.32. The yielded morphologies are then projected on a unique mesh previously chosen, with 9×10^5 dofs.

Using the set of parameters described, several realization (5) are generated, with two different volume fractions. They were chosen to be able to compare this scale results to experimental data from [Larbi, 2013], as they also used a standardized sand, and carried out diffusion experiments for a cement paste, followed by mortars, using tritiated water, which is one the elements that present very little interactions with the bulk matrix. The results are presented on FIG. 4.33.

The initial value for 0% of sand inclusions, taken from the experiments, is used as an input to our simulations.

A noticeable decrease of the effective diffusivity is observed with the increasing sand volume fractions, however it does not follow experimental trends, and decreases

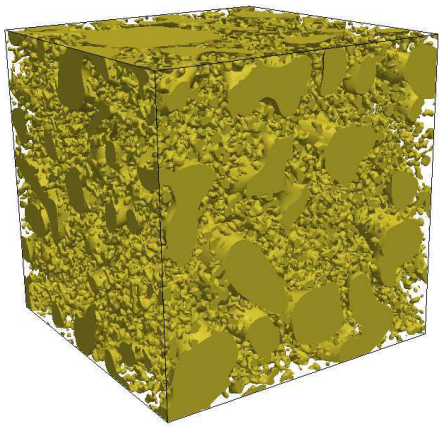

Figure 4.32: Realization of B11 mortar – T=12.5 mm

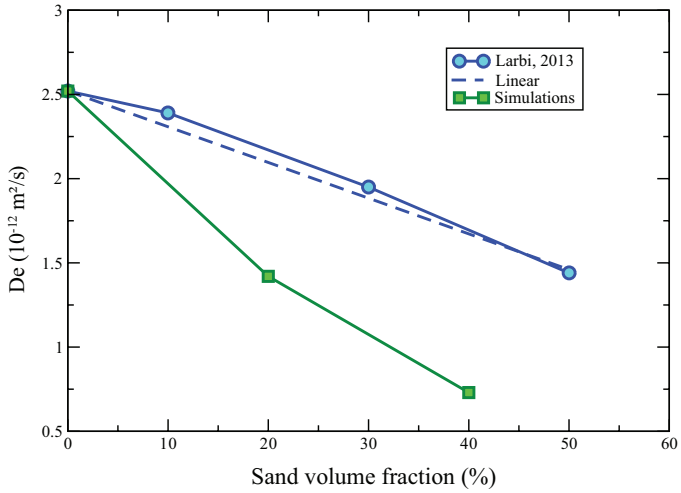

Figure 4.33: Simulated effective diffusivity, compared to experimental results from [Larbi, 2013].

faster. The main reason, at this stage, is attributed to the ITZ which is not modeled. In the actual mortars, the ITZ increased porosity allows the emergence of preferable diffusion paths. However, for low volume fraction, the effect should not be that visible. This effect should be more noticeable for high volume fractions of inclusions.

3.5.2 Comparison with glass beads experiments

As already developed in the previous chapter (sub-section 2.4.2 of the third chapter), experiments with model mortars were done at the *LMT-Cachan*, using glass beads. The experiments were carried out with 3 different volume fractions of beads: none,

Inclusions (%)	0	20	40
Experimental D_e^{exp} ($10^{-12}\text{m}^2\,\text{s}^{-1}$)	8.04	6.83	6.85
Numerical D_e^{num} ($10^{-12}\text{m}^2\,\text{s}^{-1}$)	8.04 (input value)	6.92	4.69

Table 4.3: Numerical simulation results for model mortars.

20% and 40%. The results in terms of effective diffusion coefficient are listed in the previous chapter in TAB. 3.3, and plotted against several experimental results on FIG. 3.7.

The first value assessed without glass beads provide a diffusion coefficient for the cement paste D_{CP} =$8.04 \times 10^{-12}\,\text{m}^2\,\text{s}^{-1}$, which is used as an input into our modeling scheme. The experiments results were listed in an attempt to model these tests is now presented.

Even though the actual samples were submitted to X-ray CT scans (FIG. 4.34(a) and 4.34(d)), due to an important noise in the image acquisition, no proper morphological characterization was possible. The image segmentation did not allow to properly distinguish the glass beads for the cement paste matrix, even after applying various filter to enhance the images. Usually, in such studies, either it is possible to extract the actual geometry of the sample, and then transfer it onto a FE mesh, or generate sphere packing with the matching covariance function. In the present case none of those approaches were applicable, so purely random sphere packings were generated (5 for each scenario), matching only the desired volume fraction (examples are drawn FIG. 4.34(c) and 4.34(f), projected on unstructured volume FE meshes of size 12.5 mm with 9×10^5 dofs).

Results of the corresponding simulations are listed in the following TAB. 4.3. As expected, at the first beads volume fraction, the effective diffusivity decreases, from $8.04 \times 10^{-12}\,\text{m}^2\,\text{s}^{-1}$ to $6.92 \times 10^{-12}\,\text{m}^2\,\text{s}^{-1}$. The decrease is very similar experiments, the tendency is well respected. With the inclusions the tortuosity increases, which stretches the path for the diffusive specie. For this intermediate sand's volume fraction, the dilution law is also well respected. Further on, at 40% of inclusions, the simulations keep the previous tendency as the effective diffusion coefficient is now lower: D_{eff} =$4.69 \times 10^{-12}\,\text{m}^2\,\text{s}^{-1}$. In the experiments, for this case, the effective diffusivity actually increased up to $6.85 \times 10^{-12}\,\text{m}^2\,\text{s}^{-1}$, probably due to the questionable presence of the ITZ (as discussed in sub-section 2.4.2 of the third chapter) or more likely due to micro-cracks presence. Since at this stage none of those phenomena are taken into account, it seems "normal" that the numerical results diverge from the experiments.

3.5.3 ITZ

A first set of results concerning the ITZ is presented FIG. 4.35. The actual *B11* mortar is modeled, with its proper inclusion volume fraction (46% of sand). Two different volume fraction of ITZ are tested, respectively 5 and 15%. This phase,

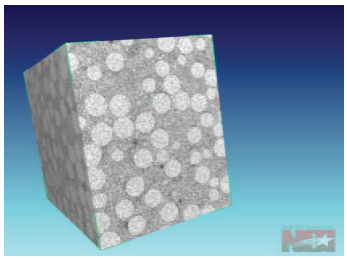

(a) X-ray CT subdomain for the 20% mortar

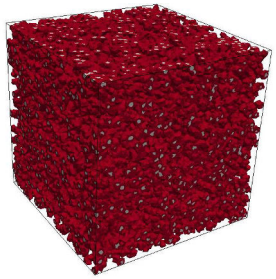

(b) random sphere packing projected on a FE mesh

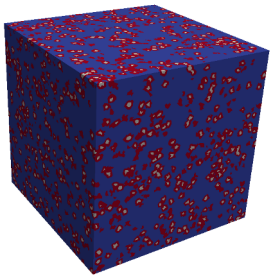

(c) Total modeled morphology for 20% of spherical inclusions

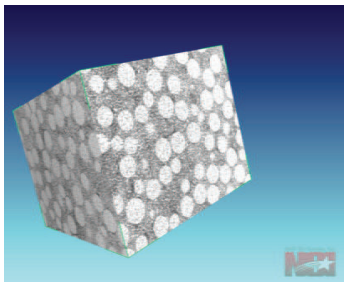

(d) X-ray CT subdomain for the 40% mortar

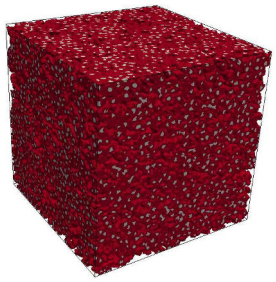

(e) random sphere packing projected on a FE mesh

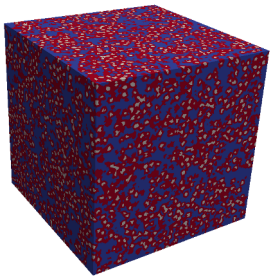

(f) Total modeled morphology for 40% of spherical inclusions

Figure 4.34: Spherical inclusions: 20 and 40% of volume fraction.

surrounding the granular inclusions was assigned a diffusion coefficient $D_{\mathrm{ITZ}} = 4 \times D_{\mathrm{CP}}$ [Kamali-Bernard et al., 2009].

A critical issue is found when modeling the ITZ. With the modeling framework based on excursion sets, it is not possible to describe the ITZ with a constant thickness, but it is possible to model a given volume fraction. However, as it is visible on Fig. 4.36 (2D slice of cube of size T =12.5 mm, with 42.5% of sand volume fraction) , for a ITZ volume fraction of 10%, one can notice that the phase distribution driven by the underlying CRF allocate most of this volume fraction around "large" aggregates, and the thinner particles have mainly a very narrow ITZ, which will "disappear" at the projection stage, due to interpolation between the morphological CRF and the FE mesh discretizations. It would require to have an elementary size of FE tetrahedron at least twice as thin as the minimal ITZ width found on Fig. 4.36. With a global size of T =12.5 mm, the elemental size of the tetrahedron should be about 0.002 mm, leading to an impossible FE discretization around 2×10^8 dofs.

Smaller samples at this particular scale should be considered to be able to rep-

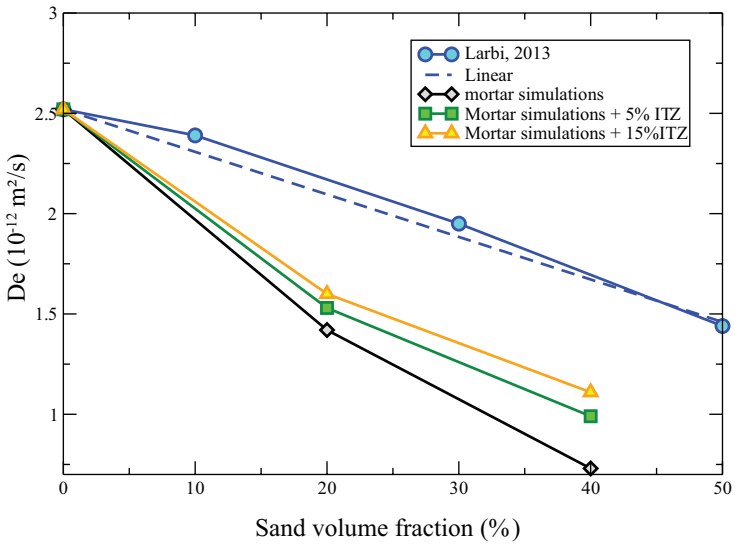

Figure 4.35: Influence of the ITZ modeling.

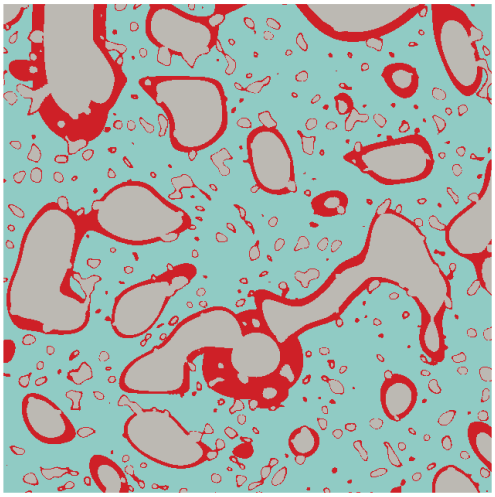

Figure 4.36: Example of ITZ modeling.

resent the ITZ with a maximal FE discretization of 1×10^6 dofs; and following the method presented for the volume fraction RVEs in Chap. 2, the RVE could still be determined over a consequent number of realizations.

In addition to the numerical issues to be able to numerically simulate diffusion phenomena on such a morphology, the actual ITZ volume fraction are found to be more important with smaller particles, as discussed in the third chapter, commenting [Caré and Hervé, 2004] results. A plausible explanation for the discrepancy found in terms of effective diffusivity, considering equal volume fraction of sands, the mortars with fine sand exhibited more ITZ than the one with coarse sand.

3.6 Concrete scale

Similarly to the *mortar* scale, at this last scale of interest, several simulations will be carried out, with first the actual generation of a typical *B11* concrete.

The *B11* concrete mix-design is given Tab. 4.2. From this composition, when dividing the aggregates into sand on one side and gravels on the other, the concrete as a two-phase material will bear a volume fraction of 55% (assuming a B11 concrete density of 2.45, and a gravel density of 2). The initial modeling volume is set at $V = 100\,\mathrm{cm}^3$ (cube side size of 4.6 cm).

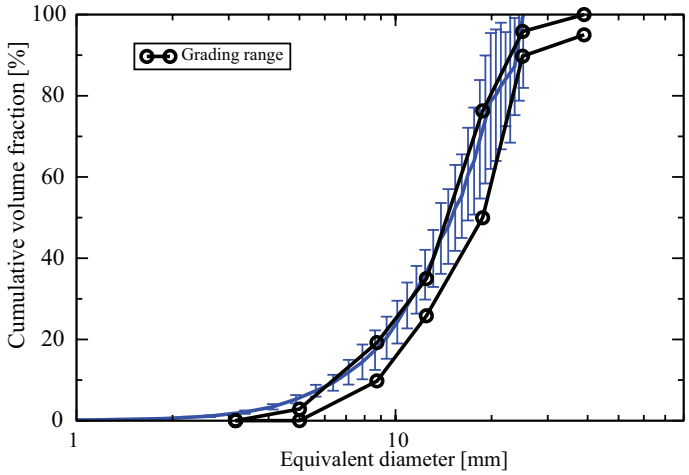

Figure 4.37: B11 concrete grading range — aggergates: Fine to coarse gravels 5/12.5 & 12.5/25 — and morphology control (*results averaged over 5 realizations, with 95%CI*).

The results in terms of effective diffusivity bear the same issues as at the mortar scale, and no proper estimation could be made.

Conclusions and Outlooks

The aim of the presented work was to establish a numerical modeling framework — suited for cementitous materials — able to predict effective diffusion coefficients at any scale of concern. It is a part of a broader modeling approach relying on fine morphological representations, and simple constitutive equations for transport phenomena. The simulation framework is part of the so-called **sequenced multi-scale** approaches, for which materials of interest are finely described at a **micro-scopic** and **meso-scopic** scale, in order to yield a homogenized response at a **macro-scopic** scale, and thus forecast effective diffusion properties.

In practice, a scale separation that follows all the obvious cementitious material scales, linked with up-to-date experimental description of every scale, should lead to a prediction of effective diffusion coefficients able to represent the material responses.

The overall model is to rely on three distinct points:

1. First, a geometrical and morphological description of cementitious materials is needed. In those regards, a hydration model able to predict the cementitous phases evolution through time is needed (with a set of physical and chemical data, like the mineral composition of the cement, the mix-design parameters (w/c ratio)), as well as descriptions as accurate as possible for the morphological inputs (cement particle, sand and gravels PaSD ; or hydrates PoSD)

2. Secondly, a modeling framework to yield 3D morphologies. It must be tractable throughout all scales, and be able to "easily" represent multi-phase morphologies.

3. Lastly, an upscalling scheme ensuring a proper numerical homogenization of diffusive properties must be used.

Micro-structural characterization, generation, and control

It was first shown, throughout a literature review, that even if studied for over a century now, the actual micro-structure of cementitious materials remains an open question, as with the evolution of experimental characterization techniques new questions arise. It should not be long before one technique finally merge all the partial descriptions into a unified approach.

At the hydrate scale, a consensus is reached for the pore modes, but the actual amount of porosity is still under debate. For the CP scale, many characterization techniques allow for comparative studies, giving the possibility to express the influence of many variables, but again, quantification of actual morphological properties is still an undergoing challenge. An attempt is made to describe the CP evolution through time with the help of a meso-scopic hydration model. Based on acknowledged models and up to date phenomenological descriptions, it allows to predict the pore and hydrates volume fractions considering multiple entry parameters, such as the cement mineralogical composition, its PaSD, or the age of the material. Finally, at the mortar and concrete scales, a additional feature arise – known as the ITZ – a zone surrounding the aggregates where an increase of porosity is observed. It can not be described as an actual *phase*, but rather a zone with a gradient of porosity. Its thickness, or volume fraction, is still the subject of many research.

Next, a morphological modeling scheme is introduced, based on the *excursion set theory* [Adler and Taylor, 2007, Roubin et al., 2015]. When adapted to cementitious materials (high volume fractions and size distributions for either inclusions or porosity), a probabilistic link is made between the phases description (both geometrical and morphological) on one side, and the CRFs parameters and the threshold on the other, allowing a good description of the generated morphologies. According the to targeted morphologies, Representative Volume Elements were defined for the *volume fraction*, to ensure a sufficient morphological ergodicity, as well as the accounting for *size effects* with regards to percolation. Actual hydrates / CP / mortars morphologies are thus generated, and it is then possible to qualify the micro-structural characteristics in terms of PoSD and tortuosity (an expression is introduced that links the later to the hydration progress, *i.e.* the overall porosity in CP).

This morphological framework, on its own, provide numerous advantages:

- It is tractable through all major scales found in cementitious materials, from the hydrates structure to the bulk concrete.
- It allows to generate "random" morphologies with targeted characteristics, and the control is only statistical as the *expectation formulae* gives expectancies of morphological descriptors. The span of possible morphological types is wide, from "inclusions / matrix" like to "sponge" like morphologies. It is now also possible to follow PaSD for the first type, or PoSD for the second.
- Overall, a very reduced set of data is necessary to describe entire manifolds. The CRFs only require, given the covariance function shape, three parameters: the mean value, the variance, and the correlation length. With an additional parameter – the threshold – the entire morphology is described.

The morphological control means are also elegant, based on *M. Hosseini* work on morphological operations, allowing to characterize the various phases size distributions (in 3D), as well as their tortuosity (lower bound).

One noticeable drawback was however found, when modeling the CP scale (the only "evolutive" one). In order to get realistic morphologies of the initial suspension of cement grains in a water "matrix", the use of multiple χ^2 CRFs was chosen to enhance the reachable volume fraction and the size distributions. However, as those morphologies "grow" (*i.e.* evolve as the threshold is decreasing from a initial value towards zero), the percolation phenomena do not follow the trends observed in a first approximation with strictly Gaussian CRFs (indeed, χ^2 CRFs are defined only in $\mathbb{R}^+$, and a threshold close to zero will yield percolated phase). Particularly at this scale, the inclusions can be generated with a proper volume fractions and their evolution is easily driven with targeted volume fractions. However, as they grow, those inclusions connect with each other, but the "depercolation" of the complementary phase almost never happen.

Multi-scale effective diffusivity

Regarding diffusion phenomena, it is shown that a number of models exist, trying to link the effective diffusive properties to a reduced set of parameters, such as the porosity or the w/c ratio. However, the link between the micro-structure and the effective properties is not yet fully understood. The present framework is based upon the assumption that a proper morphological representation will lift biases linked with percolation, and that "simple" tests should be able to forecast effective diffusive properties with a minimal number of hypothesis.

Studies were carried out with no particular emphasis on the diffusion type (molecular / ionic / isotopic), or on the species considered. As shown in the first chapter, most of the ionic species found in the interstitial solution of cement paste pores have a diffusion coefficient in a relatively small range: $5 \times 10^{-10}\,\mathrm{m^2\,s^{-1}}$ to $2.2 \times 10^{-9}\,\mathrm{m^2\,s^{-1}}$. The particular case of ionic interactions and "fixation" is not addressed, as only **effective** properties are considered. In those regards, an energy based upscalling scheme has been introduced, leading to two types of boundary conditions, ensuring a proper scale separation as well as proper effective properties bounding. It is shown that as long as the inclusions distribution is isotropic, one of the boundary condition, known as *Unitary Concentration Gradient* converge fast towards a RVE definition, and bear more physical meaning than its counterpart, the *Unitary Particle Flux* boundary condition.

Finally, concerning the application of the previous merged frameworks, the actual results unfold as follows:

- At the lowest considered scale, the C-S-H are modeled as a porous material, with a nominal porosity of 21.9%. Their porosity is qualitatively generated in an uneven layered sheets manner. The results in terms of effective diffusivity are somewhat different from the literature, with an effective diffusion coefficient set at $D_{\text{C-S-H}} = 1.9 \times 10^{-11}\,\mathrm{m^2\,s^{-1}}$. However it is shown that within the

given framework, its influence is not noteworthy: at the upper scale (CP), the $D_{\mathrm{CSH}}/D_{\mathrm{poro}}$ ratio is set at various values ranging from 10×10^{-2} to 10×10^{-5}, with no particular effect on the response.

- At the CP scale, the results are predicted mainly for a standard CEM-I cement, throughout hydration and at a "maximal" hydration degree. The morphological evolution induced by the hydration reaction is described with the help of two different hydration models introduced in the second chapter, both of which describe the evolution in terms of anhydrous phase and hydrate phases volume fractions. The morphologies are characterized by means of pore space description, ensuring quantitatively a proper pore volume fraction, and qualitatively a proper pore size distribution.

  The results in terms of effective diffusivity have an important offset and thus largely overestimate the effective diffusion coefficients for cement pastes (one to two orders of magnitude). Several attempts are made to improve the model, either by modifying the material properties or the morphological description. First with a "back-fitting" approach, trying to iteratively find the input parameters needed to get the "proper" results (*i.e.* in the experimental range), leading to a new set of parameters: $D_{\text{C-S-H}} = 4 \times 10^{-13}\,\mathrm{m^2\,s^{-1}}$ and $D_{\mathrm{poro}} = 2 \times 10^{-10}\,\mathrm{m^2\,s^{-1}}$ — which obviously are deprived of physical meaning.

  Two additional attempts were addressed, first by allowing more porosity to the C-S-H phase (the numerous models that try to describe the C-S-H phase vary a lot in terms of total gel-porosity, spanning from a dozen to over 30% of porosity), thus decreasing the capillary porosity. Secondly, we tried to embed non diffusive hydrates within the diffusive phase. Both were unsuccessful to aptly fit experimental results at this scale, and bridge the two orders of magnitude gap.

  A supplementary set of calculations has been undertaken, to study the **mechanical response** of hydrating morphologies. This time the response is supposed to be driven by the solid phase evolution and percolation, independently from the pore phase. It has been shown, qualitatively, that the Young modulus evolution follow the expected trends, even though the setting point is not very well defined. The Young modulus does start near zero, but immediately after the hydration start, it increases, first slowly, and a change of slope is observed for a hydration degree between 0.4 and 0.5. However, the various characterization methods have a clear onset (both in terms of Young modulus and percolated volume fraction) for a hydration degree between 0.2 and 0.3. So even though the volume fractions of each phases are respected, their spatial distribution is probably not representative, as we model perfectly ergodic inclusions, whereas actual water cement mixes are subject to pilling and flocculation, leading thus to preferable paths of percolated solids.

- Lastly, for the mortars and concretes scale, the homogenized effective diffu-

sive properties are addressed properly while not considering the ITZ. Unfortunately, even when modeling the latter, the expected features were not observed, due to a ITZ assignment only in terms of volume fraction, instead of local (or average) thickness. The FE discretizations needed to capture both the entire aggregate PaSD and the ITZ are too high.

When considering the unified frameworks, some general conclusion may be drawn, and this work contribution may appear more clear.

Most importantly, it has been highlighted that at the CP scale, when considering transport phenomena, the pore description is of prime importance. Historically, analytic or numeric models considered only the volume fractions of the various phases, but as it was not sufficient, the size distributions had to be incorporated, as well as arbitrary percolation thresholds. In the particular case of CP, the presented results tends to show that even a good description of those two parameters is probably not enough, and further morphological properties need to be controlled, like the constrictivity, the tortuosity, or the pore phase connectivity.

Those parameters are not easy to define and even less to control. They might arise naturally if more "physics" were to be incorporated in the hydration model, with *e.g.* precipitation / dissolution / nucleation phenomena. However, it would require additional developments within the morphological framework, to be able to yield such nucleus and let them "grow".

Further developments:

It is the authors belief that an iterative description of the hydration process, allowing the various hydrates embedment resulting in a more tortuous hydrate phase ; coupled with morphological enhancement (covariance CRFs underlying functions, towards increased roughness for the yielded morphologies), especially for the pore phase description which is a key feature to forecast more accurately diffusive properties at the CP scale, and thus throughout the entire framework.

In addition, a duality between the morphological and FE discretizations is observed, and the transition step from one to the other results in a loss of information. Morphological description can be made – given the use of the right software, *e.g.* "**R**" for the CRFs generation – almost as fine as wanted, but the FE solvers are yet limited. The multi-scale approach allows to bridge the gap between consecutive scales, however, for some given scales, like the cement paste, further discretizations are probably needed to enhance the results without considering lower scales. Only new approaches, like the Fast Fourier Transform (FFT) solvers [Brisard and Dormieux, 2010], or domain decomposition techniques, are able to solve linear problems with discretizations over 512×10^6 dofs, keeping a "reasonable" computation time.

Another key feature not incorporated in the present work, is the accounting of the relative humidity or saturation degree of the pore space. It is well known that in

non-saturated pores, the diffusion occurs at very different rates. Further studies in the spirit of [Zhang et al., 2014a] should be undertaken, with a first set of simulations to establish the RH balance, and only then consider diffusion phenomena with the two distinct rate of diffusion in liquid phase and gaz phase.

Finally, as throughout this study only pure diffusion was considered, such type of model needs to be coupled with fluid flow transport modeling, as found in [Jourdain, 2014, Massart and Selvadurai, 2014] in the pore space and / or (micro-) crack network, to perform meaningful durability assessments.

Appendices

A Percolation RVE

Percolation theory deals with connectivity issues on random stochastic patterns. First expressed by [Broadbent and Hammersley, 1957] as a statistical-geometry model, percolation was used to study a fluid flow through a rock where it was assumed to be a network of channels randomly open or close. These problems are often treated with lattice discretization of the space. Arbitrary rules (often referred as bond or site percolation) can be set in order to define clusters (open path) on those lattices. Accordingly, elements of the lattice have two states: *open* or *close*. For example, the *bond percolation* in two-dimensional models a path between two vertices by a Bernoulli distribution of parameter p. Hence, each edge is independent and has a probability p to be open and $1-p$ to be close. The quantity of interest in order to define whether a lattice is percolated or not is defined by a critical probability p_c which has the two followings properties:

If $p < p_c$
: There is a probability one chance that all clusters are finite. The lattice is not percolated.

If $p > p_c$
: There is a positive probability that a given point of the lattice is in an infinite cluster. The lattice is percolated.

This first approach presents a lot of issues. First, most of the literature cases consider infinite size problems (which is mathematically correct, but is only an approximation in applied cases). Second, the definition of a percolation cluster (a subset of connected bonds) is also made on infinite size problems. It is usually defined by the presence of an unbounded cluster, or equivalently by a continuous path from the origin to an infinitely distant point. Again, in finite size problems, these definitions have to be revised. Furthermore, these problems are subjected to lattice dependency. However, the latter problem can be dealt with by defining volumes around edges (or vertices) in order to phase out the discrete aspect of lattices. It is the first step into the continuum percolation field where instead of looking at the critical probability p_c, a critical volume fraction Φ_c (which has the same properties) is considered. First expressed in [Scher and Zallen, 1970] it is admitted that in a three-dimensional space:

$$\Phi_c \approx 16\%. \tag{A.1}$$

Most of the time, no analytic solution is known to solve these problems leading to an expensive need of numerical resources.

Given that it has been established that the topological information carried by the Euler characteristic is intrinsically linked with percolation ([Tomita and Murakami, 1994] and [Okun, 1990], where a critical volume fraction is deduced for infinite size problems analytically), a link can be made with excursion sets using the theoretical framework of Robert Adler. This section proposes the same approach but with the bound corrections introduced by [Worsley, 1996], aptly representing finite size domains. A side effect can then be observed giving the possibility of defining a statistical RVE for percolation.

1 Accounting for side effects

Herein, excursion sets are defined by Gaussian correlated Random Field over a three-dimensional cube M of finite size T. Among the four LKCs that characterize the excursion morphology, only the Euler characteristic χ and the volume fraction Φ are considered. Expected values of these measures are calculated through equation (2.17). As for the previous cases, the domain size has to be compared to the excursion set correlation length L_c. Hence, analysis will be made in terms of the ratio α:

$$\alpha = \frac{L_c}{T}. \tag{A.2}$$

The link between percolation and the Euler characteristic is stated to be when the later chnage signs. Most of the time it occurs two times and represents two different percolation states as depicted in figure 2.6(b) of A.3. The two underlying level sets are noted u_{p^+} and u_{p^-} and correspond to the followings situations:

Percolation of the excursion set at $\chi(u_{p^+}) = 0$
: By considering a high level set value, the corresponding excursion set is made of small disconnected components. As the level set value decreases, those components grow and others appear making the Euler characteristic increase up to a certain maximum point. It corresponds to the coalescence of the biggest components. The critical point of interest u_{p^+} is for a level set value just below the latter states, where the EC is null. It is stated that at this stage, the excursion set is percolated.

Percolation of the voids at $\chi(u_{p^-}) = 0$
: The same reasoning can be made in order to define the other percolation point. This time, increasing level sets starting at a very low value has to be

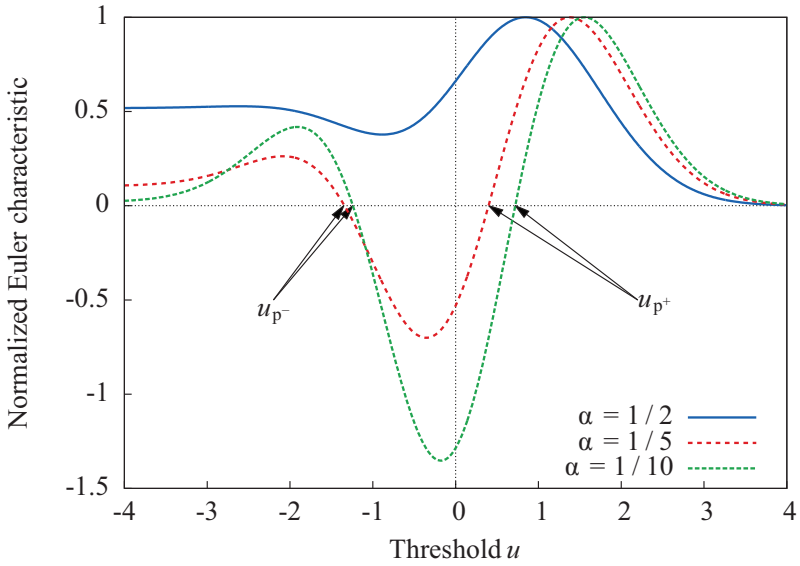

Figure A.1: Expectations of the normalized EC in terms of threshold, for Gaussian excursion sets – *from* [Roubin, 2013].

considered. The percolation point u_{p^-} is also for the first null value of the Euler characteristic and corresponds to the percolation of the voids.

As one can notice on Fig. A.3, for some values of α, percolation can not be defined ($\alpha = 1/2$ for example). Since the Euler characteristic is always positive, the volumes considered are too small to bring any relevant statistical information in terms of percolation states. However, in the other cases (for smaller α) attention is drawn to the corresponding critical volume fractions $\Phi(u_{p^+})$ and $\Phi(u_{p^-})$. Fig. A.2 shows both in terms of α. A border exists between two states, one with positive values of χ (outside) and the another with negative values (inside). The fact that the two curves diverge from their asymptotic values ($\alpha \ll 1$) and finally meet is a direct representation of side effects. It is analytically taken into account by the bound corrections [Worsley, 1996]. As the topology of an excursion can be determined whether it is inside or outside, this graph can be seen as a *phase diagram*. Unfortunately, the Euler characteristic does not give information whether positive values are due to holes in the excursion or to components. For example, an additional topological measure that counts the number of disconnected components of the excursion could define a third frontier, giving three topological states: disconnected excursion set and percolated voids ($\chi > 0$ due to components), both voids and excursion percolated ($\chi < 0$) or percolated excursion set and disconnected voids ($\chi > 0$ due to voids).

It can be seen that the asymptotic values that correspond to infinite domains are consistent with values from the literature obtained first by computer simulations [Skal et al., 1973, Lebowitz and Saluer, 1986], or by speculation on lattice problems [Zallen, 1979], and with the basic underlying symmetrical assumption:

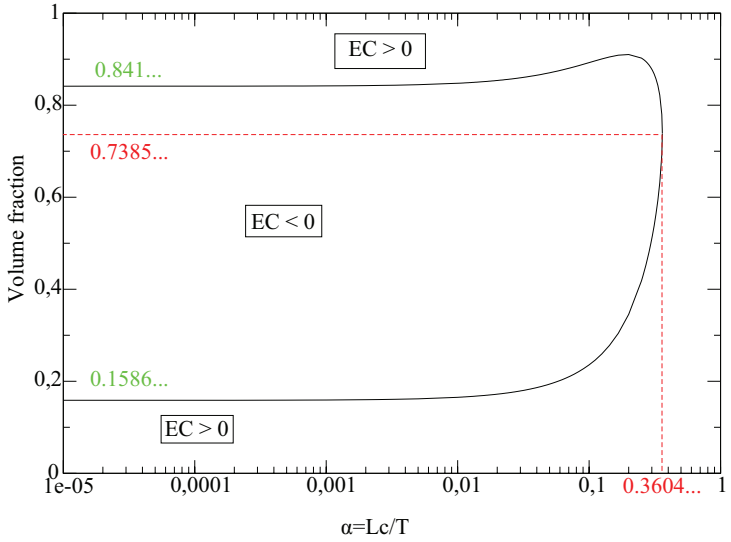

Figure A.2: Critical volume fractions with side effects for percolation of both excursion set and voids.

$$\lim_{\alpha\to 0} \Phi(u_{p^+}) = \Phi_c \approx 16\,\% \quad \text{and} \quad \lim_{\alpha\to 0} \Phi(u_{p^-}) = 1 - \Phi_c. \tag{A.3}$$

Then, as α grows, the critical volume fraction of the excursion set increases. This rather unintuitive feature can be interpreted by the fact that, in a finite size domain, there are less possible paths to link two distant points than in an infinite one. Hence, a higher volume fraction is needed. Furthermore, these stages lead to the loss of the relation $\Phi(u_{p^+}) + \Phi(u_{p^-}) = 1$, meaning that the symmetry hypothesis that exists on infinite size problems does not apply anymore.

In regards to these results, morphological RVE for percolation is now defined.

2 Representative Volume Element for percolation

Traditional approaches to define a RVE are based upon a certain number of realizations of a random media and the average properties measured for each realization (see [Kanit et al., 2003] work for detailed explanations). Theoretically, if the domain M is a RVE for a given property, the discrepancy of the results must vanish to zero. However, these RVE are usually too large to be handled numerically. Smaller realizations are thus made and from average values over all the realizations, lower and upper bounds can be defined [Huet, 1990b, Hazanov and Huet, 1994b]. Herein,

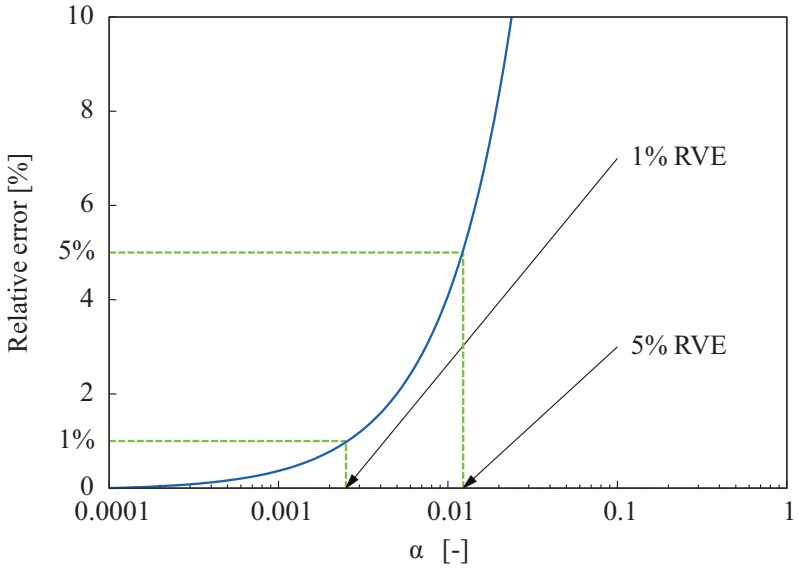

Figure A.3: Relative error between critical percolated volumes of finite and infinite size domains. – *from* [Roubin, 2013].

this statistical approach is embedded in the theoretical framework that gives the excursion set *expected* characteristics. Hence, no actual realization is computed.

Due to its monotonic shape, the RVE is defined in regards to the critical volumes of excursion set percolation $\Phi(u_{p^+})$ (and not the one corresponding to the voids), the reference value being Φ_c. The relative error between both (equation (A.4)) gives the RVE precision. Its evolution through scales is plotted Fig. A.3.

$$\epsilon = \frac{\Phi(u_{p^+}) - \Phi_c}{\Phi_c}. \tag{A.4}$$

Hence, a value of α can be determined for a given error. Results of table A.1 show that, for a given heterogeneity size L_c, a domaine size of more than 80 times L_c is needed for a 5% RVE and 400 times for 1% one.

ϵ	0%	1%	5%
$\Phi(u_{p^+})$	15.87	16.03	16.67
α	0	0.0025	0.012

Table A.1: Size ratio (α) and corresponding volume fraction (Φ) of 1% and 5% error RVE.

As far as the authors can tell, no RVE for percolation can be found in the applied science literature. However, it can be compared to classical mechanical problems linked with percolation issues such as diffusivity phenomena or permeation in cement paste material. On these matters, results are rather consistent and tend to define

RVE corresponding to a scale ratio of $\alpha = 1/100$. Among the vast literature on that subject, in [Zhang et al., 2011] the authors define a cement paste RVE for water diffusivity of $100\,\mu m^3$ with heterogeneities represented by a polydisperse spheres from $1\,\mu m$ to $50\,\mu m$. The RVE is then smaller than what the theory predicts. Several considerations can explain this difference. First, the property of interest differs. When the latter RVE is based on mechanical property (or transport property as diffusivity), the theory only takes into consideration the topological aspect of the morphology. Secondly, a size distribution of spheres is compared to an excursion set with one characteristic length.

Other authors, in different applied sciences, used the very same RVE for numerous phenomena: elastic properties [Šmilauer and Bittnar, 2006], ionic diffusion [Kamali-Bernard et al., 2009], permeability of concrete [Du and Ostoja-Starzewski, 2006] *etc.*Since all those physical phenomena are driven by percolation, authors believe that in order to avoid the bound estimation [Huet, 1990a], one can use RVE with $\alpha \geq 1/400$ to be within a 1% margin error.

Bibliography

[Abyaneh et al., 2013] Abyaneh, S. D., Wong, H., and Buenfeld, N. (2013). Modelling the diffusivity of mortar and concrete using a three-dimensional mesostructure with several aggregate shapes. *Computational Materials Science*, 78(0):63 – 73. 116, 156

[Adler, 2008] Adler, R. (2008). Some new random field tools for spatial analysis. *Stochastic Environmental Research and Risk Assessment*, 22. 3, 48, 56, 60, 91

[Adler and Taylor, 2007] Adler, R. J. and Taylor, J. E. (2007). *The Geometry of Random Fields*. Springer, Boston. 48, 56, 57, 59, 60, 164

[Allen et al., 1982] Allen, A., Windsor, C., Rainey, V., Pearson, D., Double, D., and Alford, N. (1982). A small-angle scattering study of cement porosities. *Journal of Physics D.*, V5(9):1817–1833. 34

[Amiri et al., 2001] Amiri, O., At-Mokhtar, A., Dumargue, P., and Touchard, G. (2001). Electrochemical modelling of chlorides migration in cement based materials. part ii: Experimental studycalculation of chlorides flux. *Electrochimica Acta*, 46(23):3589 – 3597. 101

[Baroghel Bouny, 1994] Baroghel Bouny, V. (1994). *Caractérisation des pâtes de ciment et des bétons : Méthodes, analyse, interprétation*. PhD thesis, École Nationale des POnts et Chaussées, France. 6, 38, 134

[Baroghel-Bouny, 2007a] Baroghel-Bouny, V. (2007a). Water vapour sorption experiments on hardened cementitious materials: Part i: Essential tool for analysis of hygral behaviour and its relation to pore structure. *Cement and Concrete Research*, 37(3):414 – 437. 30, 37, 38, 134

[Baroghel-Bouny, 2007b] Baroghel-Bouny, V. (2007b). Water vapour sorption experiments on hardened cementitious materials: Part ii: Essential tool for assessment of transport properties and for durability prediction. *Cement and Concrete Research*, 37(3):438 – 454. 37

[Barret et al., 1951] Barret, E., Joyner, L., and Halnda, P. (1951). The determination of pore volume and area distributions in porous substances. i computations

from nitrogen isotherms. *Journal of the American Chemical Society*, 73:373–380. 30

[Béjaoui et al., 2006] Béjaoui, S., Bary, B., Nitsche, S., Chaudanson, D., and Blanc, C. (2006). Experimental and modeling studies of the link between microstructure and effective diffusivity of cement pastes. *Revue européenne de génie civil*, 10(9):1073–1106. 82, 102, 103

[Benboudjema, 2012] Benboudjema, F. (2012). Prédiction de la diffusivité effective dans les matériaux à matrice cimentaires - comparaison entre des approches analytiques et numériques. Areva report, LMT. 118, 119

[Benkemoun, 2010] Benkemoun, N. (2010). *Contribution aux approches multi-échelles séquencées pour la modélisation numérique des matériaux à matrice cimentaire*. PhD thesis, École Normale Supérieure de Cachan, Cachan, FRANCE. 128

[Benkemoun et al., 2010] Benkemoun, N., Hautefeuille, M., Colliat, J.-B., and Ibrahimbegovic, A. (2010). Failure of heterogeneous materials : 3d meso-scale fe models with embendded discontinuities. *International Journal of Numerical Methods in Engineering*, pages 1671 – 1688. 119, 128, 129, 151

[Bentz, 1997] Bentz, D. (1997). Three dimensional computer simulation of portland cement hydration and microstructure development. *Journal of the American Ceramic Society*, 80(1). 66

[Bentz, 2005] Bentz, D. (2005). Cemhyd3d: A three-dimensional cement hydration and microstructure development modeling package. `http://concrete.nist.gov/monograph`. 66

[Bentz et al., 2000a] Bentz, D., Feng, X., Haecker, C.-J., and Stutzman, P. (2000a). Analysis of ccrl proficiency cements 135 and 136 using cemhyd3d. Internal report 6545, NIST. 7

[Bentz and Garboczi, 1991] Bentz, D. and Garboczi, E. (1991). A digitized simulation model for microstructural development. *Journal of the American Ceramic Society*, 16:211–226. 66

[Bentz et al., 1999] Bentz, D., Garboczi, E., Haecker, C., and Jensen, O. (1999). Effects of cement particle size distribution on performance properties of portland cement-based materials. *Cement and Concrete Research*, 29(10):1663 – 1671. 66

[Bentz et al., 1993] Bentz, D., Garboczi, E., and Stutzman, P. (1993). Computer modelling of the interfacial transition zone in concrete. *Interfaces in cementitious composites*, pages 259–268. 45

[Bentz et al., 2000b] Bentz, D., Jensen, O., Coats, A., and Glasser, F. (2000b). Influence of silica fume on diffusivity in cement-based materials: I. experimental and computer modeling studies on cement pastes. *Cement and Concrete Research*, 30(6):953 – 962. 114

[Bentz and Stutzman, 1994] Bentz, D. and Stutzman, P. (1994). Sem analysis and computer modeling of hydration of portland cement. *Petrography of Cementitious Materials*, pages 60–73. 7

[Bogue, 1952] Bogue, R. (1952). *La chimie du ciment Portland*. Édition Eyrolles. 7, 8, 14

[Bolander and Berton, 2004] Bolander, J. J. and Berton, S. (2004). Simulation of shrinkage induced cracking in cement composite overlays. *Cement and Concrete Composites*, 26(7):861 – 871. 2

[Bourbatache et al., 2013] Bourbatache, K., Millet, O., Aït-Mokhtar, A., and Amiri, O. (2013). Chloride transfer in cement-based materials. part 1. theoretical basis and modelling. *International Journal for Numerical and Analytical Methods in Geomechanics*, 37(11):1614–1627. 100

[Bourdette et al., 1995] Bourdette, B., Ringot, E., and Ollivier, J. (1995). Modelling of the transition zone porosity. *Cement and Concrete Research*, 25(4):741 – 751. 42

[Briffaut and Benboudjema, 2013] Briffaut, M. and Benboudjema, F. (2013). *Numerical Analysis of Cracking Induced by Drying Shrinkage in Concrete using a Mesoscopic Approach: Influence of Aggregates Restraint and Skin Effect*, chapter 28, pages 243–250. ASCE. 107

[Brisard and Dormieux, 2010] Brisard, S. and Dormieux, L. (2010). Fft-based methods for the mechanics of composites: A general variational framework. *Computational Materials Science*, 49(3):663–671. 167

[Broadbent and Hammersley, 1957] Broadbent, S. R. and Hammersley, J. M. (1957). Percolation process, i and II. *Proc. Cambridge Philos. Soc.*, 53:629 645. 171

[Brun et al., 1977] Brun, M., Lallemand, A., Quinson, J.-P., and Eyraud, C. (1977). A new method for the simultaneous determination of the size and shape of pores: the thermoporometry. *Thermochimica Acta*, 21(1):59 – 88. 34

[Bullard et al., 2011] Bullard, J. W., Jennings, H. M., Livingston, R. A., Nonat, A., Scherer, G. W., Schweitzer, J. S., Scrivener, K. L., and Thomas, J. J. (2011). Mechanisms of cement hydration. *Cement and Concrete Research*, 41(12):1208 – 1223. Conferences Special: Cement Hydration Kinetics and Modeling, Quebec City, 2009; CONMOD10, Lausanne, 2010. 10

[Carcassès et al., 2005] Carcassès, M., Julien, S., and Schiettekate, A. (2005). Conclusions on the performance of materials based on chlortest project, resistance of concrete to chloride ingress - from laboratory to in-field performance. *European project CHLORTEST*. Alicante, December 2005. 107, 108

[Caré and Hervé, 2004] Caré, S. and Hervé, E. (2004). Application of a n-phase model to the diffusion coefficient of chloride in mortar. *Transport in Porous Media*, 56(2):119–135. 105, 108, 118, 160

[Chen, 2006] Chen, W. (2006). *Hydration of slag cement - Theory, Modeling and Application*. PhD thesis, University of Twente, The Netherlands. 10

[Christensen, 1991] Christensen, R. M. (1991). *Mechanics of composite materials*. Krieger Publishing Company. 112, 113

[Cook and Hover, 1999] Cook, R. and Hover, K. (1999). Mercury porosimetry of hardened cement pastes. *Cement and Concrete Research*, 29. 38, 39, 85, 87, 88

[Coussy, 2004] Coussy, O. (2004). *Poromechanics*. John Wiley & Sons. 6

[De Larrard, 2010] De Larrard, T. (2010). *Variability of concrete properties: experimental characterisation and probabilistic modelling for calcium leaching*. Theses, École Normale Supérieure de Cachan - Cachan. 108

[Diamond, 2000] Diamond, S. (2000). Mercury porosimetry : An inappropriate method for the measurement of pore size distributions in cement-based materials. *Cement and Concrete Composites*, 30:1517–1525. 32, 38, 40

[Diamond, 2004] Diamond, S. (2004). The microstructure of cement paste and concretea visual primer. *Cement and Concrete Composites*, 26(8):919 – 933. 26, 27, 38, 43

[Diamond and Huang, 2001] Diamond, S. and Huang, J. (2001). The itz in concrete–a different view based on image analysis and sem observations. *Cement and Concrete Composites*, 23(2):179–188. 42

[Dirrenberger et al., 2014] Dirrenberger, J., Forest, S., and Jeulin, D. (2014). Towards gigantic rve sizes for 3d stochastic fibrous networks. *International Journal of Solids and Structures*, 51(2):359 – 376. 140

[Djerbi et al., 2006] Djerbi, A., Bonnet, S., Khelidj, A., Baroghel-Bouny, V., and Rogel, J. (2006). Migrations des ions chlorures dans les bétons fissurés. In *Transfert 2006*. 109

[Do, 2008] Do, D. P. (2008). *Application des approches d'homogénéisation à l'étude des propriétés thermo-hydro-mécanique des roches – Application aux argilites*. PhD thesis, INPL – École Nationale Supérieure de Géologie de Nancy. 112

[Dormieux et al., 2006] Dormieux, L., Kondo, D., and Ulm, F.-J. (2006). *Microporomechanics*. John Wiley & Sons. 6

[Du and Ostoja-Starzewski, 2006] Du, X. and Ostoja-Starzewski, M. (2006). On the size of representative volume element for darcy law in random media. *Proc. R. Soc. A*, 462:29492963. 119, 176

[Eshelby, 1957] Eshelby, J. (1957). The determination of the elastic field of an ellipsoidal inclusion, and related problems. In *Proceedings of the Royal Society of London A: Mathematical, Physical and Engineering Sciences*, number 1226 in 241, pages 376–396. The Royal Society. 112

[Federer, 1959] Federer, H. (1959). Curvature measures. *Transactions of the American Mathematical Society*, pages 418–491. 55

[Feldman and Sereda, 1968] Feldman, R. and Sereda, P. (1968). A model for hydrated portland cement paste as deduced from sorption-length change and mechanical properties. *Matériaux et Construction*, 1(6):509–520. 23, 37

[Feyel and Chaboche, 2000] Feyel, F. and Chaboche, J.-L. (2000). Fe^2 multiscale approach for modelling the elastoviscoplastic behaviour of long fibre sic/ti composite materials. *Computer methods in applied mechanics and engineering*, 183(3):309–330. 1

[Francy and François, 2001] Francy, O. and François, R. (2001). Modélisation du transfert couplé ions chlore-humidité dans les matériaux cimentaires. *Revue française de génie civil*, 5(2-3):377–396. 109

[Gallé, 2001] Gallé, C. (2001). Effect of drying on cement-based materials pore structure as identified by mercury intrusion porosimetry. a comparative study between oven-, vacuum-, and freeze-drying. *Cement and Concrete Research*, 31. 30, 32, 38, 41, 85

[Garboczi and Bentz, 1992] Garboczi, E. and Bentz, D. (1992). Computer simulation of the diffusivity of cement-based materials. *Journal of Materials Science*, 27(8):2083–2092. 43, 113, 115

[Garboczi and Bentz, 1996] Garboczi, E. and Bentz, D. (1996). The effect of the interfacial transition zone on concrete properties: the dilute limit. *Material for the new millennium*, 2:1228–37. 45

[Garrault-Gauffinet and Nonat, 1999] Garrault-Gauffinet, S. and Nonat, A. (1999). Experimental investigation of calcium silicate hydrate (c-s-h) nucleation. *Journal of Crystal Growth*, 200(34):565 – 574. 9

[Geuzaine and Remacle, 2009] Geuzaine, G. and Remacle, J.-F. (2001-2009). Gmsh home page. `http://www.geuz.org/gmsh`. 127

[Grassl, 2009] Grassl, P. (2009). A lattice approach to model flow in cracked concrete. *Cement and Concrete Composites*, 31(7):454–460. 1

[Guillon, 2004] Guillon, E. (2004). *Durability of cement-based materials : modeling of the influence of physical and chemical equilibria on the microstructure and the residual mechanical properties*. Theses, École normale supérieure de Cachan - ENS Cachan. 114

[Halperin et al., 1994] Halperin, W., Jehng, J.-Y., and Song, Y.-Q. (1994). Application of spin-spin relaxation to measurement of surface area and pore size distributions in a hydrating cementntz paste. *Magnetic Resonance Imaging*, 12(2):169 – 173. Proceedings of the Second International Meeting on Recent Advances in {MR} Applications to Porous Media. 35

[Hashin and Shtrikman, 1963] Hashin, Z. and Shtrikman, S. (1963). A variational approach to the theory of the elastic behaviour of multiphase materials. *Journal of the Mechanics and Physics of Solids*, 11(2):127 – 140. 111

[Hautefeuille et al., 2009] Hautefeuille, M., Melnyk, S., Colliat, J.-B., and Ibrahimbegovic, A. (2009). Failure model of heterogeneous structures using structured meshes and accounting for probability aspects. *Engineering Computation*, 26:??? 128

[Hazanov and Huet, 1994a] Hazanov, S. and Huet, C. (1994a). Order relationships for boundary conditions effect in heterogeneous bodies smaller than representative volume. *J. Mech. Phys. Solids*, 42:1995–2001. 121

[Hazanov and Huet, 1994b] Hazanov, S. and Huet, C. (1994b). Order relationships for boundary conditions eect in heterogeneous bodies smaller than the representative volume. *Journal of the Mechanics and Physics of Solids*, 43(42):1995–2011. 174

[Hershey, 1954] Hershey, A. (1954). The elasticity of an isotropic aggregate of anisotropic cubic crystals. *Journal of applied mechanics - Transaction of the ASME*, 21(3):236–240. 113

[Hill, 1963] Hill, R. (1963). Elastic properties of reinforced solids: Some theoretical principles. *Journal of the Mechanics and Physics of Solids*, 11. 3, 119, 120, 152

[Hill, 1965] Hill, R. (1965). A self-consistent mechanics of composite materials. *Journal of the Mechanics and Physics of Solids*, 13(4):213–222. 113

[Hoshino, 1988] Hoshino, M. (1988). Difference of the w/c ratio, porosity and microscopical aspect between the upper boundary paste and the lower boundary paste of the aggregate in concrete. *Materials and Structures*, 21(5):336–340. 42

[Huet, 1990a] Huet, C. (1990a). Application of variational concepts to size effects in elastic heterogeneous bodies. *J. Mech. Phys. Solids*, 38:813–841. 121, 176

[Huet, 1990b] Huet, C. (1990b). Application of variational concepts to size eects in elastic heterogeneous bodies. *Journal of the Mechanics and Physics of Solids*, 21(43):813–841. 174

[Jennings, 2004] Jennings, H. (2004). Colloid model of c-s-h and implications to the problem of creep and shrinkage. *Materials and Structures*, 37. 24

[Jennings and Johnson, 1986] Jennings, H. and Johnson, S. (1986). Simulation of microstructure development during the hydration of a cement compound. *Journal of the American Ceramic Society*, 69(11):790–795. 66

[Jennings and Pratt, 1979] Jennings, H. and Pratt, P. (1979). On the hydration of portland cement. *Proceedings of British Ceramic Society*, 28. 9

[Jennings and Tennis, 1994] Jennings, H. and Tennis, P. (1994). Model for the developing microstructure in portland cement pastes. *Journal of the American Ceramic Society*, 77(12). 14, 15, 17, 19, 134

[Jensen, 1993] Jensen, O. (1993). Autogenous deformation and rh-changeself-desiccation and self-desiccation shrinkage. appendix-measurements and notes (in danish). Technical Report 92, The Technical Universuity of Denmark. 13

[Jerauld and Salter, 1990] Jerauld, G. and Salter, S. (1990). The effect of pore-structure on hysteresis in relative permeability and capillary pressure: pore-level modeling. *Transport in porous media*, 5(2):103–151. 1

[Jiang et al., 2002] Jiang, M., Jasiuk, I., and Ostoja-Starzewski, M. (2002). Apparent thermal conductivity of periodic two-dimensional composites. *Computational Materials Science*, 25(3):329–338. 119

[Jourdain, 2014] Jourdain, X. (2014). *Étude numérique meso-macro des propriétés de transfert des bétons fissurés*. PhD thesis, LMT Cachan, France. 128, 168

[Juenger et al., 2003] Juenger, M., Lamour, V., Monteiro, P., Gartner, E., and Denbeaux, G. (2003). Direct observation of cement hydration by soft x-ray transmission microscopy. *Journal of Materials Science Letters*, 22(19):1335–1337. 35

[Juenger et al., 2005] Juenger, M., Monteiro, P., Gartner, E., and Denbeaux, G. (2005). A soft x-ray microscope investigation into the effects of calcium chloride on tricalcium silicate hydration. *Cement and Concrete Research*, 35(1):19 – 25. 35

[Justnes et al., 1992a] Justnes, H., E.J., S., and Lundevall, G. (1992a). High strength and concrete binders part a: Reactivity and composition of cement pastes with and without condensed silica fume. *Journal of the Amercain Ceramic Society*, pages 873–89. Cited by Monge. 18

[Justnes et al., 1992b] Justnes, H., Meland, I., Bjooergum, O., and Krane, J. (1992b). The mechanism of silica fume action in concrete studied by solid state ^{29}si nmr. *NMR Seminar*. Cited by Monge. 18

[Kamali-Bernard and Bernard, 2009] Kamali-Bernard, S. and Bernard, F. (2009). Effect of tensile cracking on diffusivity of mortar: 3d numerical modelling. *Computational Materials Science*, 47(1):178–185. 156

[Kamali-Bernard et al., 2009] Kamali-Bernard, S., Bernard, F., and Prince, W. (2009). Computer modelling of tritiated water diffusion test for cement based materials. *Computational Materials Science*, 45:528535. 116, 143, 159, 176

[Kanaun and Levin, 1994] Kanaun, S. and Levin, V. (1994). Effective field method in mechanics of matrix composite materials. In *Advances in mathematical modeling of composite materials*, volume 15, pages 1–58. World Scientific Singapore. 113

[Kanit et al., 2003] Kanit, T., Forest, S., Galliet, I., Mounoury, V., and Jeulin, D. (2003). Determination of the size of the representative volume element for random composites: statistical and numerical approach. *International Journal of solids and structures*, 40(13):3647–3679. 62, 119, 141, 174

[Kasiotis and Hautefeuille, 2008] Kasiotis, C. and Hautefeuille, M. (2008). cofeap's manual. `http://www.lmt.ens-cachan.fr/cofeap/files/cofeap_manual.pdf`. 129

[Knudsen, 1984] Knudsen, T. (1984). The dispersion model for hydration of portland cement i. general concepts. *Cement and Concrete Research*, 14(5):622 – 630. 15

[Kolmogorov, 1950] Kolmogorov, A. N. (1950). *Foundations of the Theory of Probability*. Chelsea Publishing Co. 49

[Korb, 2010] Korb, J.-P. (2010). Multi-scales nuclear spin relaxation of liquids in porous media. *Comptes Rendus Physique*, 11(2):192 – 203. 35, 37, 38, 45, 110, 135, 136

[Korb et al., 1994] Korb, J.-P., Delville, A., Xu, S., and Jonas, J. (1994). Nuclear relaxation of liquids in confinements. *Magnetic Resonance Imaging*, 12(2):179 – 181. Proceedings of the Second International Meeting on Recent Advances in {MR} Applications to Porous Media. 35, 37

[Korb et al., 2007a] Korb, J.-P., McDonald, P., Monteilhet, L., Kalinichev, A., and Kirkpatrick, R. (2007a). Comparison of proton field-cycling relaxometry and molecular dynamics simulations for protonwater surface dynamics in cement-based materials. *Cement and Concrete Research*, 37(3):348 – 350. Cementitious Materials as model porous media: Nanostructure and Transport processes July 2005, Centro Monte Verita, Switzerland. 110

[Korb et al., 2007b] Korb, J.-P., Monteilhet, L., McDonald, P., and Mitchell, J. (2007b). Microstructure and texture of hydrated cement-based materials: A proton field cycling relaxometry approach. *Cement and Concrete Research*, 37(3):295 – 302. Cementitious Materials as model porous media: Nanostructure and Transport processes July 2005, Centro Monte Verita, Switzerland. 110

[Korb et al., 1998] Korb, J.-P., Petit, D., Philippot, S., Zanni, H., Maret, V., and Cheyrezy, M. (1998). Nuclear relaxation of water confined in reactive powder concrete. In *Nuclear Magnetic Resonance Spectroscopy of Cement-based Materials*, pages 333–343. Springer. 3, 35

[Lange et al., 1994] Lange, D. A., Jennings, H. M., and Shah, S. P. (1994). Image analysis techniques for characterization of pore structure of cement-based materials. *Cement and Concrete Research*, 24(5):841 – 853. 38

[Larbi, 2013] Larbi, B. (2013). *Caractérisation du transport diffusif dans les matériaux à matrice cimentaires : Influence de la microstructure des mortiers*. PhD thesis, Université de Paris-Est, France. 94, 104, 107, 156, 157

[Lebowitz and Saluer, 1986] Lebowitz, J. L. and Saluer, H. (1986). Percolation in strongly correlated systems. *Physica*, 138A:194. 173

[Leemann et al., 2006] Leemann, A., Münch, B., Gasser, P., and Holzer, L. (2006). Influence of compaction on the interfacial transition zone and the permeability of concrete. *Cement and Concrete Research*, 36(8):1425–1433. 43

[Liu and Winslow, 1995] Liu, Z. and Winslow, D. (1995). Sub-distributions of pore size: A new approach to correlate pore structure with permeability. *Cement and Concrete Research*, 25(4):769 – 778. 33

[Loève, 1978] Loève, M. (1978). *Probability theory*. Number 43 in Graduate Texts in Mathematics. Springer-Verlag, 4 edition. 52

[Longuet et al., 1973] Longuet, P., Burglen, L., and Zelwer, A. (1973). La phase liquide du ciment hydraté. *Revue des Matériaux de Construction*, 676. 28

[Lura et al., 2003] Lura, P., Jensen, O. M., and van Breugel, K. (2003). Autogenous shrinkage in high-performance cement paste: An evaluation of basic mechanisms. *Cement and Concrete Research*, 33(2):223 – 232. Papers presented at the Fall 2001

Materials Research Society Symposium on Design, Characteristics and Properties of Cementitious Materials. 13

[MacTavish et al., 1996] MacTavish, J., Miljkovic, L., Peemoeller, H., Corbett, J., Jian, J., Lasic, D., Blinc, R., Lahajnar, G., Milia, F., and Pintar, M.-M. (1996). Nuclear magnetic resonance study of hydration of synthetic white cement: continuous quantitative monitoring of water and ca (oh) 2 during hydration. *Advances in Cement Research*, 8(32):155–161. 35

[Markovic et al., 2005] Markovic, D., Niekamp, R., Ibrahimbegovi, A., Matthies, H. G., and Taylor, R. L. (2005). Multiscale modeling of heterogeneous structures with inelastic constitutive behaviour. *Engineering Computations*, 22(5/6):664–683. 128

[Masoero et al., 2014] Masoero, E., Thomas, J. J., and Jennings, H. M. (2014). A reaction zone hypothesis for the effects of particle size and water-to-cement ratio on the early hydration kinetics of c3s. *Journal of the American Ceramic Society*, 97(3):967–975. 134

[Massart and Selvadurai, 2014] Massart, T. and Selvadurai, A. (2014). Computational modelling of crack-induced permeability evolution in granite with dilatant cracks. *International Journal of Rock Mechanics and Mining Sciences*, 70(0):593 – 604. 2, 168

[Matheron, 1967] Matheron, G. (1967). *Élements pour une théorie des milieux poreux*. Masson, Paris, FRANCE. 61

[Matheron, 1973] Matheron, G. (1973). The intrinsic random functions and their applications. *Advances in Applied Probability*, 5:439–468. 52

[Meakin, 1985] Meakin, P. (1985). Off lattice simulations of cluster-cluster aggregation in dimensions 2-6. *Physics Letters A*, 107:269–272. 66

[Mecke et al., 1993] Mecke, K. R., Buchert, T., and Wagner, H. (1993). Robust morphological measures for large-scale structure in the universe. *arXiv preprint astro-ph/9312028*. 56

[Mehta and Monteiro, 2005] Mehta, P. K. and Monteiro, P. J. M. (2005). *Concrete: Microstructure, Properties, and Materials*. McGraw-Hill, New York, U.S.A., 3 edition. 6, 7, 8, 22, 25, 27

[Mejlhede, 1999] Mejlhede, J. (1999). Chloride ingress in cement paste and mortar. *Cement and Concrete Research*, 29(9). 102

[Mills, 1966] Mills, R. (1966). Factors influencing cessation of hydration in water cured cement pastes. In Board, H. R., editor, *Symposium on Strucure of Portland Cement Paste and concrete*, volume 90. 18

[Mindess et al., 2003] Mindess, S., Young, J. F., and Darwin, D. (2003). *Concrete*. Upper Saddle River, NJ : Prentice Hall, 2 edition. 8, 19, 40

[Moës et al., 2003] Moës, N., Cloirec, M., Cartaud, P., and Remacle, J.-F. (2003). A computational approach to handle complex microstructure geometries. *Computational Methods in applied Mechanics and Engineering*, 192:3163–3177. 127

[Moës et al., 1999] Moës, N., Dolbow, J., and Belytschko, T. (1999). A finite element method for crack growth without remeshing. *International Journal of Numerical Methods in Engineering*, 46:131–150. 127

[Monteiro et al., 1985] Monteiro, P., Maso, J., and Ollivier, J. (1985). The aggregate-mortar interface. *Cement and Concrete Research*, 15(6):953 – 958. 42

[Mori and Tanaka, 1973] Mori, T. and Tanaka, K. (1973). Average stress in matrix and average elastic energy of materials with misfitting inclusions. *Acta metallurgica*, 21(5):571–574. 113

[Mura, 1987] Mura, T. (1987). *Micromechanics of defects in solids*, volume 3. Springer Science & Business Media. 112

[Ngala, 1995] Ngala, V. (1995). 1-diffusion in cementititous materials. 2- further investigation of chlorides and oxygen diffusion in well-cured opc and opc30. *Cement and Concrete Research*, 25. 102

[Niekamp, 1995] Niekamp, R. (1995). Component template library. `http://www.wire.tu-bs.de/forschung/projekte/ctl/`. 129

[Oberholster, 1986] Oberholster, R. (1986). Pore structure, permeability and diffusivity of hardened cement paste and concrete in relation to durability: status and prospects. In *8th International congress on chemistry of cement*, pages 323–335. 24

[Okun, 1990] Okun, B. L. (1990). Euler characteristic in percolation theory. *Journal of Statistical Physics*, 59(1/2):523–527. 172

[Oliver et al., 2006] Oliver, J., Huespe, A. E., and Sánchez, P. J. (2006). A comparative study on finite elements for capturing strong discontinuities : E-fem vs x-fem. *Computer Methods in Applied Mechanics and Engineering*, 195:4732–4752. 128

[Ollivier and Torrenti, 2008] Ollivier, J. and Torrenti, J. (2008). *La structure poreuse des bétons et les propriétés de transfert*. Presses de l'École Nationale des Ponts et Chaussées. 29, 109

[Ollivier and Vichot, 2008] Ollivier, J. and Vichot, A., editors (2008). *La durabilités des bétons*. Presses de l'École Nationale des Ponts et Chaussées. 28

[Olson and Jennings, 2001] Olson, R. and Jennings, H. (2001). Estimation of c-s-h content in a blended cement paste using water adsorption. *Cement and Concrete Research*, 31(3):351 – 356. 134

[Olson et al., 1997] Olson, R. A., Neubauer, C. M., and Jennings, H. M. (1997). Damage to the pore structure of hardened portland cement paste by mercury intrusion. *Journal of the American Ceramic Society*, 80(9):2454–2458. 33

[Ortiz, 1987] Ortiz, M. (1987). A finite element method for localized failure analysis. *Computer Methods in Applied Mechanics and Engineering*, 61:189–214. 127, 128

[Ostoja-Starzewski and Schulte, 1996] Ostoja-Starzewski, M. and Schulte, J. (1996). Bounding of effective thermal conductivities of multiscale materials by essential and natural boundary conditions. *Physical Review B*, 54(1):278. 119

[Parrott et al., 1990] Parrott, L. J., Geiker, M., Gutteridge, W. A., and Killoh, D. (1990). Monitoring portland cement hydration: Comparison of methods. *Cement and Concrete Research*, 20(6):919 – 926. 18

[Pellenq et al., 2009] Pellenq, R. J.-M., Kushima, A., Shahsavari, R., Van Vliet, K. J., Buehler, M. J., Yip, S., and Ulm, F.-J. (2009). A realistic molecular model of cement hydrates. *Proceedings of the National Academy of Sciences*, 106(38):16102–16107. 110

[Pierret et al., 2002] Pierret, A., Capowiez, Y., Belzunces, L., and Moran, C. (2002). 3d reconstruction and quantification of macropores using x-ray computed tomography and image analysis. *Geoderma*, 106(34):247 – 271. 31

[Powers and Brownyard, 1947] Powers, T. and Brownyard, T. (1947). Studies of the physical properties of hardened portland cement paste. *Journal of the American Concrete Institute*, 43. 11, 12, 17, 23, 40, 134

[Prince et al., 1999] Prince, W., Ollivier, J.-P., and Truc, O. (1999). Aspects électrochimiques de l'essai accéléré de perméabilité aux ions chlorures. *Materials and Structures*, 32(4):243–251. 100

[Promentilla et al., 2009] Promentilla, M., Sugiyama, T., Hitomi, T., and Takeda, N. (2009). Quantification of tortuosity in hardened cement pastes using synchrotron-based x-ray computed microtomography. *Cement and Concrete Research*, 39(6):548 – 557. 35, 89

[Richet, 1992] Richet, C. (1992). *Étude de la migration des radioéléments dans les liants hydrauliques – Influence du vieillissement des liants sur les mécanismes et la cinétique de transferts*. PhD thesis, Université Paris XI Orsay, France. 82, 97, 102

[Richet et al., 2004] Richet, C., Gallé, C., Le Bescop, P. ans Peycelon, H., Béjaoui, S., Tovena, I., L'HositsV?, and Lovera, P. (2004). Synthèse des connaissances sur le comportement à long terme des bétons: applications aux colis cimentés. Technical Report CEA-R-6050, CEA Saclay. 94

[Roscoe, 1952] Roscoe, R. (1952). The viscosity of suspensions of rigid spheres. *British Journal of Applied Physics*, 3(8):267. 113

[Roubin, 2013] Roubin, E. (2013). *Meso-scale FE and morphological modeling of heterogeneous media: application to cementitious materials*. PhD thesis, LMT Cachan, France. 48, 52, 57, 58, 60, 91, 128, 129, 130, 152, 173, 175

[Roubin et al., 2015] Roubin, E., Colliat, J.-B., and Benkemoun, N. (2015). Meso-scale modeling of concrete: A morphological description based on excursion sets of random fields. *Computational Materials Science*, 102(0):183 – 195. 56, 164

[Sadouki and Van Mier, 1997] Sadouki, H. and Van Mier, J. (1997). Meso-level analysis of moisture flow in cement composites using a lattice-type approach. *Materials and Structures*, 30(10):579–587. 1

[Saglik, 1992] Saglik, A. (1992). *A Mathematical Model for the Kinetics of Portland Cement Hydration*. PhD thesis, Northwestern University, Evanston, IL. 15

[Scher and Zallen, 1970] Scher, H. and Zallen, R. (1970). Critical density in percolation process. *J. Chem. Phys.*, 53:3759. 171

[Scrivener, 2004] Scrivener, K. (2004). Backscattered electron imaging of cementitious microstructures: understanding and quantification. *Cement and Concrete Composites*, 26. 24

[Scrivener et al., 1988] Scrivener, K., Bentur, A., and Pratt, P. (1988). Quantitative characterization of the transition zone in high strength concretes. *Advances in Cement Research*, 1:230–237. 31

[Scrivener and Nemati, 2004] Scrivener, K. and Nemati (2004). The percolation of pore space in the cement paste / aggregate interfacial zone of concrete. *Cement and Concrete Research*, 26. 44

[Scrivener et al., 2004] Scrivener, K. L., Crumbie, A. K., and Laugesen, P. (2004). The interfacial transition zone (itz) between cement paste and aggregate in concrete. *Interface Science*, 12(4):411–421. 42

[Scrivener and Nemati, 1996] Scrivener, K. L. and Nemati, K. M. (1996). The percolation of pore space in the cement paste/aggregate interfacial zone of concrete. *Cement and Concrete Research*, 26(1):35–40. 42

[Sen, 2004] Sen, P. N. (2004). Time-dependent diffusion coefficient as a probe of geometry. *Concepts in Magnetic Resonance Part A*, 23(1):1–21. 89

[Serra, 1982] Serra, J. (1982). *Image analysis and mathematical morphology*. Academic Press, London, U.K. 61

[Shen and Chen, 2007] Shen, L. and Chen, Z. (2007). Critical review of the impact of tortuosity on diffusion. *Chemical Engineering Science*, 62(14):3748–3755. 91

[Signes-Frehel et al., 1996] Signes-Frehel, M., Maes, P., and Haehnel, C. (1996). Etude des phases d'un clinker par diffractométrie des rayons x : vers la quantification. *Journal de Physique IV*, 06. 7

[Skal et al., 1973] Skal, A. S., Shkloviskii, B. I., and Efros, A. L. (1973). Percolation level in a three-dimensional random potential. *JETP Lett.*, 17:377. 173

[Stefan, 2009] Stefan, L. (2009). *Étude expérimentale et modélisation de l'évolution des propriétés mécaniques au jeune âge dans les matériaux cimentaires*. PhD thesis, École Normale Supérieure de Cachan - Université de Laval, France, Canada. 10, 15, 16, 116, 117

[Stefan et al., 2010] Stefan, L., Benboudjema, F., Torrenti, J.-M., and Bissonnette, B. (2010). Prediction of elastic properties of cement pastes at early ages. *Computational Materials Science*, 47(3):775 – 784. 118, 153

[Stora et al., 2008] Stora, E., Bary, B., and He, Q.-C. (2008). On estimating the effective diffusive properties of hardened cement pastes. *Transport in Porous Media*, 73(3):279–295. 113, 115

[Sugiyama et al., 2010] Sugiyama, T., Promentilla, M., Hitomi, T., and Takeda, N. (2010). Application of synchrotron microtomography for pore structure characterization of deteriorated cementitious materials due to leaching. *Cement and Concrete Research*, 40(8):1265 – 1270. 35

[Sugiyama et al., 2008] Sugiyama, T., Ritthichauy, W., and Tsuji, Y. (2008). Experimental investigation and numerical modeling of chloride penetration and calcium dissolution in saturated concrete. *Cement and Concrete Research*, 38(1):49 – 67. 102, 103

[Sukumar et al., 1999] Sukumar, N., Moës, D. L., and Belytshcko, T. (1999). Modeling holes and inclusions by level sets in the extended element method. *Computational Methods in applied Mechanics and Engineering*, 190:6183–6200. 127

[Tang, 2003] Tang, L. (2003). Chloride ingress in concrete exposed to marine environment - field data up to 10 years exposure. *European project CHLORTEST*, 16. Alicante, December 2005. 108

[Taylor, 1989] Taylor, H. (1989). Modification of the bogue calculation. *Advances in Cement Research*, 2(6):73 – 77. 7, 14

[Taylor, 1997] Taylor, H. (1997). *Cement Chemistry*. Thomas Telford, 2 edition. 7, 8, 9, 25

[Taylor et al., 2006] Taylor, J. E. et al. (2006). A gaussian kinematic formula. *The Annals of Probability*, 34(1):122–158. 56

[Taylor et al., 2015] Taylor, R., Sakdinawat, A., Chae, S. R., Wenk, H.-R., Levitz, P., Sougrat, R., and Monteiro, P. J. (2015). Developments in tem nanotomography of calcium silicate hydrate. *Journal of the American Ceramic Society*, pages n/a–n/a. 143

[Taylor, 2003] Taylor, R. L. (2003). Feap–a finite element analysis program. *Version 7.5 Theory Manual*. 129

[Tennis and Jennings, 2000] Tennis, P. and Jennings, H. (2000). A model for two types of calcium silicate hydrate in the microstructure of portland cement pastes. *Cement and Concrete Research*, 30. 16, 24, 25, 37, 134

[Tits et al., 2003] Tits, J., Jakob, A., Wieland, E., and Spieler, P. (2003). Diffusion of tritiated water and 22na+ through non-degraded hardened cement pastes. *Journal of Contaminant Hydrology*, 61(14):45 – 62. 8th Internation Conference on Chemistry and Migration Behaviour of Actinides and Fission Products in the Geosphere - Migration 01. 102

[Tognazzi, 1998] Tognazzi, C. (1998). *Couplage fissuration-dégradation chimique dans les matériaux cimentaires, caractérisation et modélisation*. PhD thesis, INSA Toulouse, Toulouse, France. 82, 102, 113, 114, 115

[Tomita and Murakami, 1994] Tomita, H. and Murakami, C. (1994). Percolation pattern in continuous media and its topology. In *Research of Pattern Formation*, page 197 203. R. Takaki, KTK scientific publishers edition. 172

[Truc and Ollivier, 2000] Truc, O. and Ollivier, J.-P.and Carcassès, M. (2000). A new way for determining the chloride diffusion coefficient in concrete from steady state migration test. *Cement and Concrete Research*, 30(2):217 – 226. 101

[Tuutti, 1982] Tuutti, K. (1982). Analysis of pore solution squeezed out of cement paste and mortar. *Nordic Concrete Research*. 96

[Underwood, 1970] Underwood, E. (1970). *Quantitative stereology*. Addison-Wesley series in metallurgy and materials. Addison-Wesley Pub. Co. 31

[Valckenborg et al., 2002] Valckenborg, R., Pel, L., and Kopinga, K. (2002). Combined nmr cryoporometry and relaxometry. *Journal of Physics D: Applied Physics*, 35(3):249 – 256. 37, 38

[van Breugel, 1997] van Breugel, K. (1997). *Simulation Hydration and Formation of Structure in Hardening Cement-Based Materials*. PhD thesis, Delft University of Technology, The Netherlands. 8, 11, 67

[Vercback and Helmuth, 1968] Vercback, G. and Helmuth, R. (1968). Structures and physical properties of hardened cement paste. In *5th International Symposium on the Chemistry of Cement*, pages 1–11. 21, 22

[Šmilauer and Bittnar, 2006] Šmilauer, V. and Bittnar, Z. (2006). Microstructure-based micromechanical prediction of elastic properties in hydrating cement paste. *Cement and Concrete Research*, 36(9):1708–1718. 176

[Vu, 2009] Vu, T.-H. (2009). *Caractérisation de la phase solide et transferts de gaz dans les milieux poreux insaturés. Etude expérimentale et modélisation appliquées à la diffusion de l'hydrogène dans les matériaux cimentaires*. PhD thesis, Université de Toulouse, Laboratoire Matériaux & Durabilité des Constructions, Toulouse, France. 31, 34, 37, 38, 43

[Waller, 1999] Waller, V. (1999). *Relationship between mix design of concrete, generation of heat during hydration and compressive strength*. PhD thesis, École Nationale de Ponts et Chaussées, Paris, France. 18

[Walther et al., 2015] Walther, E., Bogdan, M., Bennacer, R., and Desa, C. (2015). Cement paste morphologies and effective diffusivity: using the lattice boltzmann method. *Submitted to European Journal of Civil and Environmental Engineering*, page 100. 153

[Worsley, 1996] Worsley, K. J. (1996). The geometry of random images. *CHANCE*, 9(1):27–40. 172, 173

[Xu, 1995] Xu, K. (1995). *Structures multiechelles, Modèles pour la description des matériaux poreux et l'estimation de leurs propriétés de transport*. PhD thesis, Université Joseph Fourrier, Grenoble, France. 33

[Ye et al., 2003a] Ye, G., van Breugel, K., and Fraaij, A. (2003a). Experimental study and numerical simulation on the formation of microstructure in cementitious materials at early age. *Cement and Concrete Research*, 33(2):233 – 239. Papers presented at the Fall 2001 Materials Research Society Symposium on Design, Characteristics and Properties of Cementitious Materials. 68

[Ye et al., 2003b] Ye, G., van Breugel, K., and Fraaij, A. (2003b). Three-dimensional microstructure analysis of numerically simulated cementitious materials. *Cement and Concrete Research*, 33(2):215 – 222. Papers presented at the Fall 2001 Materials Research Society Symposium on Design, Characteristics and Properties of Cementitious Materials. 68

[Yoon and Monteiro, 2013] Yoon, S. and Monteiro, P. (2013). Molecular dynamics of water molecules in interlayer of 14a tobermorite. *Advanced Concrete Technology*, 11:180 – 188. 110

[Yoshida and Kishi, 2008] Yoshida, R. and Kishi, T. (2008). Proposal of a new approach for determination of pore continuity and suitable intrusion pressure based on step-by-step mercury intrusion porosimetry test. In *1st international conference on Microstructure Related Durability of Cementitious Composites*. 33

[Zallen, 1979] Zallen, R. (1979). *The Physics of Amorphous Solids*. John-Wiley and Sons. 173

[Zhang et al., 2011] Zhang, M., Ye, G., and van Breugel, K. (2011). Microstructure-based modeling of water diffusivity in cement paste. *Construction and Building Materials*, 25(42):2046–2052. 116, 117, 118, 143, 145, 176

[Zhang et al., 2012] Zhang, M., Ye, G., and van Breugel, K. (2012). Modeling of ionic diffusivity in non-saturated cement-based materials using lattice boltzmann method. *Cement and Concrete Research*, 42(11):1524 – 1533. 117

[Zhang et al., 2014a] Zhang, M., Ye, G., and van Breugel, K. (2014a). Multiscale lattice boltzmann-finite element modelling of chloride diffusivity in cementitious materials. part i: Algorithms and implementation. *Mechanics Research Communications*, 58(0):53 – 63. 117, 168

[Zhang et al., 2014b] Zhang, M., Ye, G., and van Breugel, K. (2014b). Multiscale lattice boltzmann-finite element modelling of chloride diffusivity in cementitious materials. part ii: Simulation results and validation. *Mechanics Research Communications*, 58(0):64 – 72. 117, 156

[Zhou et al., 2010] Zhou, J., Ye, G., and van Breugel, K. (2010). Characterization of pore structure in cement-based materials using pressurizationdepressurization cycling mercury intrusion porosimetry (pdc-mip). *Cement and Concrete Research*, 40(7):1120 – 1128. 33, 34, 45